UNIVERSITY OF OKLAHOMA

GRADUATE COLLEGE

Structural and Optical Properties of All-Inorganic and Hybrid Organic-Inorganic Metal (M = Zn, Cd, Hg, Cu) Halides

A DISSERTATION

SUBMITTED TO THE GRADUATE FACULTY

In partial fulfillment of the requirements for the

Degree of

DOCTOR OF PHILOSOPHY

By

RACHEL ROCCANOVA

Norman, Oklahoma

2019

Downloaded from SHAREOK. Persistent Handle URL: https://hdl.handle.net/11244/321076

STRUCTURAL AND OPTICAL PROPERTIES OF ALL-INORGANIC AND HYBRID ORGANIC-INORGANIC METAL (M = ZN, CD, HG, CU) HALIDES

A DISSERTATION APPROVED FOR THE
DEPARTMENT OF CHEMISTRY AND BIOCHEMISTRY

BY

Dr. Bayram Saparov, Chair

Dr. Daniel T. Glatzhofer

Dr. George Richter-Addo

Dr. Robert White

Dr. Ian Sellers

© Copyright by RACHEL ROCCANOVA 2019

All Rights Reserved.

ACKNOWLEDGEMENTS

None of this work would have been possible had it not been firstly for my advisor and mentor Dr. Bayram Saparov. Without his many ideas, enthusiasm and knowledge of solid-state chemistry I would have never had the chance to learn about, grow, and study these amazing materials. The opportunities that he has provided for me throughout this process to not only grow as a scientist but as a person, is something I will be forever grateful for. A portion of this work also would have never happened had it not been for Dr. Daniel Glatzhofer providing some of his many organic molecules and willing students to assist in creating some of these wonderful materials.

Secondly, I would like to thank my friends and lab family that I gained from moving all the way to Oklahoma. Without them, especially Dr. Kellye Cupp-Sutton and Dr. Matthew Houck, completing this work and program would have never been possible. Their continued support in both good and bad times always will be of great solace to me.

I will also forever be grateful for my undergraduate research mentees Simon Avery Vigil, Dillon Doss, Gavin Hettler, and Max McWhorter. Thank you all for the time that you spent learning about and making new compounds with me and of course, for all the time we spent having fun in the process.

Lastly, I would like to thank my parents and my husband—without whom I would not be here or have been able to complete this work. Moving half way across the country was hard for all of us, but without their continued support and encouragement none of this would have been possible. I would especially like to thank my husband, Scott, who provided the support and encouragement from the beginning to the end of this arduous journey.

ABSTRACT

All-inorganic and hybrid organic-inorganic metal halide materials, especially halide perovskites, have sparked the interest of the materials research community due to their excellent optoelectronic properties and their diverse tunable crystal structures and chemical compositions. $APbX_3$ (A = Cs, CH_3NH_3; X = Cl, Br, I) perovskites prepared decades ago are today's shining stars with $CH_3NH_3PbI_3$ attracting attention as a solar cell material, and $CsPbX_3$ and Cs_4PbX_6 as materials for radiation detector, display and lighting technology applications. Despite these notable achievements in the field, Pb-based perovskites suffer from lead toxicity and poor thermal, air and moisture stability which ultimately hamper their overall incorporation into marketable devices.

This dissertation largely focuses on non-Pb metal halide systems that have been underexplored in literature, primarily those based on group 11 and 12 metals (Cu, Zn, Cd and Hg). Thus, in **Chapter 2**, a summary of the results of investigations into the structural and optical properties of the $(CH_3NH_3)_2CdX_4$ (X = Cl, Br, I) family is provided in which we conclude that contrary to our expectations room temperature luminescence could not be achieved in this low-dimensional family. A summary of the studies on the $(C_5H_7N_2)_2MBr_4$ (X = Zn, Hg) family is also presented in **Chapter 2**, where we found that by substituting a known emissive organic cation, we could obtain materials that demonstrate room-temperature luminescence resulting from simultaneous emission from both organic and inorganic units. In **Chapter 3**, the incorporation of a large bulky cation in the R-M-X (R = $C_{15}H_{26}N$; M = Zn, Cd; X = Br, I) family is reported. As a result, room temperature luminescence with quantum efficiency values up to XXX was achieved. Interestingly, light emission in this family was found to originate mostly from the organic cations. In **Chapter 4**, we show that the concept of dimensional reduction can also be applied to all-inorganic halides with the preparation and characterization of compounds in the CsX-CuX (X =

Cl, Br, I) systems. Notable, the obtained materials include $Cs_3Cu_2I_5$ that demonstrates a near-unity quantum efficiency blue emission at room temperature. Finally, the dissertation is concluded in **Chapter 5** with a discussion of possible future directions.

Table of Contents

Chapter 1: Introduction to Luminescent Low-Dimensional Metal Halides 1
1.1 Introduction 1
1.2 Crystal Structures of Low-Dimensional Halides 5
1.2.1 Three-Dimensional Parent Structure 5
1.2.2 Lower-Dimensional Perovskite-Derived Structures 9
1.2.2.1 Two-Dimensional Perovskite Derivative Structures 10
1.2.2.2 One- and Zero-Dimensional Perovskite Derivative Structures 13
1.3 Optical Properties of Low-Dimensional Metal Halides 15
1.3.1 Electronic Band Structures 15
1.3.2 Electronic Density of States and Quantum Confinement 18
1.3.3 Luminescence in Low-Dimensional Metal Halides 22
1.3.3.1 Band-to-Band Absorption and the Concept of an Exciton 22
1.3.3.2 Elementary Excitons and the Effects of Quantum Confinement 23
1.3.3.2.1 Wannier-Mott and Frenkel Excitons 23
1.3.4 Photoluminescence of Low-Dimensional Halides 27
1.3.4.1 Self-trapped Excitons 29
1.4 Applications of Luminescence Metal Halides 34
1.4.1 Phosphors 37
1.4.2 Light Emitting Diodes (LEDs) 40
1.4.3 Scintillators 42
1.5 Beyond Lead Halide Perovskites 45
1.5.1 Bismuth and Antimony Based Metal Halides 46
1.5.2 Alternative Non-Pb Metal Halides 47
Chapter 2: Size Effects in Hybrid Group 12 Metal Halides 53
2.1 Methylammonium Cadmium Halides MA_2CdX_4 (X = Cl, Br, I) 54
2.1.1 Introduction 54
2.1.2 Synthesis and Methods of MA_2CdX_4 (MA = CH_3NH_3; X = Cl, Br, I) 57
2.1.2.1 Reactants 57
2.1.2.2 MABr and MAI Synthesis 57
2.1.2.3 MA_2CdX_4 Synthesis and Single Crystal Growth 57

2.1.2.4 Powder X-ray diffraction 58
2.1.2.5 Single Crystal X-ray diffraction 59
2.1.2.6 UV-vis Absorbance Measurements 60
2.1.2.7 Variable Temperature Photoluminescence Measurements 60
2.1.2.8 Electronic Structure Calculations 61
2.1.3 Room Temperature Crystal Structures 61
2.1.4 Variable Temperature X-ray Diffraction Studies 66
2.1.4.1 MA_2CdCl_4 67
2.1.4.2 MA_2CdBr_4 and MA_2CdI_4 68
2.1.5 Air and Moisture Stability 70
2.1.6 Optical Property Measurements 73
2.1.7 Band Structure Calculations 77
2.1.8 Summary 81
2.2 4-Aminopyridinium (4AMP) Zinc and Mercury Bromides $(4AMP)_2MBr_4$ (M = Zn, Hg) 83
2.2.1 Introduction 83
2.2.2 Synthesis and Methods of $4AMP_2Hg(Zn)Br_4$ 86
2.2.2.1 Reagents Used in the Synthesis of $4AMP_2Hg(Zn)Br_4$ 86
2.2.2.2 Synthesis and Crystal Growth of $4AMP_2Hg(Zn)Br_4$ 86
2.2.2.3 Single crystal X-ray diffraction 86
2.2.2.4 Powder X-ray diffraction 87
2.2.2.5 Thermal analysis 87
2.2.2.6 Optical Measurements 87
2.2.3 Crystal Structure 88
2.2.4 Ambient Air and Moisture and Thermal Stability 91
2.2.5 Optical Property Measurements 93
2.2.5 DFT Modeling 102
2.2.6 Summary 104
Chapter 3: Electronic Effects of the Organic Cation in Hybrid Group 12 Halide Systems 106
3.1 Introduction 107
3.2. Synthesis and Methods of $(C_{15}H_{26}N)$-M-X (M = Zn, Cd; X = Br, I) 109
3.2.1 Reagents Used in the Synthesis of $(C_{15}H_{26}N)$-M-X (M = Zn, Cd; X = Br, I) and $(C_{15}H_{26}N)$(Br, I) salts 109
3.2.2 Syntheses of $(C_{15}H_{26}N)_2MX_4$ (M = Zn, Cd; X = Br, I) compounds 110

3.2.2.1 Bromide-based compounds 110
3.2.2.2 Iodide-based compounds 110
3.2.3 Single Crystal X-ray Diffraction 111
3.2.4 Powder X-ray Diffraction 111
3.2.5 Energy Dispersive X-ray (EDX) Measurements 112
3.2.6 Optical Measurements 112
3.2.7 First Principles Calculations 113
3.3 Room and Low Temperature Crystal Structures 113
3.4 Stability studies 117
3.5 Optical properties 118
3.6 First-principle Calculations 128
3.7 Conclusion 132
Chapter 4: Low-Dimensional All-Inorganic Copper Halides $Cs_3Cu_2X_5$ and $CsCu_2X_3$ (X = Cl, Br, I) 134
4.1 Introduction 134
4.2 The $Cs_3Cu_2X_5$ (X= Br, I) System 137
4.2.1 Introduction 137
4.2.2 Synthesis and Methods of $Cs_3Cu_2X_5$ (X = Br, I) 138
4.2.2.1 Reagents Used in the Synthesis of $Cs_3Cu_2X_5$ (X=I, Br) 138
4.2.2.2 Synthesis of $Cs_3Cu_2X_5$ (X=I, Br) 138
4.2.2.3 Powder X-Ray Diffraction 138
4.2.2.4 Thermal Analysis 139
4.2.2.5 Optical Measurements 139
4.2.2.6 First Principle Calculations 139
4.2.3 Structure of $Cs_3Cu_2X_5$ (X = Br, I) 140
4.2.4 Stability of $Cs_3Cu_2X_5$ (X = Br, I) 144
4.2.5 Optical Properties of $Cs_3Cu_2X_5$ (X = Br, I) 148
4.2.6 Density Functional Theory Calculations for $Cs_3Cu_2X_5$ (X = Br, I) 153
4.3 The $CsCu_2X_3$ (X = Cl, Br, I) System 157
4.3.1 Synthesis and Methods for $CsCu_2X_3$ (X = Cl, Br, I) 157
4.3.1.1 Reagents Used in the Synthesis of $CsCu_2X_3$ (X = Cl, Br, I) 157
4.3.1.2 Synthesis of $CsCu_2X_3$ (X = Cl, Br, I) 157
4.3.1.3 Powder X-ray Diffraction 158

4.3.1.4 Thermal Analysis 158
4.3.1.5 Optical Measurements 158
4.3.2 $CsCu_2X_3$ (X = Cl, Br, I) Structure 159
4.3.3 Ambient and Thermal Stability of $CsCu_2X_3$ (X = Cl, Br, I) 165
4.3.4 Diffuse Reflectance and Photoluminescence 169
4.3.5 Summary 183
Chapter 5: Future Work And Conclusions 184
5.1 Summary 184
5.2 Future Work 188
References 193
Appendix 1: Supplementary Figures 224
A1.1 Chapter 2 Figures and Tables 224
A1.2 Chapter 3 Figures and Tables 241
A1.3 Chapter 4 Figures and Tables 245

Table of Tables

Table 1. Selected room temperature single crystal data collection and refinement parameters for $(CH_3NH_3)_2CdBr_4$ and $(CH_3NH_3)_2CdI_4$. 65

Table 2. Selected single crystal data and structure refinement parameters for $(C_5H_7N_2)_2HgBr_4 \cdot H_2O$ and $(C_5H_7N_2)_2ZnBr_4$. 90

Table 3. Selected room temperature single crystal data collection and refinement parameters for the compounds prepared in this work. 115

Table 4. Summary of the optical properties of the organic-inorganic hybrid compounds $(R)ZnBr_3(DMSO)$, $(R)_2CdBr_4 \cdot DMSO$ and $(R)CdI_3(DMSO)$, and the corresponding organic salts (R)Br and (R)I. 121

Table 5. Comparison of blue-light emitting solid systems. 135

Table 6. Low-dimensional compounds in the pseudo-binary CsX-CuX system.[409] 136

Table 7. PXRD refinement results for all $Cs_3Cu_2Br_{5-x}I_x$ ($0 \leq x \leq 5$) along with R_{wp} and S values. 144

Table 8. Photoluminescence and colorimetry data for all compounds. 151

Table 9. Binding energies of the unrelaxed spin-singlet ($\boldsymbol{E}B\boldsymbol{unrelax}$) and the relaxed spin-triplet ($\boldsymbol{E}B\boldsymbol{relax}$) excitons as well as the exciton excitation and emission energies of $Cs_3Cu_2Br_5$ and $Cs_3Cu_2I_5$. The exciton excitation and the emission energies were calculated based on the spin-singlet and the spin-triplet excitons, respectively. The experimentally measured excitation and emission peak energies are shown in parentheses. All the results are based on hybrid functional PBE0 calculations. 154

Table 10. Results of the tetrahedral distortion estimation indicate a linear decrease in distortion with increase in the halide ion size. 164

Table 11. Photoluminescence information table for all members. 169

Table 12. Summary of the refinement results of time resolved PL measurements of $CsCu_2X_3$. 174

Table 13. Refinement results of the temperature dependence FWHM of $CsCu_2X_3$. 180

Table of Figures

Figure 1. Increase in the number of publications on perovskites since 2000. Data obtained from Thomas Rheuters,Web of Science. 2

Figure 2. Ideal cubic ABX_3 perovskite crystal structure the blue, red and gray spheres represent A, B and X, respectively. 5

Figure 3. Derivation of low-dimensional perovskites as a result of cutting down the indicated crystallographic planes of the parental 3D perovskite. The archetype 3D lattice is shown in the center viewed along different directions. (a) <100>-oriented family $A'_2A_{n-1}M_nX_{3n+1}$: n = 1 (PEA_2PbCl_7, PEA=phenylethylammonium)[50] and n = 2 ($NBT_2(MA)Pb_2I_7$, NBT = n-butylammonium, MA = methylammonium);[51] (b) <110>-oriented family $A'_2A_mM_mX_{3m+2}$: m = 1 ($(IFA_2)(FA)SnI_5$, IFA = iodoformamidinium, FA = formamidinium)[52] and m = 2 ($APIPbBr_4$, API = N-(3-aminopropyl)imidazolium);[53] (c) <111>-oriented family $A'_2A_{q-1}M_qX_{3q+3}$: q = 1 (DMA_2SnCl_6, DMA = dimethylammonium)[54] and q = 2 ($TMA_3Sb_2Cl_9$, TMA = trimethylammonium).[55] Reproduced from Ref. 90 with permission from the Royal Society of Chemistry. 10

Figure 4. Direct and Indirect semiconductor band structures.[76] 17

Figure 5. Density of states in the conduction band for a three-, two-, one- and zero-dimensional semiconductor structures.[76] 20

Figure 6. Several types of energy level schemes that could arise at the molecular level of a hybrid organic-inorganic perovskite. The possible band alignments are analogus to the two types of quantum well structures, which are (a) type-I, and (c) type-II. **A**dapted with permission from Saparov, B.; Mitzi, D. B., Organic–Inorganic Perovskites: Structural Versatility for Functional Materials Design. *Chem. Rev.* **2016**, *116* (7), 4558-4596. Copyright 2016 American Chemical Society. 21

Figure 7. Schematic representation of absorption of a photon in a semiconductor. 23

Figure 8. The two types of excitons found in semiconductors, (a) Frenkel and (b) Wannier-Mott, which differ based the size of their radii, which is illustrated by the size of the opaque red circle. The black and white circles the electron and hole, respectively. 24

Figure 9. Systematic description of (a) discreet exciton energy levels that result from their attraction and (b) observed band edge absorption spectrum for a direct gap semiconductor as a result of excitonic emission. The dashed indicates the expected absorption when the excitonic effects are ignored. 26

Figure 10. Schematic representation of the photoluminescence process in a direct gap semiconductor. 28

Figure 11. Absorption and photoluminesce spectra of (a) $(N\text{-}MPDA)PbBr_3$ and (b) $(N\text{-}MEDA)PbBr_4$ with the near-UV excitation of the respective powders. Adapted with permission from Smith et al. Chem. Rev. 2019. Copyright 2019 American Chemical Society. 30

Figure 12. Schematic digram of the mechanism of self-trapping (red arrow) and detrapping (blue arrow) of excitons where (GS = ground state, FE = free exciton, STE = self-trapped exciton state, $E_{a,trap}$ = self-trapping activation energy, $E_{a,detrap}$ detrapping activation energy, and the pink and orange arrow depict the free exciton and self-trapped excitonic photoluminescence, respectively. Adapted with permission from Smith et al. Chem. Rev. 2019. Copyright 2019 American Chemical Society. 33

Figure 13. CIE1931 color coordinate plots of solid-state phosphors used in devices in curretly on the market. Reproduced with permission from Annual Reviews.[122] 36

Figure 14. Crystal structures and photoluminescence of single crystals of the n = 1-5 members of the 2D $(C_4H_9NH_3)_2(CH_3NH_3)_{n-1}Pb_nI_{3n+1}$ family. Turquoise, purple, blue, and gray spheres represent Pb, I, N, and C, respectively. Reprinted with permission from Smith et al. Chem. Rev. 2019. Copyright 2019 American Chemical Society. 38

Figure 15. Schematic diagram the luminescence mechanisms of scintillators.[142] 43

Figure 16. Examples of non-perovskite structures based on (a) square pyramidal $(Ph_4P)_2SbCl_5$,[156] (b) edge sharing seesaw shaped $(C_6H_5C_2H_4NH_3)HgCl_3$,[161] (c) edge sharing tetrahedra wires of $(N(CH3)_4)AgCl_2$,[162]and (d) tetrahedra Rb_2ZnI_4.[163] Organic cations are shown as wires for visual clarity. 48

Figure 17. Polyhedral views of the crystal structures of (a) $(CH_3NH_3)_2CdCl_4$, (b) $(CH_3NH_3)_2CdBr_4$ and (c) $(CH_3NH_3)_2CdI_4$. Orange, blue, red, grey, and black spheres represent Cd, halogen (Cl, Br or I), N, H, and C atoms, respectively. For clarity, only a fraction of methylammonium ions are shown in (b) and (c). 62

Figure 18. Powder X-ray diffraction (PXRD) patterns (black dots) for (CH3NH3)2CdCl4 at (a) 300 K, (b) 200 K and (c) 100 K, showing successive phase transitions upon cooling. The Pawley fits and difference plots are shown as red and blue dotted lines, respectively. 66

Figure 19. The variation in cell volume with temperature based on variable temperature PXRD and SXRD results shown in black squares and red dots respectively. The observed phase changes are denoted by a dashed line with each colored region corresponding to the orthorhombic (light yellow), tetragonal (light green) and monoclinic (light blue) phases of $(CH_3NH_3)_2CdCl_4$. In this plot, the monoclinic phase volumes are doubled to bring them to scale with the tetragonal and orthorhombic phases of $(CH_3NH_3)_2CdCl_4$. 67

Figure 20. Room temperature PXRD results for $(CH_3NH_3)_2CdBr_4$ and $(CH_3NH_3)_2CdI_4$. Pawley fits are shown in red, which overlap the gray observed spectra, and the difference maps are in blue. 69

Figure 21. Temperature dependence of unit cell volume for (a) $(CH_3NH_3)_2CdBr_4$ and (b) $(CH_3NH_3)_2CdI_4$ based on variable temperature PXRD and SXRD results, which are shown in black and gold, respectively. 70

Figure 22. Ambient stability studies of spin coated MA_2CdX_4 thin films over a period of two weeks are shown in (a-c). (a) MA_2CdCl_4 shows no degradation, whereas (b) MA_2CdBr_4 decomposes forming $MACdBr_3$[250] (marked with green asterisks) after only one day in air,

however, degradation slows thereafter. (c) MA_2CdI_4 film shows a higher degree of preferential orientation after a day in air, however, no impurity peaks are detected. After two weeks, MA_2CdI_4 PXRD pattern suggests formation of an unidentified impurity phase (labeled with orange diamond marks). Dry air stability studies of MA_2CdX_4 over a period of two weeks are shown in (d-f). (d) MA_2CdCl_4 shows no degradation, whereas (e) MA_2CdBr_4 decomposes forming $MACdBr_3$[250] (marked with green asterisks) after only two weeks in a dry air environment. (f) MA_2CdI_4 also shows no degradation over a two-week period. Moisture stability studies of MA_2CdX_4 over a period of two weeks are shown in (g-i). (g) MA_2CdCl_4 shows a higher degree of preferential orientation after two weeks in a wet nitrogen environment whereas (h) MA_2CdBr_4 begins decomposing after only 1 day. (i) MA_2CdI_4 film completely degrades after one day in a 100% saturated environment. 72

Figure 23. Absorbance vs. energy plots for $(CH_3NH_3)_2CdCl_4$ (black), $(CH_3NH_3)_2CdBr_4$ (red) and $(CH_3NH_3)_2CdI_4$ (blue). From the linear fits, the onsets of optical absorption are 5.29 eV for $(CH_3NH_3)_2CdCl_4$, 4.92 eV for $(CH_3NH_3)_2CdBr_4$, and 3.94 eV for $(CH_3NH_3)_2CdI_4$. Absorbance spectrum of the UV quartz substrate (green) is also included for comparison. 74

Figure 24. Normalized room temperature photoluminescence (PL) spectra of (a) $(CH_3NH_3)_2CdCl_4$, (b) $(CH_3NH_3)_2CdBr_4$, and (c) $(CH_3NH_3)_2CdI_4$ 75

Figure 25. Band structures (left) and density-of-states (DOS) (right) plots of (a) $(CH_3NH_3)_2CdCl_4$, (b) $(CH_3NH_3)_2CdBr_4$, and (c) $(CH_3NH_3)_2CdI_4$ calculated using PBE functionals with SOC. Note that the band gaps are underestimated in PBE calculations. 79

Figure 26. Polyhedral views of the crystal structures of (a) $4AMP_2HgBr_4 \cdot H_2O$ and (b) $4AMP_2ZnBr_4$. Gray, lilac, burgundy, red, pink, blue, and black represent Zn, Hg, Br, O, H, N, and C, respectively. Some 4AMP molecules were removed for visual clarity. 91

Figure 27. TGA (red) and DSC (blue) measurements for (a) $(C_5H_7N_2)_2HgBr_4 \cdot H_2O$ and (b) $(C_5H_7N_2)_2ZnBr_4$. 92

Figure 28. (a) Diffuse reflectance spectra of polycrystalline powders of $4AMP_2HgBr_4 \cdot H_2O$ and $4AMP_2ZnBr_4$ measured at room temperature. (b-c) Room temperature optical absorption (blue), PLE (green), and PL (red) spectra of $4AMP_2HgBr_4 \cdot H_2O$ and $4AMP_2ZnBr_4$. (d) The position of $4AMP_2HgBr_4 \cdot H_2O$ (circle) and $4AMP_2ZnBr_4$ (square) values in the CIE 1931 chart. 95

Figure 29. Temperature dependence PL of (a) $4AMP_2HgBr_4 \cdot H_2O$ and (b) $4AMP_2ZnBr_4$, under 325 nm UV irradiation. Plots of the temperature-dependence integrated intensity of (c) A1, B1, and C1 peaks of $4AMP_2HgBr_4 \cdot H_2O$ and (d) A2, B2, C2 of $4AMP_2ZnBr_4$. 98

Figure 30. The photoluminescence decay curves of (a-c) A1, B1, and C1 PL peaks of $4AMP_2HgBr_4 \cdot H_2O$ and (d-f) A2, B2, and C2 PL peaks of $4AMP_2ZnBr_4$. The excitation wavelengths are 370 and 341 nm for $4AMP_2HgBr_4 \cdot H_2O$ and $4AMP_2ZnBr_4$, respectively. 100

Figure 31. Electronic band structure and density of states (DOS) plots for $4AMP_2HgBr_4 \cdot H_2O$ (a-b) and $4AMP_2ZnBr_4$ (c-d) calculated using the PBE functional. Note that the band gap is underestimated due to well-known band gap error of PBE calculations. 102

Figure 32. Polyhedral views and close up views of the coordination of the polyhedra of the crystal structures of (a) (R)$ZnBr_3$(DMSO), (b) $(R)_2CdBr_4$·DMSO and (c) (R)CdI_3(DMSO). Blue and cyan tetrahedra represent coordination environments around Zn and Cd, respectively. Burgundy, purple, red, yellow, black, and light blue spheres represent Br, I, O, S, C, and N, respectively. For clarity, hydrogen atoms were omitted and only a fraction of organic cations and solvent molecules are shown. 116

Figure 33. Powder X-ray diffraction (PXRD) patterns (black lines) for (a) (R)$ZnBr_3$(DMSO), (b) $(R)_2CdBr_4$·DMSO and (c) (R)CdI_3(DMSO). The Pawley fits and difference plots are shown as red and blue curves, respectively. 118

Figure 34. (a-c) Room temperature optical absorption (blue solid lines) PLE (blue doted lines) and PL (red solid lines) spectra for the compounds studied in this work. The insets show the bright emission from the powder samples under irradiation with their respective maximum excitation wavelengths. (d) CIE 1931 chromaticity diagram showing the emission colors of the compounds and the organic salts. 120

Figure 35. Photoluminescence lifetime profiles (black solid circles) and fitting curves (red lines) for (a) (R)$ZnBr_3$(DMSO), (a) $(R)_2CdBr_4$·DMSO, and (c) (R)$CdBr_3$(DMSO). The insets show the excitation and emission wavelengths, and the derived lifetime constants. 121

Figure 36. Room temperature PLE (dashed lines) and PL spectra (solid lines) of the (a) (R)Br organic salt and (R)Br-based compounds, and (b) (R)I organic salt and (R)I-based compound. Spectra are normalized for clarity. 124

Figure 37. Temperature dependence of PL spectra measured for (a) (R)$ZnBr_3$(DMSO) and (b) $(R)_2CdBr_4$·DMSO under 325 nm irradiation. 125

Figure 38. Temperature dependence of (a) the integrated intensity, (b) FWHM, and (c) the position of the B1 peak of $(R)_2CdBr_4$·DMSO obtained from the PL spectra showed in Figure 37. The red lines in (a) and (b) are the best fit of the experimental data according to Eqns 9 and 10, respectively. 128

Figure 39. Band structures and density of states (DOS) plots for (a-b) (R)$ZnBr_3$(DMSO), (c-d) $(R)_2CdBr_4$·DMSO and (e-f) (R)CdI_3(DMSO). 130

Figure 40. Partial density contours of the hole (a) and the electron (b) in a relaxed exciton in (R)$ZnBr_3$(DMSO). 132

Figure 41. Crystal structures of (a) $Cs_3Cu_2Br_5$ and (b) $Cs_3Cu_2I_5$. Cs, Cu, Br and I atoms are shown in pink, blue, maroon, and purple, respectively. 141

Figure 42. Room temperature experimental PXRD patterns (black lines) of (a) $Cs_3Cu_2Br_5$ and (b) $Cs_3Cu_2I_5$ with Pawley fits (red lines) and resulting difference maps (blue lines). (c) The refined lattice parameters and (d) unit cell volume are shown as a function of I content. PXRD patters with fittings can be found in Appendix 1 in Figures A1.14 and A1.15. 143

Figure 43. PXRD patterns of (a) $Cs_3Cu_2Br_5$ and (b) $Cs_3Cu_2I_5$ compounds left in ambient air for 1 month. 146

Figure 44. Tandem thermal gravimetric analysis (blue) and differential scanning calorimetry (red) TGA/DSC plots for (a) $Cs_3Cu_2Br_5$ and (b) $Cs_3Cu_2I_5$. 147

Figure 45. PXRD patterns of (a) $Cs_3Cu_2Br_5$ and (b) $Cs_3Cu_2I_5$ after 2 heating cycles over 545 °C. Asterisks denote CsX impurity phases resulting from incongruent melting of the phases. 148

Figure 46. Photoluminescence excitation (PLE, blue lines) and emission (PL, red lines) of (a) $Cs_3Cu_2Br_5$, (b) $Cs_3Cu_2Br_{3.75}I_{1.25}$, (c) $Cs_3Cu_2Br_{2.5}I_{2.5}$, (d) $Cs_3Cu_2Br_{1.25}I_{3.75}$, (e) $Cs_3Cu_2I_5$ compounds, and (f) CIE 1931 chromaticity plot of the resulting emission of all compounds. .. 150

Figure 47. PL intensity versus excitation power density for $Cs_3Cu_2X_5$ (X = I, Br)..... 152

Figure 48. Electronic band structure and density of states (DOS) of $Cs_3Cu_2Br_5$ (a-b) and $Cs_3Cu_2I_5$ (c-d)..... 153

Figure 49. The configuration coordinate diagram for the excitation, relaxation, and emission in $Cs_3Cu_2Br_5$. (a) and (b) show the ground-state and the relaxed excited-state of the Cu_2Br_5 cluster. The curves and the straight arrows represent potential energy surfaces and optical transitions, respectively. The ground-state and the relaxed excited-state structures are shown in (a) and (b), respectively. The partial densities of the electron and the hole in the relaxed exciton are shown in (c) and (d), respectively. The Cu and the Br atoms are represented by the red and blue spheres, respectively. 155

Figure 50. Crystal structures of $CsCu_2X_3$ (X = Cl, Br, I) projected along (a) a-, (b) b- and (c) c-axes. Pink and green spheres represent Cs and the halides, respectively and the blue tetrahedron represent Cu. Di-tetrahedral cluster connectivity is represented in (d) which are labeled according to the convention in Table A1.13 in Appendix 1 and shown with all dark green and lime green halides occupying specific corresponding crystallographic positions according to the reported CIF files.[434 435] 160

Figure 51. Room temperature powder X-ray diffraction (PXRD) patterns (black lines) for (a) $CsCu_2Cl_3$, (b) $CsCu_2Br_3$, (c) $CsCu_2I_3$. Pawley fits of the data are shown in red and difference plots shown in blue. 161

Figure 52. PXRD (a) refined lattice parameters and (b) unit cell volume shown as a function of halide content as alloying progresses from Cl to Br to I..... 162

Figure 53. PXRD patterns of (a) $CsCu_2Cl_3$, (b) $CsCu_2Br_3$, and (c) $CsCu_2I_3$ left out in ambient conditions and measured over a period of 2 months..... 167

Figure 54. Tandem differential scanning calorimetry (red) and thermal gravimetric analysis (blue) of (a) $CsCu_2Cl_3$, (b) $CsCu_2Br_3$, and (c) $CsCu_2I_3$..... 168

Figure 55. Diffuse reflectance spectra of polycrystalline powders of $CsCu_2X_3$ performed at room temperature. 172

Figure 56. Photoluminescence excitation (blue) and emission (red) for (a) $CsCu_2Cl_3$, (b) $CsCu_2Cl_{1.5}Br_{1.5}$, (c) $CsCu_2Br_3$, (d) $CsCu_2Br_{1.5}I_{1.5}$, and (e) $CsCu_2I_3$. (d) CIE 1931 plot with the emission colors of all constituents. 173

Figure 57. Power dependence PL spectra of $CsCu_2X_3$ measured at 4 K, under 325 nm excitation. Black curves shows the fitting using $y = P^k$, with y, P, and k are the PL intensity, the excitation power, and the refinement coefficient, respectively.[110] 174

Figure 58. Room temperature time-resolved PL of (a) $CsCu_2Cl_3$, (b) $CsCu_2Cl_{1.5}Br_{1.5}$, (c) $CsCu_2Br_3$, (d) $CsCu_2Br_{1.5}I_{1.5}$, (e) $CsCu_2I_3$. 175

Figure 59. (a) Temperature dependence PL spectra of $CsCu_2Cl_3$, under 325 nm excitation. Thermal evolution of (b) position, (c) integrated intensity, and (d) FHWM of PL peaks of $CsCu_2X_3$. The integrated PL intensity were refined (black curves) based on Eqs (12-14). FWHM were refined based on Eq (12) (red curves). 176

Figure 60. Temperature dependence PL of (a) $CsCu_2Cl_{1.5}Br_{1.5}$, (b) $CsCu_2Br_3$, (c) $CsCu_2Br_{1.5}I_{1.5}$, and (d) $CsCu_2I_3$, under 325 nm irradiation. $CsCu_2Cl_3$ is shown in Figure 59. 178

Figure 61. Light-emitting diode (LED) fabricated using $CsCu_2I_3$ as a dopant in a mCP host. (a) Luminance-current-voltage (LIV) characteristics, (b) Quantum efficiency (inset: the device structure), and (c) Electroluminescence (EL) spectrum (inset: a photo image of the LED operating at 8 V) of the LED. 182

Portions of this dissertation have been reprinted and/or adapted in part with permission of the publishers as follows:

Chapter 2:

Section 2.1 was adapted with permission from Roccanova, R.; Ming, W.; Whiteside, V. R.; McGuire, M. A.; Sellers, I. R.; Du, M.-H.; Saparov, B., Synthesis, crystal and electronic structures, and optical properties of $(CH_3NH_3)_2CdX_4$ (X= Cl, Br, I). *Inorg. Chem.* **2017,** *56* (22), 13878-13888. Copyright 2017 American Chemical Society.

Section 2.2 was adapted with permission from Yangui, A.; Roccanova, R.; McWhorter, T. M.; Wu, Y.; Du, M.-H.; Saparov, B., Hybrid Organic–Inorganic Halides $(C_5H_7N_2)_2MBr_4$ (M = Hg, Zn) with High Color Rendering Index and High-Efficiency White-Light Emission. *Chem. Mater.* **2019,** *31* (8), 2983-2991. Copyright 2019 American Chemical Society.

Chapter 3:

Chapter 3 was adapted with permission from Roccanova, R.; Houck, M.; Yangui, A.; Han, D.; Shi, H.; Wu, Y.; Glatzhofer, D. T.; Powell, D. R.; Chen, S.; Fourati, H., Broadband Emission in Hybrid Organic–Inorganic Halides of Group 12 Metals. *ACS Omega* **2018,** *3* (12), 18791-18802. Copyright 2019 American Chemical Society.

Chapter 4:

Section 4.1 and 4.2 was adapted with permission from Roccanova, R.; Yangui, A.; Nhalil, H.; Shi, H.; Du, M.-H.; Saparov, B., Near-Unity Photoluminescence Quantum Yield in Blue-Emitting $Cs_3Cu_2Br_{5-x}I_x$ ($0 \leq x \leq 5$). *ACS Applied Electronic Materials* **2019**. Copyright 2019 American Chemical Society.

Tables and Figures in Appendix 1 have also been reprinted with permission from the above sources.

Chapter 1: Introduction to Luminescent Low-Dimensional Metal Halides

1.1 Introduction

Inspiration for the work presented in this dissertation comes from the groundbreaking recent discoveries reported in the field of hybrid organic-inorganic perovskites (HOIP), which spans the disciplines of solid-state chemistry, physics, materials science and engineering. The fascination with metal halide perovskites can be traced to their unprecedented tunability of both structure and properties which has led to the exponential growth of the performance of the paragon, $CH_3NH_3PbI_3$, as an absorber for solar cells.[1] The wide range of advantageous optoelectronic properties reported for these materials, including high optical absorption, long charge carrier lifetimes, large dielectric constants, and others make them candidates for a number of practical applications.[2] These diverse properties arise from the diversity in chemical compositions, crystal and electronic structures present within the material family, all of which can be chemically tailored to suit the needs of a specified application.

In almost two decades, research on halide perovskite-based materials has grown exponentially, with approximately 7200 papers published on the subject in 2018 alone (Figure 1). Despite these high numbers, the scientific community was not always as enthusiastic about this class of materials. Halide perovskites were sporadically studied for over 100 years before they became a hot topic after the report in 2009 of $CH_3NH_3PbI_3$ as a solution-processable solar absorber in the first perovskite solar cell reported with a 3.8% efficiency.[3] Since then, the efficiency has sky-rocketed to >24%[4] in little over ten years, making this the fastest developing solar cell material to date.[5] Prior to the material's use in solar cells, its use as a phosphor was demonstrated in the first perovskite light-emitting diode (LED), which was made from the 2D

PEA_2PbI_4 (PEA = $C_6H_5(CH_2)_2NH_3$), which emitted bright green light at 70 K.[6] In 2014, ten years after the first HOIP based LED was reported, Tan et al. reported appreciable infrared and green room temperature luminescence of $CH_3NH_3PbBr_2I$ (EQE = 0.76%) and $CH_3NH_3PbBr_3$ (EQE = 0.1%), respectively.[7] As a result of room temperature luminescence being achieved, the interest in perovskite-based light emitters has increased tremendously in the past 4 years, with reports of small changes in chemical composition resulting in tunable room temperature emission with either narrowband emission with high color purity spanning the visible to the NIR region,[8-9] or broadband emission spanning the entire visible spectrum with high color rendition[10] some with external quantum efficiencies (EQE) up to 21.5%.[11] While these recent improvements in fabrication and EQEs demonstrate the promise of perovskite materials for LED applications, improvement is still needed to be on par with the current commercially available OLED materials boasting EQEs around 37% and climbing.[12]

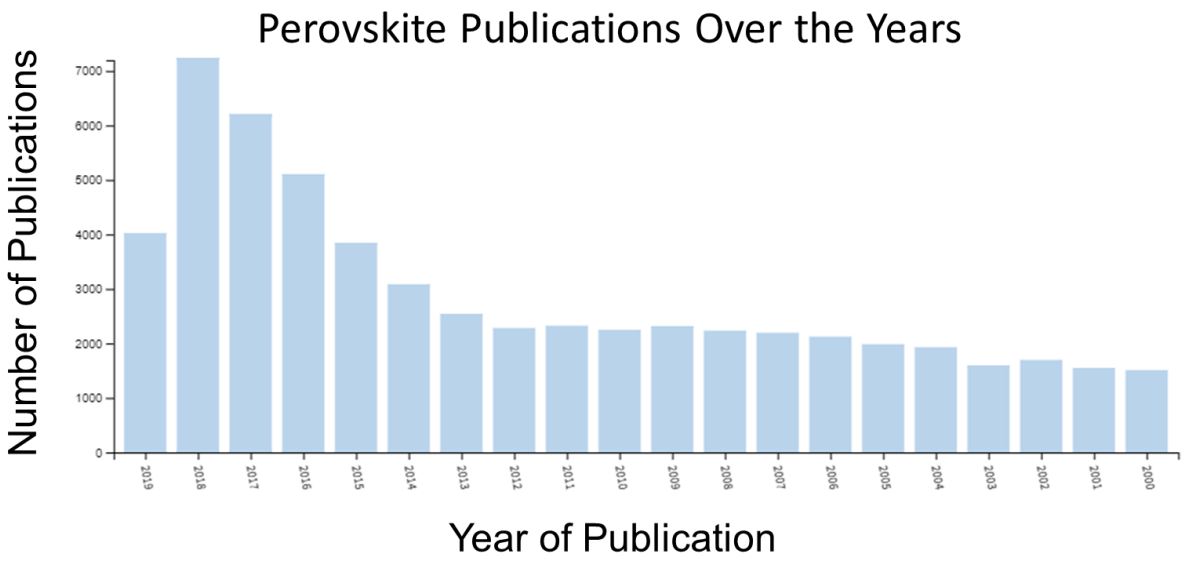


Figure 1. Increase in the number of publications on perovskites since 2000. Data obtained from Thomas Rheuters,Web of Science.

Currently, the majority of halide perovskite materials dominating the field are based on $CH_3NH_3(Pb, Sn)(Br,I)_3$ with the bulk of efforts going towards the optimization of the efficiency

and stability of these materials for low-cost-per-watt photovoltaic devices.[13] This is because these halide perovskites are not only solution-processable, but exhibit ideal semiconducting properties such as high electron-hole mobilities, small effective masses of electrons and holes, long carrier lifetimes, and large optical absorption in comparison to other semiconductors like GaAs and Si which allows more of the light spectrum to be used to generate carriers for solar cell applications.[14-15] Their all-inorganic counterparts like $CsPbX_3$ and Cs_4PbBr_6,[16] are currently being explored for photoemission applications due to their versatile photoluminescence properties such as high photoluminescence quantum yield (PLQY, > 80%) in solution, tunable band gaps and narrow full-width-at-half-maximum (FWHM, <20 nm) thus resulting in bright, pure colors. Lower-dimensional hybrid organic-inorganic halide systems have also been of interest due to their reported broadband white light emission, which is rare as the majority of white light is created through the use of multiple phosphors rather than originating from a single material.[17]

Despite the advantageous physical properties of the heavily studied Pb/Sn perovskite families, the toxicity of Pb and marked instability of Sn halides remain major concerns for the implementation of these materials in marketable devices due to demonstrated issues with air, moisture, and thermal instability.[18-20] The majority of these instability issues have been linked to the volatility of small organic cations or permeability of the structure to water within the air.[20] Thus there is a need to identify other metal halide-based systems that contain less toxic or non-toxic components as well as offer better air, moisture and thermal stability. To that end, many reports in literature show that through lowering the dimensionality of metal-halide perovskite structures through the incorporation of large organic cations with long hydrophobic aliphatic chains can lead to higher moisture and air stability than their original 3D parent

structure.[21-23] Lowering the dimensionality of these compounds also affect the properties exhibited by the materials. For instance, by changing the size and shape of the organic counter cation, the NIR emission exhibited by the 3D $CH_3NH_3PbI_3$[24] parent was tuned to visible green emission through dimensional reduction in the 2D $(C_6H_5C_2H_4NH_3)_2PbI_4$ system.[6] Other perovskite families have also shown remarkable change in photoluminescence properties as their dimensionality has been reduced.[13] Unfortunately, predictability of the exact structures and properties that will result from dimensional reduction is still poor, especially within understudied systems like many transition metal, lanthanide and actinide halide systems. However, through the systematic study of chemical substitution on different sites within the crystal structure, structure and property trends can be established for these underexplored material systems.

Purely from a fundamental perspective, we note the fact that non-Pb/Sn A-B-X halides (A = electropositive inorganic or organic cation, B = metal cation, X = Cl, Br, I) have received relatively little attention in literature so far with a few known members for alternative metal elements, whose optical and electronic properties have not been comprehensively characterized. Specifically, for light emission applications, our central hypothesis in this dissertation was that Cu- and Zn- based halides could be viable alternatives to lead halide materials. Thus, Zn and Cu are inexpensive, earth-abundant and nontoxic metal elements that are also capable of forming low-dimensional metal halide crystal structures that demonstrate enhanced excitonic properties. To study the impact of metal substitutions, we also considered halides of the heavier group 12 metal analogs, Cd and Hg. Our results presented in this dissertation confirm that indeed, A-B-X (where B = Zn, Cd, Hg, Cu) halides can be structurally engineered to exhibit localized charges, strong excitonic interactions, and consequently, high

efficiency room-temperature luminescence comparable (or better) than that reported for lead halide perovskites.

To better understand the motivation for the research reported in the following chapters of this dissertation, in the following sections of this chapter, necessary background information is provided on the structure and properties of halide perovskites. First, we begin by examining the various structures of the metal halide perovskites and how through the use of various structural components different dimensionalities can be induced. The structural discussion is followed by a review of the fundamental optical properties observed in low-dimensional halide perovskites and their potential practical applications. Finally, we conclude with a discussion of non-Pb/Sn halides, their crystal structures and physical properties.

1.2 Crystal Structures of Low-Dimensional Halides

1.2.1 Three-Dimensional Parent Structure

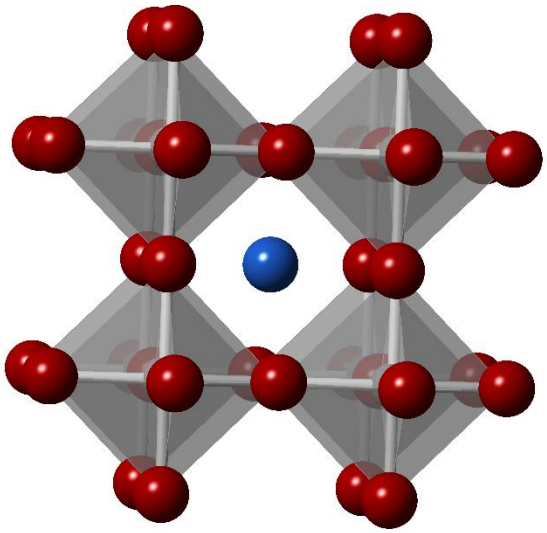


Figure 2. Ideal cubic ABX_3 perovskite crystal structure the blue, red and gray spheres represent A, B and X, respectively.

The three-dimensional (3D) halide perovskite structure has a general formula of ABX_3 and is described by its characteristic 3D corner-sharing inorganic framework comprised of BX_6 octahedra. The inorganic framework forms a cubic arrangement from a 6-fold coordinated less electropositive cations (B) bridged by halide anions (X) which surround a more electropositive cation (A) that sits in a 12-fold coordinated hole as shown in Figure 2. In order for this structure type to form, constraints such as charge balance, ionic sizes, bonding/coordination preferences of the constituents must be considered or a 3D perovskite structure will most likely not form.

Charge balance is one of the most important aspects of the formability of a perovskite because metal halides are ionic and are expected to form charge-balanced line compounds. Classically, halide perovskite structures are composed of monovalent halides at the X-site (e.g. F, Cl, Br, I), divalent metal cations located at the B-site (e.g. Pb^{2+}, Sn^{2+}, Ge^{2+}, Mn^{2+}, Cu^{2+}, Cd^{2+}, Hg^{2+}, Eu^{2+}, Yb^{2+}, etc.) and smaller monovalent A-site cations (e.g. K^+, Rb^+, or Cs^+ in all-inorganic 3D halide perovskites, and small organic cations such as methylammonium ($CH_3NH_3^+$)[25] and formamidinium ($CH_5N_2^+$) in 3D HOIPs.[26-27] While the +2 valence requirement of the B cation has been popular due to 3D perovskites containing Pb^{2+} exhibiting remarkable optoelectronic properties, it can be extended to include other valences such as +1, +3, and +4 charges in equal number or with enough vacancies at the B-site so the average charge remains +2. This has been demonstrated in some double perovskites where mixed-valent metals, like gold as seen in $Cs_2Au^{I}Au^{III}I_{6,}$[28] or two metals with different oxidation states such as in $Cs_2Ag^{I}Bi^{III}X_6$ (X = Cl, Br),[29] are used.

Due to size constraints of the ionic framework, only A cations of a certain size will fit within the pocket created by the inorganic [BX_3] sublattice. Once this size limit is surpassed, the 3D structure will no longer be accessible and lower-dimensional and/or non-perovskite

systems may result. To predict if a 3D perovskite structure may form from selected A, B and X ions, the Goldschmidt's Tolerance Factor (t) can be calculated using the ionic radii of each constituent as follows:

$$t = \frac{R_{\mathrm{A}} + R_{\mathrm{X}}}{\sqrt{2}(R_B + R_{\mathrm{X}})} \quad (1)$$

where the ionic radius of the A cation (R_{A}) and X anion (R_{X}) are inversely proportional to the square root of two times the sum the radius of the B cation (R_{B}) and the X anion (R_{X}).[30] A tolerance factor of 1 indicates the formability of an ideal perovskite structure, however it has been empirically determined that a 3D perovskite structure may form for halides within the $0.8 \leq t \leq 1.1$ limit, although they may be distorted, especially at the lower end of the empirical range.[31] If $t > 1.1$ the A cation is too large, which induces lower dimensional perovskite or non-perovskite structure formation, whereas if $t < 0.8$, the A cation is too small which will cause drastic distortion of the octahedral framework and cause the formation non-perovskite structures as well. Setting $t = 1$ for an ideal 3D cubic perovskite to form, the A cation size restriction for various [BX_3] frameworks can be calculated. For example, using R_{Pb} = 1.19 Å and R_I = 2.20 Å, it has been calculated that R_A can be no larger than 2.6 Å for the [PbI_3] perovskite framework, which consequently means organic molecules no larger than three C-C or C-N bonds will fit within the 3D perovskite structure without causing a dimensional reduction.[2] Revisions of the tolerance factor range have been suggested in recent literature,[31-32] but despite these revisions, some systems still cannot be accurately predicted despite falling within the revised tolerance factor ranges.[33] Another key factor in determining the formability of 3D perovskite parent structures is the octahedral factor (μ), which uses a simple model for the six-fold coordination ionic bonding between the metal cation, B, and halide anion, X, to

determine the formability of octahedral BX_6 units. The octahedral factor, which originates from Pauling's radius ratio rules, was first introduced to explain the formability of some oxide perovskite structures[34] and has since been adapted for use in halide perovskite systems.[35] An octahedra is formed if the octahedral factor, defined as,

$$\mu = \frac{r_B}{r_X} \quad (2)$$

where r_B is the ionic radius of B and r_X is the ionic radius of X, is kept within the range of $0.44 \leq \mu \leq 0.89$ for halides.[35] As with the tolerance factor, if μ is outside the range the ionic radii of the B metal cation is either too small or large for a stable octahedra to form. This also points to the importance of finding the correct B metal and X halide combinations if an octahedrally-based structure is desired.

Along with ionic size restraints and charge balance requirements, bonding/coordination preferences of the metal ions, especially in the metal-halide framework, greatly impact the formability of the classical 3D perovskite parent structure. Stereoactivity of lone pairs of the B-site cation can affect the coordination environment by hybridizing with other orbitals of either the metal or the coordinated halide which may negatively affect the formability of the 3D parent structure.[36] Some systems where stereochemically active s^2 electron lone pairs are known to interfere with octahedral coordination and cause distortion of the 3D perovskite framework generally contain Sn^{2+}, Pb^{2+}, Tl^{+}, Ge^{2+}, Sb^{3+}, and Bi^{3+}.[36-40] Hybridization of the metal's s^2-orbital lone pair pushes the crystallographic center of the metal halide octahedra off center, causing alternating long and short B-X bonds and produces interesting properties like ferroelectricity as seen in the distorted $CsGeCl_3$[40-41] and high ionic conductivity in $CH_3NH_3GeCl_3$.[42] In an HOIP, the organic cation can also coordinate with the metal halide

octahedra and induce distortion. By hydrogen bonding through the halide anion to the stereochemically active lone pair, the rigid organic cation can pull the octahedra towards it, causing structural distortion through its coordination, as is observed in the low temperature $CH_3NH_3SnBr_3$ structure and room temperature $CH_3NH_3GeCl_3$.[36] Jahn-Teller distortion of halide perovskites containing transition metals such as $KCuF_3$,[43] $Cs_2Au_2Br_6$[44] as well as other perovskites containing Mn^{2+}, Cr^{2+}, Fe^{2+} and Cu^{2+} have been reported.[45-49] These distortions can lead to interesting physical properties such as ferroelectricity.[27] With this and the other restraints in mind, it is clear that only certain combinations of A, B and X ions will form a 3D perovskite.

1.2.2 Lower-Dimensional Perovskite-Derived Structures

When the strict structural restraints of the 3D halide perovskite parent are relaxed, variation of the structural dimensionality becomes possible, allowing for a greater tunability of the structure and the resulting optoelectronic properties. The degree to which dimensional reduction occurs depends on similar factors as the formation of the 3D parent, with the size and shape of the A-site cation and the bonding and coordination preferences of the constituents being the most influential factors. In the 3D halide perovskite parent structure, the size of the A-site cation is restricted to the dimensions of the 12-fold coordinated cuboctahedral hole within the B-X lattice. When a cation that exceeds the size of the hole is introduced, lower-dimensional (2D, 1D, to 0D) structures will form depending on the size and shape of the A-site cation, effectively slicing the 3D parent structure down different crystallographic planes. For instance, long and narrow organic cations that can pack efficiently and act as templating agents for the inorganic framework assist in the formation of 2D HOIP. The bonding/coordination preferences of the B and X sites also play a role in the formation of the inorganic moieties within the low-dimensional structure but can allow a greater number of combinations compared

to that of the 3D parent. With the addition of the allowable structural diversity of the A-site cation, and various B and X-site combinations, low-dimensional halide structures offer more possibilities than their 3D parents.

1.2.2.1 Two-Dimensional Perovskite Derivative Structures

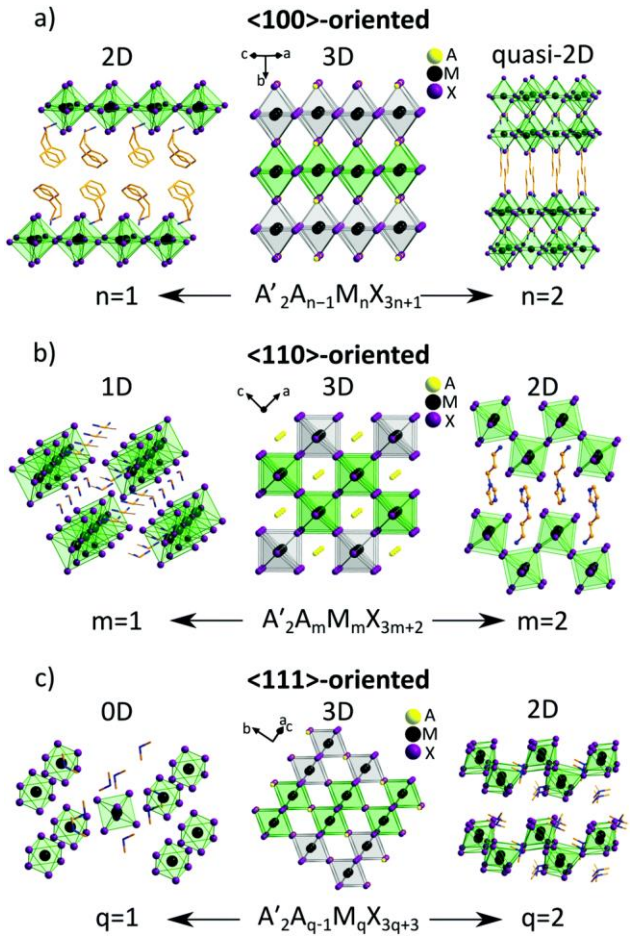


Figure 3. Derivation of low-dimensional perovskites as a result of cutting down the indicated crystallographic planes of the parental 3D perovskite. The archetype 3D lattice is shown in the center viewed along different directions. (a) <100>-oriented family $A'_2A_{n-1}M_nX_{3n+1}$: n = 1 (PEA_2PbCl_7, PEA=phenylethylammonium)[50] and n = 2 ($NBT_2(MA)Pb_2I_7$, NBT = n-butylammonium, MA = methylammonium);[51] (b) <110>-oriented family $A'_2A_mM_mX_{3m+2}$: m = 1 $(IFA_2)(FA)SnI_5$, IFA = iodoformamidinium, FA = formamidinium)[52] and m = 2 ($APIPbBr_4$, API = N-(3-aminopropyl)imidazolium);[53] (c) <111>-oriented family $A'_2A_{q-1}M_qX_{3q+3}$: q = 1 (DMA_2SnCl_6, DMA = dimethylammonium)[54] and q = 2 ($TMA_3Sb_2Cl_9$, TMA = trimethylammonium).[55] Reproduced from Ref. 90 with permission from the Royal Society of Chemistry.

The various subgroups of 2D perovskite derivatives are conceptually derived by slicing the parent 3D structure down specific crystallographic directions to create layers of corner-sharing metal halide octahedra where much larger A-site cations can reside, as shown in Figure 3. Depending on the direction by which the parent structure is cut, different structures result, with the simplest layered perovskite consisting of 2D anionic MX_4^{2-} layers of corner-sharing metal halide octahedra alternating with cation layers (represented by n = 1). The "cuts" made along different crystallographic planes are achieved through chemically targeting a specific stoichiometry that results in the desired compound, as shown in Figure 3. The thickness of the inorganic sheets can be tuned by varying the ratio between small and large cations, where the thickness is quantified by the parameter "n," (or "m" for the <110> and or "q" for the <111> family) which is the number of single octahedral layers that make up an entire inorganic layer.[13] A majority of the known 2D perovskites can be thought of as being derived from the (100) crystallographic plane, with a smaller subset being derived from the (110) or (111) planes that results in corrugated layers as seen in Figure 3c, q = 2.[27]

While the chosen stoichiometry is an important factor for the formation of specific low-dimensional structures, the A-site cation has immense influence on the formability as well. The creation of a 2D layered structure introduces a degree of freedom for the size of the A-cation with no definite restriction on its length, unlike in the 3D parent as illustrated by the guidelines set by the tolerance factor. However, the A-cation must still fit within the cavities created by the inorganic framework, therefore placing restriction on the width of the A-site cation.[27] The ability for the cation to fit within the cavity also ensures that charge balance is maintained, as a certain concentration of cations are required to stabilize the structure, and cations that are too wide or bulky would sterically hinder the packing needed for the targeted structure to form.[56]

For HOIP structures, the A-cation usually also contains terminal functional groups in order for hydrogen bonding and ionic interactions to occur within the structure, which is essential for its formation and stability.[56] The structure of the organic molecule must also not sterically interfere or chemically react with the B and X components, otherwise a 2D perovskite structure will not form. The extended 2D anionic network [MX_4^{2-}] are surrounded by the organic cations, with the ammonium heads of the organic cations hydrogen-ionic bonding to the halogens in the inorganic sheets and the organic tails extending out into the space between the layers. The hydrogen bonding schemes are also influenced by the rigidity of the inorganic framework, which is in turn is impacted by the choice of B-metal cation. A more flexible system, such as some copper(II) halides, which undergo Jahn-Teller distortion of the CuX_6 octahedra, allows for greater interaction with the interlayer organic cations as the layers have more peaks and troughs for the ammonium ends of the organic to interact with.

In many 2D perovskite systems it is common for distortion to occur within the individual octahedra of the inorganic layers. Distortion of this nature are generally caused by deviations from the ideal octahedral coordination environment about the B-site cation seen in unequal X-B-X bond lengths and angles for ideal octahedral geometry and tilting between various octahedra through the increase or decrease of the ideal 180° angle defined by the B-X-B bonds. Distortion can vary widely from family to family, even across compositions containing the same B and X ions.[27] For instance, in the fluorine substituted phenylethylammonium tin iodide system, the influence of the change in position of fluorine from the 2 to 3 to 4 position on the ring of the phenylethylammonium cation resulted in significant variation in the Sn-I-Sn angles, as the movement of the fluorine anion ligand around the ring affected the cross sectional area or width of the organic cation.[57-58] The variation of the Sn-I-Sn angles were linked to the

packing ability of the different organic cation isomers within the structure and show the templating effect that small changes in the size and shape of the A-cation has on the inorganic lattice. Other important factors linked to distortion involving the A-site cation include hydrogen bonding,[57] steric requirements,[58] charge density of the alkylammonium head,[59] and nearness to the inorganic layers,[60] which also greatly impact the templating of the inorganic framework.

1.2.2.2 One- and Zero-Dimensional Perovskite Derivative Structures

When dimensionality is lowered further, the inorganic framework is reduced in size until it is completely broken apart into building blocks. The structure then becomes better able to accept a wider range of components such as those with larger cation sizes or different oxidation states as long as charge balance is maintained.[27] The size constraints outlined by 3D perovskite tolerance factor are also lifted as a result of the inorganic framework no longer being completely intact. From the 3D parent, 1D and 0D derivatives are obtained through making multiple slices down different crystallographic planes to produce nanowire or isolated octahedral systems, as shown in Figure 3. For instance, 1D perovskites are formed by the <110>-oriented family when m = 1, resulting in corner-sharing chains of MX_6 octahedra with a general formula of A_2MX_5, and 0D perovskites are formed from the <111>-oriented family when q = 1, resulting in K_2PtCl_6-type structures with isolated MX_6 octahedra and general formula of A_2MX_6. Notice that these families produce distinctly different dimensionalities depending upon the targeted reaction stoichiometry, and that the influence of the size and shape of the A-cation trumps the influence of inorganic framework in the formation of specific orientations and dimensionalities of 1D and 0D perovskites.[27] The influence of the A-cation can be illustrated by the <100>-oriented family, where the 2D single layered inorganic compound (general formula A_2MX_4, as in PEA_2PbBr_4 shown in Figure 3a) is broken apart into

1D or 0D by the introduction of A-site cations with widths of > 40 $Å^2$, as demonstrated by the addition of cycloalkylamonium in the 1D family R_2PbX_4 (R = cycloalkylammonium, X = Cl, Br, I).[61] The influence of the size and shape of the A-cation on the formation of these structures can also be observed in the aminomethylpyridinium (AMP) lead bromide family when different stereoisomers are utilized and results in the dimensional reduction and change in orientation from 2D <100>-oriented layered structure of (2-AMP)$PbBr_4$ to the 0D <111>-oriented structure of $(4\text{-AMP})_2PbBr_6$.[62]

As in the higher dimensional structures, the majority of known 1D and 0D halide perovskite families contain Pb[62-64] and Sn,[58, 65-67] with a large number of diverse structures being reported for Pb due to its popularity in the field. Many of the Pb and Sn 1D and 0D perovskites exhibit a high degree of octahedral distortion which in some cases have been attributed to pseudo-Jahn-Teller distortion[67] and packing requirements imposed by bulky A-cations.[64] Interestingly, these distortions have been shown to have a direct relationship to the size of the A-cation as demonstrated by A_4SnBr_6 ($A = Cs^+$, Rb^+, K^+) family where the distortion of the $SnBr_6$ octahedra increases down the group.[67] Some 0D Pb-halides, such as $(H_2C_4N_2H_{10})_2PbI_6$ exhibit significant distortion around the metal center.[64] Likewise, some Sn compounds such as the 0D $(C_4N_2H_{14}Br)_4SnBr_xI_{6-x}$ (x = 3) family, also form structures with distorted isolated $SnBr_3I_3$ octahedra surrounded by aromatic organic cations.[68] Other metals halides, like Bi^{3+} and Sb^{3+}, have also been recently reported to produce 0D perovskites with highly distorted metal octahedra.[69-71]

While the required reaction stoichiometry may seem simple to achieve, there is no guarantee that 1D corner-sharing chains or 0D isolated octahedral derivative structures will form. In fact, low-dimensional perovskites are difficult to obtain with few families resulting in

the correct connectivity or coordination.[27] As mentioned above, when other types of connectivity and/or loss of octahedral coordination occur within the inorganic framework the structures are no longer technically perovskites and should be referred to as non-perovskite structures.[72] Despite this fact, multiple accounts within literature do consider structures with different connectivity as perovskites.[66, 73-74] Some low-dimensional non-perovskite structures exhibit exciting luminescent properties similar to their perovskite cousins, and are the main structure types presented in this dissertation and the subject of **Section 1.3**.

1.3 Optical Properties of Low-Dimensional Metal Halides

The optical properties of low-dimensional metal halides are strongly related to their composition, crystal structure, and dimensionality. These materials are often referred to as molecular heterostructures due to the integration of both an insulating sublattice (formed by the organic or inorganic A-cations) and semiconducting sublattice (formed by the inorganic metal halide framework) at the molecular level. To understand the relationship between crystal structure and optical properties of low-dimensional materials, the properties observed are typically likened to those observed in classical semiconductors. To this end, a brief reminder of band structure and quantum confinement in regard to classical semiconductors are offered in this section along with their treatment in low-dimensional metal halide systems.

1.3.1 Electronic Band Structures

A semiconductor is characterized by the presence of a forbidden energy band which represents the gap of the material of width, E_g, situated between the top of the valence band (VB) and bottom of the conduction band (CB) known as the band gap (or forbidden band). At the ground state, valence electrons are located in the VB while the CB is empty. Basic excitation occurs when a photon of energy ($h\nu$), higher than the band gap, is absorbed and an electron

from the VB is excited and transported to the CB, leaving behind a deficit of charge, called a hole. In classical semiconductors, electrons behave like free particles with an effective mass, m^*. The dispersion relation, E(k), relates the energy level of the band with the corresponding momentum (k) through the equation:

$$E(k)=E(k=0)+\frac{\hbar^2k^2}{2m^*} \quad (3)$$

where $k^2 = (k_x^2 + k_y^2 + k_z^2)$, and ħ is Plank's constant. Graphing E(k) vs. k gives the band structure of the semiconductor material in question.[75]

Within a semiconductors band structure, interband transitions are classified as either direct or indirect and are depicted in Figure 4. In the case of the direct band gap, the top of the VB and the bottom of the CB are aligned within the Brillouin zone, which allows optical transitions without modification to the wave vector (k ~ 0). Conversely, an indirect band gap when the maximum of the VB and minimum of the CB have different k-vectors, which require assistance from a phonon (lattice vibration) to conserve momentum.[76]

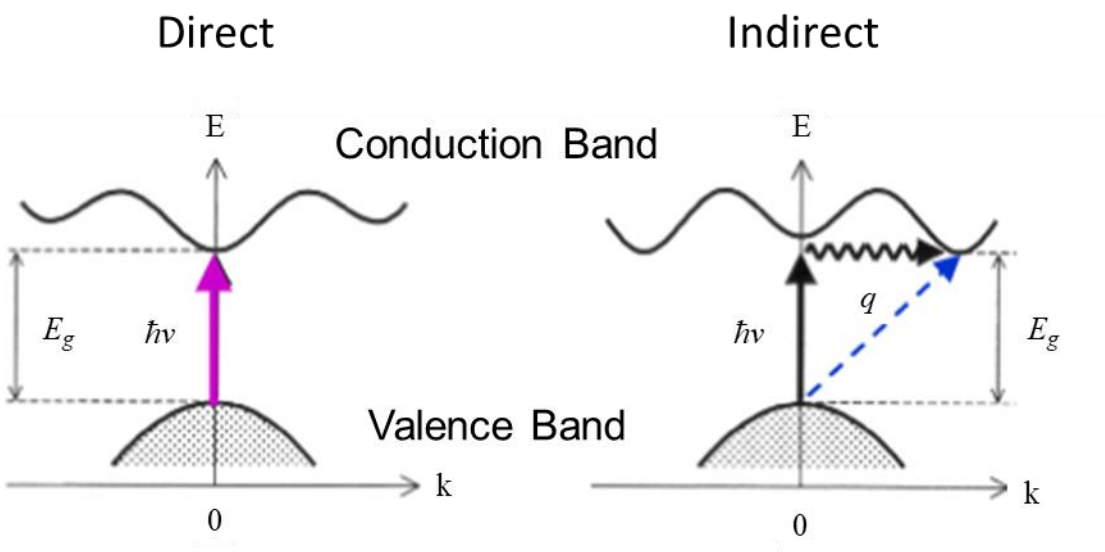


Figure 4. Direct and Indirect semiconductor band structures.

In conventional semiconductors, the VB is made up of p-orbitals and CB is made up of s-orbitals.[76] In contrast, most of the 3D and 2D hybrid perovskites have a VB made up predominantly of halide *p*-orbitals hybridized with metal *s*-orbital character and a CB predominantly made up of metal *p*-orbitals (e.g., in $CsPbI_3$, the orbitals that define the band gap are the I 5*p* and Pb 6*s* in VB and Pb 6*p* in CB).[77-79] In most 3D ABX_3 halide perovskites and their low-dimensional congeners, the electronic band structure is generally dominated by the chosen B-cation and X-anions that make up the inorganic framework and tend to dominate the electronic states around the Fermi level.[27] Although the organic cations do not typically contribute to the band extrema,[56] they can contribute when their energy levels overlap with inorganic components or when the highest occupied molecular orbitals are close to the band extrema.[13] The inorganic framework's contribution to the band structure can be attributed to the linear spatial alignment of the M^{2+} cations and the halide anions in the inorganic framework of 3D perovskites, which allows the p orbitals of each X^- anion to overlap well with the s and

p orbitals of the neighboring M^{2+} atoms with which it is shared leading to large orbital hybridization, resulting in a marked decrease in the band gap from a single MX_6^{4-} octahedral unit such as in the 0D Cs_4PbBr_6 (4 eV)[80] to a the 3D corner-sharing network of MX_6^{4-} in $CsPbBr_3$ (2.15 eV).[77] Thus, depending the composition, dimensionality, and crystal structure of a material, the dominant orbitals and their hybridization can change as can be surmised by the density of states of the material.

1.3.2 Electronic Density of States and Quantum Confinement

The electron density of a crystalline material can be described as the statistical contribution of each energy level likely to be occupied in a particular energy range. In general, the density of states is proportional to the inverse of the slope of the E(k) vs. k plot, thus the flatter the band the greater the density of states at that energy.[76] Dimensionality of a material influences the density of states and spatial confinement of the carriers (electrons and holes). Due to the hydrogenic nature of electrons and holes in the CB and VB, respectively, their behavior can be related to a particle in a box problem.[76] When the dimensionality of the box is reduced, such as in the case of a 2D hybrid perovskite, the boundary conditions of the box are set to zero, creating potential barriers so the carriers can be treated as standing waves. As carriers are confined to lower dimensions, a generalization of the density of states in k-space (ρ(k)) is obtained ($\rho(k) \cong k^{d-1}$, where d is the number of dimensions) where the density of states in one, two and three dimensions is expressed through a constant, linear, and quadratic function of k, respectively.[81] The density of states of an electron in the CB and hole in the VB in "energy space" are described as:[76]

$$\rho_{CB}(E) \sim (E - E_g)^{d/2-1}, \quad E > E_g \tag{4}$$

$$\rho_{VB}(E) \sim |E|^{d/2-1}, \quad E < 0. \tag{5}$$

The corresponding shapes of the densities of states for an electron are illustrated in Figure 5 where 3D structures are considered bulk, 2D structures as quantum wells, 1D structures as quantum wires, and 0D structures as quantum dots.[76] From the point of view of optical transitions, the key feature here is the finite value of the density of states at the bottom of the conduction band, in contrast to 3D semiconductors where the density of states approach zero at the bottom of the band. The 1D system has (in its simplest description) a singularity at the bottom of the band and then decreases a $1/\sqrt{E}$ with increasing energy.[76] For 0D systems, the density of states can be expected to form discrete δ-functions, and thus have density of states resembling atoms and the highest occupied molecular orbital (HOMO) and lowest unoccupied molecular orbital (LUMO) levels.[81] This is why quantum dots, which are 0D systems, are sometimes called 'artificial atoms' as the electrons have discrete energy levels akin to an atom rather than continuous bands like a typical 3D solid.[76]

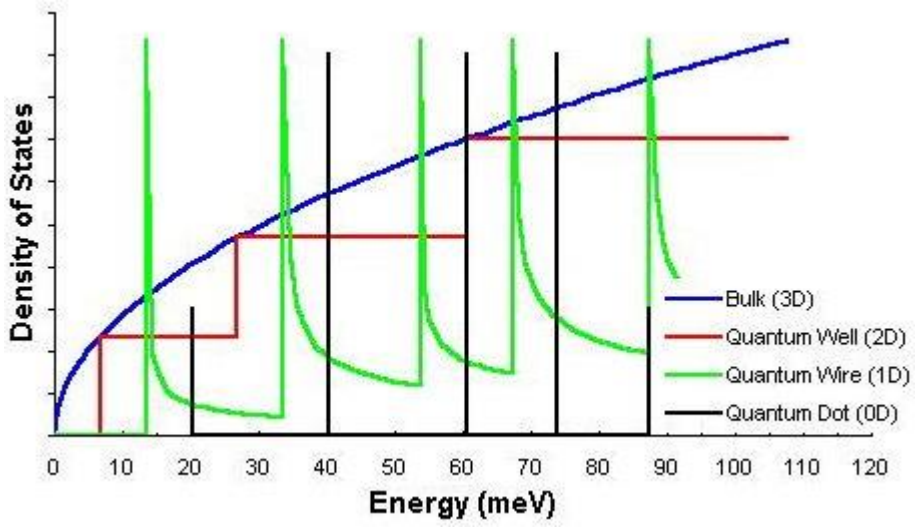


Figure 5. Density of states in the conduction band for a three-, two-, one- and zero-dimensional semiconductor structures.[76]

In the case of 2D hybrid perovskites, the layered structures form natural quantum wells in which the inorganic layers act as the low energy gap, high dielectric constant semiconductor where the carriers can be localized and the organic layers act as the high energy gap, low dielectric constant insulating barriers between the inorganic framework, as illustrated by Figure 6.[27, 56, 82]

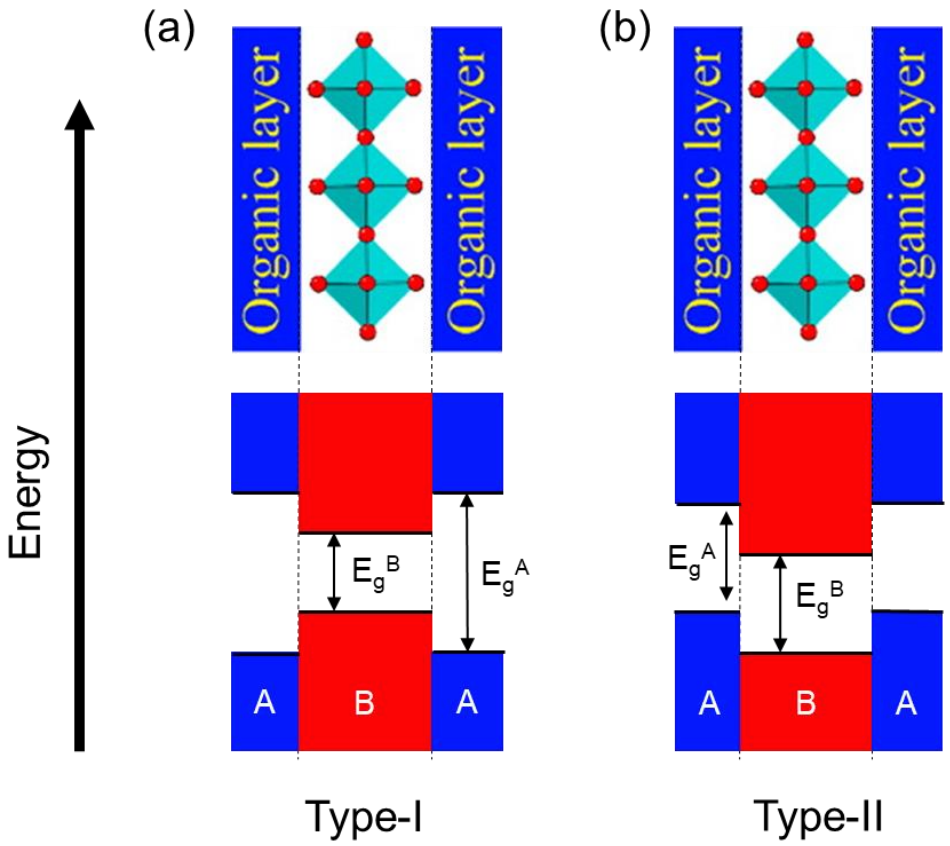


Figure 6. Several types of energy level schemes that could arise at the molecular level of a hybrid organic-inorganic perovskite. The possible band alignments are analogus to the two types of quantum well structures, which are (a) type-I, and (c) type-II. Adapted with permission from Saparov, B.; Mitzi, D. B., Organic–Inorganic Perovskites: Structural Versatility for Functional Materials Design. *Chem. Rev.* **2016**, *116* (7), 4558-4596. Copyright 2016 American Chemical Society.

Depending upon the alignment of the HOMO-LUMO gap of the organic layers and the band gaps of the inorganic framework in energy space, different band alignments arise as depicted in Figure 6. Type-I band alignment is classified by the minimum of the CB and the maximum of the VB both being situated in the same layer (Figure 6a). Analogously, type-I band alignment can be realized in a hybrid organic-inorganic material when the HOMO-LUMO gap of the organic layer is much wider than the band gap of the inorganic layer (Figure 6a) or

when the band gap of the inorganic layer is larger than the HOMO-LUMO gap of the organic layer (Figure 6b).[76] When the CB minimum and VB maximum lie in different (neighboring) layers (materials), it is considered a type-II band alignment. This is achieved in a hybrid organic-inorganic material by shifting the electron affinity of the organic layers relative to the inorganic layers which causes a staggering of the energy levels that result in the CB minimum and VB maximum lying in separate layers.[82]

1.3.3 Luminescence in Low-Dimensional Metal Halides

1.3.3.1 Band-to-Band Absorption and the Concept of an Exciton

A semiconductor absorbs a photon by promoting an electron from the VB to the CB and thus creating an electron-hole pair as shown in Figure 7. This transition can only take place when the energy of the incident photon is greater than the band gap energy (E_g). When an electron jumps from the VB to the CB, it creates a hole in the VB at the same point in space and can attract each other through a mutual Coulombic interaction. Thus the electron and its hole form a neutral quasi-particle, called an exciton, through the Coulomb-attraction force.[83] The strength of this attraction (in terms of energy, called the exciton binding energy (E_b)), depends on two factors: the dielectric constant and the effective masses of the electron and hole. The dielectric constant, which is the susceptibility of the atoms within a material to be polarized by an electric field, affects the E_b as it is responsible for the screening of the Coulomb force by other electrons in the material which shields the attraction between the electron and hole and thus effects the radius by which an electron orbits its hole. Thus, the higher the dielectric constant, the smaller the E_b and the bigger the radius of the exciton and vice versa. The effective masses of the electron and hole directly affect the E_b as the masses determine the magnitude by which the Coulombic force can be felt by both particles, e.g. the higher the effective mass the

higher the E_b and the more stable the exciton should be. It is important to note that both the dielectric constant and effective masses of electrons and holes must be taken into account in the determination of the stability of an exciton.[81]

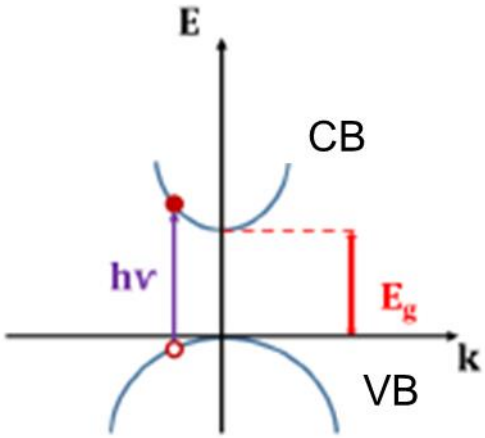


Figure 7. Schematic representation of absorption of a photon in a semiconductor.

1.3.3.2 Elementary Excitons and the Effects of Quantum Confinement

1.3.3.2.1 Wannier-Mott and Frenkel Excitons

The type of excitons observed in many crystalline materials depends on the nature of the material itself. Ionic (insulator) and molecular (e.g., organic molecules) crystals generally have excitons of the Frenkel type, which have a small radius (around tens of Angstroms) and large binding energies (>100 meV) that keep them localized within a small area on single atoms or molecules (Figure 8a).[84] In inorganic semiconductors with a degree of covalent character, excitons are generally classified as Wannier-Mott or free excitons, which are characterized by their small binding energies (10 - 30 meV) and large radii (30 - 100 Å) which are typically much larger than the size of the material's unit cell (Figure 8b).[81, 83] Stable excitons will only form if the binding energy is adequate to protect the exciton against collisions with phonons.[76]

Since the maximum energy of a thermally excited phonon at temperature T is approximately equal to the Debye temperature (~ k_BT, where k_B is Boltzmann's constant), stable free excitons can exist only if the exciton binding energy is greater than k_BT.[81] At room temperature, k_BT ~ 26 meV, which means that while Frenkel excitons will be stable at room temperature, Wannier-Mott excitons in many materials will only be observable at low temperatures.[76]

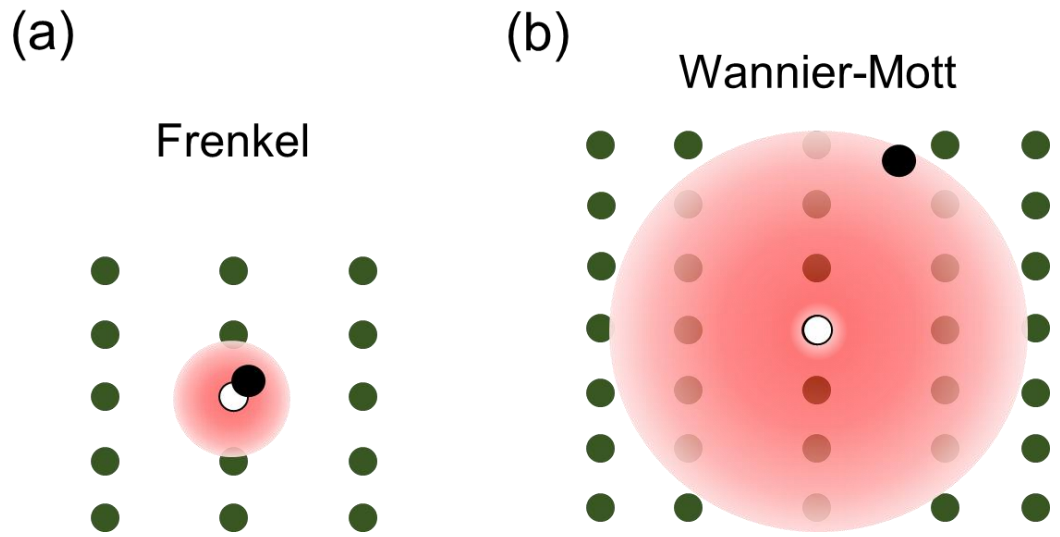


Figure 8. The two types of excitons found in semiconductors, (a) Frenkel and (b) Wannier-Mott, which differ based the size of their radii, which is illustrated by the size of the opaque red circle. The black and white circles the electron and hole, respectively.

Since an exciton is composed of a single electron and hole which are attracted to one another just like the electron and proton in a hydrogen atom, an exciton is considered hydrogenic and is modeled using the Bohr model. In this model, it is assumed that the exciton is free and that the electron and hole are moving through a medium with a high dielectric constant (ε_r).[76] The theoretical treatment of an exciton as a hydrogen atom allows us to conclude that the energy of the exciton created in a direct transition in a direct gap semiconductor at k =

0 is equal to the energy required to create the electron-hole pair (E_g), minus the binding energy due to the Coulomb interaction. Hence the energy of the exciton can be given by:

$$E_{\mathrm{n}} = E_g - \frac{E_b}{\mathrm{n}^2} \quad where\ E_b = \frac{\mu e^2}{32\pi^2 \hbar^2 \varepsilon_r^2} \tag{6}$$

where n is the principle quantum number, $\mu = m_e^* m_h^*/(m_e^* + m_h^*)$ is the reduced mass of the exciton and E_b is the exciton binding energy.[76] The exciton binding energy is the amount of energy needed to dissociate an exciton into a free electron and hole.[76, 85] The average distance between the electron and hole when the exciton is in the ground state is represented by the 3D Bohr radius (a_b), which is calculated by:

$$a_b = \frac{4\pi \hbar^2 \varepsilon_r^2}{\mu e^2}. \tag{7}$$

where ħ is Plank's constant.[76] Both the binding energy and exciton radius are important parameters for the classification of excitons present within semiconductors.

During the formation of an exciton, the energy threshold is reduced by an amount of energy between 1 meV - 1 eV which corresponds to the binding energy of the exciton (E_b).[76] The exciton dispersion curve, represented by the purple lines in Figure 9a, is associated with an effective mass equal to the sum of the effective masses of the electron and hole. Discreet levels appear due to the Coulombic attraction between the electron and hole and correspond to the creation of an exciton, which causes the appearance of atomic lines within the spectrum of the material (as shown in Figure 9b).[81] The probability for the formation of excitons is expected to be high as formation of excitons is more energetically favorable than free carriers, which is also why we expect to observe strong optical absorption lines equal to E_n which will appear in the optical spectra at energy just below the fundamental band gap, shown in Figure 9b.[76]

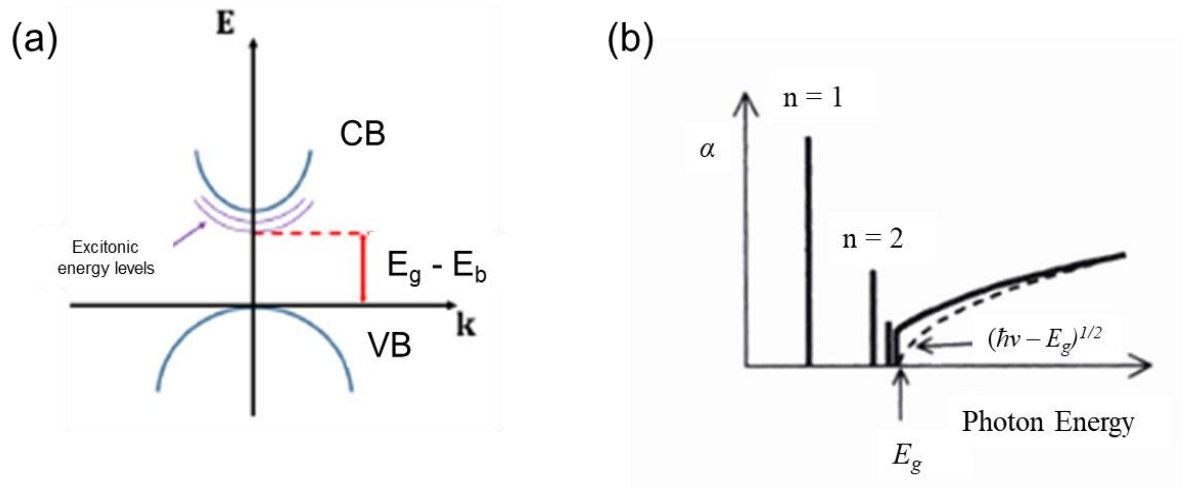


Figure 9. Systematic description of (a) discreet exciton energy levels that result from their attraction and (b) observed band edge absorption spectrum for a direct gap semiconductor as a result of excitonic emission. The dashed indicates the expected absorption when the excitonic effects are ignored.

A 3D semiconductor with a sufficiently high dielectric constant will typically have free excitons that can move freely through the crystalline lattice.[76] 3D halide perovskites have a polarizable lattice that screens the electrostatic attraction between excited charge carriers which results in small exciton binding energies (E_b).[17] In 3D lead iodide perovskites, the exciton binding energy is less than the thermal energy ($E_b < k_BT$) at room temperature which results in the formation of free carriers rather than excitons.[86] However, when the connectivity of the crystalline lattice is reduced, i.e. though dimensional reduction, the space through which the free excitons can move is drastically reduced. Quantum confinement is directly related to the dimensionality of a nanostructure. It occurs when their structural dimensions are on the order of the de Broglie wavelength or Bohr radius (1-10 nm) or smaller. In particular, the density of states become more atomistic as the dimensionality is reduced (as shown in Figure 5) .[76, 81] Dielectric confinement occurs when a thin layer of material with a large dielectric constant is sandwiched between another material that has a greater dielectric constant.[76] The electrostatic

force between the charges in the material with the higher dielectric constant increases due to the electric field generated by a charge extending into the lower dielectric constant material where it is less effectively screened, which is called the image-charge effect.[79, 87] Quantum and dielectric confinement effects in low-dimensional hybrid metal halides, increase the effective band gap and the exciton binding energy (up to a few hundred meV) compared to their 3D parents.[88-90] For instance, the exciton binding energy within a 2D perovskites increases by more than an order of magnitude from ~10 meV to greater than 300 meV from 3D to 2D perovskites.[88-89, 91] This large increase is due to the confinement of the exciton's wave function within the 2D inorganic layers.[17] The organic layers typically have low dielectric constants so they poorly screen the attraction between electrons and holes in the inorganic layers, which further enhances the exciton binding energy.[88, 92] With an increase in the exciton binding energy and a corresponding decrease in the exciton radius as dimensionality is reduced, the excitons present within lower-dimensional halide perovskites should become far more Frenkel-like.[93] This should result in excitonic properties that resemble those of free-excitonic states. However, excitons in 2D perovskites are currently classified as Wannier-Mott excitons,[94] while 1D and 0D are thought to be self-trapped excitons that arise from the deformability of the crystalline lattice or structural reorganization in the excited state.[77]

1.3.4 Photoluminescence of Low-Dimensional Halides

The principle of photoluminescence (PL) is as follows: a photon from a light source is optically absorbed, inducing the transition of an electron from its ground state in the VB to an unoccupied state in the CB, leaving a hole in its place. The hole and electron interact with the vibrations of the atomic network and emit (or absorb) phonons. Then, the electron and the hole radiatively recombine by emitting a photon whose energy differs from that of the excitation

photon. Thus, PL is the consecutive light emission following excitation of the energy states via the absorption of light. The mechanisms that control the signal of the PL can be classified in three stages as shown in Figure 10. First, excess carriers are created in the semiconductor by absorption of light, i.e. electron-hole pairs are generated and distributed within the semiconductor. Next, radiative recombination of electrons and excess holes occur. Finally these recombination result in the emission of the PL signal by the surface of the material since the emission signal is limited by the reabsorption of the photons and internal reflection at the surface. Excitonic emission occurs in the same way albeit the electron will recombine from an energy state lower than the band gap (E_g), hence the exciton energy $E_{em} = E_g - E_b$ as shown in Figure 10.

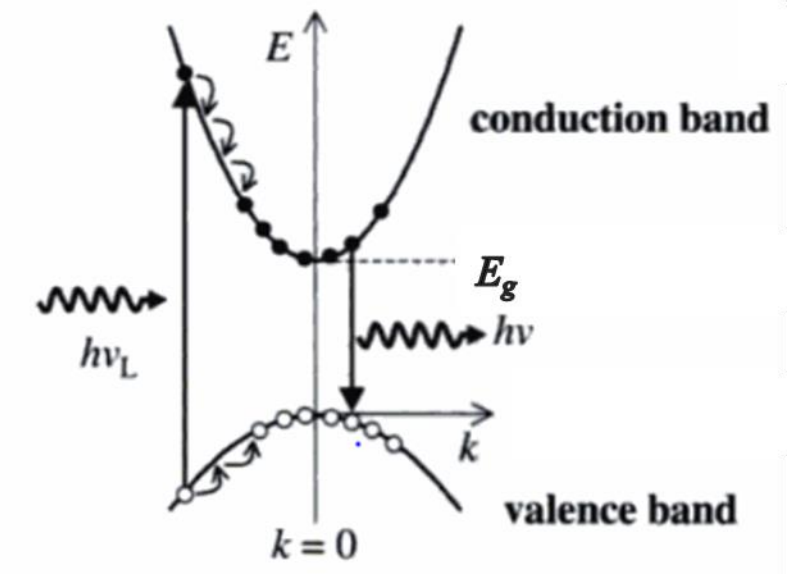


Figure 10. Schematic representation of the photoluminescence process in a direct gap semiconductor.

The study of photoluminescence properties of low-dimensional halides provides important insight into the mechanisms of emission present within these materials, and a way to study the effect of structure and composition on the properties that result. Emission in 2D lead-

halide perovskites has been studied for several decades using low-temperature and field dependent spectroscopy.[95-97] These studies indicated the presence of intense narrow green for $(PEA)_2PbBr_4$ or blue for $(C_nH_{2n+1}NH_3)_2PbI_4$ room temperature PL with a FWHM of ~100 meV and a minimal Stokes shift (~10 meV) from the radiative recombination of free excitons with high E_b and large oscillator strength as shown in Figure 11a.[98-100]

1.3.4.1 Self-trapped Excitons

When a semiconductor has a flexible lattice, charge carriers (electron/hole) can interact with it which induces elastic structural distortions that lower the energy of the overall system. This interaction between a charge carrier with a local lattice distortion is called a polaron, which is a quasi-particle that, like an exciton, is classified by the strength of the interaction between the lattice and charge carrier (coupling constant) and distance between them (radius).[76, 101] Large polarons generally have a long-range Coulombic interaction between the charge carrier and lattice and thus can be delocalized across several unit cells.[102 103] Changes to local bonding due to the charge on the localized carrier creates shorter-range lattice distortions (decreasing its effective radius), resulting in its classification as a small polaron.[101] Excitons can also interact with a deformable lattice and cause local lattice distortions creating small polarons which are termed self-trapped excitons (STEs).[13] STEs feature small exciton Bohr radii and large associated lattice deformations,[102] and their formation is promoted by high ionicity, low dimensionality and the deformability of the lattice which typically leads to narrow conduction and valence bands.[104] These features help to promote the creation of bound exciton levels within the band gap, while the deformable lattice reduces the energy needed for local structural distortion to occur.[104]

Several origins of emission in perovskites have been proposed and depend upon the composition and structure of the material, but . In 3D lead chloride perovskites weak broad red emission below 175 K has been attributed to STEs.[105] The 2D <110>-oriented perovskite (3API)$PbBr_4$ (3API = 3-aminopropyl imidazolium) exhibits broad yellow emission which was attributed to the π to π^* transition of the organic cations within the interstitial spaces of the corrugated 2D inorganic framework.[53] The broad Stokes-shifted white-light PL from the 2D perovskites $APbBr_4$ (where A = N1-methylethane-1,2-diammonium (N-MPDA), and 2,2′-(ethylenedioxy)bis(ethylammonium) (N-MEDA))[106-107] reported by the Karunadasa group (Figure 11) was attributed to the radiative decay of STEs formed within the inorganic lattice.[17] Since then, other white-light emitting 2D layered lead-halide perovskites have also been reported[108-109] as well as from other metal-halide perovskites containing Cd[85] that attribute their emission from the recombination of STEs localized on the inorganic framework.

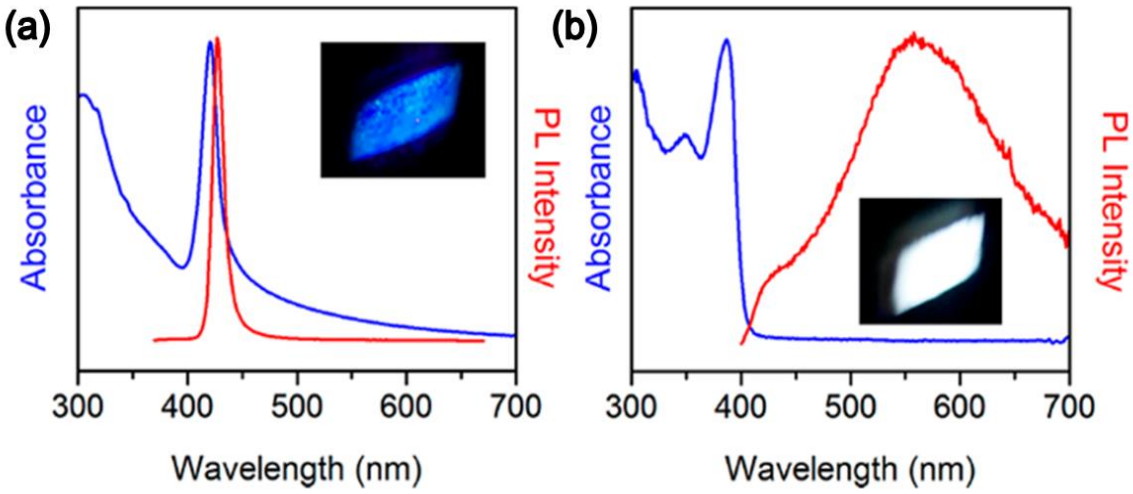


Figure 11. Absorption and photoluminesce spectra of (a) (N-MPDA)$PbBr_3$ and (b) (N-MEDA)$PbBr_4$ with the near-UV excitation of the respective powders. Adapted with permission from Smith et al. Chem. Rev. 2019. Copyright 2019 American Chemical Society.

Orientation of the layers within a 2D perovskite structure drastically affects the emission response. As shown in Figure 11, the <100>-oriented 2D lead halide perovskite (N-MPDA)$PbBr_3$ exhibit sharp free exciton PL at room temperature, while the <110>-oriented (N-MPDA)$PbBr_4$ exhibits broad PL.[17] The white emission exhibited by (N-MPDA)$PbBr_4$ is blue shifted from warm (yellowish) to cool (blueish) white light as chloride is alloyed in the halide position of (N-MEDA)$PbBr_{4-x}Cl_x$.[17] Altering the halide composition by adding more electronegative halide states affects the states at the VB maximum and ultimately increases the band gap energy, as reflected in the blueshift of the reported PL of the (N-MEDA)$PbBr_{4-x}Cl_x$ family.[106] From this prime example, as well as the examples provided within this dissertation, variation of the chemical composition provides a controllable way to tune the PL emission of any low-dimensional metal halide family.

To better determine the origin of the broad emission, power-dependent and temperature-dependent PL measurements are used. In power-dependence measurements, the power of the excitation light source is varied and the intensity of the resulting PL is recorded. The radiant power of the source is varied because the normalized PL intensity (I) is directly proportional to the radiant power (P) (amount of light that hits a sample per unit solid angle per unit projected area) of the source to an exponential constant (k) (where $I \propto P^k$ and $k = (d/d\log P)\log I$).[110] The constant, k, in the power-dependence relationship roughly describes the origin of emission.[110] A k-value of $k < 1$ indicates the presence of free carrier transition, whereas a value between $1 < k < 2$ indicates the presence of an exciton-like transition[110] with $1.2 < k < 1.5$ being a reported range for the existence of STEs in low-dimensional metal halides.[111-113] These values can be determined by plotting PL intensity vs. exciton power and fitting the data to determine the exponential constant.[110] Emission involving defects typically demonstrates linear behavior until

the defects states become saturated upon which a plateau is reached. In contrast, excitonic emission exhibits linear or slightly exponential behavior. In the above discussed 2D (N-MEDA)$PbBr_{4-x}Cl_x$ family, power-dependent PL measurements indicated a linearly dependent relationship suggesting that the broad band emission originated from excitonic states rather than defects.[108] Temperature-dependent PL builds on the information gained from power-dependent PL as lowering the temperature allows less interaction between the lattice and charge carriers which normally results in thermal broadening (broadening of PL spectra at higher temperatures leading to the loss of fine structure within the spectra) and results in a change of observed PL. For example, when searching for evidence of STE emission, cooling a material from room to low temperature decreases the ability of STEs to detrap and return to the free exciton state ($k_BT < E_{a,detrap}$; shown in blue in Figure 12), which increases the intensity of the broad PL peak.[17] At temperatures lower than 80 K, the carriers are less able to surmount the activation energy barrier to self-trap ($k_BT < E_{a,detrap}$; shown in red in Figure 12), which leads to a decrease in intensity of the broad PL peak and an increase in intensity and/or appearance of a narrow free exciton PL peak.[80] In low dimensional structures, PL Stokes shifts at low temperature have been attributed to localization of excitons in potential minima created by structural distortions.[99] As the temperature rises, exciton trapping becomes less efficient and as a result, the Stokes shift decreases with temperature and eventually disappears as the thermal energy (k_BT) overpowers the trapping potential.[99] Thus, large Stokes shifts at low temperature provides evidence of exciton self-trapping.[99] Other phenomena can also be observed at low temperatures, such as tunneling from free to self-trapped states,[114] free excitons bound to permanent defects,[100, 115] and formation of biexcitons,[84, 97] which add to the complexity of the observed PL. Despite the complexity of the spectra, various mathematical models have been

proposed to help elucidate the PL mechanisms occurring in the material, such as the Varshini model,[116] of which can be found in the following chapters of this dissertation.

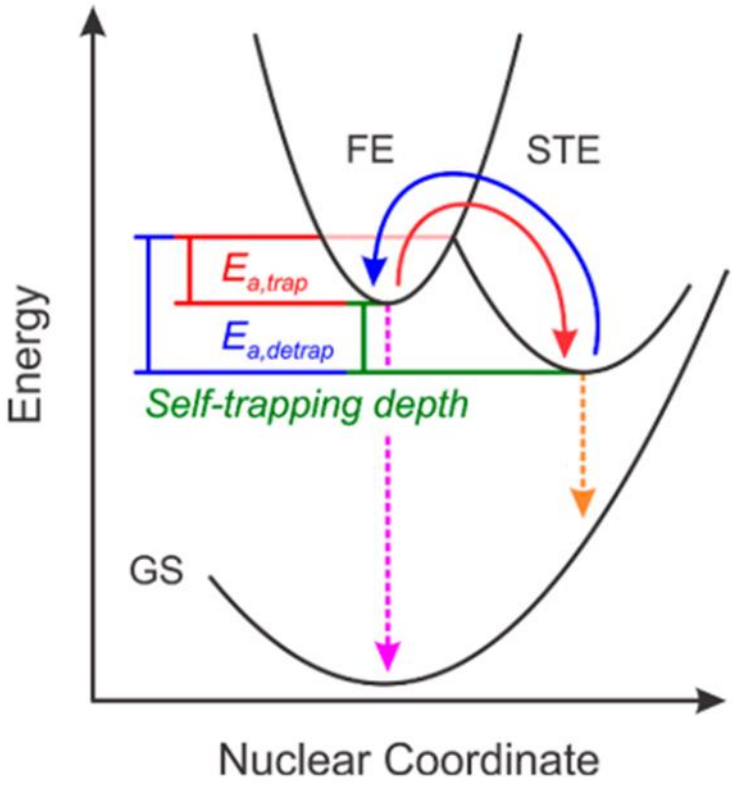


Figure 12. Schematic digram of the mechanism of self-trapping (red arrow) and detrapping (blue arrow) of excitons where (GS = ground state, FE = free exciton, STE = self-trapped exciton state, $E_{a,trap}$ = self-trapping activation energy, $E_{a,detrap}$ detrapping activation energy, and the pink and orange arrow depict the free exciton and self-trapped excitonic photoluminescence, respectively. Adapted with permission from Smith et al. Chem. Rev. 2019. Copyright 2019 American Chemical Society.

While these methods are only some of the general types of PL techniques available to aid in the characterization of the optical properties of solids, they are indispensable for the identification of possible real-world applications for new materials. For new materials to be considered for use as possible phosphors in solid-state lighting, the photoluminescence quantum yield (PLQY) is used as a measure of its internal luminescence efficiency. PLQY is

defined as the number of photons emitted as a fraction of the number of photons absorbed as described by:

$$PLQY(\phi) = \frac{N_{em}}{N_{abs}} = \frac{\int_{\lambda_1}^{\lambda_2} \frac{\lambda}{hc}\left(I_{emission}^{sample}(\lambda) - I_{emission}^{reference}(\lambda)\right)\mathrm{d}\lambda}{\int_{\lambda_3}^{\lambda_4} \frac{\lambda}{hc}\left(I_{excitation}^{sample}(\lambda) - I_{excitation}^{reference}(\lambda)\right)\mathrm{d}\lambda}\ x\ 100\% \qquad (8)$$

where N_{abs} and N_{em} are the number of photons absorbed and emitted by a sample, *h* is Planck's constant, *c* is the velocity of light, $I_{emission}^{sample}$ and $I_{emission}^{reference}$ are the emission intensities measured with and without a sample over the emission spectral interval (λ_1, λ_2) in wavelength, and $I_{excitation}^{sample}$ and $I_{excitation}^{reference}$ are the integrated intensities of the excitation radiation measured with and without a sample over the excitation wavelength interval (λ_3, λ_4).[117-118] While there are numerous standards for determination of PLQY of liquid solutions, few exist for solid samples.[117] Currently two solid standards, sodium salicylate (excitation at 360 nm resulting in 56% PLQY) and commercial grade YAG:Ce^{3+}(excitation at 340 and 460 nm resulting in 95% PLQY), are accepted as solid standards in literature.[118] These values act as benchmarks for the determining if a phosphor is worth pursuing for use in devices, as current phosphors with high PLQYs above 50% only being considered for industrial applications.

1.4 Applications of Luminescence Metal Halides

When considering a material for use in optical applications, some of the most important factors are the emission color and broadness of emission. The human eye's response to light spans the visible region of the electromagnetic spectrum from approximately 400 nm to 750 nm, however not everyone can perceive all of the shades within this spectrum. To standardize the colors seen by the naked eye as detected by detectors during spectroscopy experiments, the Commission Internationale de l'Eclairage (International Commission for Illumination, or CIE)

convened in 1931 to create a standardized method for the unbiased quantitative determination of the colors seen by photopic (bright-light) vision. Their standardization is represented by the 1931 CIE diagram shown in Figure 13a where the monochromatic wavelengths form the locus which outline the colored area. Within that colored area every color in the visible spectrum is represented by x and y coordinates. In the center of the diagram is white light which correspond to the coordinates (0.33, 0.33). The Planckian locus, shown as the black parabola in the middle of Figure 13, represents the emission color of a blackbody radiator at temperatures. The color of a blackbody radiator is characterized only the temperature, with higher color temperatures corresponding to bluer colors and lower temperatures corresponding redder colors.[119] For example, diffuse sunlight has a color temperature of between 5,700 and 6,500 K, whereas the CIE standard candle flame has a color temperature of approximately 2,000 K.[120] When referring to white light, any light source within the range of the Planckian locus can be assigned a correlated color temperature (CCT), which is the temperature of an ideal black body radiator that it is closest to. Light quality is standardized using the color rendering index (CRI), which specifies the ability of a light source to reproduce the colors of a specific object when compared with a natural light source. The CRI is found by comparing the difference in the CIE color coordinates of an object illuminated first with a test source and then separately with a black body radiator with the same CCT and is given a score that ranges from 0 to 100. For example, commercially available blue LEDs coated in YAG:Ce^{3+} phosphor typically have a CCT of between 4,000 K and 8,000 K a CRI that ranges from 70 to 80 depending upon the thickness of the phosphor.[121]

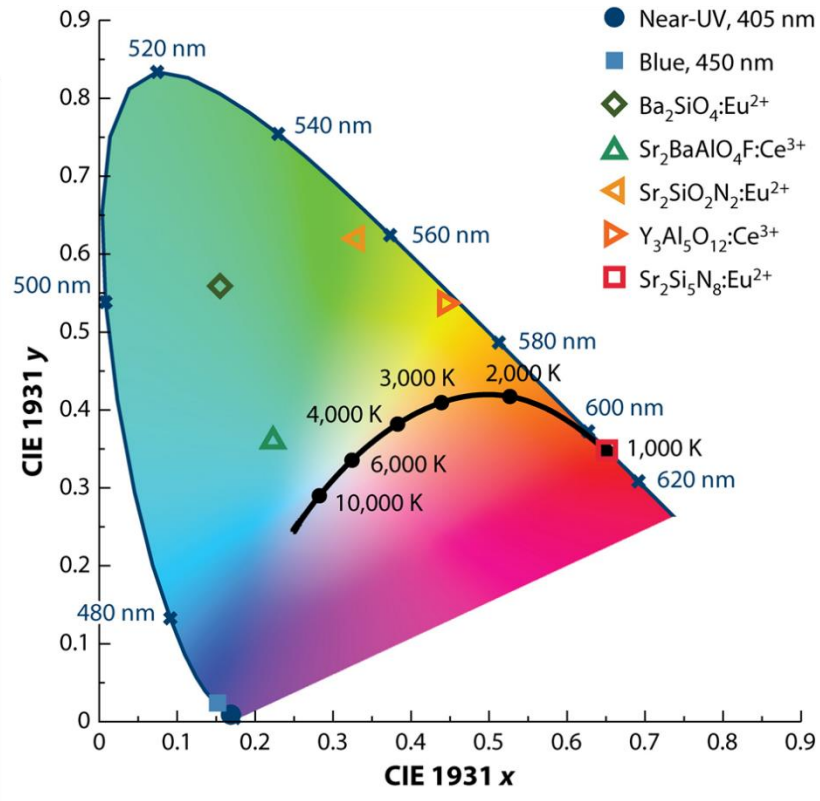


Figure 13. CIE1931 color coordinate plots of solid-state phosphors used in devices in curretly on the market. Reproduced with permission from Annual Reviews.[122]

The structural properties of low-dimensional metal halides can be engineered to modulate the PL energy and bandwidth, making them highly attractive for solid-state lighting (SSL) and integration in light emitting diodes. In particular, high CRI values (>80) are required for human eye health and color-critical high-level applications such as for televisions and computer monitor displays, and museum and office lighting and required for the improvement and use of SSL in the current market.[123] Nowadays, white-light emission in solid state devices is typically achieved by mixing different phosphors, leading to issues such as poor color rendition, self-absorption and different degradation rates.[124]

1.4.1 Phosphors

The most logical application for luminescent low-dimensional metal halides which exhibit both narrow and broad emission is as phosphors for various lighting applications.[123, 125] Color conversion phosphors[126-127] are used to coat UV-light-emitting diodes (LEDs) to yield specific colors for displays which require a wide color gamut.[13] As shown in Figure 14, some 2D lead halide perovskites exhibit free excitonic PL which results in narrow band emission. This narrow emission is required to produce highly pure colors that span the visible spectrum.[128] PLQY of bulk samples exhibit a strong structural dependence as not only the crystal structure but the composition and amount of distortion present within the inorganic framework influences the resulting luminescence efficiency.[129] For instance, increased distortion of the Pb-halide inorganic sublattice of some blue-light-emitting Pb−Br perovskites, has been correlated with the increased quantum efficiency (22%) in PEA_2PbBr_4 in comparison to $(C_6H_5CH_2NH_3)_2PbBr_4$ (3.8%).[129] This increase in efficiency is important as high efficiency blue phosphors are still rare.[111] Another factor that affects the PLQY is the method of synthesis. Although it is poorly understood, the chosen route of synthesis seems to drastically affect the resulting PLQY values, as the synthesis route influences the number of defects within a material and thus affects the recombination rates responsible for the PLQY. This lack of understanding presents an opportunity for more enhanced studies to be done to better elucidate these relationships and enable the design of more efficient phosphors.[13] This could be beneficial for the development of better semiconducting phosphors with narrow emission and high PLQY values, as they are needed for the improvement of LEDs relying on III−V semiconductors like InGaAs.[130]

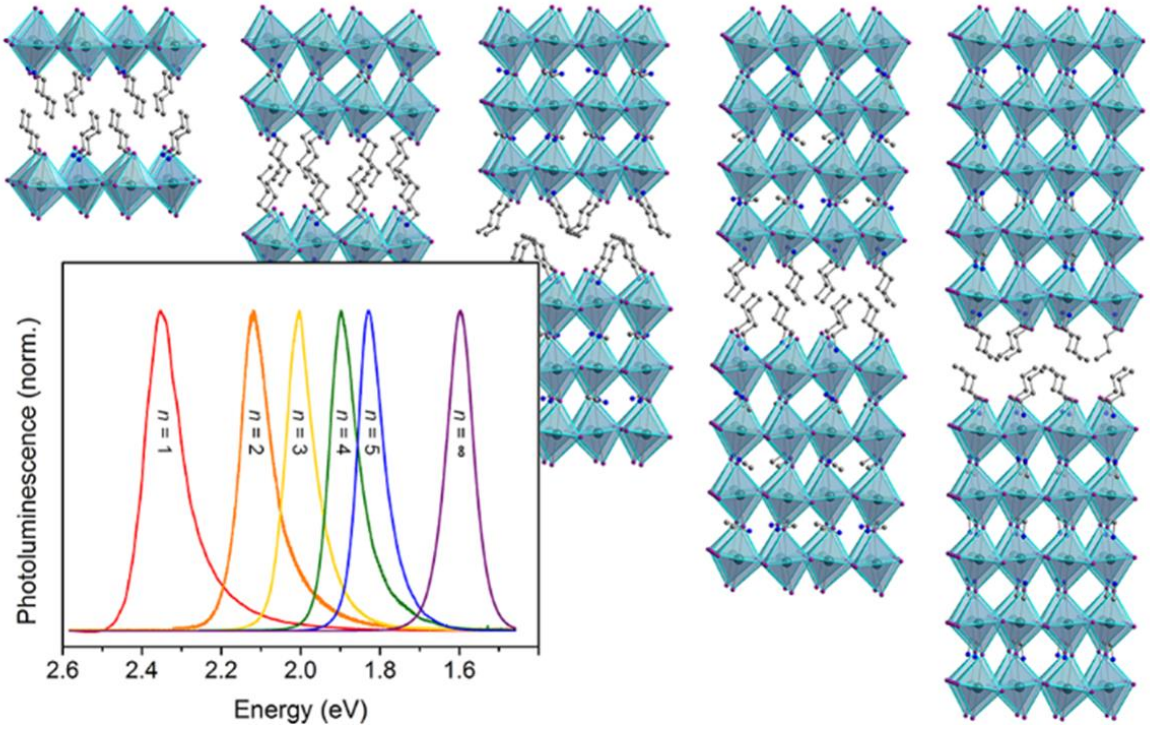


Figure 14. Crystal structures and photoluminescence of single crystals of the n = 1-5 members of the 2D $(C_4H_9NH_3)_2(CH_3NH_3)_{n-1}Pb_nI_{3n+1}$ family. Turquoise, purple, blue, and gray spheres represent Pb, I, N, and C, respectively. Reprinted with permission from Smith et al. Chem. Rev. 2019. Copyright 2019 American Chemical Society.

While narrow, free excitonic emission is great for achieving high color purity and important in resolution for display technology, broadband emission (which ranges from 400−800 nm) is needed for the high color rendition required by commercial lighting applications like museum and office lighting.[13] The ability of a white light source to properly render (or separate) colors of an object is quantified using the color rendering index (CRI) which is on a scale of 0-100 where 100 is the value given to broad daylight in sun light.[131] A high CRI is obtained by using a light source that contains all colors of the visible spectrum.[127] Despite this fact, emission from commercial phosphors like YAG:Ce^{3+} is not continuous, as it is missing parts of the visible spectrum and thus must be used along with other phosphors to obtain a high

CRI which adds to the cost and complexity of fabricating these devices.[131] Unfortunately, the multiple phosphor approach has several issues including self-absorption due to absorption and emission overlap and alteration of emission color due degradation of separate components.[131] A single phosphor with broadband emission covering the entire visible spectrum would eliminate these problems. With their broadband emission, low-dimensional white-light-emitting metal halides have potential as single-source phosphors in SSL devices.[127] Of the few reported Pb-halide white-light emitters, the majority of them exhibit CRI values greater than 80.[126] Color temperature, or the amount of blue or yellow in white light, is related to the temperature (in Kelvin) at which a black body radiator emits the same color through its correlated color temperature (CCT).[131] Through systematic halide substitution, white light emission from low-dimensional metal halides can be tuned to produce warm (CCT < 3000 K) or cold (CCT > 5000 K) emission.[13] For instance, Dohner et al. reported that through increasing the Cl content in (N-MEDA)$PbBr_{4-x}Cl_x$, blue shifts the emission from a yellowish white (CCT = 4669) to a bluish-white (CCT = 6502).[106] Despite the progress made in the past few years in understanding white-light emission in perovskites,[17] challenges such as optimizing internal quantum yields as well as stability remain before these materials will be ready for commercial use. For instance, films of (EDBE)$PbBr_4$[107] (EDBE = 2,2′-(ethylenedioxy)bis(ethylammonium)) and small crystals of the 1D $(H_3CNH_2(CH_2)_2NH_2CH_3)PbBr_4$ [73] exhibit PLQY values of ~9% and ~12%, respectively. Unfortunately, these numbers are significantly lower than what is needed for commercial use and are nowhere close to those reported for the inorganic yellow phosphors like YAG:Ce^{3+}.[126] However, unlike current inorganic phosphors on the market that are expensive to fabricate, solution processable thin films of low-dimensional metal halide phosphors can be inexpensively

deposited.[13] Phosphor stability is also important.[126] Initial studies of white-light-emitting perovskites suggest promising stability, with a thermal stability reported over 200 °C being reported for perovskites such as (EDBE)$PbBr_4$,[107] which is above the typical LED operating temperature.[126] However, more work is still needed including the need to assess the stability of these materials after they have been incorporated into SSL devices and as they have been subjected to typical LED operating conditions.[132-133]

1.4.2 Light Emitting Diodes (LEDs)

Light-emitting diodes (LEDs), unlike conventional light sources, provide direct transfer of electrical energy into light which results in a more efficient use of consumed energy. Conventional incandescent and fluorescent lamps rely on either heat or discharge of gases to create illumination which inevitably causes a large loss of energy through to the creation of heat.[134] With the advent of the blue InGaN LED chip coated with yellow YAG:Ce phosphor, introduced by Nichia Chemical Co. in 1996, a new style of lighting based on solid-state phosphor converted LEDs was born.[135] These new devices revolutionized the state of lighting with their many advantages over conventional light sources such as increased luminous efficiency and decreased use of energy, which is important since 22% of global energy used is for lighting purposes.[124] Solid-state lighting (SSL) materials also offer controllability of their spectral power and spatial distribution, color temperature, and polarization properties that other lighting materials do not making them one of the most promising classes of luminescent materials for LED applications to date.[124]

Currently, three main approaches are used to produce white light LEDs which differ in their efficiency, color stability and color rendering capability.[124] The three approaches are as follows: (1) a blue LED coated with yellow phosphors; (2) a UV-LED coated with blue and

yellow phosphors or red, green and blue phosphors; and (3) a full device that directly combines red, green and blue LEDs.[136] The use of a blue LED together with a yellow phosphor has been considered to be more advantageous compared with the other two methods as it is theoretically more effective at creating white light, not to mention that it is much cheaper to fabricate compared to the other two methods.[136] Unfortunately, the use of just a blue LED and a yellow phosphor greatly lowers the CRI value to a point where the devices become undesirable for indoor use.[136] The use of UV-LEDs with different mixtures of phosphors provides a better CRI value in comparison to the blue LED and yellow phosphor, but despite making them suitable for indoor applications but are more expensive and less efficient (as UV-LEDs still suffer from poor luminescence efficiency).[136-137] The third approach of combining three (or more) LED materials with different emission wavelengths to fabricate an LED, while being the most expensive option of the three, it is highly attractive, as these devices may have higher efficacies than the LED with phosphor(s) device architectures.[136]

Attractive optoelectronic properties of low-dimensional halide perovskites, such as tunable band gaps, strong excitonic luminescence, and ease of synthesis may be the answer to the current problems plaguing SSL. These attractive optoelectronic properties along with solution processability spurred early studies of their electroluminescence,[6] with the use of 2D perovskites for LED applications predating the use of 3D perovskites by over two decades.[7] The first report of electroluminescence from low-dimensional perovskites was reported in 1992 by Hong et al, where green electroluminescence was observed from a rudimentary device made from $PEA_2Pb_2I_7$ and silver contacts.[138] Soon after, full devices consisting of 2D lead iodide based perovskite thin films on a transparent conductive oxide substrate followed.[7, 139] Despite the initial improvements in device architecture, bright electroluminescence was only detected upon cooling below 110 K, and extremely high voltages (>24 V) were required needed to be

applied to yield luminescence.[7, 139] Since then room temperature LED devices containing thin films of PEA_2PbBr_4 have been reported to exhibit violet electroluminescence but with poor external quantum efficiency (EQE) values below 0.05%.[140]

Currently multiple 3D and 2D lead halide perovskites have been reported to achieve CRIs >80 their PLQY values are still too low (<9%) for use in commercial devices. Interestingly the 2D perovskites with the highest CRI values exhibited the strongest octahedral distortion which suggests that strong structural distortion is linked to both high CRI and low PLQY values. It has also been shown that through decreasing the dimensionality of a material and increasing the quantum confinement effects, STE formation is relaxed, and the emission efficiency and PL lifetime are increased, causes a red-shift in the luminescence which worsens the overall quality of white-light emission. To date, $(EDBE)PbBr_4$, $(DMEDA)SnBr_6$, $(PEA)_2PbBr_xCl_{4-x}$ and $Cs_2Ag_{0.60}Na_{0.40}InCl_6$ have been used in the fabrication of white light emitting LEDs using a down-conversion approach, where a commercial UV-LED is used to excite the low-dimensional perovskite layer coated on top of it. As an alternative approach to emission tunability, the ultrabroad PL spectrum of these WL materials could be modified by engineering their photonic environment so that the PL is suppressed or enhanced in specific spectral regions as was recently demonstrated by the incorporation of $(EDBE)PbCl_4$ in a polymer microcavity.[141] This along with other techniques such as lithography, could be applied for high color tunability in low-cost, flexible LEDs based on broadband emitters that do not solely rely on the emitters composition.[141]

1.4.3 Scintillators

Scintillators are important luminescence materials as they allow for high energy radiation, such as X-ray and gamma radiation, to be detected and used in the medical field, for

homeland security work, and in certain types of spectroscopy instrumentation.[142-143] Scintillation is a luminescence process where light of a certain energy is emitted after radiation is absorbed. The general mechanism by which inorganic scintillators function can be described in three main steps, as illustrated in Figure 15. First, radiation is absorbed where it creates an inner shell hole, an energetic primary electron, either radiative decay, nonradiative decay or electron-electron scattering, and creates electron-hole pairs. Next, thermalization occurs where the electrons move to the bottom of the CB and the holes move to the top of the VB. Finally, radiative recombination occurs through either the recombination of electron-hole pairs at sites within the crystallin lattice or through energy transfer to luminescence centers which is followed by emission.[142] Room temperature scintillation materials require a high mass density, components with a high mass number (Z) and a wide band gap so that impurity activator levels may fall within the gap. Inorganic scintillators currently on the market such as (NaI:Tl) and while other (SrI_2:Ce) are higher in resolution and cost less to make. However, these materials are difficult to grow as large single crystals which is important for industrial applications such in PET and CT-scanning instruments.[142]

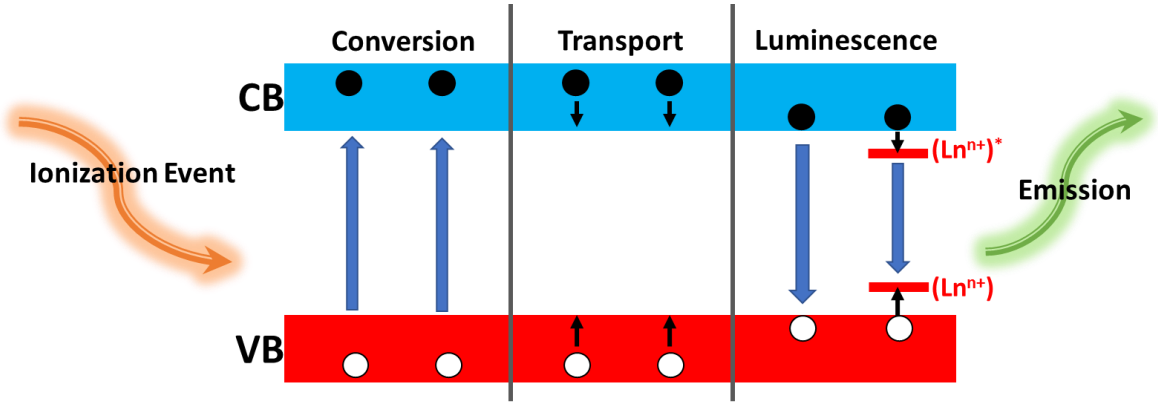


Figure 15. Schematic diagram the luminescence mechanisms of scintillators.[142]

The luminescence properties of the low-dimensional metal halides make them attractive scintillator materials as they can facilitate down conversion of high energy photons to lower energy photons over the rand of UV to IR radiation, which can be detected by conventional detectors like a PMT.[13] Unfortunately, inorganic scintillators are limited by slow response times on the order of tens of nanoseconds, which limits their spectral range and thus application.[144] But the characteristic short PL lifetime of excitonic luminescence in some low-dimensional metal halides like the 2D lead halide perovskites could offer a solution for the applications requiring a fast response time.[144] For example, $(C_6H_{13}NH_3)_2PbI_4$ exhibits a luminescence decay of 390 ps (28%), which was attributed to free-exciton recombination, and at the time was the fastest of any known scintillator, even surpassing organic scintillators.[145] Undoped scintillators are known to suffer from significant losses in efficiency at higher temperatures, which complicates their use as they require cooling with a cryostat.[13] By using low-dimensional metal halides that exhibit significant exciton binding energies, the impact of temperature fluctuation on emission efficiency in these materials are expected to be greatly reduced, which would be important in the development of higher temperature scintillation materials.[144, 146] For example, in a study at low temperature, the efficiency of the 3D $(CH_3NH_3)PbBr_3$ is comparable to NaI:Tl and greatly outdoes that of the 2D $(C_6H_{13}NH_3)_2PbI_4$ as the weakly bound excitons in $(CH_3NH_3)PbBr_3$ remain bound at lower temperatures.[145] However, when the temperature is raised to room temperature, excitons in $(CH_3NH_3)PbBr_3$ easily dissociate while those in the $(C_6H_{13}NH_3)_2PbI_4$ remain bound resulting in a higher efficiency for the 2D material (6.5%) compared to the 3D (0.075%).[145]

Low-dimensional perovskites have several other properties that make them great choices for scintillation materials. Under such intensely ionizing radiation, it has been shown

that 2D perovskites can remain stable under standard source operating levels encountered in practical applications which supports their eventual use in industry.[144-145] The smaller band gap of many low-dimensional metal halides in comparison to other common scintillator materials offers a specific advantage as the theoretical limit of a material's light yield is inversely proportional to its band gap, so the smaller the band gap the higher the theoretical light yield.[13] Additionally, since low-dimensional metal halides have tunable luminesce in the visible region, more efficient detectors can be coupled to them than are currently used on the market.[142, 147] Despite these advantages, several drawbacks still exist for the use of low-dimensional metal halide scintillators. If the chosen material exhibits a minimal Stokes shift of its excitonic emission, self-absorption will occur, which will decrease the light yield and an overall decrease in resolution.[146, 148] Some white-light-emitting 2D perovskites have been proposed as a solution for minimizing self-absorption, which would be advantageous, however, these materials suffer from lower light yields and slower response times due to differences in the emission mechanisms which hamper their use as alternative scintillation materials.[107] Therefore, further studies and new materials in this area are needed to overcome the current challenges of bringing low-dimensional metal halide scintillators to market.

1.5 Beyond Lead Halide Perovskites

Lead halide perovskites have been shown to demonstrate a wide array of properties from high charge carrier mobilities to high exciton binding energies depending upon the chemical composition and dimensionality of the structure (as discussed above). For the purpose of designing luminescent materials, the ability to tailor the charge localization at the molecular level is one of the main reason perovskites are so exciting. However, despite the positive aspects of using lead halide perovskites, the Pb toxicity and poor thermal, air and moisture stability

make their use in commercial applications far less appealing.[149] Therefore, it is imperative to explore the effects of replacing lead with an alternative metal that is ideally less toxic and more air stable.

The first logical step would be to replace Pb with other group 14 metals like Sn and Ge. Unfortunately, the resulting 3D and even 2D materials have proven to be more unstable than their Pb counterparts as Sn^{2+} and Ge^{2+} rapidly oxidize to their +4 oxidation states, not to mention that both Sn and Ge are toxic as well.[150-151] In the case of some Sn-based compounds, the combination of lowering the dimensionality to 0D and incorporating larger more hydrophobic organic cations has proven to increase the stability of the resulting structures while also providing highly emissive compounds (PLQY upwards of 75%) ranging from yellow to red in color that has been attributed to the formation of STEs.[66] Since our main concern in this work is the tunable luminescence of these materials across the visible spectrum, the challenge remains to find other materials that fill the color gaps or cover the entire spectrum.

1.5.1 Bismuth and Antimony Based Metal Halides

Recently, less toxic Sb- and Bi-based families have been considered as alternative systems, with many compositions resulting in materials with room temperature emission.[133, 152-154] For example, the 1D Sb-based perovskite family $(CH_3SC(NH_2)_2)_2SbX_5$, exhibit greater stability and higher exciton binding energies than 3D $CH_3NH_3PbI_3$ making them good candidates for optoelectronic devices.[155] Other Sb-based systems form 0D non-perovskite structures based on isolated square pyramidal $SbCl_5^{2-}$ units, such as $(Ph_4P)_2SbCl_4$ depicted in Figure 16a, which exhibits broadband red emission with a large Stokes-shift of 1.77 eV and a PLQY of 87%.[156] Interestingly, Zhou et al. report that the PLQY for $(Ph_4P)_2SbCl_4$ can be further enhanced to 99% through injecting an antisolvent to force precipitation of the product, which

they attribute to formation of fewer defects within the obtained crystals.[156] 1D Bi-based materials have also been reported, such as $(C_6H_{14}N)_2BiBr_5$ which exhibits strong blue emission with a direct band gap of ~2.02 eV and long PL lifetime attributed to radiative recombination of strongly bound excitons.[157] Interestingly, $(C_6H_{14}N)_2BiBr_5$ exhibited photoconductive behavior and high stability in moist environments, making it a viable replacement material in optoelectronics.[157]

In addition to 0D metal halide hybrids based on isolated polyhedrons, metal halide clusters have also been reported. One such compound, $(CH_3NH_3)_3Bi_2I_9$, composed of small clusters of two face-sharing octahedra, allows for the localization of excitons on within the clusters, resulting in large exciton binding energies (>300 meV) and blue emission at room temperature.[158] Furthermore, blue emission has been reported from the doping of Bi^{3+} into non-emissive Cs_2SnCl_6. The resulting emission is largely Stokes shifted with a high PLQY value of ~80%, which was concluded to arise from STEs and was successfully used as the excitation source in the fabrication of a yellow phosphor down converted LED.[159] Although Bi- and Sb-based halides show interesting luminescent properties with high quantum yields, the known materials currently do not span the whole color gamut which limits their use in optoelectronic devices.

1.5.2 Alternative Non-Pb Metal Halides

Many theorists have calculated the formability of the halide perovskite with other B-site metals that are based on both the tolerance and octahedral factors, within which various metal halide systems are predicted to form perovskite structures.[31, 160] Out of all of the predicted systems, many of the non-Pb metal halide systems remain relatively unexplored in both their structures and their optical and electronic properties. For example, perovskite structures are

predicted to form from cadmium and mercury halides, but not from zinc due to its smaller ionic radius which typically result in isolated ZnX_4 tetrahedra. Thus, with the small number of reports on the physical properties of perovskite and non-perovskite halide materials containing group 11 or 12 metal halides, it is important to investigate these systems with hope of finding new and useful properties. .

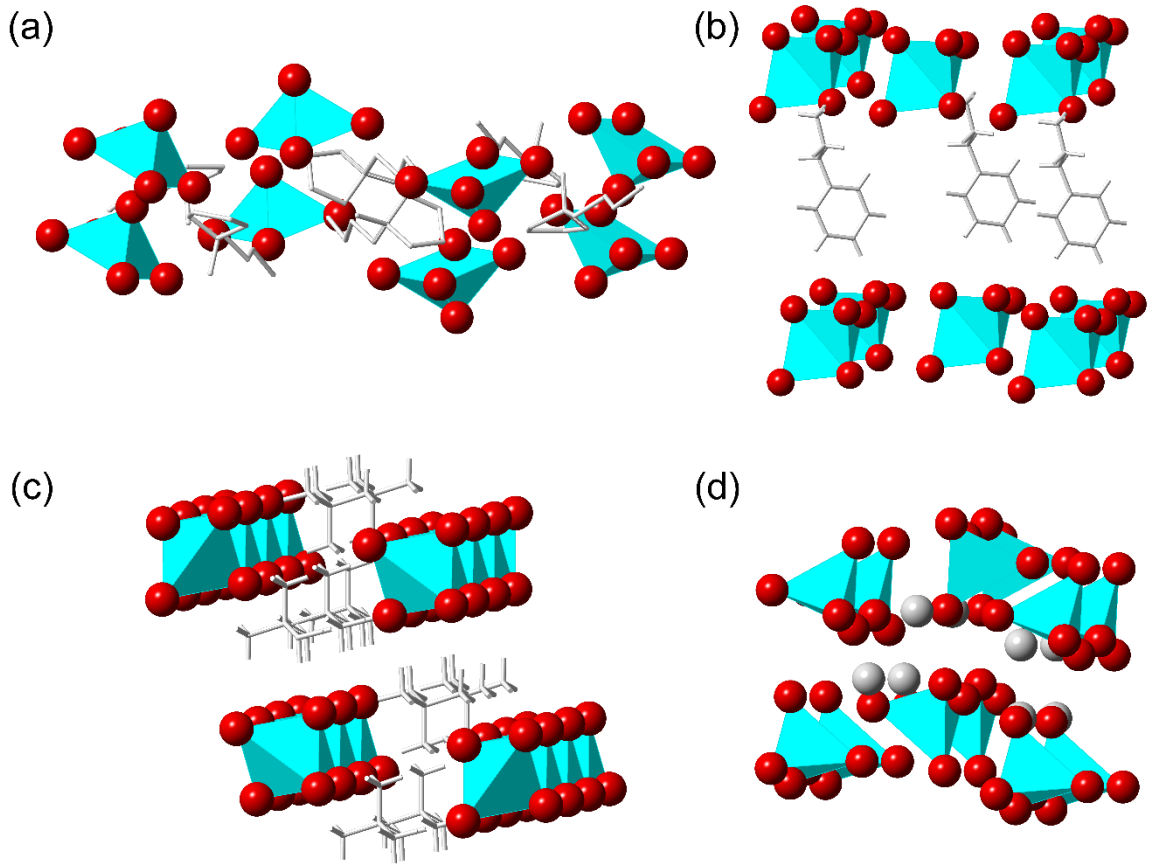


Figure 16. Examples of non-perovskite structures based on (a) square pyramidal $(Ph_4P)_2SbCl_5$,[156] (b) edge sharing seesaw shaped $(C_6H_5C_2H_4NH_3)HgCl_3$,[161] (c) edge sharing tetrahedra wires of $(N(CH3)_4)AgCl_2$,[162]and (d) tetrahedra Rb_2ZnI_4.[163] Organic cations are shown as wires for visual clarity.

The luminescence of the Group 11 binary halides such as CuCl and AgCl, have been studied for almost 50 years as they display fascinating excitonic behavior.[164-166] In CuX (X = Cl, Br, I), multiple types of excitonic behavior have been reported, a large majority of which

has been attributed to intrinsic excitonic emission that results of the annihilation of Wannier-Mott excitons.[165] Excitonic emission in CuCl and CuBr have been reported with exciton binding energies of 190 meV for CuCl, 108 meV for CuBr, and 68 meV for CuI,[167-168] which results in highly inefficient blue-violet emission at room temperature (PLQY values < 05%, according to our measurements).[169] In comparison, AgCl and AgBr do not luminesce above 50 K, but do luminesce at low temperatures.[166] AgI, on the other hand exhibits blue room temperature luminescence.[170] The luminescence exhibited by AgX (X = Cl, Br, I) has been attributed to STE.[166, 170] Interestingly, very few studies of the luminescence of the binary halides AuX and AuX_3 (X = Cl, Br, I) exist in literature. From what is known, both AuCl and AuBr exhibit blue-green luminescence below room temperature, whereas $AuBr_3$ exhibits red luminescence at room temperature.[171-172] The emission in AuCl has been attributed to the annihilation of free excitons,[172] whereas emission below room temperature for $AuCl_3$ has been attributed to self-trapped excitons.[173] Luminescence studies of AuI and AuI_3 are unfortunately missing, whereas reports of luminescence with other metal halides like CuI and AgI have been reported instead.[174-176] Thus, all-inorganic or hybrid organic-inorganic compounds containing isolated clusters of these metal halides should exhibit excitonic emission that can be harnessed to create efficient phosphors or scintillators.

Many low-dimensional Cu^{2+} halide perovskite systems were studied for their ideal quasi-2D Heisenberg ferromagnetic behavior in the early 1960s.[56] Interestingly, studies on halide perovskites containing Ag or Au are remarkably absent until the past 20 years where they are mostly reported in double perovskites such as $(CH_3NH_3)_2AgBiBr_6$,[177] $Cs_2InAgCl_6$,[178] $Cs_2Au_2X_6$ (X = Cl, Br, I)[179-180] and our groups recent paper on $(CH_3NH_3)AuX_4$ (X = Cl, Br).[181] However, there is a severe lack of knowledge on systems like these as well as all-inorganic and

hybrid organic-inorganic metal halides containing Ag and Au halides. Hybrid halide systems containing copper also remain relatively underexplored with a few examples of divalent Cu-based perovskites such as $(CH_3NH_3)_2CuCl_xBr_{4-x}$.[182] In comparison, Cu^I halides remain essentially unexplored. And while many structures for all inorganic Cu-halides have been reported, no luminescent properties had been reported until recently when our group began to study the CsX-CuX system.[111, 183] As for the Ag and Au halides, little has been reported on the discovery of new structures as well as luminescence properties, with the most recent report coming from our group involving the synthesis and study of the optical properties of the $(CH_3NH_3)AuX_4$ (X = Cl, Br) family.[181] In our study we found that the $(CH_3NH_3)AuX_4$ family crystallizes in an exotic way where the members create alternating perovskite and non-perovskite layers.[181] While this family exhibited weak emission at room temperature, it was clear from the weak blue emission that the luminescence originated from the inorganic units, although further PL studies are needed to confirm if excitonic emission is present within these materials.[181] Based on the excitonic nature of their binary metal halides, it could also be inferred that materials based on group 11 halides should result in interesting excitonic luminescence properties.

Group 12 binary halides, in particular ZnI_2, CdI_2,[184] and HgI_2[185] have been reported to exhibit excitonic absorption at low temperature, which points to the possibility of the creation of excitonic emission in systems that contain these metal halide clusters. This hypothesis is proven by the report of multiple hybrid organic-inorganic group 12 halide systems exhibiting room temperature PL of various colors. Some of the first reports of broadband white light emission have been attributed to the formation of STEs within the 2D perovskites $(C_2H_5NH_3)_2CdCl_4$[186] and $(C_6H_{11}NH_3)_2CdBr_4$.[85]. While $(C_2H_5NH_3)_2CdCl_4$ only exhibits

emission below 50 K, room temperature broadband white light emission was reported for $(C_6H_{11}NH_3)_2CdBr_4$.[85] Room temperature blue emission has also been reported from the 1D edge-sharing square pyramidal $(C_5N_2H_9)CdCl_3$[187] and the 1D perovskite $(C_6H_{14}N_2)CdCl_4 \cdot H_2O$.[188] Recent reports of the 0D non-perovskite family $(C_{18}H_{13}N_2O_2)_2MX_4$ (M = Zn, Cd, Hg; X = Cl, Br) based on isolated tetrahedra show that all members exhibit room temperature blue emission, although the origin of the emission has yet to be probed.[189] Our group has also synthesized a similar family of Hg-based compounds, $(C_3H_5N_2)_2Hg_3Cl_8$ and $(C_3H_5N_2)HgI_3$ which contain the imidazolium cation. $(C_3H_5N_2)_2Hg_3Cl_8$ forms 0D clusters formed by edge-sharing tetrahedral dimers separated by linear $HgCl_2$ moieties whereas $(C_3H_5N_2)HgI_3$ forms 0D edge-sharing tetrahedral dimers. Both compounds exhibit broadband light yellow room temperature emission which has been attributed to STEs.[190]

Out of all the group 12 metal halides, the zinc halides are the most exciting due to their low toxicity, earth abundance and their reported broad emission. Very few Zn-based all-inorganic and hybrid organic-inorganic metal halide materials have been reported, with only a handful of previous studies reporting the PL of these materials. In the all-inorganic 0D isolated tetrahedra-based compounds Rb_2ZnI_4 and Tl_2ZnI_4 (depicted in Figure 16d) ,room temperature emission is not present but at lower temperatures broadband emission centered around 1.9 eV in Rb_2ZnI_4[191] and 2.5 eV in Tl_2ZnI_4[192-193] which is attributed to the recombination of excitons. In the 0D hybrid organic-inorganic compound (4,4'-H_2bipy)$ZnBr_4$, broadband room temperature emission centered on 567 nm was observed.[194] However, the origin of emission was never probed further, leaving room for further studies and development in this area.

From the standpoint of generating light-emission, the use of low dimensional group 12 metal halides could be beneficial due to their ability to create highly confined charges within

their dimensionally reduced inorganic substructures.[93] Through large spatial separation of inorganic subunits, highly-localized charges in these materials results in remarkably high exciton binding energies (> 300 meV) which can provide enough stability for the formation of stable excitons at room temperature and play a critical role in determining if the use of these materials are feasible for specific optoelectronic applications.[93, 195] For instance, technology that is based on electron-hole recombination for the emission of light such as phosphors, LEDs and scintillators, could benefit from materials with high binding energies, as discussed in **Section 1.4**.[27, 104] The added benefit of using group 12 metal halides, especially materials that utilize Zn, offer lower toxicity in comparison to Pb halides.[196] Interestingly, as mentioned above, many of these metal halide systems[197-201] have remained relatively unexplored and are thus worthy of exploration.

To this end, we have begun to address this gap in knowledge with the Cu, Zn, Cd and Hg halide families reported in the following chapters. In Chapter 2 and 3 the crystal structure and optical properties are reported for hybrid organic-inorganic group 12 halide families $(CH_3NH_3)_2CdX_4$, $(C_5H_3N_2H_3)_2ZnBr_4$ and$(C_5H_3N_2H_3)_2HgBr_4$, and R-M-X (R = $C_{15}H_{26}N$, M = Zn, Cd; X = Br, I). Through the progression of the development of these families it is shown how room temperature emission can be achieved through the tuning of the chemical composition of the group 12 families. In Chapter 4, the luminescence properties are further tuned to result in greater light yield in the $Cs_3Cu_2X_5$ and $CsCu_2X_3$ families. These unique Cu halide families have interesting 0D cluster and 1D wire structures that offer greater air and moisture stability compared to lead halide materials while also being highly efficient blue, green and yellow emitters.

Chapter 2: Size Effects in Hybrid Group 12 Metal Halides

Low-dimensional hybrid organic-inorganic materials (HOIMs) are being widely investigated for their unique optoelectronic properties and use in applications such as light-emitting diodes[9] and transistors,[202] laser cooling,[203] laser gain media,[204] photodetectors,[205] scintillators,[206] and solar cells.[23, 207-208] The broad range of applications considered in literature is due to the vast compositional and structural tunability offered by hybrid halide A–B–X materials (A = organic cation, B = metal cation, X = halide anion), which in principle can allow a variety of substitutions to be carried out at each of the A, B and X sites. Variation of the organic cation size via A-site substitution allows control of the material's dimensionality, which can be freely varied from 0D cluster compounds to 3D networks.[27] In addition to the A cation size effects, substitutions of the B- and X-sites allow fine-tuning of electronic structure and optoelectronic properties since the B and X element states are the dominant contributors to the states around the Fermi level.[27]

In this chapter we begin our study of structure-property relationships within low-dimensional halides by investigating the size effects on the optoelectronic properties of hybrid group 12 halides with the MA_2CdX_4 (MA = $CH_3NH_3^+$; X = Cl, Br, I) and $4AMP_2MBr_4$ (4AMP = $C_5H_7N_2^+$; M = Zn, Hg) families. Both unique families provide different yet complementary insight into the effects of systematical changes of the A, B and X constituents on the structures and physical properties of d^{10} metal-based hybrid systems. In the first section of this chapter, the results of the systematic change in halogens are examined in the MA_2CdX_4 family. Whereas in the second half, the effect of systematically changing the metal is examine in the $4AMP_2MBr_4$ family. In combination, the consideration of these two families also provides an insight into the impact of the organic cation on the observed structures and properties. The

impact of the organic cation is especially evident in the observed luminescent properties—the MA_2CdX_4 members do not luminesce at room temperature whereas, the $4AMP_2MBr_4$ members demonstrate bright room temperature white-light (WL) emission. Our findings on the MA_2CdX_4 and $4AMP_2MBr_4$ families have been summarized in recent publications in *Inorganic Chemistry*[209] and *Chemistry of Materials*,[112] respectively, which are provided below.

2.1 Methylammonium Cadmium Halides MA_2CdX_4 (X = Cl, Br, I)

2.1.1 Introduction

In recent years, hybrid organic-inorganic halide materials have emerged as excellent candidates for optoelectronic applications including solar cells,[1] light-emitting diodes (LED), lasers,[210] and photodetectors.[27, 211-212] In addition to their outstanding optoelectronic properties, low temperature solution processability and broad tunability of their chemical compositions, crystal, and electronic structures[27] make hybrid halides the focus of global attention. Among hybrid materials, the perovskite $MAPbI_3$ ($MA = CH_3NH_3$) and its other Pb- and Sn-derivatives are the most extensively studied types due to their performance in high efficiency solar cells.[1] The grand challenges of hybrid organic-inorganic materials research[27] include the exploration of compositions beyond the dominant Pb- and Sn-based systems, the systematic study of compounds that are based on different types of polyhedra (e.g. tetrahedral building blocks) and connectivity (e.g. edge-sharing, face-sharing), among others.[27] These future goals are also relevant for solar cell research due to the fact that the state-of-the-art photovoltaic (PV) material, $MAPbI_3$, suffers from Pb-toxicity and poor stability in air, and their Sn-based alternatives have also proven to be air-sensitive.[149] Therefore, studies of non-Pb/Sn hybrid halide compositions are primarily fueled by the desire to make air stable, Pb-free solar cells, and so far has mostly focused on Sb- and Bi-based compositions.[133, 152-154]

Considering the compositional and structural tunability of hybrid halide A–B–X materials (A = organic cation, B = metal cation, X = halide anion), in principle, a variety of substitutions can be carried out targeting each of A, B and X sites. Variation of the organic cation size via A-site substitution allows control of the material's dimensionality, which can be freely varied from 0D cluster compounds to 3D networks.[27] In addition to the size effects, substitutions of the B- and X-sites allow fine-tuning of electronic structure and optoelectronic properties since the B and X element states are the dominant contributors to the states around the Fermi level.[27] Through control of structural dimensionality and chemical compositions, one can design organic-inorganic halides for specific applications including materials for lighting[213] and scintillator applications.[129, 214-217] For impurity-doped scintillators, the design of which are targeted in this work, large band gaps (e.g., > 5 eV for NaI:Tl^+ and $LaBr_3$:Ce^{3+}) are desirable to accommodate dopant levels and to avoid thermal quenching at room temperature.[93]

The large band gaps and highly localized charges with remarkably high exciton binding energies and stable excitonic emission can be realized in low-dimensional hybrid organic-inorganic materials.[27, 218] Briefly, excitons (a bound pair of an excited electron and a hole) in inorganic semiconductors, called Wannier excitons, typically have large radii (30-100 Å) and low binding energies (10-30 meV) on the order of k_BT at room temperature (~26 meV).[219] Charge transport and emission in such systems are typically non-excitonic, i.e., excitons are broken apart at room temperature into free charge carriers and the emission from the recombination of the delocalized charges produces lower light output.[93] In contrast, by selectively combining organic and inorganic components, exciton binding energies (60 to 545 meV) and radii (22.9 to 6.2 Å) can be tuned over a broad range in hybrid materials.[27, 218] Decay of stable excitons via recombination of the electron-hole pair results in spontaneous light

emission, which can be used for lighting and high-light-yield scintillator applications. To obtain large band gap materials with high exciton binding energies and localized charges, a low electronegativity B metal element, such as Cd (1.69),[220] can be paired with halogen elements in hybrid organic-inorganic halides.[221]

Here, we report a systematic study of prospective scintillator materials MA_2CdX_4 (X = Cl, Br, I) including their low temperature solution synthesis, variable temperature single crystal and powder X-ray diffraction studies, band structure calculations, and optical properties. Several studies focusing on crystal structures of MA_2CdCl_4 and MA_2CdBr_4 have been previously reported,[222-224] whereas MA_2CdI_4 is a new compound reported here for the first time. Despite the compositional similarity, the crystal structures of MA_2CdX_4 differ from each other with MA_2CdCl_4 adopting a ⟨100⟩-oriented 2D layered perovskite structure, while MA_2CdBr_4 and MA_2CdI_4 crystallize in 0D K_2SO_4-derived structures built upon isolated CdX_4-tetrahedra. MA_2CdCl_4 undergoes two structural transitions upon cooling from room temperature down to 20 K, consistent with the earlier reports,[222-223] whereas MA_2CdBr_4 and MA_2CdI_4 do not have phase transitions in the measured range. According to density functional theory (DFT) band structure calculations, MA_2CdX_4 have direct band gaps. The measured optical absorption data suggest band gaps larger than 3.9 eV with onsets of absorption at 5.29 eV for MA_2CdCl_4, 4.92 eV for MA_2CdBr_4, and 3.94 eV for MA_2CdI_4. The valence and conduction bands feature flat bands suggesting a high degree of charge localization that paves the way for the formation of stable excitons in MA_2CdX_4. Room temperature photoluminescence (PL) measurements give broad PL peaks within 375 – 955 nm range with full width at half maximum (FWHM) values up to 208 nm. We discuss the potential of MA_2CdX_4 for optical applications based on our combined experimental and theoretical work.

2.1.2 Synthesis and Methods of MA_2CdX_4 (MA = CH_3NH_3; X = Cl, Br, I)

2.1.2.1 Reactants

Chemicals used in this study were either used as purchased or synthesized from the starting materials listed: (i) methylammonium hydrochloride, 99%, Sigma-Aldrich; (ii) methylamine solution, 40 wt. % in H_2O, Sigma-Aldrich; (iii) hydrobromic acid, 48 wt. % in H_2O; (iv) hydroiodic acid, 57 wt. % in H_2O; (v) cadmium chloride, 99.99%, Sigma-Aldrich; (vi) cadmium bromide, 98%, Alfa Aesar; (vii) cadmium iodide, 99.999%, Alfa Aesar; (viii) absolute ethanol, 200 proof; (ix) diethyl ether, 98%, Alfa Aesar; (x) benzene, >99.9% HPLC grade, Aldrich; (xi) N,N-dimethylformamide (DMF), 99%, Fisher; (xii) methanol, reagent grade, Aldrich.

2.1.2.2 MABr and MAI Synthesis

MABr and MAI were synthesized using the methods previously reported in literature.[225] Briefly, stoichiometric amounts of HBr(aq) and HI(aq) were added dropwise to cooled (0 ºC) methylamine solutions under vigorous stirring and allowed to mix for up to 1.5 hr. After removing excess solvent under vacuum at 60 ºC, the powder product was re-dissolved in ethanol to make a slurry from which white powder products of MABr and MAI were precipitated by adding excess diethyl ether. The resulting crystals were washed with 200 proof ethanol and benzene, then dried under vacuum overnight under inert atmosphere. Typical yields of these reactions ranged from 45-65%.

2.1.2.3 MA_2CdX_4 Synthesis and Single Crystal Growth

MA_2CdCl_4, MA_2CdBr_4, and MA_2CdI_4 crystals were all grown through slow evaporation of their stoichiometric (2:1 molar ratio of MAX to CdX_2) solutions. All solution synthesis and crystal growth experiments were carried out in small vials (2 – 20 mL) at around room

temperature (20 – 65 °C). Initially, various solvent systems including pentane, dimethylacetamide (DMA), N,N-dimethylformamide (DMF), dimethyl sulfoxide (DMSO), water, and methanol were tried for crystal growth. The best quality crystals resulted from a 1M MA_2CdCl_4 water solution, and 1M MA_2CdBr_4 and MA_2CdI_4 methanol solutions. The MA_2CdCl_4 solution readily formed colorless plates whereas the MA_2CdBr_4 and MA_2CdI_4 formed aggregations of small colorless and pale yellow blocks, respectively (sub-mm crystal sizes). Crystals were also grown at an accelerated rate by evaporating saturated solutions on low heat (between 40 – 65 ° C) in ambient air; however, the quality of crystals produced from fast growth were generally poorer compared to the ambient temperature growth described above. Large single crystals of MA_2CdCl_4 were grown using 1M DMF solutions under ambient conditions in crystallization dishes and by applying low vacuum to a solution enclosed in a 5 mL vial over two weeks. In this method, the crystal sizes are limited by the container dimensions with the largest crystal size of $4 \times 3 \times 2$ mm^3 (Figure S1).

Elemental analysis for $(CH_3NH_3)_2CdI_4$: calculated C 3.51, H 1.77, N 4.09, I 74.19%; found C 3.55, H 1.69, N 4.03, I 73.97%.

2.1.2.4 Powder X-ray diffraction

Powder X-ray diffraction (PXRD) measurements were performed on a Rigaku MiniFlex600 system with a D/tex detector using Ni-filtered Cu-Kα radiation. Typical scans were done to determine phase identity and purity and were performed in the 3-90° (2θ) range, with a step size of 0.02°. Data analysis was performed using Rigaku's PDXL software package. The collected data were fitted using the decomposition method (also called Pawley fitting) embedded in the PDXL package. Noticeable wetting of the MA_2CdI_4 powdered samples occurred when samples were left out in the air for more than one day, whereas moisture

instability of the other analogues was not observed over the same period. However, as a precaution, powder samples were stored in nitrogen flushed containers or in a N_2-filled glovebox.

For controlled air stability studies, MA_2CdX_4 thin films prepared by spin coating 50 µL of 1M methanol solutions were left in ambient air on a laboratory bench for a period of 2 weeks. During this time, PXRD measurements were regularly performed using the conditions described above. In order to distinguish between oxygen and moisture stability of MA_2CdX_4, powder and thin-film samples were also left in a dry air chamber fabricated from a desiccator containing Drierite desiccant, and periodically tested for O_2 stability. For moisture stability studies, a vacuum desiccator was used to remove ambient air and introduce dry nitrogen gas into the chamber with 2 mL of distilled water to induce a humid N_2 environment.

Variable temperature powder X-ray diffraction measurements were carried out using an Oxford PheniX closed-cycle cryostat on a PANalytical X'pert Pro MPD diffractometer using Cu Kα1 radiation with an X'celerator position sensitive detector. Partial decomposition of the MA_2CdBr_4 and MA_2CdI_4 samples used for these measurements was observed. Therefore, low temperature diffraction results for these compounds were analyzed by fitting the target phase component only.

2.1.2.5 Single Crystal X-ray diffraction

The X-ray intensity data for MA_2CdX_4 were collected on a Bruker Apex CCD area detector diffractometer with graphite-monochromated Mo-Kα (λ = 0.71073 Å) radiation. For low temperature measurements, crystals were cut to suitable sizes in a DOW Chemical vacuum grease and cooled under a stream of nitrogen to 100(2) K. For room temperature measurements, crystals were selected from their mother liquors, covered with Super Glue and affixed to the goniometer

head. Once dry, the measurements were conducted at room temperature, 298(2) K. The crystals structures for all analogs were determined from a non-linear least-squares fit. The data were corrected for absorption by the semi-empirical method based on equivalents and the structures were solved by direct methods by use of the SHELXTL program and refined by full matrix least-squares on F^2 by use of all reflections.[226-227] All non-hydrogen atoms were refined with anisotropic displacement parameters and all occupancies within two standard deviations, whereas all hydrogen atom positions were determined by geometry. Details of the crystallographic results are given in Table 1. Atomic coordinates, equivalent isotropic displacement parameters, and selected interatomic distances and bond angles are provided in Tables S1-S8. Further details of the crystal structure studies are summarized in the CIF (Crystallographic Information File) files and have been deposited in The Cambridge Crystallographic Data Centre (CCDC) and can be found under deposition numbers 1563635-1563638.

2.1.2.6 UV-vis Absorbance Measurements

Optical absorption measurements were carried out on an HP 8452A Diode Array UV Vis Visible Spectrophotometer over a 190 nm – 820 nm range. For absorption measurements, thin films of MA_2CdX_4 were prepared by spin coating 50 µL of 1M methanol solutions of the respective MA_2CdX_4 on cleaned UV quartz slides for 30 seconds at 2000 rpm using the Laurell model WS-650MZ-23NPPB spin processor.

2.1.2.7 Variable Temperature Photoluminescence Measurements

Photoluminescence (PL) measurements were conducted over a spectral range from 360 nm to 1025 nm using a He-Cd laser set at an excitation wavelength of 325 nm using a silicon CCD detector. Samples were spin coated on cleaned UV quartz slides and allowed to dry in

ambient conditions as detailed above. PXRD was performed on the samples to verify phase purity both before and after the PL measurements.

2.1.2.8 Electronic Structure Calculations

Our calculations were based on density functional theory (DFT) with Perdew−Burke−Ernzerh (PBE) exchange-correlation functional[228] as implemented in the plane-wave basis VASP code.[229] The projector augmented wave method was used to describe the interaction between ions and electrons.[230] The kinetic energy cutoff was 520 eV. The lattice parameters were fixed at the experimentally measured values while the atomic positions were optimized until the force on each atom was less than 0.01 eV/Å. The k-point meshes of 4×4×1, 3×2×2, and 3×2×1 were used for structural optimization of MA_2CdCl_4, MA_2CdBr_4, and MA_2CdI_4, respectively, while denser k-point meshes of 8×8×1, 8×4×4, and 6×4×1 were used for the calculations of density of states (DOS). Spin-orbit coupling (SOC) was also included in these calculations.

2.1.3 Room Temperature Crystal Structures

Since MA_2CdCl_4 and MA_2CdBr_4 structures have already been reported in literature,[2,3] studies were performed to complement this work as well as focus on a brand new compound MA_2CdI_4. A summary of the room temperature single crystal X-ray diffraction studies of these compounds is provided in Table 1 and the corresponding crystal structures are depicted in Figure 17. Although the compounds in this family are isoelectronic, their structures are markedly different. The crystal structure of MA_2CdCl_4 features 2D inorganic $[CdCl_4]^{2-}$ layers built upon corner-sharing $CdCl_6$ octahedra separated by organic cation layers. Consequently, MA_2CdCl_4 belongs to the large family of ⟨100⟩-oriented layered hybrid organic-inorganic

perovskites.[4] In contrast, the 0D crystal structures of MA_2CdBr_4 and MA_2CdI_4 feature isolated $CdBr_4^{2-}$ and CdI_4^{2-} anions separated by MA^+ cations.

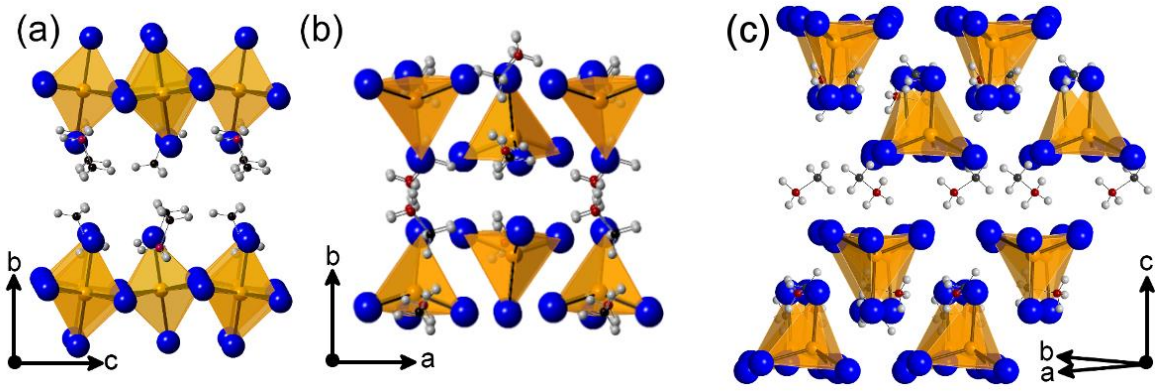


Figure 17. Polyhedral views of the crystal structures of (a) $(CH_3NH_3)_2CdCl_4$, (b) $(CH_3NH_3)_2CdBr_4$ and (c) $(CH_3NH_3)_2CdI_4$. Orange, blue, red, grey, and black spheres represent Cd, halogen (Cl, Br or I), N, H, and C atoms, respectively. For clarity, only a fraction of methylammonium ions are shown in (b) and (c).

To the best of our knowledge, a parent 3D hybrid organic-inorganic perovskite compound based on cadmium halides have never been reported. Reported structures of inorganic and hybrid organic-inorganic halides based on cadmium are predominantly of the NH_4CdCl_3-type, which features 1D double chains made of edge-sharing $CdCl_6$ octahedra.[231] Examples of cadmium halides adopting the NH_4CdCl_3-type structure include $ACdCl_3$ (A = K, Rb, Tl, NH_4) and $ACdBr_3$ (A = Rb, In, NH_4).[225, 232-235] These observations cannot be simply explained using either the tolerance (t) or octahedral (μ) factors as detailed in **Chapter 1**[27, 31, 35, 236-237] as many of the compositions cited above fall within the acceptable tolerance and octahedral factor ranges. For example, tolerance factors of $MACdCl_3$, $MACdBr_3$ and $MACdI_3$ compositions are 1.02, 1.00, and 0.98, respectively, and their octahedral factors are 0.50, 0.48, and 0.44, respectively. A recent comprehensive analysis of the formability of perovskite structures suggest that acceptable ranges of the tolerance and octahedral factors for the formation of 3D perovskites are 0.8 to 1.1 (t) and 0.44 to 0.895 (μ).[27, 35] Therefore, in principle,

3D perovskites $MACdCl_3$, $MACdBr_3$ and $MACdI_3$ should be accessible; however, $MACdCl_3$ and $MACdI_3$ have not been reported to form, whereas $MACdBr_3$ has been reported to crystallize in the $BaNiO_3$-derived 1D chain structure.[238] NH_4CdCl_3, the crystal structure type most cadmium halides crystallize in is also within the acceptable range with $t = 0.84$ and $\mu = 0.50$, but forms 1D edge-sharing octahedral chains. This analysis clearly demonstrates the limitations of crystal structure predictions based on the tolerance and octahedral factors alone.

In contrast, A_2CdCl_4 (A = Rb, Cs) compounds are known to adopt layered perovskite derived K_2NiF_4-type structures[238-239] whereas Cs_2CdBr_4 and Cs_2CdI_4 crystallize in the K_2SO_4-type structure featuring 0D structures with isolated tetrahedral CdX_4^{2-} anions with cations filling the voids in between.[231] Similarly, in the MA_2CdX_4 series, MA_2CdCl_4 is a perovskite derivative whereas MA_2CdBr_4 and MA_2CdI_4 structures can be likened as derived from the K_2SO_4 structure through replacing K^+ with MA^+. The exact arrangement of CdX_4^{2-} anions and organic cations in MA_2CdBr_4 and MA_2CdI_4 differ, leading to different space groups for the two compounds. Thus, MA_2CdBr_4 is isostructural with MA_2HgBr_4[240-242] crystallizing in the monoclinic space group $P2_1/c$, whereas MA_2CdI_4 crystallizes in the orthorhombic space group *Pbca*.

Structural distortions of hybrid materials not only impact their formability and stability but also have a major influence on their optoelectronic and semiconducting properties.[27] Since divalent Cd^{2+} in MA_2CdX_4 has a $5s^0\ 4d^{10}$ electronic configuration, distortions of the B-metal halide polyhedra due to a stereochemically active lone pair, which regularly occurs for Pb- and Sn-based compounds,[27] is not expected. Indeed, the $CdBr_4$ and CdI_4 tetrahedra are almost regular with the Br-Cd-Br and I-Cd-I tetrahedral angles ranging from 105.17(3) to 112.16(2)° and 106.78(5) to 115.88(5)° (Tables A1.2, A1.5, A1.7-8). The narrow deviation from the ideal tetrahedral angle can be attributed to the distortions of the CdX_4^{2-} units caused by hydrogen

bonding interactions, another major source of structural distortions in hybrid organic-inorganic perovskites.[27] In the case of MA_2CdCl_4, the reported room temperature structure (space group *Cmca*) also features nearly regular $CdCl_6$ octahedra with the Cl-Cd-Cl angles of 89.54° and 90.46°.[222]

Table 1. Selected room temperature single crystal data collection and refinement parameters for $(CH_3NH_3)_2CdBr_4$ and $(CH_3NH_3)_2CdI_4$.

Formula	**$(CH_3NH_3)_2CdBr_4$**	**$(CH_3NH_3)_2CdI_4$**	**$(CH_3NH_3)_2CdCl_4$**	**$(CH_3NH_3)_2CdBr_4$**
Formula weight (g/mol)	496.18	684.14	318.34	496.18
Temperature (K)	298 (2)		100 (2)	
Radiation, wavelength (Å)	Mo Kα, 0.71073		Mo Kα, 0.71073	
Crystal system	Monoclinic	Orthorhombic	Monoclinic	
Space group, Z	$P2_1/c$, 4	$Pbca$, 8	$P2_1/c$, 2	$P2_1/c$, 4
Unit cell parameters	a = 8.1257(5)	a = 10.9692(14)	a = 10.375(4) Å	a = 8.0734(8)
(Å)	b = 13.4317(8)	b = 12.1583(15)	b = 7.424(3) Å	b = 13.2215(13)
	c = 11.4182(7)	c = 20.861(3)	c = 7.349(3)	c = 11.3649(11)
	β = 96.1840(10)º		β = 110.829(5)º	β = 96.082(2)º
Volume (Å^3)	1238.95(13)	2782.2(6)	529.1(4)	1206.3(2)
Density (ρ_{calc}) (g/cm^3)	2.660	3.267	1.998	2.732
Absorption coefficient (μ) (mm^{-1})	14.609	10.400	3.010	15.005
$\theta_{min} - \theta_{max}$ (º)	2.3491 – 26.9605	1.95 – 26.44	4.04 – 27.25	2.3708 – 30.8818
Reflections collected	27253	20954	13540	25703
Independent reflections	7755	2408	1190	2777
R^a indices ($I > 2\sigma(I)$)	R_1 = 0.0293	R_1 = 0.0524	R_1 = 0.0726	R_1 = 0.0208
	wR_2 = 0.0653	wR_2 = 0.1488	wR_2 = 0.1750	wR_2 = 0.0481
Goodness-of-fit on F^2	1.031	1.041	1.063	1.076
Largest diff. peak and hole (e$^-$/Å^3)	1.995 and -1.625	1.778 and -1.821	2.519 and -2.035	0.764 and -0.940

[a] $R_1 = \sum||F_o| - |F_c||/\sum|F_o|$; $wR_2 = \{|\sum|w(F_o^2 - F_c^2)^2|/\sum|w(F_o^2)^2||\}^{1/2}$, where $w = \{1/|\sigma^2 F_o^2 + (AP)^2 + BP|\}$, with $P = (F_o^2 + 2F_c^2)/3$ and weight coefficients A and B.

2.1.4 Variable Temperature X-ray Diffraction Studies

Hybrid organic-inorganic materials notoriously undergo successive phase transitions, especially upon cooling, which are often associated with the motion of organic cations, hydrogen bonding interactions, and subsequent distortions of the inorganic substructure.[27, 223, 243] Since structural distortions and phase transitions have a strong influence on the resultant semiconducting, optoelectronic, and excitonic properties of the hybrid materials,[27] variable temperature X-ray diffraction experiments were performed on MA_2CdX_4.

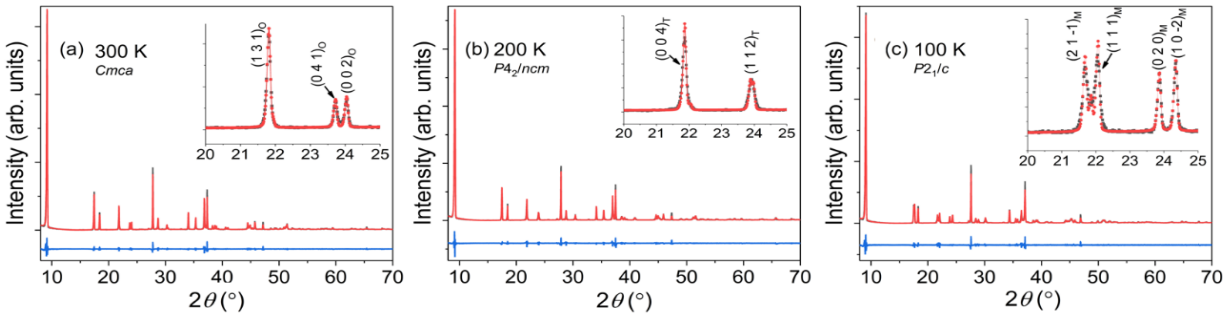


Figure 18. Powder X-ray diffraction (PXRD) patterns (black dots) for (CH3NH3)2CdCl4 at (a) 300 K, (b) 200 K and (c) 100 K, showing successive phase transitions upon cooling. The Pawley fits and difference plots are shown as red and blue dotted lines, respectively.

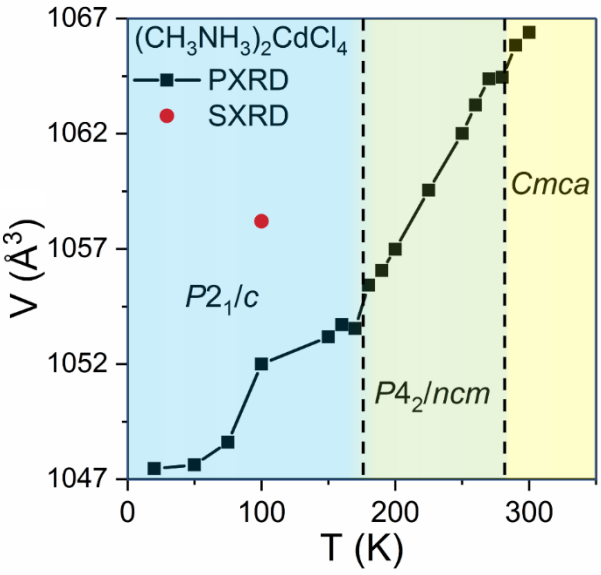


Figure 19. The variation in cell volume with temperature based on variable temperature PXRD and SXRD results shown in black squares and red dots respectively. The observed phase changes are denoted by a dashed line with each colored region corresponding to the orthorhombic (light yellow), tetragonal (light green) and monoclinic (light blue) phases of $(CH_3NH_3)_2CdCl_4$. In this plot, the monoclinic phase volumes are doubled to bring them to scale with the tetragonal and orthorhombic phases of $(CH_3NH_3)_2CdCl_4$.

2.1.4.1 MA_2CdCl_4

Variable temperature structural studies have already been conducted on MA_2CdCl_4 by Chapuis et al.[222-223] MA_2CdCl_4 undergoes three phase transitions: (1) at 484 K from the high temperature tetragonal *I*4/*mmm* phase to the orthorhombic *Cmca* phase, (2) at 283 K from the *Cmca* phase to the tetragonal $P4_2/ncm$ phase, and (3) at 173 K from the $P4_2/ncm$ phase to the monoclinic $P2_1/a$ phase.[2,3] Our variable temperature powder X-ray diffraction measurements (Figures 19 and 20) on MA_2CdCl_4 have largely confirmed these findings, including the transition temperatures. The transition temperatures were determined based upon the appearance of splitting peaks, especially in the 20-25° range, as shown in the Figure 19 insets. Importantly, the temperature dependence of the unit cell volume (Figure 20) indicates some deviation from the normal linear cell contraction with cooling at ~100 K. This could indicate a

possible missed phase transition at this temperature, especially considering the structural transitions in the hybrid materials are often subtle due to slight changes in the atomic positions of the organic moieties. Furthermore, upon closer inspection, we noticed that the interlayer distance in the reported low temperature monoclinic $P2_1/a$ phase[223] is unusually and unphysically large (Figure A1.2 in **Appendix 1**). To determine the correct structure of the low temperature form of MA_2CdCl_4, we carried out single crystal X-ray diffraction experiments for MA_2CdCl_4 and MA_2CdBr_4 at 100 K, which are summarized in Table 1 and Table A1.2 and A1.5 in **Appendix 1**. As expected, the correct structure refined in the space group $P2_1/c$ has a much smaller interlayer distance with the interlayer unit cell parameter of b = 7.424(3) Å compared to the interlayer parameter c = 19.37(1) Å in the previous report (Figure A1.2).[223]

2.1.4.2 MA_2CdBr_4 and MA_2CdI_4

Several structural studies have been previously reported for MA_2CdBr_4 utilizing X-ray diffraction, differential scanning calorimetry (DSC), infrared spectroscopy, ^{1}H nuclear magnetic resonance (NMR), and nuclear quadrupole resonance (NQR).[224, 244-246] The study conducted by Rao et al. suggests that structural transitions exist at 167 K and 400 K based on DSC and infrared spectroscopy measurements.[244] However, Nakayama et al. reported that there is no evidence of a phase transition from 4.2 K to 300 K.[245] Given the discrepancy in literature regarding the low temperature phase transitions in MA_2CdBr_4, we performed variable temperature PXRD and SXRD experiments (Table 1, Figures 21a and 22a). Our results further support the findings of Nakayama et al., demonstrating that there is no evidence of a phase transition in the 20 – 295 K range.[245] Upon cooling, a regular contraction of the unit cell volume is observed for MA_2CdBr_4 (Figure 22a). Interestingly, Nakayama et al.[245] also reported the observation of an anomaly at 120 K in their NQR readings, which they attributed to anisotropic

thermal expansion of the unit cell. In contrast, we were not able to confirm any structural anomalies at this temperature (Figure 22).

Variable temperature measurements were also performed on MA_2CdI_4 to probe for possible phase transitions. Based on our measurements, as shown in Figure 22b, MA_2CdI_4 exhibits a normal contraction of unit cell volume from 295 K to 100 K and then begins to deviate from 100 K to 20 K with an abnormal increase in cell volume as the temperature is decreased. This unexpected deviation is not accompanied by structural transitions at these temperatures based on our PXRD results. In literature, hybrid organic-inorganic compounds have been shown to exhibit anisotropic thermal expansion, zero thermal expansion, and negative thermal expansion effects that deviate from the normal contraction of the cell volume with cooling.[247-249]

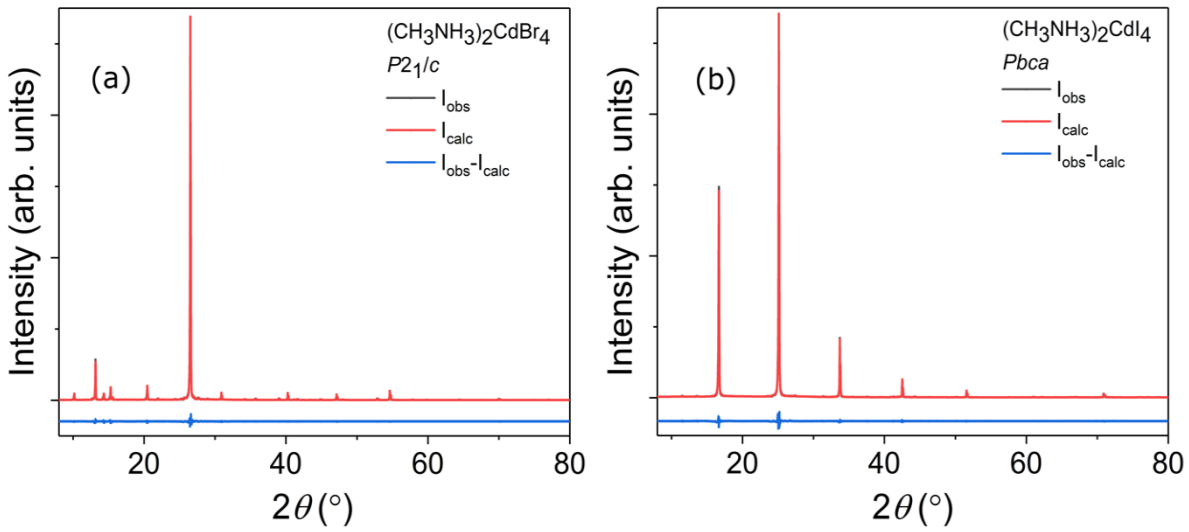


Figure 20. Room temperature PXRD results for $(CH_3NH_3)_2CdBr_4$ and $(CH_3NH_3)_2CdI_4$. Pawley fits are shown in red, which overlap the gray observed spectra, and the difference maps are in blue.

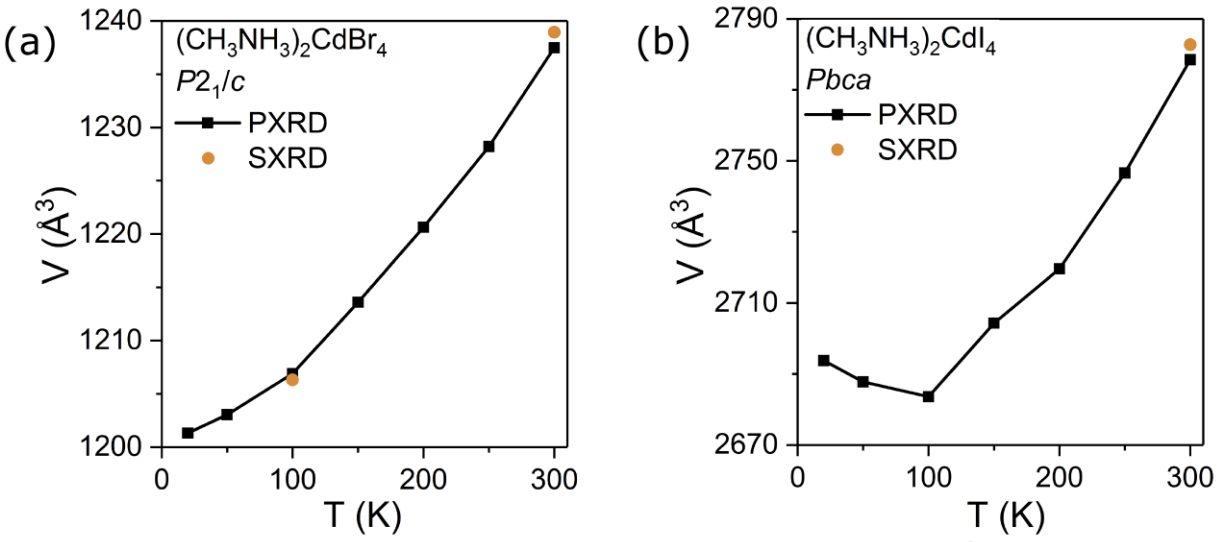


Figure 21. Temperature dependence of unit cell volume for (a) $(CH_3NH_3)_2CdBr_4$ and (b) $(CH_3NH_3)_2CdI_4$ based on variable temperature PXRD and SXRD results, which are shown in black and gold, respectively.

2.1.5 Air and Moisture Stability

Given their highly ionic nature, some hybrid organic-inorganic halides are unstable in ambient air, especially in a humid environment.[27] In fact, this is a major shortcoming of the high performance photovoltaic material $MAPbI_3$,[133, 149] making air stability studies very important for the evaluation of prospective optoelectronic applications of hybrid halides. In this study, air stabilities of spin-coated MA_2CdX_4 films, some of which show high preferential orientation, were studied by exposing them to ambient air for over 2 weeks (Figure 23). For MA_2CdCl_4, no observable change was recorded during the two-week period, whereas MA_2CdBr_4 and MA_2CdI_4 show signs of degradation. In the case of MA_2CdBr_4, impurity peaks are clearly noticeable after leaving the thin film sample out for one day in ambient air. These impurity peaks have successfully been assigned to $MACdBr_3$. Interestingly, after a quick partial decomposition, degradation of MA_2CdBr_4 slows and no further change has been observed after

exposing the sample to ambient air for two weeks. In the case of MA_2CdI_4, its thin film shows a higher degree of preferential orientation after one day in air. Note here that powder MA_2CdI_4 samples show noticeable wetting when left in air overnight; therefore, the observed change in the degree of preferential orientation of the MA_2CdI_4 can be explained by the wetting of the film and the crystallites reorienting to form a highly oriented film. Beyond the change in preferential orientation, after two weeks in air, a strong impurity peak is also observed. However, we were not able to assign this impurity peak to any known compound in this system.

In order to distinguish between the impacts of oxygen and water, we also monitored the stabilities of MA_2CdX_4 samples in dry air and wet N_2 environments (Figure 23). MA_2CdCl_4 and MA_2CdI_4 exhibited no observable change over the two-week period in our dry air chamber, whereas MA_2CdBr_4 showed clear signs of degradation after two weeks as evidenced by the emergence of $MACdBr_3$[250] peaks (Figure 22b). In the wet N_2 environment, MA_2CdCl_4 sample showed a higher degree of preferential orientation due to moisture absorption, but as expected, the sample remained largely unchanged. In contrast, MA_2CdBr_4 and MA_2CdI_4 demonstrated signs of complete degradation and loss of crystallinity after one day within the chamber.

Based on these results, MA_2CdX_4 compounds have contrasting air and moisture stabilities. MA_2CdCl_4 is air and moisture stable, MA_2CdBr_4 is unstable both in dry air and wet N_2 environments, and the instability of MA_2CdI_4 is primarily caused by water. The marked difference in the air stabilities of these compounds can be attributed to the fact that chlorides are generally more stable in air compared to bromides and iodides.[251] Additionally, stability has also been shown to be affected by structural dimensionality,[23] the 2D layered structure of MA_2CdCl_4 featuring protective organic cation layers could prevent fast degradation of the material as opposed to the 0D cluster structures of MA_2CdBr_4 and MA_2CdI_4.

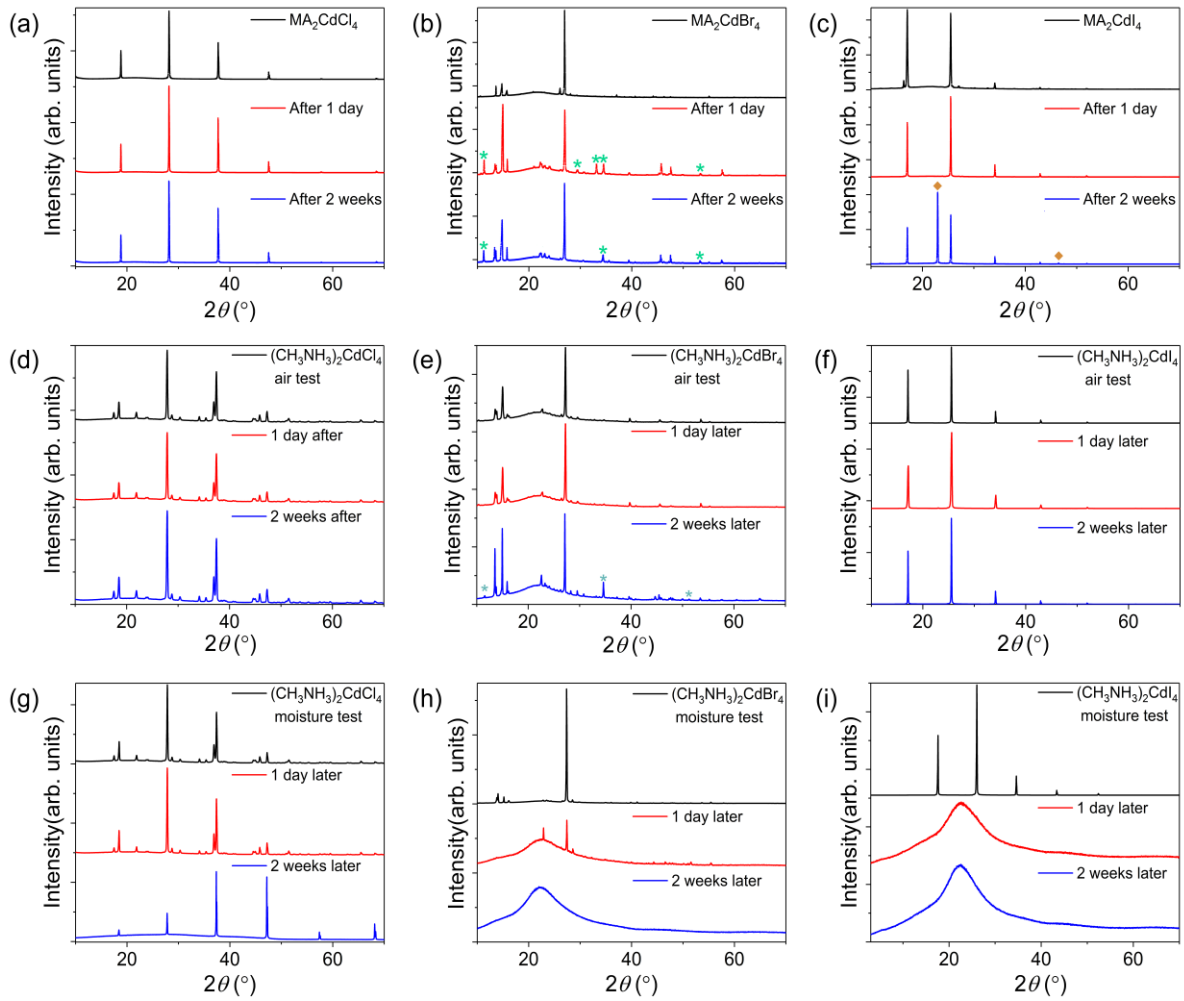


Figure 22. Ambient stability studies of spin coated MA_2CdX_4 thin films over a period of two weeks are shown in (a-c). (a) MA_2CdCl_4 shows no degradation, whereas (b) MA_2CdBr_4 decomposes forming $MACdBr_3$[250] (marked with green asterisks) after only one day in air, however, degradation slows thereafter. (c) MA_2CdI_4 film shows a higher degree of preferential orientation after a day in air, however, no impurity peaks are detected. After two weeks, MA_2CdI_4 PXRD pattern suggests formation of an unidentified impurity phase (labeled with orange diamond marks). Dry air stability studies of MA_2CdX_4 over a period of two weeks are shown in (d-f). (d) MA_2CdCl_4 shows no degradation, whereas (e) MA_2CdBr_4 decomposes forming $MACdBr_3$[250] (marked with green asterisks) after only two weeks in a dry air environment. (f) MA_2CdI_4 also shows no degradation over a two-week period. Moisture stability studies of MA_2CdX_4 over a period of two weeks are shown in (g-i). (g) MA_2CdCl_4 shows a higher degree of preferential orientation after two weeks in a wet nitrogen environment whereas (h) MA_2CdBr_4 begins decomposing after only 1 day. (i) MA_2CdI_4 film completely degrades after one day in a 100% saturated environment.

2.1.6 Optical Property Measurements

Cadmium halides are large band gap materials, for example, $CdCl_2$, $CdBr_2$ and CdI_2 are reported to have band gaps of 6.4 eV, 5.4 eV and 4.3 eV.[252] Optical absorption and photoluminescence measurements for such large band gap materials require specialized instrumentation that extends into the deep UV region. For MA_2CdX_4, we were able to carry out optical absorption measurements in the 190 – 820 nm (1.5 – 6.5 eV) range (Figure 6), which narrowly captures the UV region where onsets of absorption appear. From the linear fits of the absorbance data, the onsets of optical absorption were determined to be 5.29 eV for MA_2CdCl_4, 4.92 eV for MA_2CdBr_4, and 3.94 eV for MA_2CdI_4. This trend in the onsets of optical absorption for halides going from chloride to iodide is consistent with the trend in electronegativity and calculated band structures (see below), i.e., with decreasing electronegativity of halogen element, the band gap is expected to decrease.

However, we note that the onsets of optical absorption for MA_2CdX_4 cannot be directly used to extract band gap information for hybrid organic-inorganic materials with strong excitonic features. Indeed, most low-dimensional hybrid materials exhibit room temperature excitonic features in their absorption spectra appearing before the features that can be ascribed to band-to-band transitions.[27, 88, 252-254] In fact, MA_2CdX_4 are expected to have a strong charge localization in the inorganic CdX_4^{2-} substructures due to their large band gaps and low dimensional crystal structures (see DFT results below); therefore, the exact determination of the optical band gaps of MA_2CdX_4 cannot be done solely based on our optical absorbance results.

Further inspection of the optical absorption data for MA_2CdI_4 reveals a noticeable subgap absorption, which is reproducible in two different UV-vis spectrometers. The presence

of such weak subgap absorption may be indicative of defect states in MA_2CdI_4. Given the fact that MA_2CdI_4 band gap is larger than 3.9 eV, MA_2CdI_4 crystals should be colorless instead of their actual pale-yellow color. Therefore, the yellow color of MA_2CdI_4 crystals may be due to the defect-induced states, which are also responsible for the sub-band gap absorption.

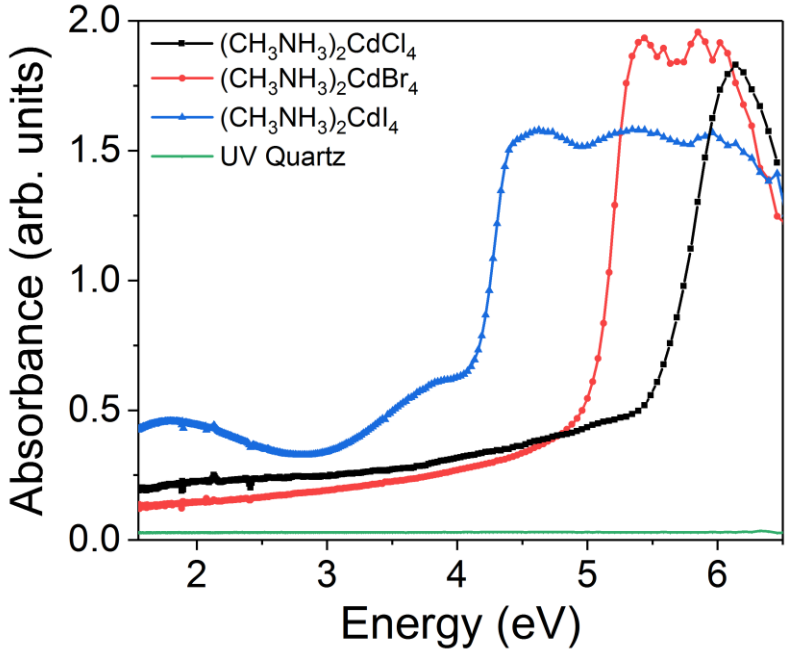


Figure 23. Absorbance vs. energy plots for $(CH_3NH_3)_2CdCl_4$ (black), $(CH_3NH_3)_2CdBr_4$ (red) and $(CH_3NH_3)_2CdI_4$ (blue). From the linear fits, the onsets of optical absorption are 5.29 eV for $(CH_3NH_3)_2CdCl_4$, 4.92 eV for $(CH_3NH_3)_2CdBr_4$, and 3.94 eV for $(CH_3NH_3)_2CdI_4$. Absorbance spectrum of the UV quartz substrate (green) is also included for comparison.

In the presented absorption data in Figure 24, we were not able to observe excitonic fine structures or band-to-band transitions. However, comparisons can be made with the literature reported data for the parent CdX_2 and hybrid organic-inorganic Cd-based halides. Pollini et al.[252] reported reflectivity and deep UV absorption spectra that show multiple subgap excitonic features for CdX_2 that have been assigned to excitons formed from halogen *p*-band holes and

Cd 5*s* band electrons. The lowest excitonic features are located at 6.05 eV for $CdCl_2$, 4.90 eV for $CdBr_2$ and 3.68 eV for CdI_2, which suggest exciton binding energies of 0.35-0.62 eV for CdX_2. Using similar exciton binding energy values for MA_2CdX_4, the optical band gaps can be estimated to be 5.3 – 5.9 eV for MA_2CdCl_4, 4.9 – 5.5 eV for MA_2CdBr_4 and 3.9 – 4.5 eV for MA_2CdI_4. In literature, there have been only a few optical studies of hybrid organic-inorganic Cd-based halides.[186, 255] Interestingly, one of the few papers reporting optical properties of hybrid Cd-based halides suggest that the optical band gap of the layered perovskite compound $(C_2H_5NH_3)_2CdCl_4$ is 1.866 eV.[255] In another report,[186] the same authors report a larger band gap value of 3.11 eV for the same compound. The discrepancy and the very low optical band gap values reported in these studies given the colorless nature of Cd-halides, especially the chlorides, are likely due to the noticeably poor-quality optical absorption data. Ohnishi et al. reported a more comprehensive study of $(C_2H_5NH_3)_2CdCl_4$ including low temperature (7 K) optical reflection spectra on single crystals that show the lowest exciton absorption band at 6.19 eV and optical band gap of 6.8 eV,[256] which are values much closer to that observed for our samples.

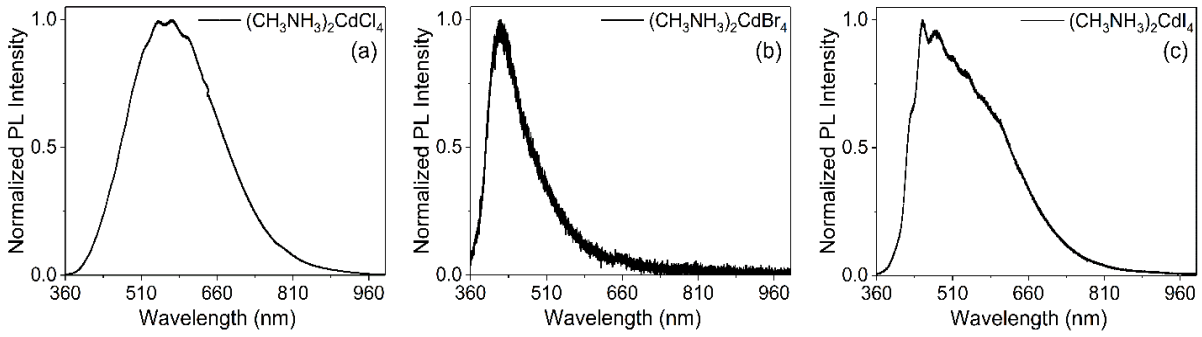


Figure 24. Normalized room temperature photoluminescence (PL) spectra of (a) $(CH_3NH_3)_2CdCl_4$, (b) $(CH_3NH_3)_2CdBr_4$, and (c) $(CH_3NH_3)_2CdI_4$.

Photoluminescence (PL) experiments were performed to further study optical properties of MA_2CdX_4. Each sample was subjected to an excitation wavelength of 325 nm (3.81 eV) and

the resulting PL spectra are summarized in Figure 25. Since our source energy is below the band gaps of MA_2CdX_4, such measurements are considered subgap excited PL measurements.[219, 257-258] Based on these preliminary studies, the PL spectra for MA_2CdX_4 feature broad peaks centered at ~2.2 eV (560 nm) for MA_2CdCl_4, ~3 eV (415 nm) for MA_2CdBr_4 and ~2.5 eV (500 nm) for MA_2CdI_4. These broad peaks with full width at half maximum (FWHM) values of 0.81 eV (208 nm) for MA_2CdCl_4, 0.61 eV (94 nm) for MA_2CdBr_4, and 0.96 eV (203 nm) for MA_2CdI_4, are likely composed of several components, as evidenced by the fine structure clearly noticeable in the MA_2CdCl_4 and MA_2CdI_4 PL spectra. These PL peaks, especially for the chloride analog, are reminiscent of the broadband white-light emitting hybrid organic-inorganic perovskites including α-(DMEN)$PbBr_4$ (DMEN = 2-(dimethylamino)ethylamine), which has a ~550 nm peak with a FWHM of 183 nm,[259] (N-MEDA)[$PbBr_4$] (N-MEDA = N^1-methylethane-1,2-diammonium), which has a PL peak maximum at 558 nm and a FWHM of 165 nm,[106] and (EDBE)[PbX_4] (EDBE = 2,2′-(ethylenedioxy)bis(ethylammonium); X = Cl, Br), which also have PL peaks at 538 – 578 nm and FWHM values of 208 – 215 nm.[107] For these reported white-light emitters, the photoluminescence quantum efficiencies (PLQE) remain low (< 10%). We were also able to observe blue and white-green emission from MA_2CdBr_4 and MA_2CdI_4, respectively, when excited using a 325 nm laser source at 4 K (Figure A1.3 in **Appendix 1**). However, no visible emission is observed at room temperature, consistent with the weaker PL peaks, especially for MA_2CdBr. This is attributed to a significant thermal quenching at room-temperature, also observed for other known cadmium halide materials (see below).

In literature, extensive luminescence studies of pure CdX_2 and their halide solid solutions, (e.g. $CdCl_2$-$CdBr_2$) have been carried out, however, mostly at low (liquid nitrogen

and liquid helium) temperatures due to the fact that emissions are much weaker at room temperature due to thermal quenching effects.[260-266] According to these reports, CdX_2 exhibit strong self-trapped exciton (STE) luminescence observed in the 2 – 3.8 eV range, with exact peak positions dependent on the measurement temperature and excitation source. Self-trapped excitons in ionic crystals form due to lattice distortions caused by optically created excitons, which are subsequently trapped at the distortions they create.[263] Decay time studies indicate that the observed STE's in CdX_2 can be both spin-singlet and spin-triplet in nature.[264-265] Interestingly, the STE luminescence in CdX_2 halides have been observed both using above the gap excitation and subgap excitation. For example, when excited with 3.53 eV light, melt grown single crystals of CdI_2 showed 3 emission bands at 2.12 eV, 2.43 eV and 3.36 eV at 2 K.[262] Emission spectra of hybrid Cd-based halides are largely similar to that of CdX_2, for example, $(C_2H_5NH_3)_2CdCl_4$ has an emission at 2.50 eV with a FWHM value of 0.66 eV when excited into the excitonic absorption range at 11 K.[267] Temperature dependence of emission intensity studies showed that the 2.50 eV band decays rapidly above 50 K due to thermal quenching.[267] Drawing parallels to these studies, we tentatively assign the observed PL peaks for our MA_2CdX_4 compounds to self-trapped excitons. The exact mechanism and nature of emission in MA_2CdX_4, however, warrant further scrutiny through time-resolved, temperature- and power-dependent PL studies.

2.1.7 Band Structure Calculations

Figure 26 shows the calculated band structures and DOS of MA_2CdCl_4 (RT phase), MA_2CdBr_4, and MA_2CdI_4. All three halides have direct band gaps at the Γ point. The calculated band gaps of MA_2CdCl_4, MA_2CdBr_4, and MA_2CdI_4 are 3.41 eV, 3.46 eV, and 2.87 eV, respectively, which are expected to be underestimated due to the well-known band gap error in

DFT. Typically, the band gap of the chloride should be significantly larger than that of the bromide with common cations due to the higher electronegativity of Cl. Here, the small band gap difference between MA_2CdCl_4 and MA_2CdBr_4 is due to their different crystal structures, namely the 2D layered structure of MA_2CdCl_4 as compared to the 0D cluster structure of MA_2CdBr_4. The significant intra-layer coupling of electronic states in the layered MA_2CdCl_4 leads to relatively dispersive conduction and valence bands (see Figure 26a). On the other hand, the 0D compounds MA_2CdBr_4 and MA_2CdI_4 have weak inter-cluster coupling and consequently very small band dispersion (see Figures 26b-c), which widens their band gaps. This observation is consistent with the reported trend for hybrid perovskites, for which it has been shown that dimensional reduction leads to larger band gaps.[27]

The conduction and the valence bands of the three halides are dominated by the Cd-halogen hybridization; their primary features are described below using MA_2CdBr_4 as an example. In Figure 26b, the narrow bands near -3 eV and 4 eV are mainly derived from the bonding and the anti-bonding states between Br-4*p* and Cd-5*s*, respectively. The bonding and the anti-bonding states between Br-4*p* and Cd-5*p* contribute strongly to the bands between -2 eV and -1 eV and those above 5 eV, respectively. The MA-related bands are far away from the band gap, having negligible contribution to chemical bonding. The above electronic structure features also exist for MA_2CdCl_4 and MA_2CdI_4 as shown in Figure 26a and c.

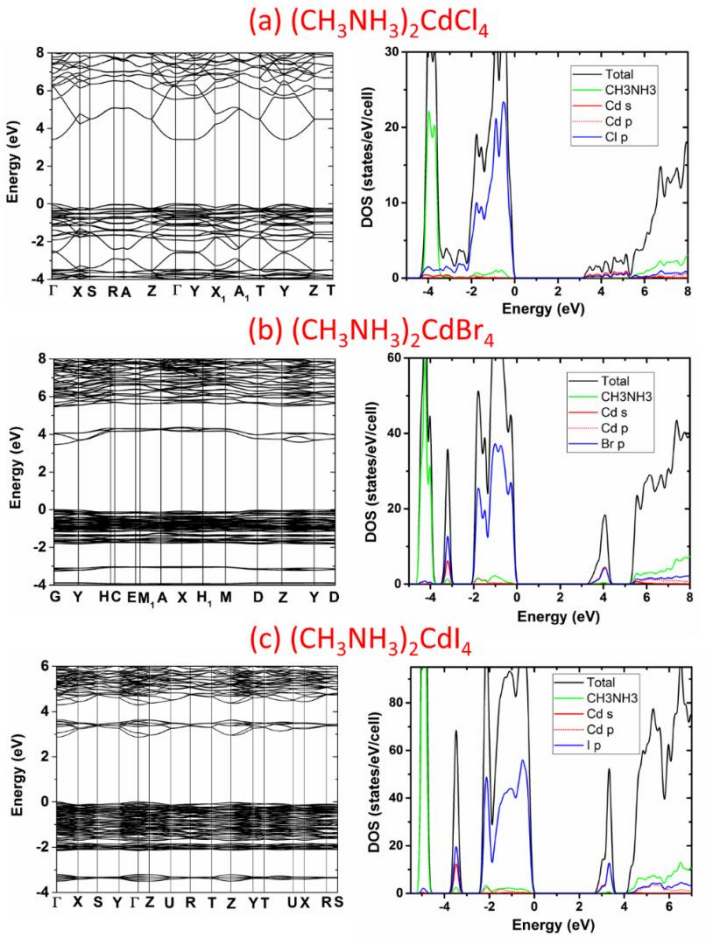


Figure 25. Band structures (left) and density-of-states (DOS) (right) plots of (a) $(CH_3NH_3)_2CdCl_4$, (b) $(CH_3NH_3)_2CdBr_4$, and (c) $(CH_3NH_3)_2CdI_4$ calculated using PBE functionals with SOC. Note that the band gaps are underestimated in PBE calculations.

Despite the similarities described above, there are distinct differences in electronic structures between the 0D compounds (MA_2CdBr_4 and MA_2CdI_4) and 2D MA_2CdCl_4. It can be seen in Figure 26 that both the conduction and the valence bands in 0D MA_2CdBr_4 and MA_2CdI_4 are much less dispersive than those in 2D MA_2CdCl_4 because the electronic states originating from the Cd-Br(I) bonds in $MA_2CdBr(I)_4$ are highly localized within the $CdBr(I)_4$ clusters, which are spatially separated from each other by MA molecular cations. The lack of sufficient band dispersion leads to a narrow Cd-5*s*-derived conduction band, which is completely separated from the higher Cd-5*p*-derived band, as shown in Figure 26b-c. Similar

isolated narrow conduction bands have been found in double-perovskite halide materials.[268-270] The highly localized electronic states near the conduction band minimum (CBM) and the valence band maximum (VBM) promote charge localization, leading to the formation of electron and hole polarons and self-trapped excitons (STEs). The formation of STEs with sufficient binding energies is important for stabilizing excitons and enabling exciton emission. The PL peaks of MA_2CdBr_4 and MA_2CdI_4 (Figure 25), therefore, are likely due to the STE emission. High light output due to STE emission has been reported in double perovskite halides, which also have highly localized states near the CBM and the VBM.[271] Compared to MA_2CdBr_4 and MA_2CdI_4, MA_2CdCl_4 with its layered structure has relatively more dispersive electronic bands on the *ab*-plane and flat bands along the *c* direction. The localization level of the VBM and the CBM states is likely still sufficient to stabilize STE and enable STE emission. This is supported by the strong STE emission observed in other 2D halide perovskites.[106, 259, 268, 272-274]

The formation of STEs in 0D MA_2CdBr_4 or MA_2CdI_4 may simply involve the elongation of the Cd-halogen bonds within an isolated $CdBr_4$ or CdI_4 tetrahedral cluster, respectively. As such, the hole is localized on the four halogen ions while the electron is localized on the Cd ion within a tetrahedral cluster. On the other hand, a STE in MA_2CdCl_4 likely involves the formation of a V_k center (a commonly observed hole polaron in halides, which can trap an electron at the nearby cation). The formation of a V_k center requires strong lattice relaxation, i.e., the formation of a Cl_2^- molecule,[268] which should result in a large stokes shift and may explain the lower emission energy in MA_2CdCl_4 than in MA_2CdBr_4 and MA_2CdI_4 (see Figure 26).

2.1.8 Summary

In summary, we report low temperature solution synthesis, crystal and electronic structures, and optical properties of the HOIM MA_2CdX_4 (X = Cl, Br, I). High quality single crystals were obtained through slow evaporation of DMF, water and methanol solutions of MA_2CdX_4 with optimized conditions; i.e., slow evaporation at room temperature, yielding mm-sized colorless (X = Cl, Br) and pale yellow (X = I) crystals. In future studies, large single crystal growth (> 1 cm in all dimensions) will be necessary to accurately assess scintillation properties of MA_2CdX_4. Single crystal and variable temperature powder X-ray diffraction measurements confirm the literature reported 2D layered perovskite structure for MA_2CdCl_4, which undergoes two phase transitions at 283 K and 173 K. In contrast, MA_2CdBr_4 and MA_2CdI_4 adopt 0D K_2SO_4-derived crystal structures based on isolated $CdBr(I)_4$ tetrahedra, and show no phase transition down to 20 K. The contrasting crystal structures and chemical compositions in MA_2CdX_4 family impact their air stabilities; the 2D layered compound MA_2CdCl_4 is air stable, whereas the 0D cluster compounds MA_2CdBr_4 and MA_2CdI_4 partially decompose when left in air for a two-week period.

Our band structure calculations show that the states around the Fermi level are dominated by the bands from Cd and halogen elements in MA2CdX4 consistent with the simple charge counting according to $(MA^+)2(Cd^{2+})(X^-)_4$. Thus, the upper valence band (VB) is primarily composed of halogen p states with a small contribution from the full Cd 4d states, whereas the bottom of the conduction band (CB) is predominantly made of Cd 5s states. Because of the large differences in the electronegativities of Cd and halogen elements, MA2CdX4 have large optical band gaps above 3.9 eV based on optical absorption experiments.

Interestingly, MA_2CdX_4 are potential broadband white-light emitting materials with photoluminescence (PL) peaks centered at ~560 nm with FWHM = 208 nm for MA_2CdCl_4, 415 nm with FWHM = 94 nm for MA_2CdBr_4, and 500 nm with FWHM = 203 nm for MA_2CdI_4. These PL peaks are tentatively assigned to self-trapped excitons (STEs) in MA_2CdX_4 using an analogy to the related CdX_2 and $(C_2H_5NH_3)_2CdCl_4$. This view is further supported by the results of the DFT calculations, which indicate that the bands in VB and CB have small dispersions, suggesting high charge localization with significant exciton binding energies in MA_2CdX_4. The degree of charge localization is also impacted by the structural dimensionality, i.e., the band structure of the 2D layered compound MA_2CdCl_4 features flat bands in the interlayer direction but more dispersive bands along the intralayer direction, whereas the 0D cluster compounds MA_2CdBr_4 and MA_2CdI_4 have a much stronger charge localization. Based on both experimental and computational results, therefore, the 0D compounds MA_2CdBr_4 and MA_2CdI_4 could be promising candidates as self-activated scintillators, whereas the 2D layered perovskite MA_2CdCl_4 may require doping with an activator such as Ce^{3+} or Eu^{2+}. In conclusion, the presented results in this work including the ease of synthesis using inexpensive low temperature solution methods, single crystal growth, large band gaps, and highly localized charges indicate that MA_2CdX_4 and related compounds may be of interest for WL-emitting phosphors and scintillator applications.

2.2 4-Aminopyridinium (4AMP) Zinc and Mercury Bromides $(4AMP)_2MBr_4$ (M = Zn, Hg)

2.2.1 Introduction

U.S. Energy Information Administration reported that 21% of all energy consumed in the U.S. in 2017 was for lighting applications. By replacing incandescent bulbs with light-emitting diodes (LEDs), 40% power consumption reduction is predicted to be achieved by 2030.[137] To achieve these goals, scientists are focusing on the development of brand new materials technologies that produce finely tuned white light (WL). The development of white LEDs (WLEDs) is the key step for the implementation of solid-state lighting (SSL) technologies, which are expected to address the low efficiencies of conventional incandescent and fluorescent lighting sources.[275-277] To produce WL, three technologies are mainly used: first, by coating a yellow phosphor on a blue LED,[278-279] second, by coating a mixture of red, green, and blue (RGB) phosphors on an ultraviolet LED,[280-281] and finally by directly using a mixture of RGB LEDs to produce WL. However, each of these three technologies has their own disadvantages including poor color rendition, low efficiency and discontinuity in the WL spectrum,[282-287] and there is a growing interest in a single-component phosphor material for SSL that could address these concerns.[288]

In this context, hybrid organic-inorganic materials (HOIMs) have attracted enormous attention due to their structural diversity[289-294] and outstanding optoelectronic properties,[295-296] which make them promising candidates for LEDs,[297-298] light-emitting transistors,[202] laser cooling,[203] laser gain media,[204] photodetectors,[205] and solar cells.[23, 207-208] In 2014, broadband WL emission was first reported in (110)-oriented two-dimensional (2D) hybrid halides perovskites (N-MEDA)-PbX_4 (N-MEDA = N^1-metylethane-1,2-diammonium) and (EDBE)PbX_4 (EDBE = 2,2'-(ethylenedioxy)bis-(ethylammonium)) with X = Br, Cl and in

2015, a new example of WL emission in the (100)-oriented 2D HOI perovskite $(C_6H_{11}NH_3)_2PbBr_4$. The physical origin of the unusual WL emission was attributed to self-trapped excitons (STEs) in a distorted lattice resulting from strong electron-phonon coupling.[85, 274, 299-303] Follow-up studies by several research groups yielded new examples of HOIM WL emitters[304-315] and confirmed their great potential in SSL applications. It was demonstrated that lowering the structural dimensionality of HOIMs enables strong quantum confinement and highly localized charges resulting in high exciton binding energies and stable excitonic emission.[289, 306] Among notable examples of highly luminescent HOIMs is $C_4N_2H_{14}PbBr_4$,[316] which has a 1D crystal structure and shows an efficient bluish WL emission with photoluminescence quantum yield (PLQY) of 20% and 12% for bulk single crystals and microscale crystals, respectively.[316] More recently, new examples of broadband WL emitters have been reported and the specific role of the organic cation in terms of providing emissive centers has also been discussed in low dimensional HIOMs.[85, 317-320] Beyond hybrid halide perovskites, Luo et al. recently reported a highly efficient and stable warm-WL emission from the all-inorganic lead-free halide double perovskites $Cs_2(Ag_xNa_{1-x})InCl_6$ with 86% PLQY and stability over 1,000 hours. Moreover, Wang et al.[318] reported that non-perovskite HOIMs can also have remarkable light emission properties, such as in the cases of $(H_2DABCO)Pb_2Cl_6$ and $(H_3O)(Et_2\text{-}DABCO)_8Pb_{21}Cl_{59}$ compounds that demonstrate WL emission with high color rendering index (CRI) values of 96 and 88, respectively. In these two materials, inorganic parts contribute to the blue emission, while the yellow/orange emission originates from the organic parts, resulting in an overall broadband WL emission.[318] Notably high CRI values of 96 and 88 reported for $(H_2DABCO)Pb_2Cl_6$ and $(H_3O)(Et_2\text{-}DABCO)_8Pb_{21}Cl_{59}$ are important; at present, the CRI of most commercial LEDs is around 80, which is considered good for use in everyday

lighting.[321] Nonetheless, for high level color-critical applications such as museums galleries, cinematography, cosmetic sales counters, and surgery, WL emission with a CRI > 90 is desired.[322] The work on $(H_2DABCO)Pb_2Cl_6$ and $(H_3O)(Et_2\text{-}DABCO)_8Pb_{21}Cl_{59}$ confirms that non-perovskite HOIMs could also demonstrate outstanding light emission properties.[318] However, the development of highly-efficient broadband WL emitting HOIMs with high CRI is still in its infancy, with only a few demonstrated examples so far.

In this study, we report two new examples of HOIMs, namely $(C_5H_7N_2)_2HgBr_4{\cdot}H_2O$ and $(C_5H_7N_2)_2ZnBr_4$ that demonstrate excellent light emission properties. X-ray crystallography studies suggest the presence of discrete molecular building blocks, organic $C_5H_7N_2^+$ cations and inorganic tetrahedral MBr_4^{2-} anions, in the zero-dimensional (0D) crystal structures of $(C_5H_7N_2)_2MBr_4$ results in strongly localized charge carriers and bright WL emission with a corresponding Commission Internationale de l'Eclairage (CIE) Color Coordinates of (0.34, 0.38) and (0.25, 0.26), and a CRI values of 87 and 96 for $(C_5H_7N_2)_2HgBr_4{\cdot}H_2O$ and $(C_5H_7N_2)_2ZnBr_4$, respectively, which are, to the best of our knowledge, among the highest values reported in the literature to date, and the highest value for Pb-free HOIMs . Metal substitution (Hg/Zn) allows us to tune the light emission from "warm" to "cold" WL with a calculated correlated color temperatures (CCT) of 5206 K for $(C_5H_7N_2)_2HgBr_4{\cdot}H_2O$ and 11630 K for $(C_5H_7N_2)_2ZnBr_4$. In addition to the record CRI values, measured room temperature PLQY values of 14.87 and 19.18% for $(C_5H_7N_2)_2HgBr_4{\cdot}H_2O$ and $(C_5H_7N_2)_2ZnBr_4$, respectively are among the highest reported for HOIMs. In particular, the 19.18% PLQY of $(C_5H_7N_2)_2ZnBr_4$ is the highest value reported for non-toxic HOIMs WL emitters to date. Our optical investigations supported by density functional theory (DFT) calculations suggested that the WL emission resulting from 4AMP-related molecular.

2.2.2 Synthesis and Methods of $4AMP_2Hg(Zn)Br_4$

2.2.2.1 Reagents Used in the Synthesis of $4AMP_2Hg(Zn)Br_4$

Chemicals listed were used as purchased and without further purification: (i) 4-aminopyridinium, 98%, Sigma; (ii) hydrobromic acid, 47% w/w, Sigma-Aldrich; (iii) zinc bromide, 99.999%, Alfa Aesar; (iv) mercury bromide, 99.9%, Fisher Scientific; (v) methanol, ACS reagent grade, Aldrich; (vi) N,N-dimethylformamide (DMF), 99%, Fisher.

2.2.2.2 Synthesis and Crystal Growth of $4AMP_2Hg(Zn)Br_4$

Crystals of **1** and **2** were grown through slow evaporation at room temperature under ambient conditions from stoichiometric (2:1:1 molar ratio of 4AMP to HBr to MBr_2) methanol solutions. The 4AMP and MBr_2 solids were solvated separately then combined and mixed for 5 mins. A stoichiometric amount of HBr was added and the solution was stirred for another 5 mins and then allowed to sit at room temperature to slowly evaporate.

$4AMP_2CdBr_4{\cdot}H_2O$ can also be obtained using the same experimental conditions as for the Zn and Hg compounds studied in this section. While the Zn and Hg thin films were deemed clean (see Figure A7 in Appendix 1 for PXRD results), the Cd film had too many impurities to include in this study. Materials with unidentifiable impurities cannot be considered for optical investigation, as it would be too difficult to attribute the mechanisms underlying their properties to a single phase.

2.2.2.3 Single crystal X-ray diffraction

The X-ray intensity data for all compounds were collected on a Bruker D8 Quest Kappa-geometry diffractometer with a Photon II cpad area detector and an Incoatec Imus microfocus Mo Kalpha source. The samples were cooled to 100(2) K by an Oxford Cryostream 800 LT device. All crystal structures were determined from a nonlinear least-squares fit. The data were

corrected for absorption by the semi-empirical method based on equivalents and structures were solved by direct methods using the SHELXTL program and refined by full matrix least-squares on F^2 by use of all reflections. All non-hydrogen atoms were refined with anisotropic displacement parameters, all occupancies were refined within two standard deviations, and all hydrogen atom positions were determined by geometry. CCDC 1887021 and 187022 contains the supplementary crystallographic data for this paper. These data can be obtained free of charge from The Cambridge Crystallographic Data Centre via www.ccdc.cam.ac.uk/data_request/cif.

2.2.2.4 Powder X-ray diffraction

Powder X-ray diffraction measurements were carried out on polycrystalline powder of **1** and **2**. A Rigaku MiniFlex600 system equipped with a D/tex detector, and a Ni-filtered Cu-Kα radiation source was used for these measurements. Scans were performed in the 3-90° (2θ) range, with a step size of 0.02°.

2.2.2.5 Thermal analysis

Simultaneous thermogravimetric analysis (TGA) and differential scanning calorimetry (DSC) measurements were carried out on a TA Instruments SDT650 unit. Measurements were done in 90 μL alumina crucibles on 10-11 mg samples under a 100 mL/min flow of nitrogen in the 50 – 475 °C range with 5 °C/min heating rate. DSC onset temperatures were determined using TA Instrument's TRIOS software analysis package.

2.2.2.6 Optical Measurements

The UV-vis diffuse reflectance measurements were measured on polycrystalline powder samples of **1** and **2**, using a PerkinElmer Lambda 750 UV/VIS/NIR Spectrometer equipped with a 100mm Spectralon InGaAs Integrating Sphere attachment over a 250-1100 nm range.

Room temperature PLE and PLQY measurements were performed on a HORIBA Jobin Yvon Fluorolog-3 spectrofluorometer using a Xenon lamp and Quanta-φ integrating sphere using the two-curve method in a varied range from 280-860 nm. Temperature dependence and power dependence PL measurements were done under excitation by the 325 nm line of a HeCd laser (Kimmon Electric HeCd dual-wavelength laser, model: IK552R-F). The sample was placed on the cold finger of a helium closed-cycle cryostat and the measurements were performed from 4 to 295 K. PL decay was measured on a HORIBA Jobin Yvon Fluorolog-3 spectrofluorometer using a time-correlated-single-photon counting module. HORIBA Jobin Yvon NanoLEDs (pulsed light-emitting diodes) were used as the excitation source. The color rendering index (CRI) values were calculated using OSRAM Company's ColorCalculator software available from https://www.osram-americas.com.

Computational methods: All calculations were based on density functional theory (DFT) implemented in the VASP code.[229] The interaction between ions and electrons was described by projector augmented wave method.[323] The kinetic energy cutoff of 400 eV for the plane-wave basis was used for all calculations. Experimental lattice parameters of **1** and **2** were used while the atomic positions were fully relaxed until the residual forces were less than 0.02 eV/Å. Electronic band structures and density of states (DOS) were calculated using Perdew−Burke−Ernzerhof (PBE) exchange-correlation functional.[324]

2.2.3 Crystal Structure

$4AMP_2HgBr_4{\cdot}H_2O$ and $4AMP_2ZnBr_4$ crystallize in the orthorhombic space group *Pbcm* and $P2_12_12_1$, respectively (see Table 2). Interestingly, although there is no connectivity between the adjacent MX_4 units, both compounds exhibit pseudo-layered structures that effectively isolate the metal halide units from the organic layer, as shown in Figure 27, which is a feature

found in several other group 12 metal halide systems.[85, 113, 306] The shortest distance between Br atoms on two adjacent MBr_4 units is 4.069 Å in $4AMP_2HgBr_4 \cdot H_2O$ and 4.419 Å in $4AMP_2ZnBr_4$, only slightly longer than double of the bromide Shannon ionic radius ($2 \times r(Br^-) = 3.92$ Å).[325] The close-packing of halide anions can have a great impact on the optoelectronic properties. For example, whilst the vacancy-ordered double perovskites such as Rb_2SnI_6,[326] Cs_2SnI_6[326] and $(NH_4)_2PtI_6$[327] have 0D crystal structures, the presence of close-packed halogen sublattice leads to the overlap of neighboring halogen *p*-orbitals providing dispersive electronic states in the vicinity of the Fermi level.

Typically, 4AMP-based hybrid organic-inorganic halides of Sb and Bi are known to result in octahedral MX_6 units with varying connectivity such as isolated bi-octahedra in 4AMP-Bi_2Cl_{11}[328] and 1D SbI_4^- chains formed by edge-sharing SbI_6 octahedra in 4AMP-SbI_4.[329] Interestingly, Ga,[330] Cd,[331] Cu[332] and Co[333] are also known, however, their structures are based on isolated MX_4 tetrahedra similar to that in $4AMP_2HgBr_4 \cdot H_2O$ and $4AMP_2ZnBr_4$, whereas Pd-analog features square planar $PdCl_4$ units.[334] Similar to the close analogs based on Cd, $4AMP_2CdBr_4 \cdot H_2O$[331] and $4AMP_2CdI_4 \cdot H_2O$,[335] MX_4 tetrahedra in $4AMP_2HgBr_4 \cdot H_2O$ and $4AMP_2ZnBr_4$ are slightly distorted (presumably to optimize the hydrogen bonding network), which can be seen in the selected bond distances and angles showed in Table A1.9 in **Appendix 1**. In contrast, the Cu analog exhibits Jahn-Teller distorted $CuCl_4$ tetrahedra, whereas distortions in Sb- and Bi-based halides of 4AMP cation are attributed to the presence of lone pair on the metal cations.[328-329]

Table 2. Selected single crystal data and structure refinement parameters for $(C_5H_7N_2)_2HgBr_4 \cdot H_2O$ and $(C_5H_7N_2)_2ZnBr_4$.

Formula	**$(C_5H_7N_2)_2HgBr_4 \cdot H_2O$**	**$(C_5H_7N_2)_2ZnBr_4$**
Formula weight (g/mol)	728.50	575.26
Temperature (K)	100(2)	100(2)
Radiation, wavelength (Å)	Mo Kα, 0.71073	Mo Kα, 0.71073
Crystal system	Orthorhombic	Orthorhombic
Space group	*Pbcm*	$P2_1\ 2_1\ 2_1$
Z	4	4
Unit cell parameters (Å)	a = 6.7934(7)	a = 7.2941(5)
	b = 13.8808(15)	b = 15.3229(10)
	c = 18.685(2)	c = 15.3893 (10)
Volume (Å^3)	1762.0(3)	1720.01(20)
Density (ρ_{calc}) (g/cm^3)	2.746	2.221
Absorption coefficient (μ) (mm^{-1})	17.806	10.712
$\theta_{min} - \theta_{max}$ (º)	2.18 – 29.39	2.65 – 27.16
Reflections collected	37840	28581
Independent reflections	2167	3943
R^a indices ($I > 2\sigma(I)$)	R_1 = 0.238	R_1 = 0.0180
	wR_2 = 0.0322	wR_2 = 0.0348
Goodness-of-fit on F^2	1.008	1.010
Largest diff. peak and hole (e$^-$/Å^3)	0.678 and -0.711	0.227 and -0.236

[a] $R_1 = \sum\big||F_o| - |F_c|\big| / \sum|F_o|$; $wR_2 = \{|\sum|w(F_o^2 - F_c^2)^2| / \sum|w(F_o^2)^2||\}^{1/2}$,

where $w = \{1/|\sigma^2 F_o^2 + (AP)^2 + BP|\}$, with $P = (F_o^2 + 2F_c^2)/3$ and weight coefficients *A* and *B*.

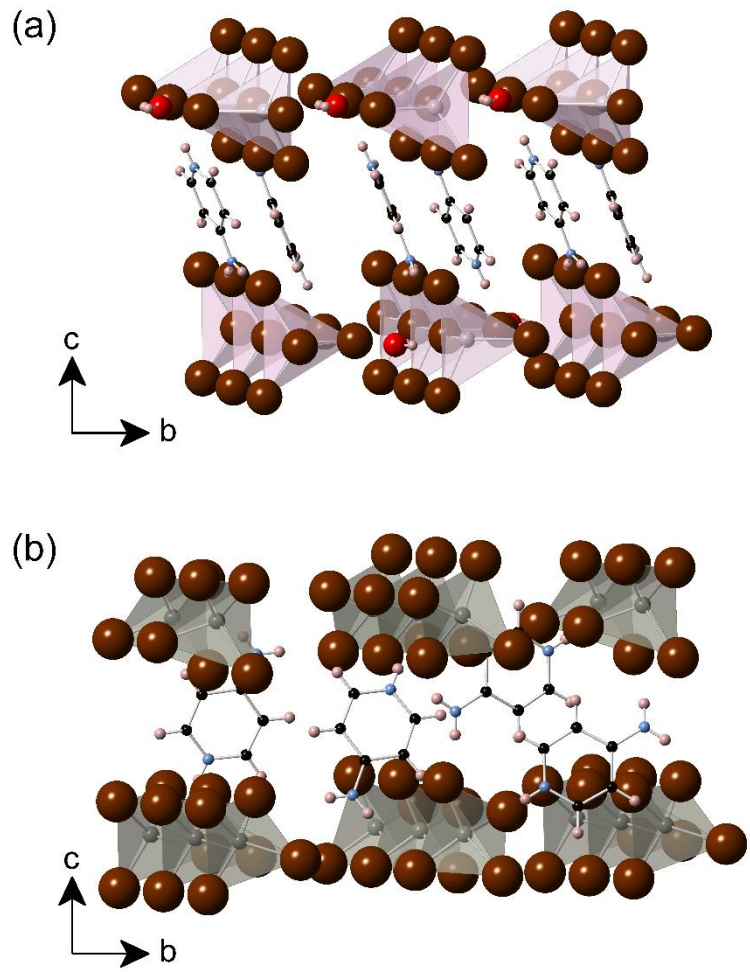


Figure 26. Polyhedral views of the crystal structures of (a) $4AMP_2HgBr_4{\cdot}H_2O$ and (b) $4AMP_2ZnBr_4$. Gray, lilac, burgundy, red, pink, blue, and black represent Zn, Hg, Br, O, H, N, and C, respectively. Some 4AMP molecules were removed for visual clarity.

2.2.4 Ambient Air and Moisture and Thermal Stability

Instability of HOIM halides is a widely known issue in literature and remains a major barrier for their industrial-scale implementation in applications such as solar cells.[336-338] The air and thermal stability of $4AMP_2HgBr_4{\cdot}H_2O$ and $4AMP_2ZnBr_4$ compounds were investigated through PXRD measurements taken over a period of two months and simultaneous thermogravimetric analysis (TGA) and differential scanning calorimetry (DSC) measurements. Phase purity was first verified on powders of the bulk phase using PXRD as shown in Figure

A1.4 and. Figure A1.5 in **Appendix 1** shows that the sample $4AMP_2HgBr_4 \cdot H_2O$ is stable in ambient air for several weeks, which is more air-stable than similar HOIMs such as $(CH_3NH_3)_2CdX_4$ (X = Cl, Br, I).[113, 306, 337] However, especially for $4AMP_2ZnBr_4$, the crystallinity slightly decreases over time, and emergence of small impurity peaks are noticeable in both $4AMP_2HgBr_4 \cdot H_2O$ and $4AMP_2ZnBr_4$ after 1-2 months.

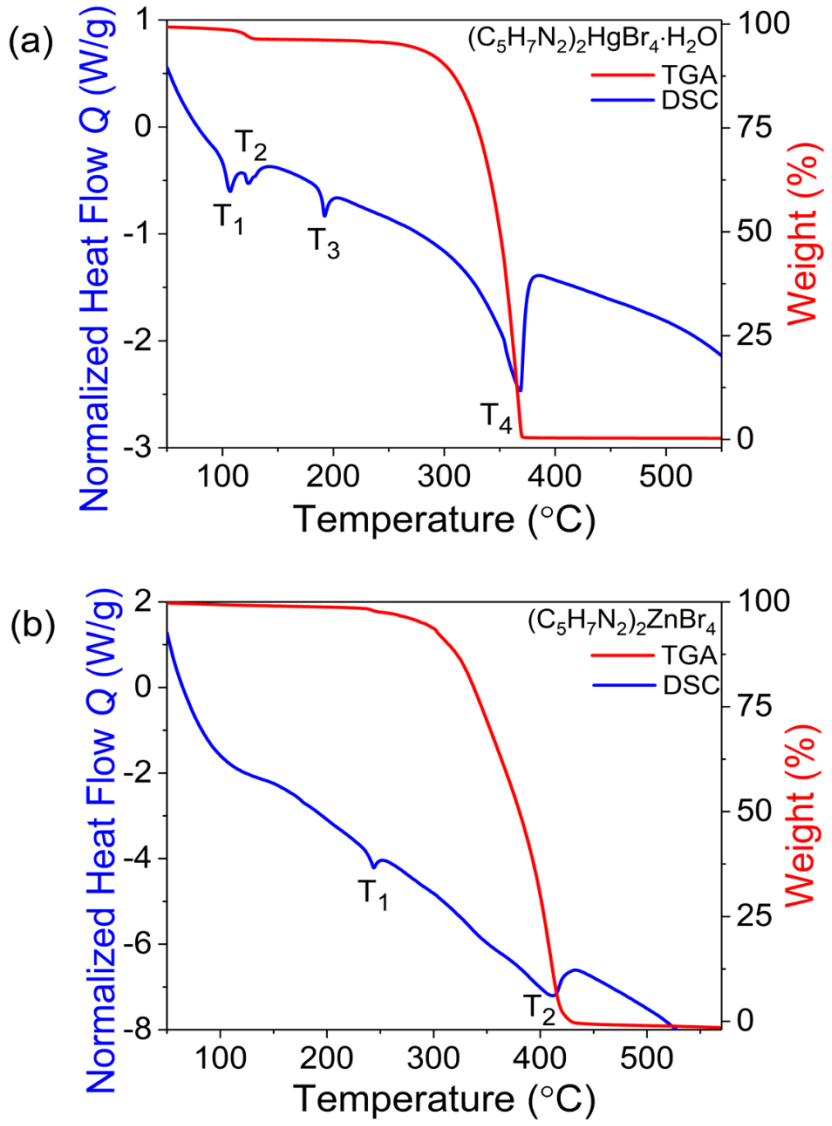


Figure 27. TGA (red) and DSC (blue) measurements for (a) $(C_5H_7N_2)_2HgBr_4 \cdot H_2O$ and (b) $(C_5H_7N_2)_2ZnBr_4$.

On the other hand, DSC/TGA measurements presented in Figure 27 show the typical mass loss above 300 °C as seen in many HOIMs.[339-340] Thus, as shown in Figure 27a, $4AMP_2HgBr_4{\cdot}H_2O$ first loses its solvated water at 110 °C (T_1) and undergoes an associated structural transition at 119 °C (T_2). This is followed by a third transition at 189 °C (T_3), attributed to melting, and evaporation of sample with onset temperature of 345 °C (T_4). In comparison, the DSC/TGA curves of non-hydrated $4AMP_2ZnBr_4$, shown in Figure 27b, are simpler with only two thermal events at 239 and 415 °C labeled as T_1 and T_2, respectively. The first event (T_1) likely corresponds to a melting transition whereas T_2 corresponds to the vaporization of the sample. Note that some of the other well-known HOIMs decompose at lower temperatures such as $CH_3NH_3PbBr_3$ at 176 °C, $FASnPbI_3$ (FA = formamidinium) at 150 °C, and $FASnI_3$ at 100 °C[341] which suggest that $4AMP_2HgBr_4{\cdot}H_2O$ and $4AMP_2ZnBr_4$ are relatively more thermally stable than these compounds.

2.2.5 Optical Property Measurements

Figure 28a shows room temperature diffuse reflectance spectra of polycrystalline powders of $4AMP_2HgBr_4{\cdot}H_2O$ and $4AMP_2ZnBr_4$. Sharp band edges were observed, characteristic of a direct gap semiconductor. As explained in **Chapter 1**, the band gap energies from the Tauc plots $[F(R)h\nu]^{1/\gamma}$ as a function of the photon energy ($h\nu$), where γ is equal to 1/2 for direct transitions and 2 for indirect transitions can be estimated based on the Kubelka-Munk function.[342] This method it is often used to estimate an optical band gap of a given semiconductor with parabolic bands at the Fermi energy level. Using the direct and indirect fitting scenarios, band gaps energies of 3.44 and 4.02 eV (direct) and 3.20 and 3.90 eV (indirect) are estimated for powder samples of $4AMP_2HgBr_4{\cdot}H_2O$ and $4AMP_2ZnBr_4$, respectively (Figure A1.7 in **Appendix 1**). Note here that while this treatment follows the commonly applied

procedures in literature,[305-308, 343] and the obtained values are reasonable, the present case is quite different due to low dimensional crystal and electronic structures of $4AMP_2HgBr_4{\cdot}H_2O$ and $4AMP_2ZnBr_4$ compounds. Thus, $4AMP_2HgBr_4{\cdot}H_2O$ and $4AMP_2ZnBr_4$ show an excitonic absorption features at 370 and 320 nm for $4AMP_2HgBr_4{\cdot}H_2O$ and $4AMP_2ZnBr_4$, respectively, which may obscure the absorption onset (Figure 28a-c). Therefore, we directly measured the optical absorption spectra on spin-coated thin films of $4AMP_2HgBr_4{\cdot}H_2O$ and $4AMP_2ZnBr_4$. Based on the absorption spectra shown in Figure A1.8 in **Appendix 1**, we deduced a band gaps of 3.64 eV and 4.1 eV for $4AMP_2HgBr_4{\cdot}H_2O$ and $4AMP_2ZnBr_4$, respectively.

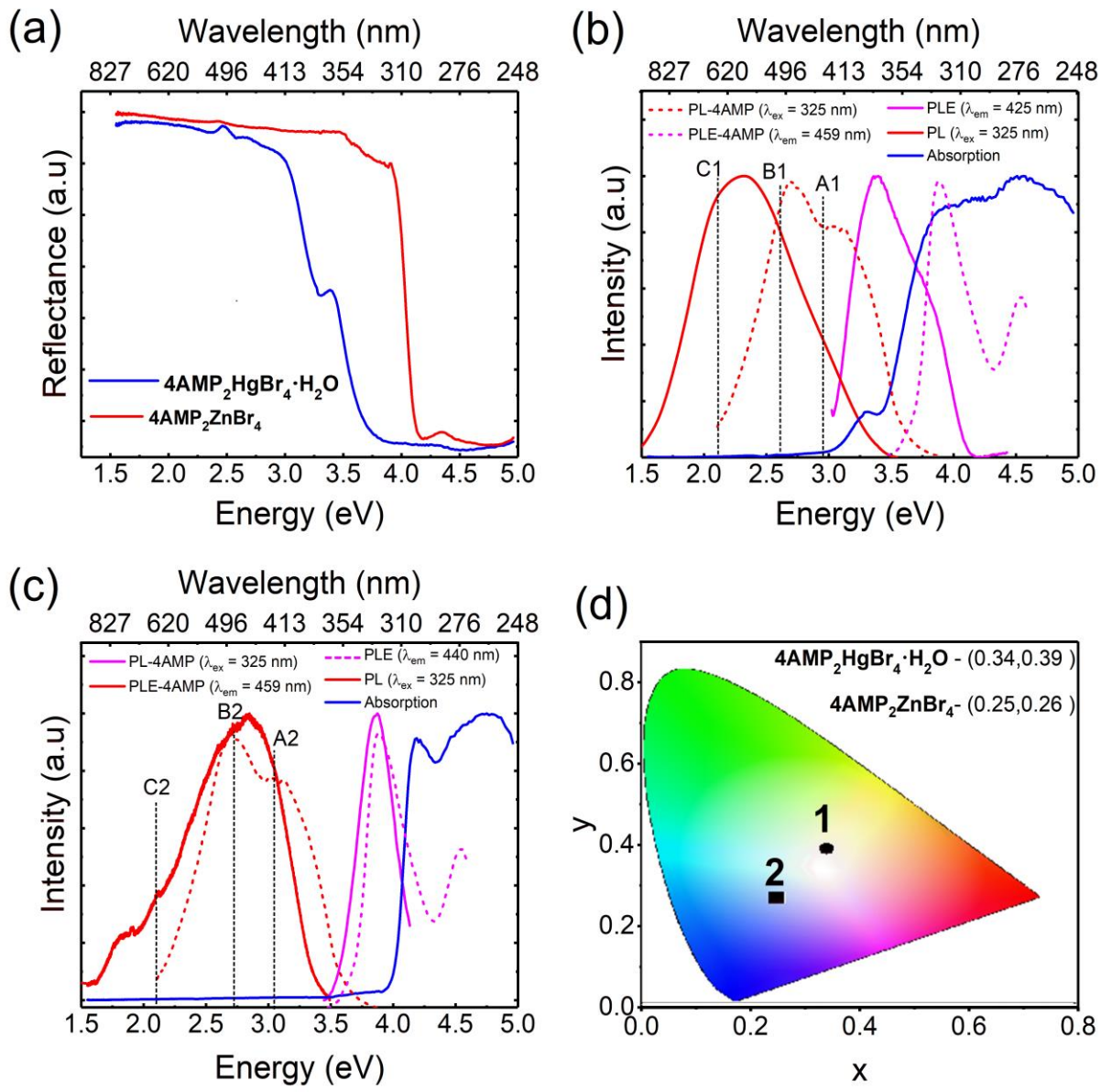


Figure 28. (a) Diffuse reflectance spectra of polycrystalline powders of $4AMP_2HgBr_4 \cdot H_2O$ and $4AMP_2ZnBr_4$ measured at room temperature. (b-c) Room temperature optical absorption (blue), PLE (green), and PL (red) spectra of $4AMP_2HgBr_4 \cdot H_2O$ and $4AMP_2ZnBr_4$. (d) The position of $4AMP_2HgBr_4 \cdot H_2O$ (circle) and $4AMP_2ZnBr_4$ (square) values in the CIE 1931 chart.

Under 325 nm UV irradiation, PL spectrum of $4AMP_2HgBr_4 \cdot H_2O$ shows very broad Gaussian shaped emission with a maximum intensity at 535 nm, a FWHM of 233 nm, and a

large Stokes-shift (~170 nm) compared to the excitonic absorption (Figure 28b). Moreover, PLE spectrum shows a sharp excitonic peak located at 370 nm in excellent agreement with the absorption spectrum peak (Figure 28b and Figure A1.8 in **Appendix 1**), attributed to excitonic absorption. Similarly, for $4AMP_2ZnBr_4$, room temperature PL spectrum shows a bright broadband emission with a maximum at 438 nm accompanied with a shoulder at 490 nm and a weaker emission band at 610 nm. Likewise, PLE spectrum of $4AMP_2ZnBr_4$ shows a sharp peak at 320 nm characteristic of the excitonic absorption (Figure 28c). A large Stokes shift of 118 nm was also observed for $4AMP_2ZnBr_4$, which is often the case in 0D HOIMs.[66, 68] Importantly, the broadband emission of the studied compounds yield CIE Color Coordinates of (0.34, 0.38) and (0.25, 0.26), and very high CRI values of 87 and 96 for $4AMP_2HgBr_4{\cdot}H_2O$ and $4AMP_2ZnBr_4$, respectively (Figure 28d), which are among the highest reported in the literature to date.[66] It is well-known that CRI is an important parameter for WL emissive materials, reflecting the ability of a light source to accurately render the colors of an object compared to daylight. Other notable examples of WL emitting HOIMs with high CRI values include distorted 2D corrugated hybrid perovskites such as $EA_4Pb_3Br_{10-x}Cl_x$ (EA = ethylammonium), (N-MEDA)$PbBr_4$, (N-MEDA)$PbBr_4Cl_{0.5}$, and (DMEN)$PbBr_4$ with CRI ranging from 66 to 85[299, 305, 343] and more recently CRI value of 93 was reported by Z. Wu et al. for the 2D corrugated (110)-oriented hybrid perovskite N-(3-aminopropyl)imidazole tetrachloroplumbate.[344] Here, the CRI value of 96 for $4AMP_2ZnBr_4$ present matches the record high CRI of $(H_2DABCO)Pb_2Cl_6$ for single-component WL emissive materials,[318] however, advantageously, $4AMP_2ZnBr_4$ is based on a nontoxic Zn-based composition as opposed to the toxic heavy element Pb-based compound $(H_2DABCO)Pb_2Cl_6$. On the other hand, the CIE coordinates, especially for $4AMP_2HgBr_4{\cdot}H_2O$, are very close to the for white point coordinates

(0.33,0.33). Furthermore, the room temperature WL PLQY of 14.87 ($4AMP_2HgBr_4 \cdot H_2O$) and 19.18% ($4AMP_2ZnBr_4$) are higher than the values reported for the lead halide perovskites.[345]

Usually, the physical origin of broadband WL emission based on HOIMs is attributed to STEs in a highly distorted inorganic sublattice resulting from strong electron-phonon coupling.[85, 274, 299-303, 305-310, 315, 346-349] However, a few recent examples attribute the broadband emission to the coexistence of STEs PL peak on inorganic units and a fluorescence peak from emissive centers of the organic molecules, which combine to form a broadband emission covering the entire visible spectrum.[85, 317-318, 320] On the other hand, our recent report on photophysical properties of some 0D HOIMs based on group 12 metals (Zn and Cd) showed that broadband emission could be the consequence of exciton localization on the aromatic organic molecular cations.[113] Here, to investigate the origin of the broadband luminescence for $4AMP_2HgBr_4 \cdot H_2O$ and $4AMP_2ZnBr_4$, we measured the room temperature PL and PLE spectra of the organic salt 4AMP. As shown in Figures 28b and 28c, under 325 nm excitation, the maximum emission of 4AMP lies in the blue region with the presence of a sharp peak at 457 nm accompanied with a shoulder at 395 nm, and PLE spectrum show a sharp peak at 325 nm. Moreover, by comparing the PL spectrum of $4AMP_2ZnBr_4$ with that of the corresponding 4AMP, we observed an unmistakable and significant correspondence between the high-energy peaks near the band edge (A2 and B2) with that of the 4AMP (Figure 28c). Likewise for $4AMP_2HgBr_4 \cdot H_2O$, the presence of a very broadband emission could be the result of the overlap of at least three emission sub-bands noted A1, B1, and C1 in Figure 28b. Importantly, the deconvolution of the room temperature PL spectrum of $4AMP_2HgBr_4 \cdot H_2O$ using three Gaussian function and the aid of OriginPro shows a good matching between the position of the two emission bands of 4AMP and the two high energy PL bands A1 and B1 (see Figure A1.9

in **Appendix 1**). According to this, we attribute the high energy A1, B1 and A2, B2 PL bands to the 4AMP-related organic molecules emission.

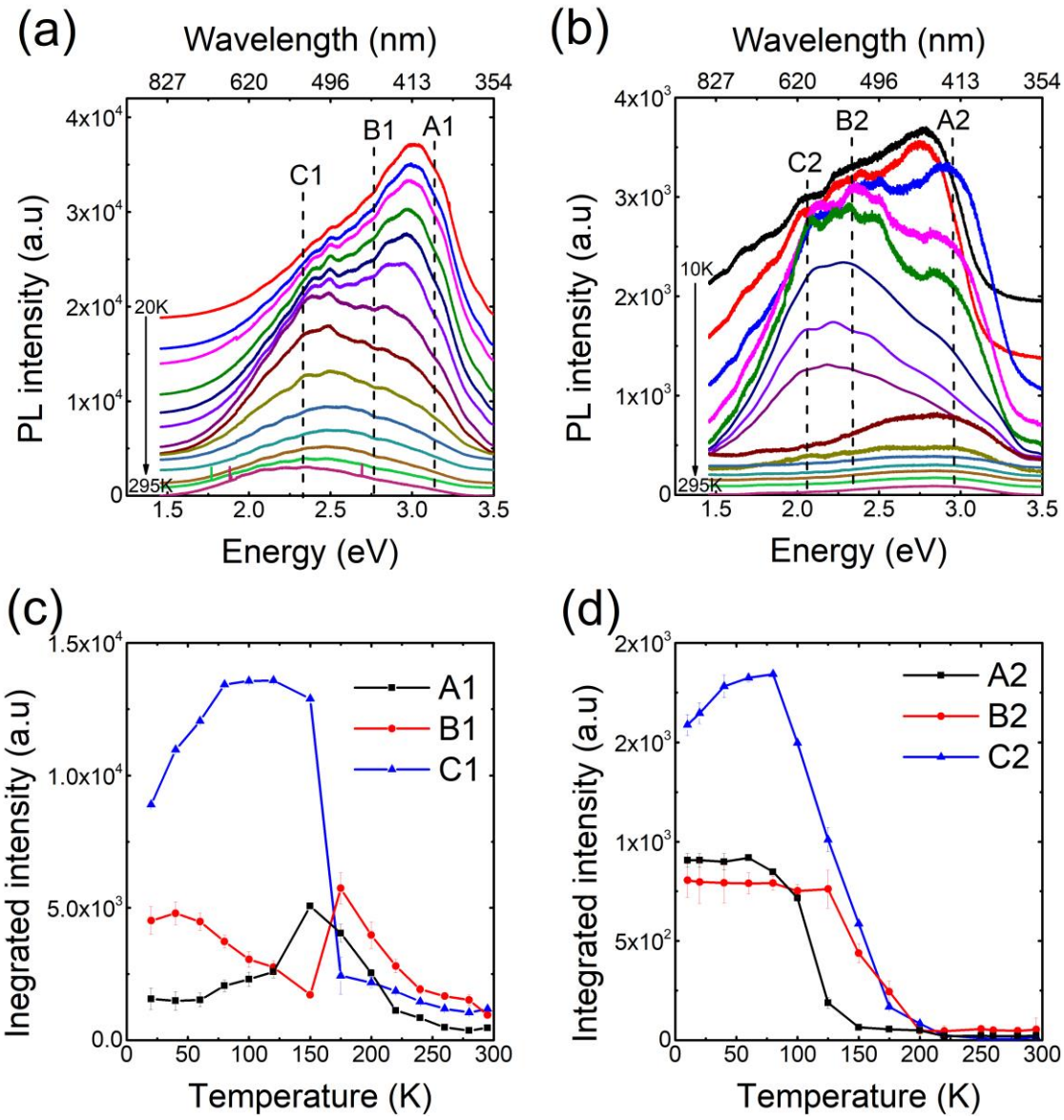


Figure 29. Temperature dependence PL of (a) $4AMP_2HgBr_4 \cdot H_2O$ and (b) $4AMP_2ZnBr_4$, under 325 nm UV irradiation. Plots of the temperature-dependence integrated intensity of (c) A1, B1, and C1 peaks of $4AMP_2HgBr_4 \cdot H_2O$ and (d) A2, B2, C2 of $4AMP_2ZnBr_4$.

Figures 29a and 29b show the temperature dependence PL measurements for $4AMP_2HgBr_4 \cdot H_2O$ and $4AMP_2ZnBr_4$ under 325 nm excitation. Significant changes were

observed as a function of temperature for both compounds. For $4AMP_2HgBr_4 \cdot H_2O$, the room temperature broadband WL emission clearly splits into at least three sub-bands at low temperature noted as A1, B1, and C1 in Figure 29a, which are located around 400, 450 and 535 nm, respectively. Based on the deconvolution of the PL spectra using 3 Gaussian functions with the aid of OriginPro (fitting shown in Figure A1.9 in **Appendix 1**), we deduced the thermal evolution of the integrated intensity, FWHM, and position of each PL peak of $4AMP_2HgBr_4 \cdot H_2O$ and $4AMP_2ZnBr_4$ (Figure 13c-d and Figure A1.10 in **Appendix 1**). Upon cooling, the integrated PL intensity of A1 first increases then decreases below 150 K. However, the integrated intensities of B1 and C1 first increases by cooling then dramatically quench bellow 150 K (Figure 29c). Similar behavior was also observed for $4AMP_2ZnBr_4$ (Figure 29d) and in several HOIMs.[309, 343, 345, 350] Moreover, the thermal evolution of the position and the FWHM of PL peaks show an abrupt shift of the position and the width of peaks in 150-175 K temperature range. Such a critical behavior was observed in several HOIMs and was attributed to structural phase transition, which could have an important impact on the optical properties.[292, 296, 302] However, for $4AMP_2HgBr_4 \cdot H_2O$ and $4AMP_2ZnBr_4$, the possibility of the presence of structural phase transition in 150-175 K temperature range has been ruled out, as a result of the well matching of the room temperature PXRD data and the single crystal XRD data measured at 100K (see Figure A1.4 in **Appendix 1**). Thus, in 150-175K temperature range, the unusual emission behavior could be the result of competition in the recombination process between multiple emission peaks.

It is also worth noticing that the presence of permanent defect states in semiconductors could create a broadband emission. [66, 276] However, permanent defect recombination lifetime and concentration are finite, thus their PL could be saturated at high excitation intensity.[351] As

shown in Figure A1.11 in **Appendix 1**, the intensity of C1 and C2 PL peaks present a linear dependence with excitation intensity, and the absence of saturation exclude the possibility of permanent defects emission.[108, 274, 309] However, the evolution of the integrated intensity of A1, B1 and A2, B2 PL peaks of $4AMP_2HgBr_4{\cdot}H_2O$ and $4AMP_2ZnBr_4$ as a function of excitation power show small quenching above 20 W/cm^2 excitation power which is probably due to the degradation of the organic molecules at high excitation intensity (Figure A1.11).

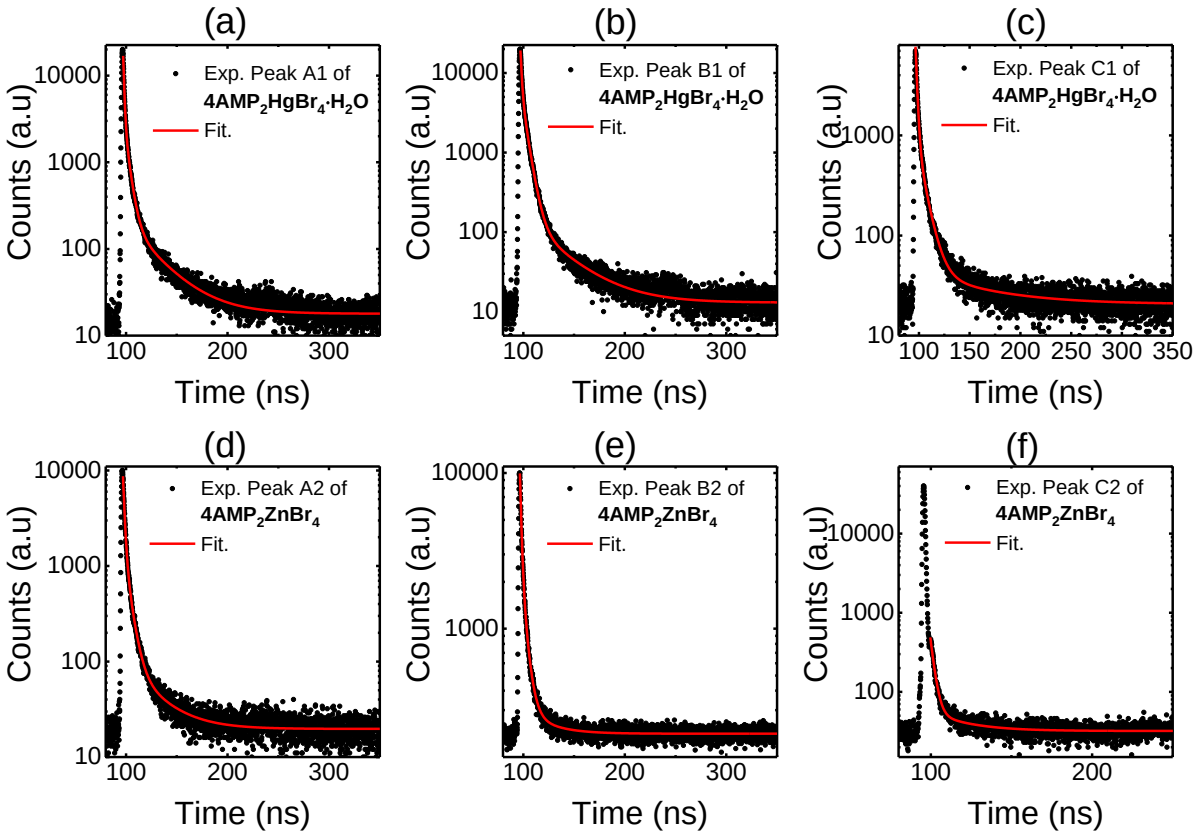


Figure 30. The photoluminescence decay curves of (a-c) A1, B1, and C1 PL peaks of $4AMP_2HgBr_4{\cdot}H_2O$ and (d-f) A2, B2, and C2 PL peaks of $4AMP_2ZnBr_4$. The excitation wavelengths are 370 and 341 nm for $4AMP_2HgBr_4{\cdot}H_2O$ and $4AMP_2ZnBr_4$, respectively.

To understand the nature of excitons and the origin of the broadband WL emission of $4AMP_2HgBr_4{\cdot}H_2O$ and $4AMP_2ZnBr_4$, time-resolved PL measurements for each PL peak were taken (Figure 30). The excitation wavelengths used are 370 and 314 nm for $4AMP_2HgBr_4{\cdot}H_2O$

and $4AMP_2ZnBr_4$ respectively, resulting in emission wavelengths of 400 (A1), 450 (B1) and 535 nm (C1) for $4AMP_2HgBr_4{\cdot}H_2O$, and 438 (A2), 550 (B2), and 650 nm (C2) for $4AMP_2ZnBr_4$. All decay profiles were fitted using a three-exponential function similar to that of the function used in analyzing the same measurements used for the $CsCu_2X_3$ system in **Chapter 4**. The first lifetime component of 1-2 ns for all peaks of $4AMP_2HgBr_4{\cdot}H_2O$ and $4AMP_2ZnBr_4$ is due to the instrumental response since the duration of the light pulse (2 ns). Results slow that the fast component is dominant for all PL peaks of $4AMP_2HgBr_4{\cdot}H_2O$ and $4AMP_2ZnBr_4$ and measure t_2(A1) = 4.3 ns, t_2(B1) = 5.1 ns, t_2(C1) = 7.5 ns, t_2(A2) = 5.3 ns, and t_2(B2) = 4.7 ns, and t_2(C2) = 2.4 ns. As discussed above, the PL peaks of A and B are most likely due to the emission by 4AMP molecules. This is further supported by their fast decay (on the order of nanoseconds) due to spin-singlet excitons in aromatic molecules typically having lifetimes of nanoseconds.[113] However, the low-energy C1 PL band of $4AMP_2HgBr_4{\cdot}H_2O$ could be due to the emission of STEs localized at $HgBr_4$ inorganic tetrahedra (see DFT results below). The fast decay of C1 (7.5 ns) is likely the result of significant nonradiative decay. Note that the reported spin-triplet STE decay times at room temperature in Pb-based HOIMs range from a few nanoseconds to hundreds of ns.[305, 316, 318, 345, 352] Short STE decay times typically correlate with relatively low PLQYs (<20%)[86 316] while long decay times were observed in those with high PLQYs (>80%), indicating the strong influence of nonradiative recombination in PL decay. The C2 PL band of $4AMP_2ZnBr_4$, which is dominant at low temperature (see Figure 29d), could be the result of possible inhomogeneity of organic molecules, which may significantly perturb electronic states. The attribution of the dominant PL peaks at room temperature to STEs in inorganic anions in $4AMP_2HgBr_4{\cdot}H_2O$ and 4AMP organic molecules in $4AMP_2ZnBr_4$ is supported by band structure calculations (see below).

2.2.5 DFT Modeling

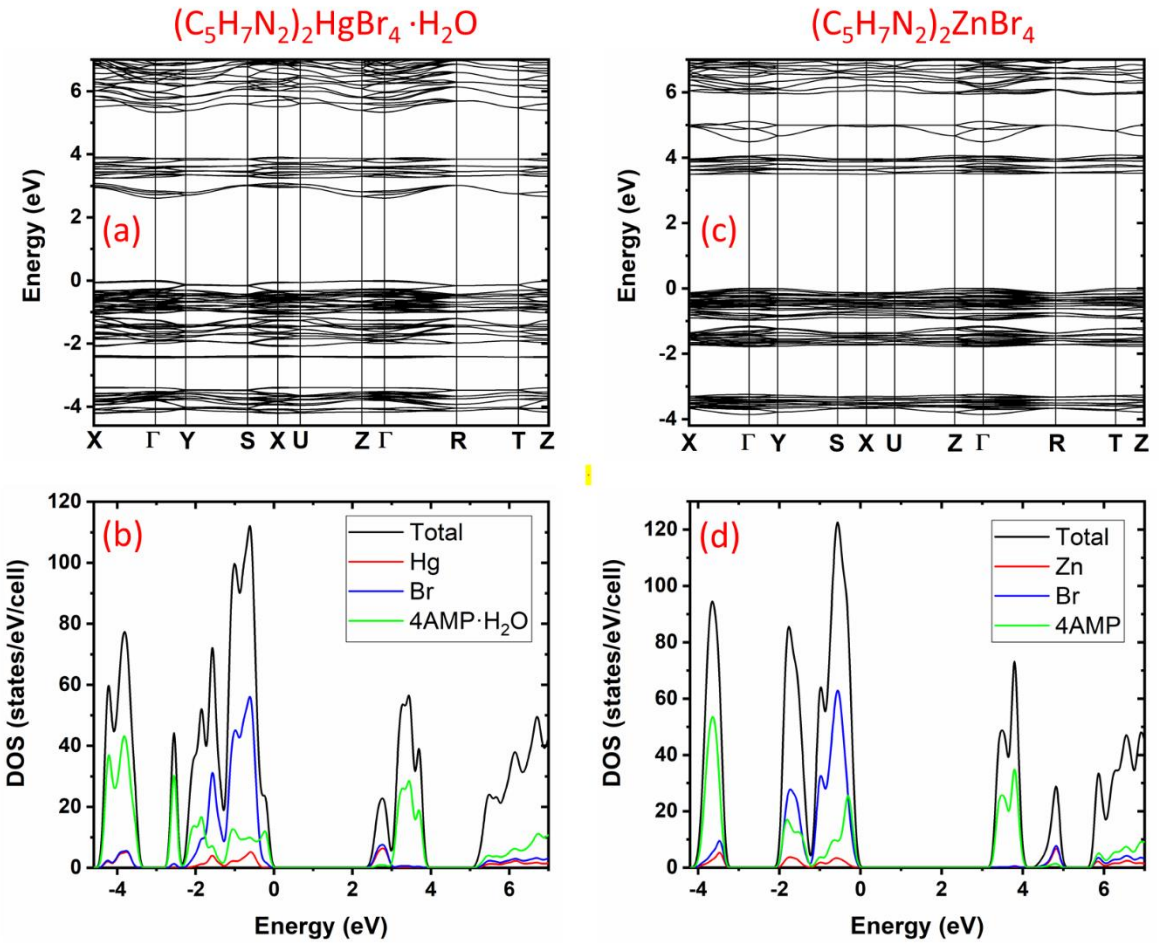


Figure 31. Electronic band structure and density of states (DOS) plots for $4AMP_2HgBr_4 \cdot H_2O$ (a-b) and $4AMP_2ZnBr_4$ (c-d) calculated using the PBE functional. Note that the band gap is underestimated due to well-known band gap error of PBE calculations.

DFT-PBE calculations show that $4AMP_2HgBr_4 \cdot H_2O$ has a direct band gap of 2.61 eV at the Γ point, and $4AMP_2ZnBr_4$ has a slightly indirect band gap of 3.49 eV; the direct band gap at the Γ point is only 0.02 eV higher in energy. The valence band maximum (VBM) of $4AMP_2ZnBr_4$ is at the Γ point and the conduction band minimum (CBM) is located between the X and the Γ points (Figure 31). Note that the above band gap values are lower than the experimentally measured values due to the well-known band-gap error in the PBE calculation.

As shown in Figure 31 the conduction and valence bands of the two compounds have very small dispersion especially in the case of $4AMP_2ZnBr_4$. The conduction band of $4AMP_2HgBr_4 \cdot H_2O$ (between 2.5 eV and 3.0 eV in Figure 31a) is distributed on $HgBr_4$ clusters as shown by the partial density of states (DOS) in Figure 31b. The higher-energy flat band between 3.0 eV and 4.0 eV is made up of highly localized organic molecular orbitals. The valence band of $4AMP_2HgBr_4 \cdot H_2O$ has a mixing of organic and inorganic states; however, the organic molecular states are dominant near the VBM. A careful examination of the eigenstates reveals that the energy gap for the inorganic cluster is about 0.28 eV smaller than that for the organic molecules. This result suggests that the lowest-energy exciton should be localized at $HgBr_4$ clusters. The conduction band of $4AMP_2ZnBr_4$ (about 3.5 eV - 4 eV in Figure 31c) is made up of highly localized organic molecular orbitals (see DOS in Figure 31d) as evidenced by the flatness of the bands. The more dispersive band above 4.5 eV with about half an eV band width is distributed among $ZnBr_4$ clusters. The bands near the VBM have strong character of both organic and inorganic components. The energy gap for the organic component is about 1 eV lower than that of the inorganic component. Therefore, it is expected that an exciton prefers to be localized on a 4AMP organic molecule. The experimentally measured short PL decay time indeed suggests fast singlet-exciton emission from organic molecules. Moreover, despite the two compounds have a quite similar structural coordination environment (see Figure 30), the PLQY of $4AMP_2ZnBr_4$ is higher than $4AMP_2HgBr_4 \cdot H_2O$. This may be explained by the fact that the conduction band of $4AMP_2HgBr_4 \cdot H_2O$ is more disperse than that of $4AMP_2ZnBr_4$ (see Figure 31) which suggests that excitons in $4AMP_2HgBr_4 \cdot H_2O$ may be more delocalized and more mobile than those in $4AMP_2ZnBr_4$. The larger spectral overlap between excitation and emission in $4AMP_2HgBr_4 \cdot H_2O$ (Figure 28b-c) should also promote exciton migration by

resonant transfer of excitation energy.[353-354] More efficient exciton migration could lead to a higher probability of encountering defects, resulting in increased energy loss and lower PLQY.[77] Thus, the lower PLQY in $4AMP_2HgBr_4 \cdot H_2O$ compared to $4AMP_2ZnBr_4$ is likely due to more mobile excitons in $4AMP_2HgBr_4 \cdot H_2O$.

2.2.6 Summary

In summary, we report new examples of low-dimensional HOIM for WL emission applications. The 4AMP cation configured orthorhombic 0D crystal structures feature $HgBr_4$ and $ZnBr_4$ isolated tetrahedra in **1** and **2**, respectively. The presence of discrete molecular building blocks in the 0D structures result in strongly localized charges and bright WL luminescence with a corresponding CIE Color Coordinates of (0.34, 0.38) and (0.25, 0.26), a very high CRI of 87 and 96, CCT values of 5206 K and 11630 K for **1** and **2**, respectively. The substitution of Hg with Zn leads to tune the emission from "warm" to "cold" WL with a calculated correlated color temperatures (CCT) of 5206 K for **1** and 11630 K for **2**. Importantly, high PLQY values of 14.87 and 19.18% were measured for **1** and **2**. Our optical investigations supported by DFT calculations suggested that the WL emission resulting from excitons localized in 4AMP and structural defects within 4AMP. The observation of non-toxic (for **2**), highly efficient "cold" WL emission with a record CRI opens interesting perspectives in the design of single-component WLEDs. Therefore, we believe that this work will enrich HOIMs family with WL emission by arousing a renewed research on low cost, ecofriendly raw materials (in the case of Zn-based compound), with facile synthesis and excellent optical properties. Within this context, we anticipate that these results will stimulate research on single-emitter-based WL-emitting phosphors and diodes for next-generation lighting and display

technologies to replace conventional inorganic rare-earth- and quantum dot-based phosphors that currently dominate the field of optically pumped WLEDs.

Chapter 3: Electronic Effects of the Organic Cation in Hybrid Group 12 Halide Systems

In this chapter, bromide and iodide salts of a large fully methylated organic cation, trimethyl(2,3,4,5,6-pentamethylbenzyl)ammonium[355] (denoted as R for the remainder of the discussion) were used in the preparation of novel luminescent 0D hybrid R-M-X halide materials where M = Zn, Cd and X = Br, I. Single crystals of all new compounds within the studied systems were obtained using low-temperature solution reactions. Based on our X-ray crystallography work, all compounds form 0D crystal structures featuring alternating layers of organic cations and inorganic anions that are based on tetrahedral coordination around the metal cations. In $RZnBr_3$(DMSO) and $RCdI_3$(DMSO), DMSO molecules directly coordinate to metal cations through M-O bonds yielding MX_3DMSO^- units, whereas R_2CdBr_4·DMSO features $CdBr_4^{2-}$ anions and DMSO molecules that act as spacers in between organic and inorganic ions. Optical properties of R-M-X were investigated using steady state photoluminescence (PL) as a function of temperature, photoluminescence excitation (PLE), time-resolved photoluminescence (TRPL), PLQY, as well as density functional theory (DFT). The compounds are shown to demonstrate rare light emission from the organic component of the hybrid organic-inorganic halides including deep blue emission and broadband white-light emission with PLQY values up to 3.07%. This interesting family of compounds also demonstrates the controllable creation of both type I and type II band alignments.

3.1 Introduction

Solution-processable hybrid organic-inorganic materials (HOIMs) have been at the forefront of optical and electronic material research in the past decade owing to their rich crystal chemistry and broadly tunable physical properties.[212, 289, 356-359] Among these, Pb- and Sn-based hybrid halide perovskites have been the focus of global attention due to their excellent performance in solar cells, which now have record power conversion efficiencies exceeding 22%.[360] In addition, excellent light emission properties of halide perovskites have also been reported including efficient blue emission[361-362] and broadband white-light emission.[106-108, 344, 363-364] Inspired by these findings, further experimental studies show that non-perovskite hybrid organic-inorganic halides can also have remarkable light emission properties, such as in the case of $(H_2DABCO)Pb_2Cl_6$ and $(H_3O)(Et_2\text{-}DABCO)_8Pb_{21}Cl_{59}$ compounds that demonstrate white-light emission with high color rendering index (CRI) values of 96 and 88, respectively.[365]

The light-emission properties of hybrid organic-inorganic perovskites are strongly dependent on their structural dimensionality with 3D perovskites behaving as typical all-inorganic multinary halides with small exciton binding energies (typically below 50 meV).[289, 366-367] Conversely, low-dimensional hybrid halides demonstrate much stronger charge localization and exciton binding energies in excess of 500 meV, values that are comparable to that of tightly-bound Frenkel excitons in organic materials.[289, 306] Such high exciton binding energies can accordingly result in room temperature stable excitons and intense excitonic emission. Therefore, preparation and characterization of low-dimensional organic-inorganic hybrid halides for light emission applications has been the focus of several studies published in recent years.[17, 74, 85]

Highest charge localization and exciton binding energies are often observed for 0D compounds,[212] which feature molecular inorganic anions and organic cations in their crystal structures. Indeed, numerous Cu-, Sn- and Sb-based 0D non-perovskite hybrid halides have recently been reported to exhibit remarkable light emission properties including photoluminescence quantum yields (PLQY) approaching unity[66, 74, 368-369] and large Stokes shifts above 300 nm.[370] The large Stokes shifts are primarily attributed to the pronounced excited state structural distortions,[368, 370] and therefore, are rarely observed for materials in the solid state due to the rigidity of solid structures which restricts significant structural reorganization. However, 0D hybrid halides featuring molecular organic and inorganic units are more amenable to structural reorganization, and hence, exhibit broadband photoluminescence (PL) spectra with large Stokes shifts.

Unlike the Pb-based and Sn-based hybrid halides, the optical and electronic properties of the hybrid halides of group 12 metals remain largely unexplored. Notwithstanding a few recent publications focusing on the light emission properties of group 12 metal hybrid halides,[85, 306, 371] most published articles focus on their intriguing structural properties including structural dimensionalities, impact of hydrogen bonding, molecular orientations of organic cations, etc.[372-374] These group 12 metal-based hybrid halides show a remarkable structural flexibility in their tunable dimensionality[306, 371] and incorporation of functional organic cations, such as chromophores and polymers,[374-375] in 2D perovskite structures both of which can be utilized to prepare functional materials for practical applications including solid state lighting applications. This fact is further evidenced by a recent discovery of broadband white-light emission in the 2D layered perovskite compound $(C_6H_{11}NH_3)_2CdBr_4$ originating from both organic and inorganic layers.[85]

Single crystals of all new compounds within the studied systems were obtained using low-temperature solution reactions. Based on our X-ray crystallography work, all compounds form 0D crystal structures featuring alternating layers of organic cations and inorganic anions that are based on tetrahedral coordination around the metal cations. In (R)$ZnBr_3$(DMSO) and (R)CdI_3(DMSO), DMSO molecules directly coordinate to metal cations through M-O bonds yielding MX_3DMSO^- units, whereas $(R)_2CdBr_4$·DMSO features $CdBr_4^{2-}$ anions and DMSO molecules that act as spacers in between organic and inorganic ions. Optical properties of R-M-X were investigated using steady state photoluminescence (PL) as a function of temperature, photoluminescence excitation (PLE), time-resolved photoluminescence (TRPL), PLQY, as well as density functional theory (DFT). The compounds are shown to demonstrate rare light emission from the organic component of the hybrid organic-inorganic halides including deep blue emission and broadband white-light emission with PLQY values up to 3.07%.

3.2. Synthesis and Methods of ($C_{15}H_{26}N$)-M-X (M = Zn, Cd; X = Br, I)

3.2.1 Reagents Used in the Synthesis of ($C_{15}H_{26}N$)-M-X (M = Zn, Cd; X = Br, I) and ($C_{15}H_{26}N$)(Br, I) salts

Chemicals utilized in this study were either used as purchased or synthesized from the starting materials listed: (i) zinc bromide, 99.999%, Sigma; (ii) zinc iodide, 99.995%, Alfa Aesar; (iii) cadmium bromide, 98% Alfa Aesar; (iv) cadmium iodide, 99.999%, Alfa Aesar; (v) dimethyl sulfoxide, ACS grade, Fisher; (vi) methanol, ACS reagent grade, Pharmco-AAPER. (vii) pentamethylbenzene, Aldrich; (viii) paraformaldehyde, 95%, Aldrich; (ix) hydrobromic acid, 48%, Sigma Aldrich; (x) cetyltrimethyl ammonium bromide, Sigma; (xi) acetic acid, ACS reagent grade, 99.8%, Sigma Aldrich; (xii) o-phosphoric acid, ACS Certified, 85%, Fisher; (xiii) methyl iodide, Aldrich; (xiv) trimethylamine hydrochloride, 98% Aldrich.

3.2.2 Syntheses of $C_{15}H_{26}N)_2MX_4$ (M = Zn, Cd; X = Br, I) compounds

For the syntheses of hybrid organic-inorganic halides of group 12 metals, various solvents including N,N-dimethylformamide (DMF), dimethyl sulfoxide (DMSO), and methanol were tried. Among these, DMSO was selected as the most suitable solvent due to the highest solubility of the precursor organic salts trimethyl(2,3,4,5,6-pentamethylbenzyl)ammonium halides (R)X (X = Br, I). Details of the syntheses and characterizations of the organic salts are described in the Supplementary Information (see Figures S1-S4). It was determined that single crystals of target compounds can be grown in 20 mL drams at 65 °C by separately solvating (R)X (X = Br, I) in 2 mL of DMSO and MX_2 (M = Zn, Cd) in 1 mL of methanol, then mixing the stoichiometric 1:1 molar ratio solutions together.

3.2.2.1 Bromide-based compounds

(R)$ZnBr_3$(DMSO) crystals were grown through slow evaporation of their stoichiometric solutions as described above. $(R)_2CdBr_4$·DMSO was first obtained by reacting (R)Br and $CdBr_2$ in a nonstoichiometric 1:1 molar ratio. A subsequent stoichiometric reaction with 2:1 molar ratio of (R)Br:$CdBr_2$ also afforded $(R)_2CdBr_4$·DMSO. In all cases, colorless block crystals measuring up to 3 mm formed over a 3 week crystallization period.

3.2.2.2 Iodide-based compounds

(R)CdI_3(DMSO) crystals were grown through slow evaporation of their stoichiometric solutions as light-yellow blocks measuring up to 2 mm in size over a 3 week crystallization period. Syntheses of Zn analogues, (R)ZnI_3 and $(R)_2ZnI_4$, were tried in different loading ratios of DMF, DMSO, and methanol solutions, but proved unsuccessful.

3.2.3 Single Crystal X-ray Diffraction

The X-ray intensity data for all compounds were collected on a Bruker Apex CCD diffractometer with a graphite monochromated Mo-Kα (λ = 0.71073Å) radiation. For room temperature measurements (298(2) K), crystals with good clarity were selected from their mother liquor, cut to size, covered with Super Glue, affixed to a goniometer head, and allowed to dry. For low temperature measurements, crystals were selected from their mother liquor, placed in Dow Chemical vacuum grease, cut to size, and then cooled to 100(2) K. The crystal structures for all compounds were determined from a nonlinear least-squares fit. The data were corrected for absorption by the semi-empirical method based on equivalents and the structures were solved by direct methods using the SHELXTL program and refined by full matrix least-squares on F^2 by use of all reflections.[226, 376] All non-hydrogen atoms were refined with anisotropic displacement parameters, all occupancies were refined within two standard deviations, and all hydrogen atom positions were determined by geometry. Single crystal data collection and refinement parameters are summarized in Tables 1 and S1. Atomic coordinates, equivalent isotropic displacement parameters and selected interatomic distances and bond angles can be found in Tables S2 – S3. Full details of the crystal structures are summarized in the CIF (Crystallographic Information File) files have been deposited in the Cambridge Crystallographic Data Centre (CCDC) database and can be found under deposition numbers 1840612, 1840614-1840618.

3.2.4 Powder X-ray Diffraction

For powder X-ray diffraction (PXRD) measurements, solution-processed samples were dried overnight under vacuum and then ground into powdered forms. PXRD measurements were carried out on a Rigaku MiniFlex600 system equipped with a D/tex detector using Ni-

filtered Cu-Kα radiation source. Typical PXRD scans were performed in the 5-90° (2θ) range, with a step size of 0.02° to determine phase identity and purity. Data analysis was performed using Rigaku's PDXL2 software package. The baseline originating from the glass slides used to collect data was corrected using the embedded tool in the PDXL2 software, and the data were fitted using the decomposition method (also known as Pawley fitting) embedded in the PDXL2 software package.

3.2.5 Energy Dispersive X-ray (EDX) Measurements

EDX measurements were performed on polycrystalline samples using a Zeiss Neon EsB equipped with an Oxford Instruments EDX system. Elemental analysis yields an average composition of 26.45% of Rb, 11.95% of Ag, 5.85% of Bi, and 55.75 % of Br, which present a good agreement with the calculated values; 25% of Rb, 12.5% of Ag, 6.25% of Bi, and 56.25% of Br (see Figure S1(b)).

3.2.6 Optical Measurements

Room temperature PLE, PL and PLQY measurements were performed on a HORIBA Jobin Yvon Fluorolog-3 spectrofluorometer using a Xenon lamp and Quanta-φ integrating sphere using the two-curve method in a varied range from 280-860 nm. UV-vis diffuse reflectance was measured to study the optical absorption properties of the compounds. Measurements were performed on polycrystalline powder samples using a PerkinElmer Lambda 750 UV/VIS/NIR Spectrometer equipped with a 100mm Spectralon InGaAs Integrating Sphere attachment over a 250-1100 nm range. TRPL was measured on a HORIBA Jobin Yvon Fluorolog-3 spectrofluorometer using a time-correlated-single-photon counting module. HORIBA Jobin Yvon NanoLEDs (pulsed light-emitting diodes) were used as the excitation source. The duration of the light pulse was shorter than 2 ns. Temperature

dependence PL spectra were measured on single crystal samples using a double monochromator U1000 equipped with a photomultiplier. The excitation wavelength was the 325 nm (3.815 eV) line of a Spectra-Physics beamlock 2085 argon laser. The samples were placed in a helium bath cryostat and the measurements were performed between 2 and 300 K. Room temperature solid-state mid-IR measurements were performed on a Bruker Tensor27 IR over the range of 400 – 4000 cm^{-1} on solid samples ground and then pressed into a matrix of KBr.

3.2.7 First Principles Calculations

All calculations were based on DFT implemented in the VASP code.[229] The interaction between ions and electrons was described by the projector augmented wave method.[323] The kinetic energy cutoff of 400 eV for the plane-wave basis was used for all calculations. Experimental lattice parameters were used while the atomic positions were fully relaxed until the residual forces were less than 0.02 eV/ Å. Electronic band structures and density of states (DOS) were calculated using the Perdew−Burke−Ernzerhof (PBE) exchange-correlation functional[228] while excitons were treated by using the more advanced hybrid PBE0 functional,[377] which has 25% non-local Fock exchange. Previous PBE0 calculations have provided accurate results on exciton properties in hybrid organic-inorganic halide perovskites.[77, 368, 370]

3.3 Room and Low Temperature Crystal Structures

Room temperature and low temperature single crystal X-ray diffraction (SXRD) experiments for hybrid bromide and iodides of Zn and Cd metals are summarized in Figure 32, and Tables 3 and A1.10-A1.12 in **Appendix 1**. Based on the obtained results, there are no structural transitions between room temperature and 100 K for all reported compounds; instead, normal contraction of the unit cell volume is observed upon cooling (Tables 3 and A1.10). As

expected, the use of bulky non-linear organic cation results in 0D crystal structures for (R)$ZnBr_3$(DMSO), $(R)_2CdBr_4$·DMSO and (R)CdI_3(DMSO) featuring alternating layers of isolated inorganic anions and organic cations. In all cases, DMSO solvent molecules are incorporated into the crystal structures of the resultant compounds. In the case of $(R)_2CdBr_4$·DMSO, the coordination environment around Cd^{2+} only consists of bromide anions giving $CdBr_4^{2-}$ anions and DMSO molecules acting as spacers in between organic and inorganic ions. However, in (R)$ZnBr_3$(DMSO) and (R)CdI_3(DMSO), DMSO molecules and halide anions form the coordination environment around metal cations through direct M-O bonds yielding MX_3DMSO^- units (Figure 32). Notice that the formula for $(R)_2CdBr_4$·DMSO is written differently compared to (R)$ZnBr_3$(DMSO) and (R)CdI_3(DMSO) to emphasize direct coordination of DMSO molecules to the metals in the latter. The measured M-O bond distances of $d_{Zn\text{-}O}$ = 2.024(5) Å and $d_{Cd\text{-}O}$ = 2.247(7) Å in (R)$ZnBr_3$(DMSO) and (R)CdI_3(DMSO) (Table A1.11), respectively, follow the expected trend based on the sizes of Zn^{2+} and Cd^{2+} ions.[378] These values are slightly longer than the literature-reported Zn-O and Cd-O bond distances in oxyhalides such as $Zn_{0.902}SbBrO_2$ ($d_{Zn\text{-}O}$ = 1.897 Å) and $BiCdIO_2$ ($d_{Cd/Bi\text{-}O}$ = 2.239 Å).[231] On the other hand, the metal halide bond distances are in the $d_{Zn\text{-}Br}$ = 2.38-2.40 Å range for (R)$ZnBr_3$(DMSO), $d_{Cd\text{-}Br}$ = 2.58-2.61 Å for $(R)_2CdBr_4$·DMSO, and $d_{Cd\text{-}I}$ = 2.72-2.73 Å for (R)CdI_3(DMSO). These values compare well with that reported for other hybrid organic-inorganic halides of Zn and Cd, including [4,4′-H_2bipy][$ZnBr_4$] ($d_{Zn\text{-}Br}$ = 2.39-2.43 Å),[373] $(CH_3NH_3)_2CdBr_4$ ($d_{Cd\text{-}Br}$ = 2.57-2.59 Å), and $(CH_3NH_3)_2CdI_4$ ($d_{Cd\text{-}I}$ = 2.72-2.75 Å).[306] In all compounds, the tetrahedral coordination around the metal cations are distorted with bond angles ranging from 98.97(19)º to 118.37(3)º in (R)CdI_3(DMSO) (Table A1.11). It should be noted that the presence of DMSO in the coordination sphere of Cd^{2+} undoubtedly contributes to the

observed distortion in (R)CdI_3(DMSO), however, tetrahedral distortions are also observed for cadmium halides with no coordinating solvent molecules including $(R)_2CdBr_4$·DMSO, which features $CdBr_4^{2-}$ units, and in literature, for $(CH_3NH_3)_2CdBr_4$ and $(CH_3NH_3)_2CdI_4$.[306]

Table 3. Selected room temperature single crystal data collection and refinement parameters for the compounds prepared in this work.

Formula	**(R)$ZnBr_3$(DMSO)**	**(R)$CdBr_4$·DMSO**	**(R)CdI_3(DMSO)**
Formula weight (g/mol)	603.59	950.90	791.59
Temperature (K)	298 (2)		
Radiation, wavelength (Å)	Mo Kα, 0.71073		
Crystal system	Orthorhombic	Triclinic	Orthorhombic
Space group, *Z*	$P2_12_12$, 4	*P*-1, 2	$P2_12_12$, 4
a (Å)	9.116(2)	8.9894(6)	9.3959(6)
b (Å)	28.767(7)	14.3500(9)	29.5322(19)
c (Å)	8.892(2)	15.9925(10)	9.3829(6)
α, º	90	72.1342(11)	90
β, º	90	89.0598(12)	90
γ, º	90	89.2993(11)	90
Volume (Å^3)	2331.8(10)	1963.1(2)	2603.6(3)
Density (ρ_{calc}) (g/cm^3)	1.719	1.609	2.019
Absorption coefficient (μ) (mm^{-1})	6.289	4.706	4.481
$\theta_{min} - \theta_{max}$ (º)	2.29 – 26.41	1.34 – 25.70	1.38 – 29.67
Reflections collected	34552	44472	66620
Independent reflections	4544	7464	7362
R^a indices ($I > 2\sigma(I)$)	R_1 = 0.0398 wR_2 = 0.0892	R_1 = 0.0324 wR_2 = 0.0690	R_1 = 0.0370 wR_2 = 0.0977
Goodness-of-fit on F^2	0.918	1.008	1.013
Largest diff. peak and hole (e$^-$/Å^3)	0.626 and -0.739	0.816 and -0.626	1.320 and -0.926

[a] $R_1 = \sum\big||F_o| - |F_c|\big| / \sum|F_o|$; $wR_2 = \{|\sum|w(F_o^2 - F_c^2)^2| / \sum|w(F_o^2)^2||\}^{1/2}$, where $w = \{1/|\sigma^2 F_o^2 + (AP)^2 + BP|\}$, with $P = (F_o^2 + 2F_c^2)/3$ and weight coefficients *A* and *B*.

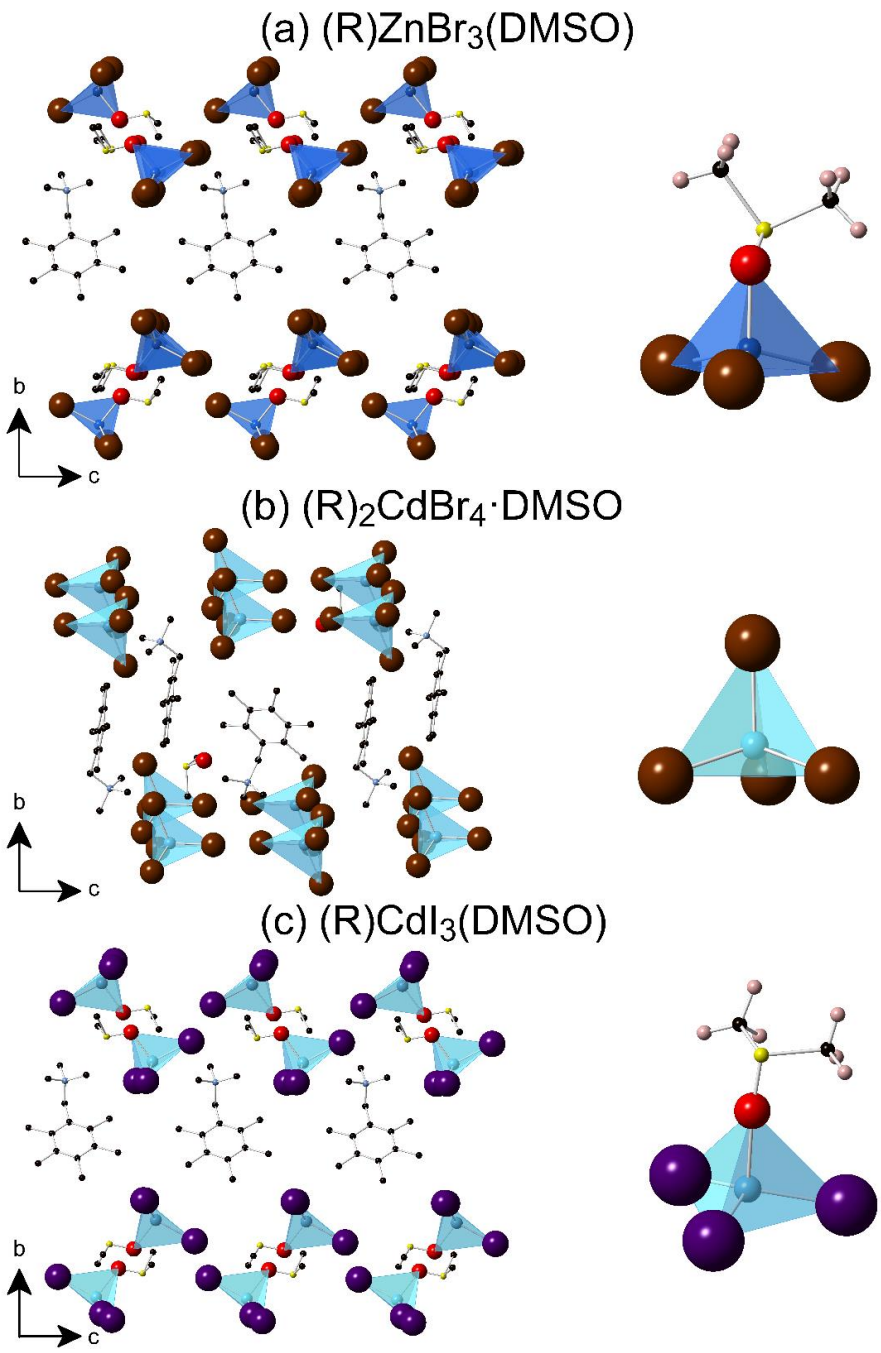


Figure 32. Polyhedral views and close up views of the coordination of the polyhedra of the crystal structures of (a) (R)$ZnBr_3$(DMSO), (b) $(R)_2CdBr_4$·DMSO and (c) (R)CdI_3(DMSO). Blue and cyan tetrahedra represent coordination environments around Zn and Cd, respectively. Burgundy, purple, red, yellow, black, and light blue spheres represent Br, I, O, S, C, and N, respectively. For clarity, hydrogen atoms were omitted and only a fraction of organic cations and solvent molecules are shown.

3.4 Stability studies

Based on the results of our powder X-ray diffraction (PXRD) measurements, all compounds form phase pure products (Figure 33). The PXRD patterns in all cases have several characteristic low angle peaks indicative of large unit cell parameters stemming from the use of the bulky organic cation. Poor stability in air is an often-cited deficiency of some of the most well-known hybrid organic-inorganic halides including the state-of-the-art photovoltaic material $CH_3NH_3PbI_3$.[251, 379] To test air stability of our compounds, powdered samples were allowed to sit undisturbed under ambient conditions over a period of one month. Periodic PXRD scans taken on the samples exposed to ambient air (Figure A1.13 in **Appendix 1**) indicate that all samples are stable for at least several days. Noticeable changes are recorded for (R)CdI_3(DMSO), which shows lowered peak intensities and peak broadening after 2 weeks (Figure A1.13), indicative of reduced crystallinity. These results are consistent with the trend we recently observed for the $(CH_3NH_3)_2CdX_4$ (X = Cl, Br, I) series, discussed in **Chapter 2**, in which air stability is markedly worse for the iodide compared to the chloride analog.[306] Furthermore, extensive studies on halide perovskites also suggest reduced air stabilities going from chlorides to iodides.[251]

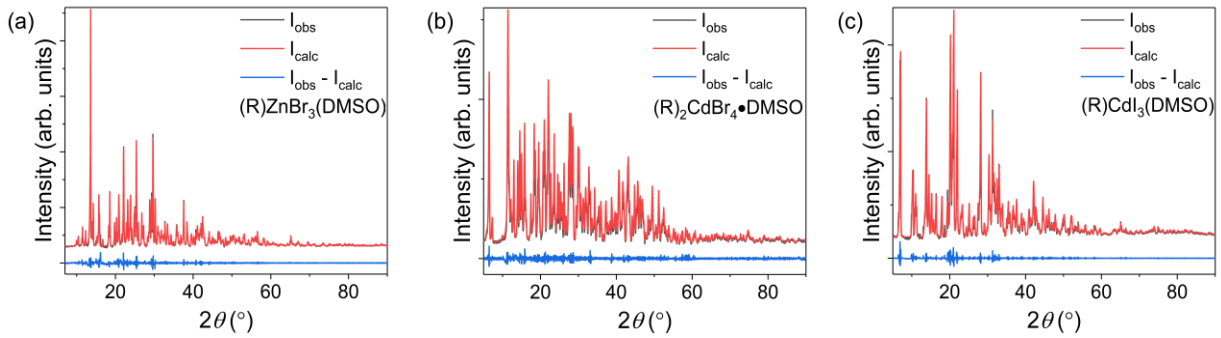


Figure 33. Powder X-ray diffraction (PXRD) patterns (black lines) for (a) (R)$ZnBr_3$(DMSO), (b) (R)$_2$$CdBr_4$·DMSO and (c) (R)$CdI_3$(DMSO). The Pawley fits and difference plots are shown as red and blue curves, respectively.

3.5 Optical properties

The highly tunable light emission properties in this series studied through room temperature optical absorption, PL and PLE measurements are summarized in Figure 34 and Table 4. Optical absorption spectra show sharp absorption peak at ~ 290 nm accompanied with a shoulder at 290 nm, 320 nm and 360 nm for (R)$ZnBr_3$(DMSO), (R)$_2$$CdBr_4$·DMSO and (R)$CdI_3$(DMSO), respectively. These optical absorption bands were attributed to the organic molecule. Moreover, PLE spectra shows the presence of a sharp peak at 386 nm, 399 nm, and 445 nm, for (R)$ZnBr_3$(DMSO), (R)$_2$$CdBr_4$·DMSO and (R)$CdI_3$(DMSO), respectively. These peaks were assigned to the excitonic absorption.[380] Similar to the earlier reports on Cd-based and Pb-based hybrid halide perovskites,[17, 85, 108, 305-306, 343, 381] all compounds studied in this work exhibit broadband emission spectra with full width at half maximum (FWHM) values ranging from 162 nm for (R)CdI_3(DMSO) to 188 nm for (R)$ZnBr_3$(DMSO). Importantly, bright broadband white-light emission is observed for (R)$ZnBr_3$(DMSO). The corresponding Commission Internationale de l'Eclairage (CIE) Color Coordinates (*x*, *y*) of (0.26, 0.30) for (R)$ZnBr_3$(DMSO) are close to the white point (0.33, 0.33) coordinates. (R)$_2$$CdBr_4$·DMSO emits

bluish-white light with CIE coordinates of (0.24, 0.35), whereas (R)CdI_3(DMSO) emits green light (0.29, 0.57). For the compounds with emission on the Planckian locus, the calculated correlated color temperatures (CCT) using the approach proposed by Hernández-Andrés et al.[382] are 11044 K for (R)$ZnBr_3$(DMSO) and 10384 K for $(R)_2CdBr_4$·DMSO.[382] Such high values suggest that these compounds emit "cool" bluish-white and white colors similar to the cold white-light emitting Pb-based halide perovskites.[305]

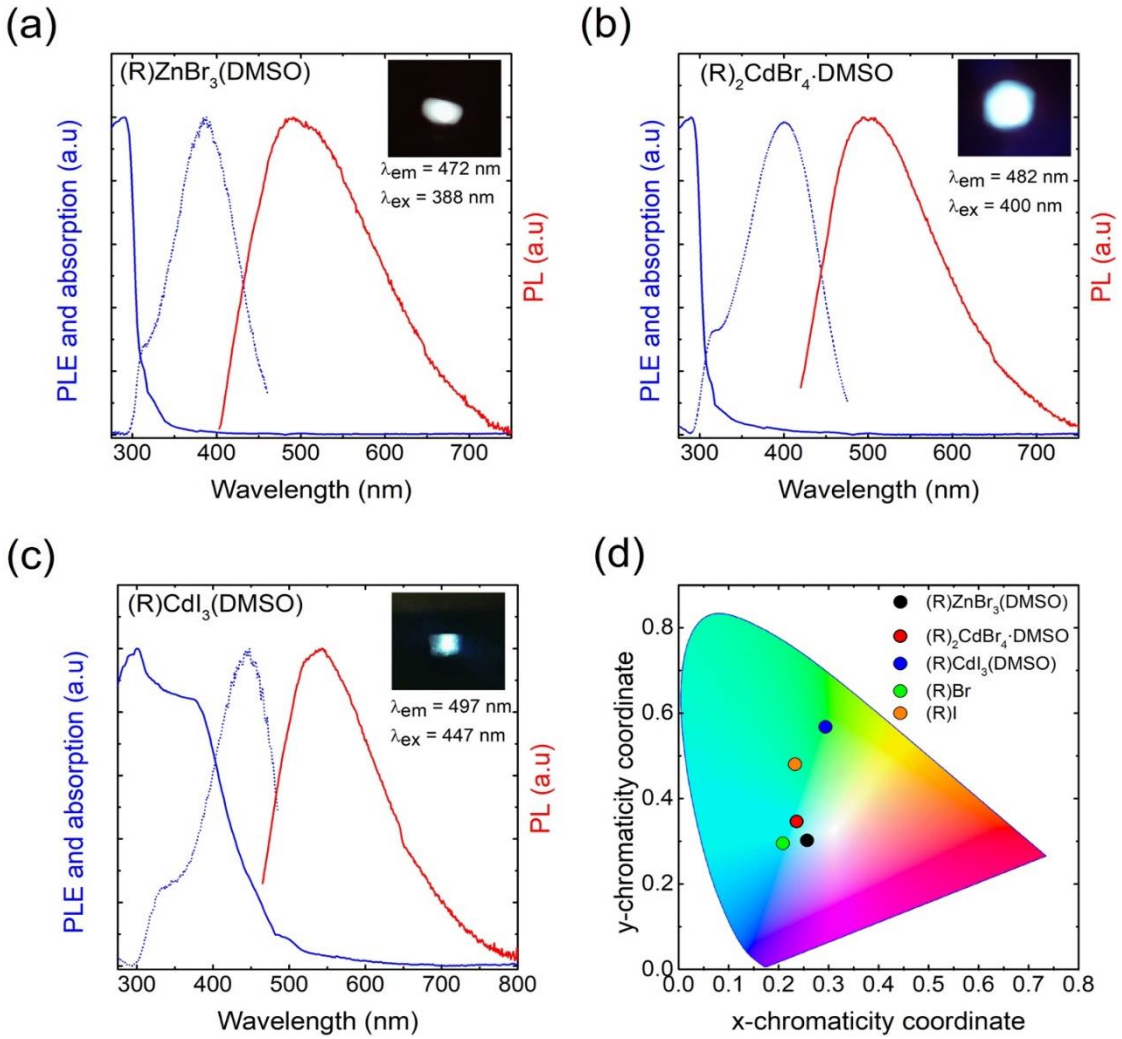


Figure 34. (a-c) Room temperature optical absorption (blue solid lines) PLE (blue doted lines) and PL (red solid lines) spectra for the compounds studied in this work. The insets show the bright emission from the powder samples under irradiation with their respective maximum excitation wavelengths. (d) CIE 1931 chromaticity diagram showing the emission colors of the compounds and the organic salts.

Table 4. Summary of the optical properties of the organic-inorganic hybrid compounds (R)$ZnBr_3$(DMSO), (R)$_2CdBr_4$·DMSO and (R)CdI_3(DMSO), and the corresponding organic salts (R)Br and (R)I.

Compound	PLQY (%)	FWHM (nm)	PLE_{max} (nm)	PL_{max} (nm)	Stokes shift (nm)	CIE coordinates	
(R5)$ZnBr_3$(DMSO)	3.07	188	386	491	105	0.26	0.30
(R5)$_2CdBr_4$·DMSO	0.32	164	399	501	102	0.24	0.35
(R5)CdI_3(DMSO)	0.27	162	445	515	70	0.29	0.57
(R5)Br	2.44	153	378	462	84	0.21	0.29
(R5)I	0.42	168	416	514	98	0.23	0.48

The room-temperature PL lifetime profiles of the compounds prepared in this work are plotted in Figure 35. All the profiles monitoring emission at the wavelength of maximum intensity can be well fitted by two-exponential functions, as described in **Chapter 4, Section 4.2.3**. The first lifetime component of 1-2 ns for all compounds is due to the instrumental response because of the duration of the light pulse (2 ns). The measured PL lifetimes of these compounds range from 9 to 21.1 ns (Figure 35). In the literature, a spread in PL lifetimes of Pb-based hybrid halides are reported ranging from subnanosecond up to 54.1 ns,[17, 305, 365] attributed to self-trapped excitonic states (STEs), and for some 0D Pb-free hybrid halides phosphorescent lifetimes in microseconds are reported.[368, 370, 383]

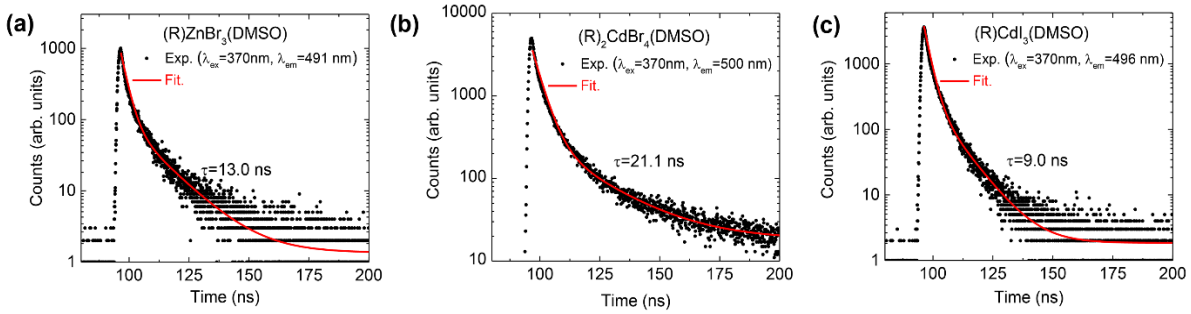


Figure 35. Photoluminescence lifetime profiles (black solid circles) and fitting curves (red lines) for (a) (R)$ZnBr_3$(DMSO), (a) (R)$_2CdBr_4$·DMSO, and (c) (R)$CdBr_3$(DMSO). The insets show the excitation and emission wavelengths, and the derived lifetime constants.

In hybrid metal halide perovskites, tunable broadband emission has been attributed to structural distortions, in particular to the distortions of the MX_6 octahedra.[85, 108, 303] According to these studies, structural distortions directly impact band gaps and the spread in the structural distortions, therefore, broadening the emission spectra. Although the compounds studied in this work are not perovskites and are not based on octahedral inorganic frameworks, tetrahedral distortions around metal cations are clearly evident for each compound (Table A1.11). However, in the present case, we cannot establish a clear correlation between tetrahedral distortions and the measured FWHM values due to the differing crystal structures and coordination environments around the metal cations in this family. Nevertheless, the structural distortions observed in our compounds could, in principle, aid in the generation of more transient photo-excited STEs similar to those in Pb-halide perovskites.[305, 384-385] For 0D hybrid halides of Sn and Sb, it has been shown that the significant structural distortions of the excited state also leads to large Stokes shifts of 200-350 nm.[368, 370] Although we observe smaller Stokes shifts ranging from 70 nm for (R)CdI_3(DMSO) to 105 nm for (R)$ZnBr_3$(DMSO), these values are still much higher than that for higher dimensional (2D and 3D) hybrid halide perovskites.[254] The impact of distortions of the inorganic anions would be greatest if light emission originates from the inorganic molecules, i.e., if the excitons are localized on the inorganic units. Unlike the heavily studied Sn and Pb halide systems, in the present case we employed group 12 metals (Zn and Cd), which have lower electronegativities,[220] and hence higher lying conduction bands for the inorganic anions. Consequently, excitons in (R)$ZnBr_3$(DMSO), $(R)_2CdBr_4$·DMSO, and (R)CdI_3(DMSO) could be localized on the organic molecules, and the relatively smaller Stokes shifts in our compounds (between 70 and 105 nm) could be a direct consequence of this fact. Recently, broadband white-light emission in the 2D layered perovskite compound

$(C_6H_{11}NH_3)_2CdBr_4$ was reported and attributed to both organic and inorganic layers emissions.[85] Another recent report of yellowish white-light emission in the 1D hybrid perovskite namely $(C_9H_{10}N_2)PbCl_4$ attributed its emission properties to a resonant energy transfer mechanism from the inorganic $PbCl_4$ to the organic molecules.[381] To further study the origin of the broadband light emission in our compounds, we have also carried out photoluminescence measurements on the precursor organic salts (R)Br and (R)I, which are provided in Figure 36. The corresponding binary inorganic halides do not luminesce at room temperature due to thermal quenching effects.[129, 262-263, 266, 306, 383, 386] As shown in Table 4, (R)Br emits light blue with CIE coordinates of (0.21, 0.29), whereas (R)I emits light green with CIE coordinates of (0.23, 0.48). Importantly, the PL and PLE spectra of $(R)ZnBr_3(DMSO)$, $(R)_2CdBr_4{\cdot}DMSO$, and $(R)CdI_3(DMSO)$ (Figure 34) are largely similar to that of (R)Br and (R)I (Figure 36), suggesting that the emission in our hybrid halides originates from the organic molecules. The red shift of the PL peaks of the hybrid halides compared to the organic salts, can be attributed to the difference in the crystal structures of the precursor organic salts and hybrid halides, and the resultant higher charge localization in hybrid halides.

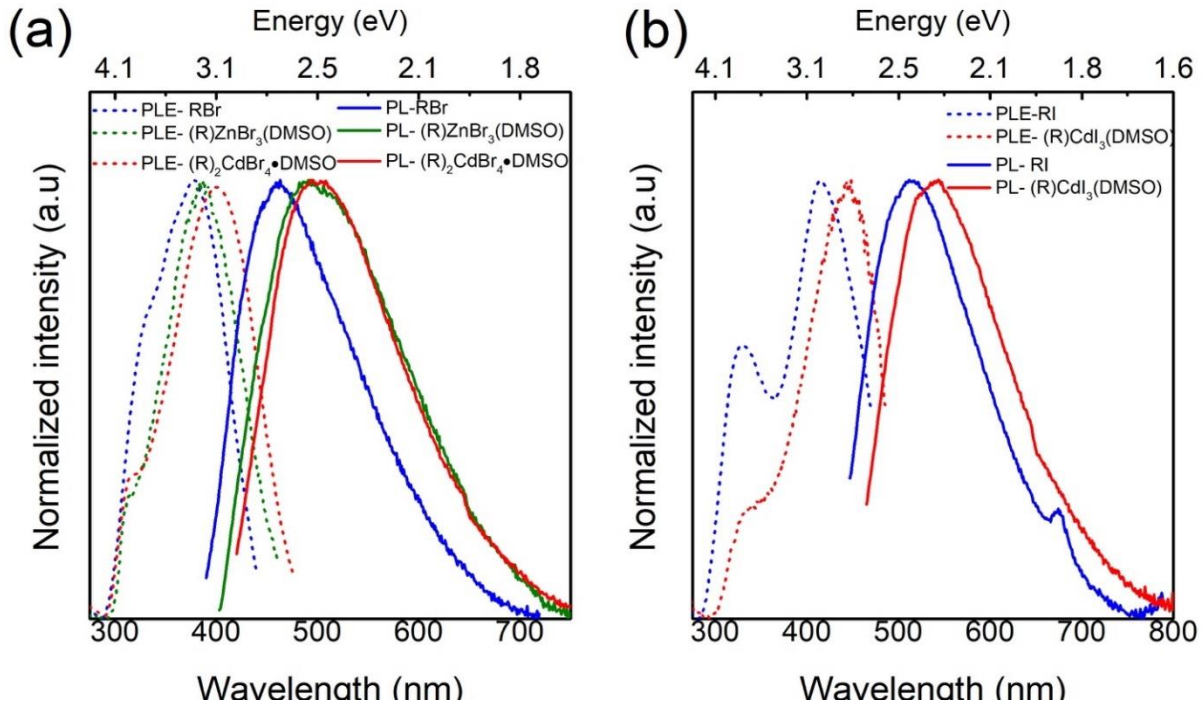


Figure 36. Room temperature PLE (dashed lines) and PL spectra (solid lines) of the (a) (R)Br organic salt and (R)Br-based compounds, and (b) (R)I organic salt and (R)I-based compound. Spectra are normalized for clarity.

The measured room temperature PLQY values range from 0.27% for (R)CdI_3(DMSO) to 3.07% for (R)$ZnBr_3$(DMSO), which are comparable or higher than most of the reported broadband light emitters based on lead halide perovskites.[17, 106, 350, 387] The precursor salts (R)Br and (R)I demonstrate PLQY values of 2.44 and 0.42%, respectively. Therefore, the emission efficiency is increased upon incorporation of the organic molecule into (R)$ZnBr_3$(DMSO) but is decreased in $(R)_2CdBr_4$·DMSO and (R)CdI_3(DMSO). A direct comparison with PLQY values for other hybrid halides of group 12 metals cannot be made due to the apparent lack of in-depth investigations of their light emission properties. However, our recent study on $(CH_3NH_3)_2CdX_4$ (X = Cl, Br, I)[306] reports that these compounds do not luminesce at room temperature, which seems to confirm the validity of the strategy of using bulky luminescent

organic cations to create 0D structures with molecular organic and inorganic ions in order to prepare room-temperature luminescent hybrid halides as employed in this work.

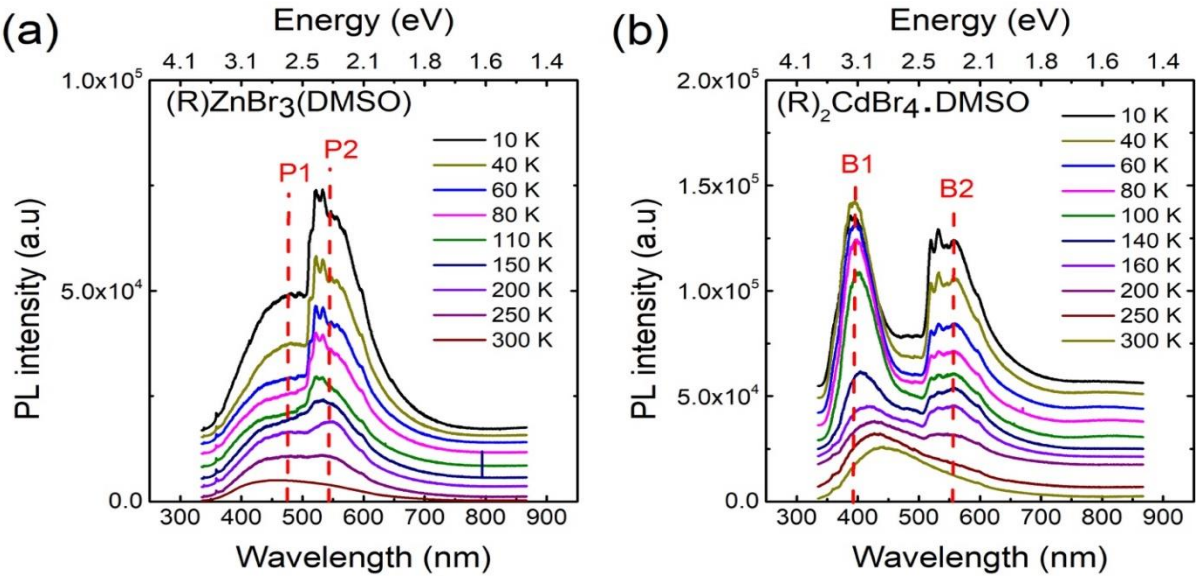


Figure 37. Temperature dependence of PL spectra measured for (a) $(R)ZnBr_3(DMSO)$ and (b) $(R)_2CdBr_4{\cdot}DMSO$ under 325 nm irradiation.

To get further information about the thermally-activated processes and the origin of the broadband emission, we measured the temperature dependence PL spectra for two of the more stable compounds in this family, $(R)ZnBr_3(DMSO)$ and $(R)_2CdBr_4{\cdot}DMSO$, under 325 nm laser excitation (Figures 37a and b). Significant temperature-dependent changes were revealed. For both Zn-based and Cd-based compounds, the room temperature PL spectrum shows the presence of only one broad band, denoted as P1 and B1 in Figures 37a and b for $(R)ZnBr_3(DMSO)$ and $(R)_2CdBr_4{\cdot}DMSO$, respectively. Upon cooling, additional PL peaks (denoted as P2 for $(R)ZnBr_3(DMSO)$ and B2 for $(R)_2CdBr_4{\cdot}DMSO$ emerge at around 550 nm. These peaks split into multiple sub-bands bellow 200 K. The splitting of PL peaks is often observed in organic-inorganic hybrid materials and may originate from the presence of free-

and bi-excitons,[115] free-excitons and excitons-phonon interactions,[88] free and bound excitons,[359] or could even result from the presence of structural phase transitions often observed in these hybrid materials. The latter possibility is ruled out in the present case by our room temperature and 100 K single crystal X-ray diffraction measurements suggesting the absence of structural phase transitions in the 100-300 K range.[388-390] In the present case, very similar thermal behavior was observed for (R)$ZnBr_3$(DMSO) and for $(R)_2CdBr_4$·DMSO, which suggests that the appearance of additional low temperature PL peaks could results from the emission of the organic cation.

Based on the temperature dependence PL data shown in Figure 37b, the thermal dependence of the integrated intensity, the FWHM, and the position of B1 PL band of $(R)_2CdBr_4$·DMSO was plotted in Figure 38. The quenching of the B1 peak could be described by the following Arrhenius-type model,[88]

$$I_{\mathrm{PL}} = \frac{I_0}{1 + a\ exp(\frac{-E_a}{k_{\mathrm{B}}T})} \tag{9}$$

where I_0 is the low-temperature PL intensity, k_{B} is the Boltzmann constant, T is the temperature, a is the ratio between the radiative and the nonradiative decay rates, and E_a is the activation energy. The best fit of the experimental data presented in Figure 37a, gives $I_0 = 9.2 \times 10^4 \pm 830$, $a = 76 \pm 8$ and $E_a = 48 \pm 4$ meV. This activation energy presents a good agreement with those reported in similar organic-inorganic hybrid materials such as $(C_6H_{11}NH_3)_2PbBr_4$[108] and $(C_6H_{11}NH_3)_2CdBr_4$.[85] Moreover, the remarkable broadening of B1 PL peak as a function of temperature (Figure 38b) can be attributed to exciton-phonon interactions, described within the following law, [391]

$$\Gamma(\mathrm{T}) = \Gamma_0 + \Gamma_{\mathrm{AC}} \times T + \frac{\Gamma_{LO}}{\exp\left(\frac{E_{\mathrm{LO}}}{k_{\mathrm{B}}T}\right) - 1} \tag{10}$$

where the first term represents the natural line width at 0 K, the second term is the broadening induced by acoustic phonons, and the third term corresponds to the contribution of optical phonons to the peak broadening. The best fit parameters yield $\Gamma_0 = 440 \pm 38$ meV, $\Gamma_{\mathrm{AC}} = 0.76 \pm 0.03$ meV.K^{-1}, $\Gamma_{\mathrm{LO}} = 22 \pm 4$ meV, and $E_{\mathrm{LO}} = 16 \pm 2$ meV. Once again, these values are in good agreement with those reported in organic-inorganic hybrid materials such as $(C_6H_{11}NH_3)_2CdBr_4$[85] as those of the inorganic perovskite $CsCdBr_3$,[392] and $CdBr_2$ crystals.[393] On the other hand, the B1 PL peak of $(R)_2CdBr_4$·DMSO shows a continuous red shift as a function of temperature (Figure 38c), which is usually the case for excitonic PL peaks accompanied with a clear regime change around 150 K. This is attributed to the impact of the appearance of the B2 PL peak at low temperature, which may cause a competition in the recombination process between B1 and B2 PL bands.

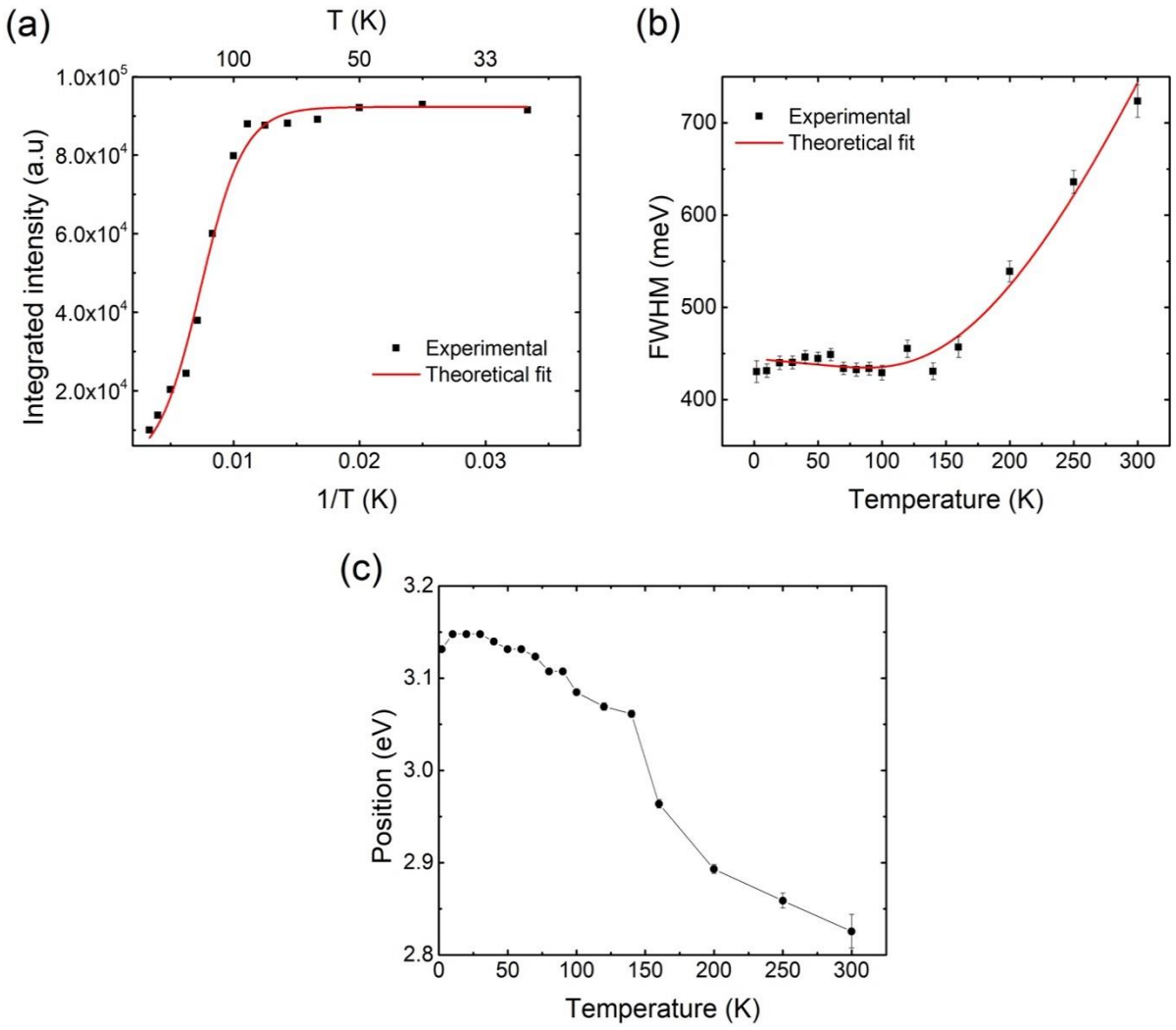


Figure 38. Temperature dependence of (a) the integrated intensity, (b) FWHM, and (c) the position of the B1 peak of $(R)_2CdBr_4 \cdot DMSO$ obtained from the PL spectra showed in Figure 37. The red lines in (a) and (b) are the best fit of the experimental data according to Eqns 9 and 10, respectively.

3.6 First-principle Calculations

Electronic band structure calculations were performed in order to further investigate the optical properties of the compounds prepared in this work. Figure 39 displays the electronic band structures and DOS plots for $(R)ZnBr_3(DMSO)$, $(R)_2CdBr_4 \cdot DMSO$ and $(R)CdI_3(DMSO)$, which show the PBE-calculated band gaps of 3.82 eV, 3.61 eV and 3.39 eV, respectively.

Although the PBE band gaps are typically underestimated and do not take into account the exciton binding energies, the trend of the calculated band gaps is consistent with that of the exciton excitation energies, which are 3.21 eV for (R)$ZnBr_3$(DMSO), 3.11 eV for $(R)_2CdBr_4$·DMSO, and 2.79 eV for (R)CdI_3(DMSO). All three compounds show small dispersion for the electronic bands near the band gap, indicating that these bands are made up of highly localized electronic states. The band gaps of these compounds are slightly indirect. The VBM and the CBM are located at the Γ and the Y points, respectively, for (R)$ZnBr_3$(DMSO), at the N and the Γ points for $(R)_2CdBr_4$·DMSO, and at the Z and the Γ points for (R)CdI_3(DMSO). In luminescent 0D hybrid Sn and Pb based halides, the inorganic Sn/Pb-halide clusters are usually the luminescent centers due to their relatively small energy gaps of the inorganic substructures compared to those of organic molecules.[368, 370, 377] The low energy gaps of the inorganic substructures in such cases are ensured by the relatively small electronegativity difference between Sn/Pb and halogen elements, which results in valence bands dominated by halogen orbitals and conduction bands primarily made of metal orbitals. In principle, the band alignment in hybrid halides can be altered by (1) combining pairs of metal and halogen elements with large electronegativity difference to accommodate organic molecules' frontier orbitals, or (2) by utilizing low-gap aromatic molecular cations. The hybrid metal halides studied in this work feature electropositive metals Zn and Cd[251] and an aromatic organic cation, yielding unusual band alignments at the organic-inorganic interface.[289] The DOS plots in Figure 39 show that (R)$ZnBr_3$(DMSO) exhibits the type I band alignment with its valence band maximum (VBM) and conduction band minimum (CBM) derived from the bonding and the antibonding π-orbitals of the aromatic molecule cations, while $(R)_2CdBr_4$·DMSO and (R)CdI_3(DMSO) display the type II band alignment with the VBM and

the CBM containing π-orbitals of the organic cations and the metal-s orbitals of the inorganic anions, respectively.

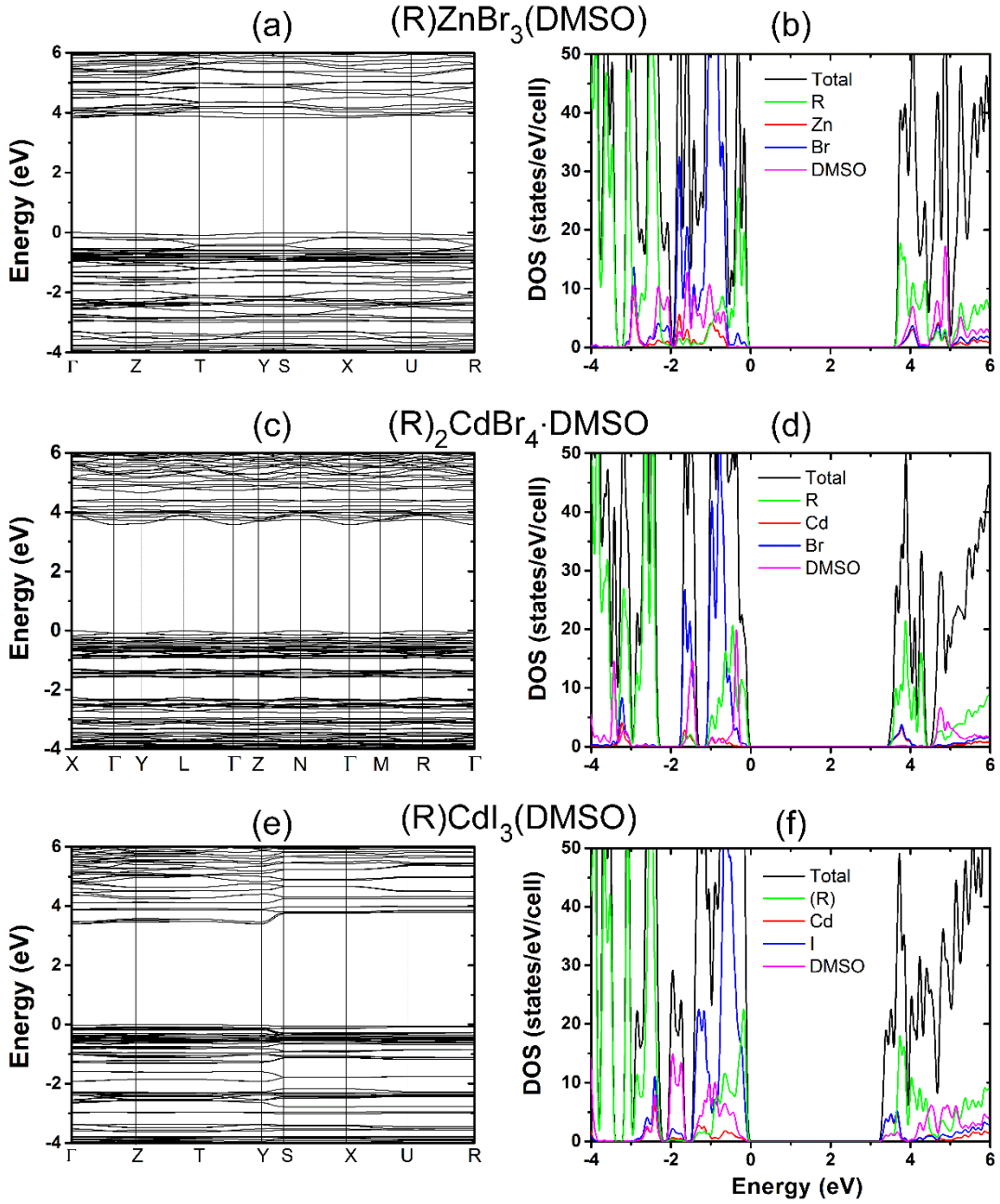


Figure 39. Band structures and density of states (DOS) plots for (a-b) (R)$ZnBr_3$(DMSO), (c-d) (R)$_2CdBr_4$·DMSO and (e-f) (R)CdI_3(DMSO).

It is, thus, expected that the optical emission from (R)$ZnBr_3$(DMSO) is due to the excitons localized on the organic molecular cations. Although the ground-state band structures of $(R)_2CdBr_4$·DMSO and (R)CdI_3(DMSO) show the type II band alignment, the lowest unoccupied molecular orbital of the molecular cation is close to the CBM as shown in Figure 39d and 8f. The strong Coulomb binding could localize the exciton at the organic cation, in analogy to the case of $(Ph_4P)_2SbCl_5$, in which the exciton is localized at the $SbCl_5$ cluster despite that the ground-state band structure shows the type II band alignment at the organic-inorganic interface.[368] The fast decay of the luminescence in the three hybrid metal halides as shown in Figure 35 (9 ns - 21 ns) are consistent with the fast emission from the π-conjugated organic molecules (decay times ranging from a few ns to a few tens of ns);[394] thus, supporting the attribution of the excitonic emission in these hybrid halides to the organic molecules. In comparison, an exciton that is localized at the inorganic metal halide cluster in hybrid metal halides usually has the lifetime on the order of μs.[143, 368, 370] Figure 40 shows the hole and the electron wavefunctions of an exciton in (R)$ZnBr_3$(DMSO), which is optimized by the PBE0 hybrid functional calculation. It can be seen that the exciton is indeed localized on the π-orbitals of the C_6 ring in the molecular cation, which, thus, should act as a luminescent center.

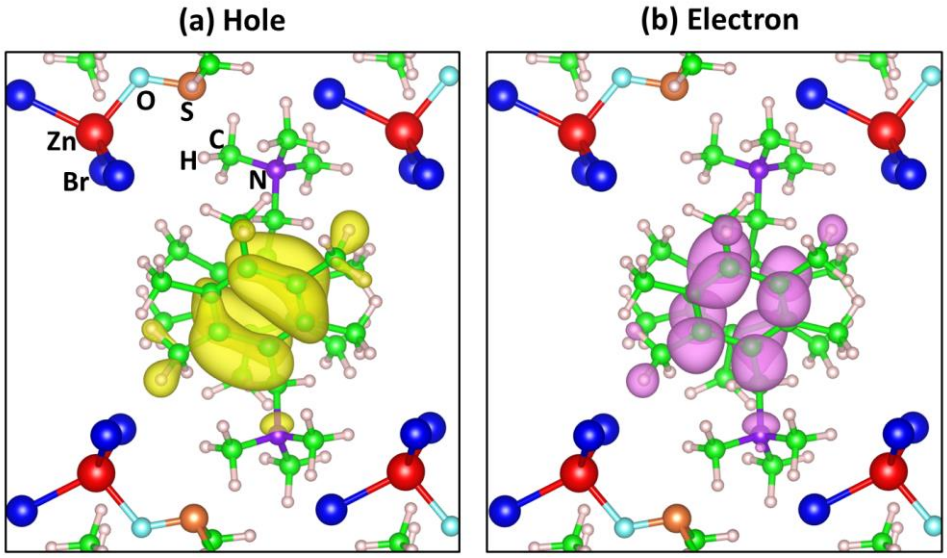


Figure 40. Partial density contours of the hole (a) and the electron (b) in a relaxed exciton in (R)$ZnBr_3$(DMSO).

3.7 Conclusion

In summary, we report the preparation, crystal and electronic structures, and optical properties of three new hybrid organic-inorganic halides of group 12 metals. Due to the presence of the bulky organic $(R)^+$ cation, all compounds form 0D crystal structures featuring alternating layers of isolated inorganic anions based on metal tetrahedra and organic cations. The separation of the crystal structure into distinct inorganic and organic molecular units leads to flat bands near the band gap indicative of the highly localized electronic states. Furthermore, the 0D molecular structures allow for the localization of the excitons on either anionic or cationic molecular units depending on their chemistries. Thus, based on our computational work, the excitons are localized on the organic molecular cation in (R)$ZnBr_3$(DMSO), suggesting a rare example of light emission from the organic component of hybrid organic-inorganic materials.[17, 108, 212, 395] The computational results are supported by the PL

measurements including the measured fast decay of the luminescence (9 ns - 21 ns), which is consistent with the fast emission from the π-conjugated organic molecules.

The compounds exhibit broadband emission ranging from bluish-white to white to green light depending on the choice of the halide and metal cations. The luminescence properties derive from the intricacies of their crystal and electronic structures (e.g., packing of the organic cations). Temperature dependence of PL measurements showed the emergence of additional peaks around 550 nm at lower temperatures, attributed to the organic salt emission. For $(R)_2CdBr_4 \cdot DMSO$ an excitonic activation energy $E_a \sim 50$ meV was estimated from the thermal dependence of the intensity of B1 PL peak showing a good agreement with Cd-based organic-inorganic hybrid materials.

The 0D crystal structures designed in this work demonstrate a luminescence efficiency with PLQY values up to 3.07% for the white-light emitting $(R)ZnBr_3(DMSO)$, which also happens to be the most stable (thermally and in air) member of the family. The combinations of the organic cation and inorganic components used in this work, therefore, are responsible for the preparation of room-temperature luminescent materials that have comparable or better PLQY values to other Pb-based and Cd-based hybrid halides reported in literature. Importantly, this work paves the way to band alignment engineering of organic and inorganic components in hybrid organic-inorganic halides to controllably create type I and type II band alignments, and to fabricate materials where the emission originates from organic, inorganic or both components. The fast emission from the hydrogen-rich organic cations, observed for the compounds prepared in this work, may enable the development of fast scintillators that are capable of detecting fast neutrons via proton *recoil*.

Chapter 4: Low-Dimensional All-Inorganic Copper Halides $Cs_3Cu_2X_5$ and $CsCu_2X_3$ (X = Cl, Br, I)

4.1 Introduction

Human productivity has soared since the introduction and integration of electrical lighting almost 90 years ago.[396] According to the U.S. Energy Information Administration, 21% of all energy consumed in the U.S. in 2017 was from lighting, with the U.S. using 13 times more electricity than in 1950 (Source: U.S. Energy Information Administration (Oct 2018)). Thus, to lower the lighting related electricity usage, more efficient lighting technology is needed.[396] To achieve this goal, new highly efficient luminescent phosphors of all colors will be needed to address the current technology's deficiencies.

Of the current luminescent materials being considered in literature, lead halides have been shown to exhibit desirable highly tunable emission properties needed to successfully incorporate into practical applications. [7, 397]Recently, their successful incorporation in light emitting diode (LED) devices exceeding 20% external quantum efficiency (EQE) is evidence to their outstanding potential in this area.[398] However, there is still room for growth as this efficiency is still far below that of LEDs made from organic[399] and inorganic quantum dots.[400] One route for advancing the hybrid halide materials technology is by replacing lead halides with nontoxic halides that have lower dimensional structures, such as one- (1D) chains and/or zero-dimensional (0D) clusters.[401]. This is because such dimensionally-reduced materials contain spatially isolated molecular cations and metal-halide anion polyhedra that create quantum well-like structures, which cause the generation and isolation of excitons (bound electron and hole pairs) to a much greater degree than their three-dimensional (3D) counterparts. A higher degree of exciton formation will result in the higher luminescent yields

needed for use in devices.[27, 77] Lowering dimensionality can also can provide an increase in exciton binding energy not typically found within 3D halides; for instance, the 3D $CsPbBr_3$ has an exciton binding energy of 18 meV,[402] whereas the 0D $Cs_3Sb_2I_9$ exhibits a one order of magnitude higher exciton binding energy of 175 meV.[403] Recently, a number of blue emitting hybrid organic-inorganic lead halide perovskites like $(C_6H_5CH_2NH_3)_2PbBr_4$[130] and $(C_4N_2H_{14})PbBr_4$,[73] and all-inorganic halides like $Cs_3Sb_2Br_9$[404] were reported with high photoluminescence quantum yields (PLQY) (Table 5). By comparison, it can be seen that reduction of the structural dimensionality generally results in the increase of PLQY, although though there is an added effect of chemical composition variation that cannot be ignored.

Table 5. Comparison of blue-light emitting solid systems.

Material	**Structure Type**	**PLQY (%)**	**Measurement Method**	**Ref.**
$(CH_3NH_3)PbCl_3$	3D perovskite crystals	< 1	Integration sphere	[362]
$(C_6H_5CH_2NH_3)_2PbBr_4$	2D perovskite exfoliated crystals	79	Integration sphere	[130]
$Cs_3Sb_2Br_9$	2D quantum dots in solution	46	Integration sphere	[404]
$(C_4N_2H_{14})PbBr_4$	1D perovskite multiple crystals	20	Integration sphere	[73]
$CsPbClBr_2$	0D quantum dots in solution	70	Integration sphere	[405]
$Cs_3Cu_2I_5$	0D single crystal	91	Integration sphere	[183]
$Cs_3Cu_2Br_{5-x}I_x$ $(0 \leq x \leq 5)$ x = 5 x = 3.75 x = 2.5 x = 1.25 x = 0	0D single crystals	 98.71 ± 0.047 60.36 ± 0.045 55.15 ± 0.036 53.80 ± 0.038 50.07 ± 0.035	Integration sphere	This work

Copper possesses excellent attributes such as low toxicity, low cost, and earth abundance, making it an ideal candidate for use in modern technology from superconducting magnets and electrical wiring to W-LEDs.[406-407] Despite these advantages, very few all-inorganic Cu-halide-based families have been studied for luminescence purposes. Binary copper halides do not appreciably emit at room temperature due to the rapid thermal quenching within their 3D structures. Based on the impact of the dimensional reduction observed in lead halides, we hypothesized that through the addition of a large cation such as Cs^+, the 3D binary halide structure could be dimensionally reduced, as illustrated by the known dimensionalities of different the CsX-CuX (X = Cl, Br, I) families shown in Table 6, and appreciable room temperature emission could be achieved.

Table 6. Low-dimensional compounds in the pseudo-binary CsX-CuX system.[408]

Family	Space Group	Type	Dimensionality
$CsCuX_3$	$P6_122$	Perovskite	1D
$CsCu_2X_3$	*Cmcm*	Non-perovskite	1D
Cs_2CuX_4	*Pnma*	Non-perovskite	0D
$Cs_3Cu_2X_5$	*Pnma*	Non-perovskite	0D

In this chapter, we present the results of our in-depth studies of $Cs_3Cu_2X_5$ and $CsCu_2X_3$ which exhibit low-dimensional crystal structures. Based on our results, both families are remarkably stable under ambient conditions (air/moisture) and demonstrate relatively higher thermal stability as compared to some known lead halide materials. Importantly, confirming our initial hypotheses, visibly bright tunable (blue, green and yellow) room temperature emission with high PLQY values up to 98% (for $Cs_3Cu_2I_5$) are observed. We attribute the physical mechanism of luminescence in these materials to self-trapped excitons (details in **Sections 4.2 and 4.3**). The development of highly efficient, nontoxic and earth-abundant all-inorganic halides with light emitting materials such as $Cs_3Cu_2Br_5$ and $Cs_3Cu_2I_5$ represents a

major step forward in bringing the next generation solid-state lighting technologies to marketplace.[131]

4.2 The $Cs_3Cu_2X_5$ (X= Br, I) System

4.2.1 Introduction

Historically, the development of solid-state blue emitters has significantly lagged behind that of red and green, which severely hampered the development of white-light LEDs (WLED).[279] The rarity of blue emission makes the number of hybrid organic-inorganic lead halide perovskites such as $(C_6H_5CH_2NH_3)_2PbBr_4$[130] and $(C_4N_2H_{14})PbBr_4$[73] have been reported to demonstrate blue emission with high photoluminescence quantum yields (PLQY) quite remarkable. Whilst significant progress has been made in the development of efficient blue-emitting lead halides, these materials continue to suffer from lead toxicity and poor thermal and air stability.

Other means of producing more efficient room-temperature blue emitters could be done through guided material design of nontoxic halides with zero-dimensional (0D)[401] crystal structures. Lowering the dimensionality would provide an increase in exciton binding energy not typically found within 3D halides. For instance, 3D $CsPbBr_3$ has an exciton binding energy of 18 meV,[402] whereas the 0D $Cs_3Sb_2I_9$ exhibits a one order of magnitude higher exciton binding energy of 175 meV.[403] Copper possesses excellent attributes such as low toxicity, low cost and earth abundance, making it an ideal candidate for use within materials used for the ubiquitous WLED.

$Cs_3Cu_2Br_{5-x}I_x$ ($0 \leq x \leq 5$) were synthesized via solid-state synthesis and exhibit bright blue emission under UV irradiation with maximum photoluminescence (PL) emission ranging

from 443 to 456 nm, full-width at half-maximum (FWHM) values ranging from 75 to 98 nm, and PLQY values ranging from 50.1% ($Cs_3Cu_2Br_5$) to 98.7% ($Cs_3Cu_2I_5$). Power-dependent PL measurements supported by DFT calculations suggest that the emission results from self-trapped excitons (STE).

4.2.2 Synthesis and Methods of $Cs_3Cu_2X_5$ (X = Br, I)

4.2.2.1 Reagents Used in the Synthesis of $Cs_3Cu_2X_5$ (X=I, Br)

Chemicals utilized in this study were used as purchased: (i) copper(I) bromide, 99.999%, Aldrich; (ii) copper iodide, 99.9%, Aldrich; (iii) cesium bromide, 99.9%, Acros Organics; (iv) cesium iodide, 99.999%, Acros Organics. Polycrystalline powder of $Cs_3Cu_2Br_5$ and $Cs_3Cu_2I_5$ were prepared by reacting a 3:2 stoichiometric ratio of CsX:CuX reactants.

4.2.2.2 Synthesis of $Cs_3Cu_2X_5$ (X=I, Br)

The alloyed $Cs_3Cu_2Br_{5-x}I_{5x}$ compositions were synthesized using stoichiometric amounts of required binary halide reactants. To ensure the homogeneity of all studied compounds, respective reactants were ground multiple times under inert atmosphere, pelletized to ensure no loss of reactants, and then sealed in evacuated quartz ampules. Reaction mixtures were then annealed at 400 ˚C for 12 hrs and slowly cooled to room temperature over a period of 21 hrs.

4.2.2.3 Powder X-Ray Diffraction

Powder X-ray diffraction (PXRD) measurements were performed on a Rigaku MiniFlex600 system with a D/tex detector using a Ni-filtered Cu-Kα radiation source. All scans were performed, at room temperature, in the 5-90˚ (2θ) range, with a step size of 0.2˚. Data analysis was performed using Rigaku's PDXL2 software package. The collected PXRD data

was corrected for glass slide background and fitted using the decomposition method (also known as the Pawley fitting method) using the embedded software in Rigaku's PDXL2 software package. For air stability testing, PXRD was performed by leaving the representative compounds out in the ambient air for over a period of a month and periodically scanning the same sample with PXRD.

4.2.2.4 Thermal Analysis

Simultaneous thermogravimetric analysis (TGA) and differential scanning calorimetry (DSC) measurements were carried out on a TA Instruments SDT650 unit. Measurements were done in 90 µL alumina crucibles on 10-11 mg samples under a 100 mL/min flow of nitrogen in the 25 – 475 °C range with 5 °C/min heating rate.

4.2.2.5 Optical Measurements

Photoluminescence excitation (PLE), emission, and PLQY measurements were performed, at ambient temperature, using a HORIBA Jobin Yvon Fluorolog-3 spectrofluorometer using a Xenon lamp and Quanta-φ integrating sphere. PLQY data were analyzed using the two-curve method in a varied range from 280 – 800 nm. Care was taken to avoid any appearance of or interference from primary and secondary overtones from the source lamp as the measurements were taken. For power dependence PL measurements, we used 325 nm line of He-Cd laser (Kimmon Electric HeCd dual-wavelength laser; model: IK552R-F). The PL spectra was collected and dispersed in a Princeton Instruments PIXIS-eXcelon silicon CCD.

4.2.2.6 First Principle Calculations

All calculations were based on density functional theory (DFT) implemented in the VASP code.[229] The interaction between ions and electrons was described by projector augmented wave method.[323] The kinetic energy cutoff of 295 eV for the plane-wave basis was

used for all calculations. Experimental lattice parameters of $Cs_3Cu_2X_5$ (X = Br, I) were used while the atomic positions were fully relaxed until the residual forces were less than 0.02 eV/Å. Electronic band structures, density of states (DOS), as well as exciton properties were calculated using the hybrid PBE0 functional,[228] which includes 25% non-local Fock exchange. Previous PBE0 calculations have provided accurate results in exciton excitation and emission energies in hybrid organic-inorganic halide perovskites.[77, 156, 409-410]

Following the Franck-Condon principle, the exciton excitation and emission energies were obtained by calculating the total energy differences between the excited and the ground states using PBE0-optimized ground-state and excited-state structures, respectively. A spin-singlet exciton was considered when calculating the excitation energy because this is a spin-allowed transition while a spin-triplet exciton was considered for calculating the emission energy because the spin-triplet exciton is more stable than the spin-singlet one.

4.2.3 Structure of $Cs_3Cu_2X_5$ (X = Br, I)

Crystal structures[411-412] and phase diagrams[413-414] of $Cs_3Cu_2Br_5$ and $Cs_3Cu_2I_5$ were previously reported in literature. Both compounds are isostructural and crystallize in the orthorhombic space group *Pnma*[231] with unit cell parameters a = 9.601(5) Å, b = 10.965(1) Å, and c = 13.634(9) Å and a = 10.170(6) Å, b = 11.649(3) Å, and c = 14.360(6) Å for $Cs_3Cu_2Br_5$ and $Cs_3Cu_2I_5$, respectively (Table 7 lists the PXRD refinement results for all $Cs_3Cu_2Br_{5-x}I_x$ ($0 \leq x \leq 5$) presented in this section). The 0D $Cs_3Cu_2X_5$ structures contain unique $[Cu_2X_5]^{3-}$ dimers made of a trigonal planar CuX_3 sharing an edge with a tetrahedral CuX_4 unit, all surrounded by Cs^+ (Figure 41). To the best of our knowledge, the dimeric $[Cu_2X_5]^{3-}$ cluster has not been reported in any other copper halide compounds. Instead, other known 0D copper halides feature

clusters such as the edge-sharing ditrigonal planar units found in $[N(C_2H_5)_4]_2Cu_2Br_4$[415] and the edge-sharing ditetrahedral units found in $(C_8H_{14}N_2)_2Cu_2Br_6$.[416] The dimeric clusters are the most probable bonding model in this ionic structure type compared to the possible formation of ditetrahedral clusters for two reasons: the bond distance between the Cu and adjacent halide in question and the lack of distortion in the trigonal planar moiety. Foremost, the distance between the trigonal planar Cu and the capping tetrahedrally coordinated halide (~ 3.7 Å) needed to form a ditetrahedral cluster is much too large, especially in reference to the Shannon ionic radii of copper and halogen elements ($r(Cu^+)$ = 0.6 Å, $r(Br^-)$ = 1.96 Å, $r(I^-)$ = 2.2 Å).[417] Secondly, in the trigonal planar $CuBr_3$ and CuI_3 units, out-of-plane distortion toward the capping halide is minimal based on the crystal structures.

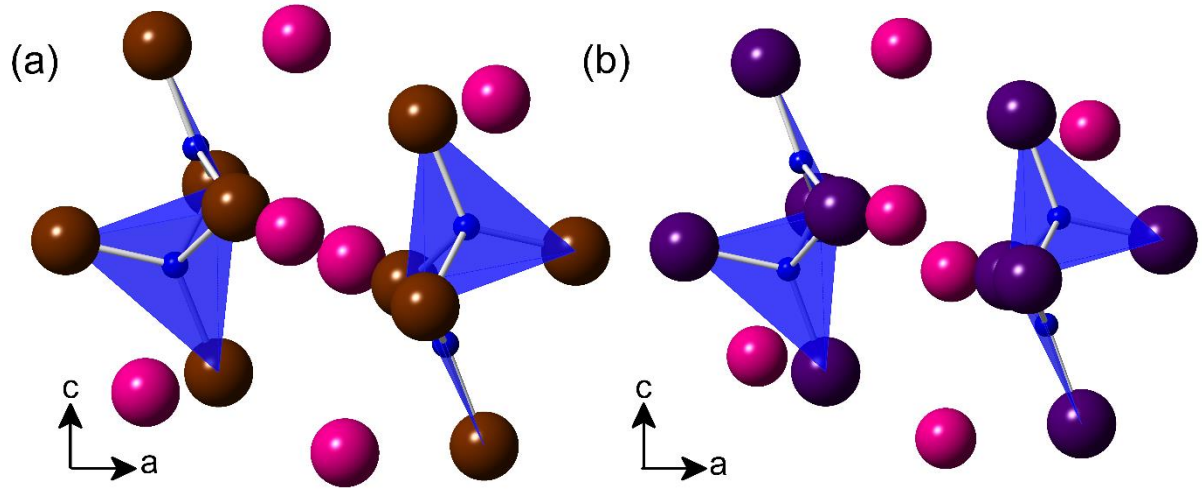


Figure 41. Crystal structures of (a) $Cs_3Cu_2Br_5$ and (b) $Cs_3Cu_2I_5$. Cs, Cu, Br and I atoms are shown in pink, blue, maroon, and purple, respectively.

Interestingly, these structural considerations have not been discussed in a previous study on $Cs_3Cu_2I_5$, which attributes the observed large Stoke-shifted emission to the Jahn-Teller distortion of Cu tetrahedral site.[130] Notwithstanding the fact that the Jahn-Teller effect is weak

for tetrahedral geometry, Cu^{+} with d^{10} electronic configuration is not Jahn-Teller active. In addition, as mentioned above, the structure is more accurately described as a $Cu_2X_5^{3-}$ made of a tetrahedral and trigonal planar Cu halide unit, rather than two Jahn-Teller distorted tetrahedra. In $Cs_3Cu_2Br_5$ angles close to ideal tetrahedral angles (109.5°) are present along with the larger angle of 125.22° between Br3-Cu2-Br4 and slightly smaller at 105.22° between Br1-Cu2-Br3.[411] Within the trigonal planar portion of the Cu_2Br_5 cluster, all angles are very close (119.42°) to the ideal trigonal planar angle of 120°.[411] In $Cs_3Cu_2I_5$, distortions can be seen in the tetrahedral part of the $Cu_2I_5^{3-}$ cluster with the largest I3-Cu2-I4 angle of 122.31° and the smallest I1-Cu2-I3 angle of 103.64°.[412] In the trigonal planar portion of the $Cu_2I_5^{3-}$ cluster, all angles are close to the ideal 120°.[412]

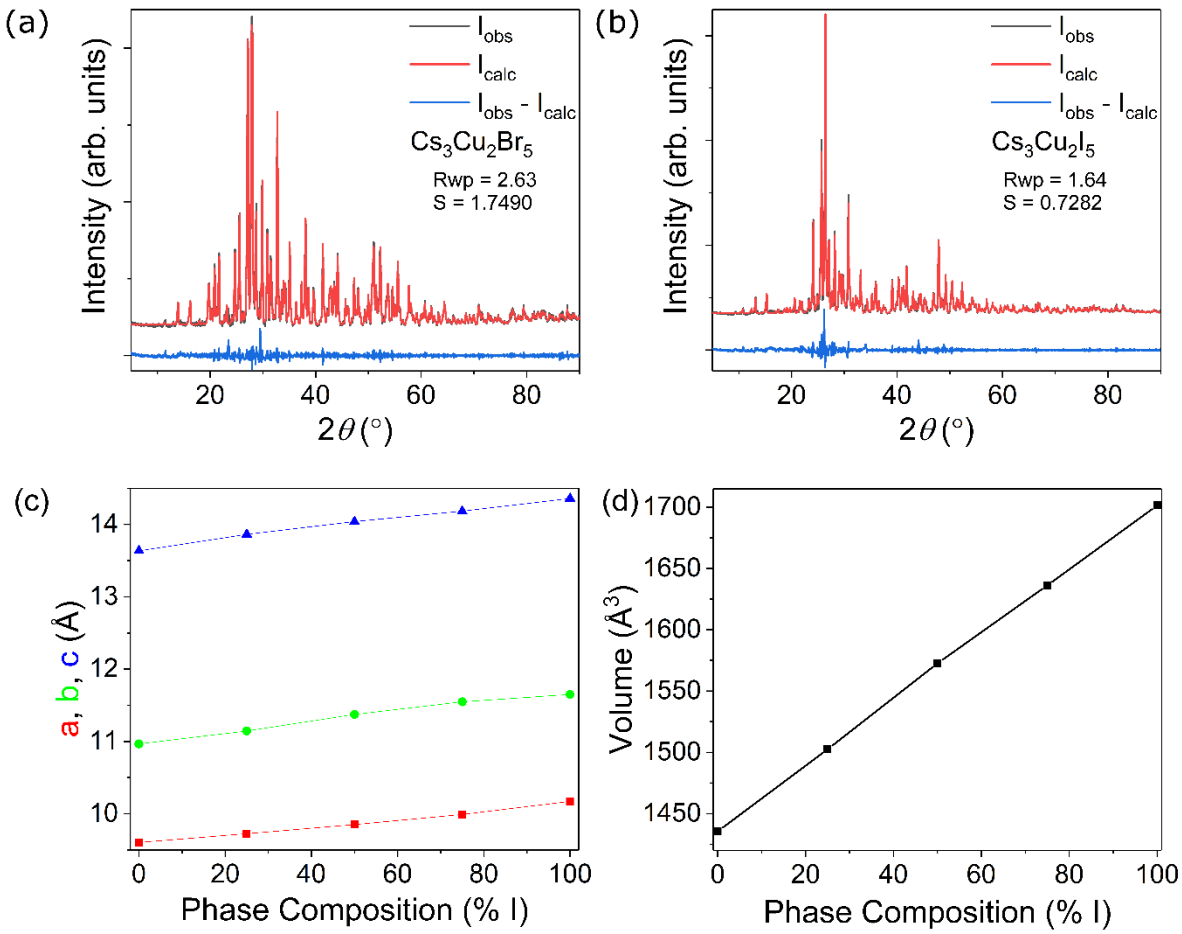


Figure 42. Room temperature experimental PXRD patterns (black lines) of (a) $Cs_3Cu_2Br_5$ and (b) $Cs_3Cu_2I_5$ with Pawley fits (red lines) and resulting difference maps (blue lines). (c) The refined lattice parameters and (d) unit cell volume are shown as a function of I content. PXRD patters with fittings can be found in **Appendix 1** in Figures A1.14 and A1.15.

Details of the preparation of $Cs_3Cu_2Br_{5-x}I_x$ ($0 \leq x \leq 5$) can be found in **Appendix 2**. Whilst the bulk compounds can be prepared using both solution[183] and solid-state synthesis techniques, the sample quality as judged by phase purity from powder X-ray diffraction (PXRD) measurements is higher when using the solid-state technique. Attempts were made to synthesize $Cs_3Cu_2Cl_5$, however a pure phase product could not be obtained through either solid-state or solution synthesis. Instead, according to PXRD analysis, $CsCu_2Cl_3$ and Cs_2CuCl_4 form

with only trace amounts of $Cs_3Cu_2Cl_5$. For this reason, only the $Cs_3Cu_2Br_{5-x}I_x$ ($0 \leq x \leq 5$) are considered herein. In addition to the phase purity shown in Figure 42a-b, the measured PXRD patterns confirm the solid solution behavior in the $Cs_3Cu_2Br_{5-x}I_x$ series. As shown in Figures 42c-d, the unit cell parameters and volume follow Vegard's law as a function of iodide concentration.

Table 7. PXRD refinement results for all $Cs_3Cu_2Br_{5-x}I_x$ ($0 \leq x \leq 5$) along with R_{wp} and S values.

Composition	***a* (Å)**	***b* (Å)**	***c* (Å)**	***V* (Å^3)**	**R_{wp} (%)**	**S**
$Cs_3Cu_2Br_5$	9.601(5)	10.965(1)	13.634(9)	1435.5(06)	2.63	1.7490
$Cs_3Cu_2Br_{3.75}I_{1.25}$	9.724(2)	11.144(1)	13.864(0)	1502.4(4)	2.36	1.5378
$Cs_3Cu_2Br_{2.5}I_{2.5}$	9.849(0)	11.372(6)	14.039(8)	1572.6(2)	3.84	2.3322
$Cs_3Cu_2Br_{1.25}I_{3.75}$	9.989(6)	11.547(3)	14.184(2)	1636.18(15)	1.63	1.0071
$Cs_3Cu_2I_3$	10.170(6)	11.649(3)	14.360(6)	1701.44(11)	1.64	0.7282

4.2.4 Stability of $Cs_3Cu_2X_5$ (X = Br, I)

Of practical importance are the thermal and air stability of materials for optical and electronic applications. In fact, along with the presence of toxic Pb, poor ambient condition stability of the photovoltaic hybrid organic-inorganic lead perovskites remains a major barrier for its industrial-scale implementation.[19] In contrast, all-inorganic compositions are expected to exhibit higher stability owing to the lack of volatile organic molecules[418-419] and less number of phase transitions compared to hybrid structures that undergo changes due to the temperature-dependent motion of the organic cations.[20] Thus to better elucidate the stability of $Cs_3Cu_2Br_{5-x}I_x$, we monitored the ambient stability of the end member phases through PXRD over a period of one month and found no significant changes for $Cs_3Cu_2Br_5$ (Figure 43a). However, as seen in Figure 43b, a few noticeable changes occur in the $Cs_3Cu_2I_5$ phase as it begins losing intensity

in the lower angle region and the small peaks at 7° and 10° disappear after 2 weeks of ambient exposure. The higher stability of the bromide analog compared to the iodide is consistent with literature reports of decreasing stability of halides going down the halogen group.[2, 420]

The results of thermal analysis studies of $Cs_3Cu_2Br_{5-x}I_x$ are summarized in Figure 44. The TGA results suggest little to no mass loss upon heating to 475 °C. In contrast, Pb- and Sn-based halides such as PEA_2PbI_4 (PEA = phenethylammonium cation) and Cs_2SnI_6 show significant weight losses below 300 °C consistent with their decomposition into volatile components.[421-422] Similar issues are seen with hybrid organic-inorganic perovskites with $MAPbBr_3$ decomposing at 176 °C,[177] $FASnI_3$ decomposing at 100 °C, and $FASnPbI_3$ decomposing at 150 °C.[423]

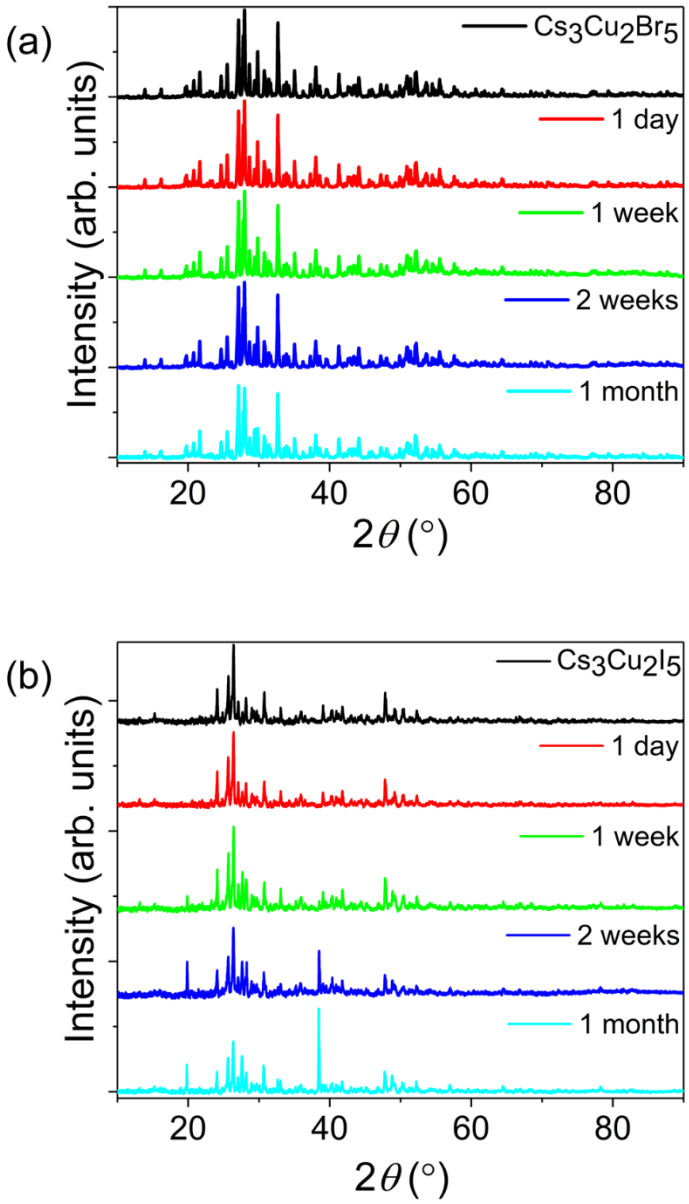


Figure 43. PXRD patterns of (a) $Cs_3Cu_2Br_5$ and (b) $Cs_3Cu_2I_5$ compounds left in ambient air for 1 month.

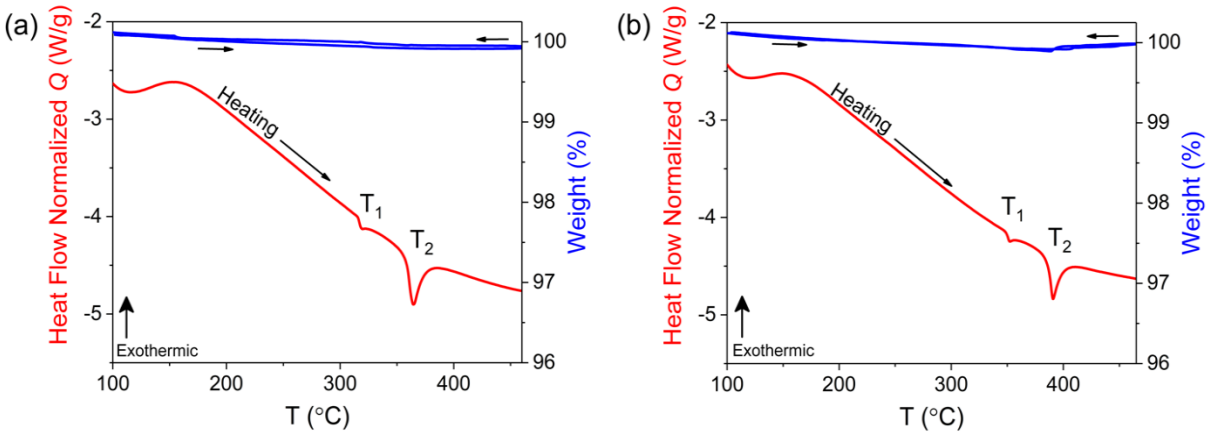


Figure 44. Tandem thermal gravimetric analysis (blue) and differential scanning calorimetry (red) TGA/DSC plots for (a) $Cs_3Cu_2Br_5$ and (b) $Cs_3Cu_2I_5$.

The DSC scans suggest that in both $Cs_3Cu_2Br_5$ and $Cs_3Cu_2I_5$, two different thermal events occur, which are labeled as T_1 and T_2 in the corresponding plots in Figure 44. According to the reported CuI-CsI phase diagrams, $Cs_3Cu_2I_5$ exhibits narrowly incongruent melting behavior at 390 °C, which is corroborated by the T_2 peak.[413] The T_1 feature is close to the eutectic isotherm at 350 °C, which is visible in CuI rich compositions in the reported phase diagram, however, we note that no CuI impurity was detected in our PXRD measurements, shown in Figure 45b. In the case of $Cs_3Cu_2Br_5$, this compound was not entered in the reported phase diagram, but the DSC scan provided in Figure 44a is consistent with the reported binary phase diagram.[414] Thus, $Cs_3Cu_2Br_5$ decomposes peritectically at 318 °C into liquid and $CsCu_2Br_3$ phases, and further melts at 364 °C producing CsBr. Indeed, small impurities of CsX appear in the PXRD after multiple heating and cooling cycles as shown in Figure 45a, especially for $Cs_3Cu_2Br_5$ which clearly supports the notion that it melts incongruently.

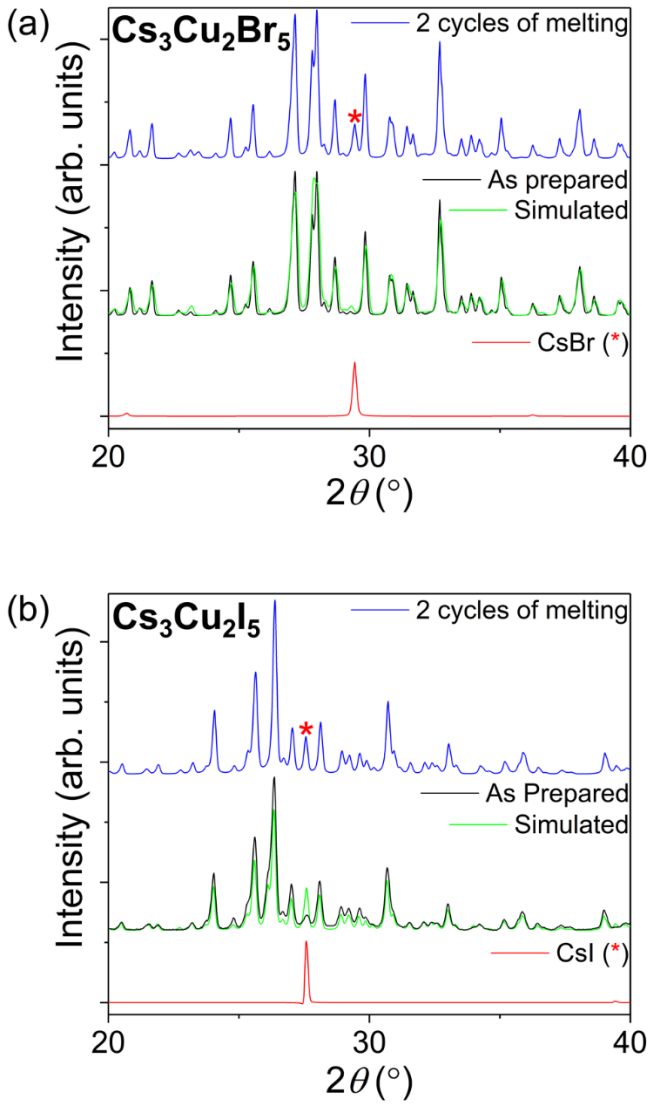


Figure 45. PXRD patterns of (a) $Cs_3Cu_2Br_5$ and (b) $Cs_3Cu_2I_5$ after 2 heating cycles over 545 °C. Asterisks denote CsX impurity phases resulting from incongruent melting of the phases.

4.2.5 Optical Properties of $Cs_3Cu_2X_5$ (X = Br, I)

Room temperature PL measurements for $Cs_3Cu_2Br_{5-x}I_x$ ($0 \leq x \leq 5$) are summarized in Figure 46 and Table 8. Under UV excitation, $Cs_3Cu_2Br_{5-x}I_x$ demonstrate intense blue emission with a PL peaks ranging from 443 nm to 455 nm. The PL peaks are broad with FWHM values increasing linearly from 75 nm for $Cs_3Cu_2Br_5$ to 99 nm for $Cs_3Cu_2I_5$. In contrast, narrower

emission was observed for some of the lead halide perovskites such $MAPbX_3$ for which the reported FWHM values are in the 20 – 32 nm range.[130] Nevertheless, the obtained FWHM values for $Cs_3Cu_2Br_{5-x}I_x$ are comparable to that of state-of-the-art blue organic[424] and inorganic phosphors.[130] The observed PL emission spectra are characterized by colors ranging from a lighter blue with Commission Internationale de l'Eclairage (CIE) Color Coordinates (*x*, *y*) of (0.15, 0.067) for $Cs_3Cu_2Br_5$ to a deeper blue (0.15, 0.048) for $Cs_3Cu_2I_5$ (Figure 46f). Interestingly, the PL emission peaks also demonstrate approximately linear blue shift going from 455 nm for $Cs_3Cu_2Br_5$ to 443 nm for $Cs_3Cu_2I_5$, contrary to the expectations based on electronegativity arguments assuming band-to-band emission. Indeed, our results indicate that the emission in this system is not due to band-to-band transitions but rather has STE origins (see below). The blue shift of PL emission going from bromide to iodide is also observed for binary copper halides CuBr and CuI. Thus, in both CuBr and CuI, the observed excitonic blue emission is characterized with a PL peak at 420 nm for CuBr,[425] and at 410 nm for CuI.[426] Bright excitonic emission in binary copper halides are typically observed at low temperatures, with CuCl being one of the first semiconductors found to exhibit biexcitons in both nanocrystal and bulk forms,[427] as well as being a model system for strong exciton-photon coupling.[428] The proximity in PL peak maximums of $Cs_3Cu_2Br_{5-x}I_x$ ($0 \leq x \leq 5$) to the binary halides suggests that the emission seen in the $Cs_3Cu_2Br_{5-x}I_x$ ($0 \leq x \leq 5$) solid solution originates from the copper halide clusters themselves, and that the isolation of $[Cu_2X_5]^{3-}$ molecular dimers leads to greater charge localization and stronger excitonic effects, ultimately providing highly efficient room temperature emission in $Cs_3Cu_2Br_{5-x}I_x$. In accordance with the visible intense blue emission clearly noticeable even with a naked eye, the measured PLQY values for $Cs_3Cu_2Br_{5-x}I_x$ ($0 \leq x \leq 5$), summarized in Table 3, are also among the record high observed for organic and inorganic

phosphors.[130] Thus, PLQY values increase linearly from 50.1% for $Cs_3Cu_2Br_5$ to 98.7% for $Cs_3Cu_2I_5$. Such high PLQY values, especially the observed near-unity PLQY value for the iodide member is unprecedented as most of the literature reported luminescent metal halides are either bromides or chlorides.

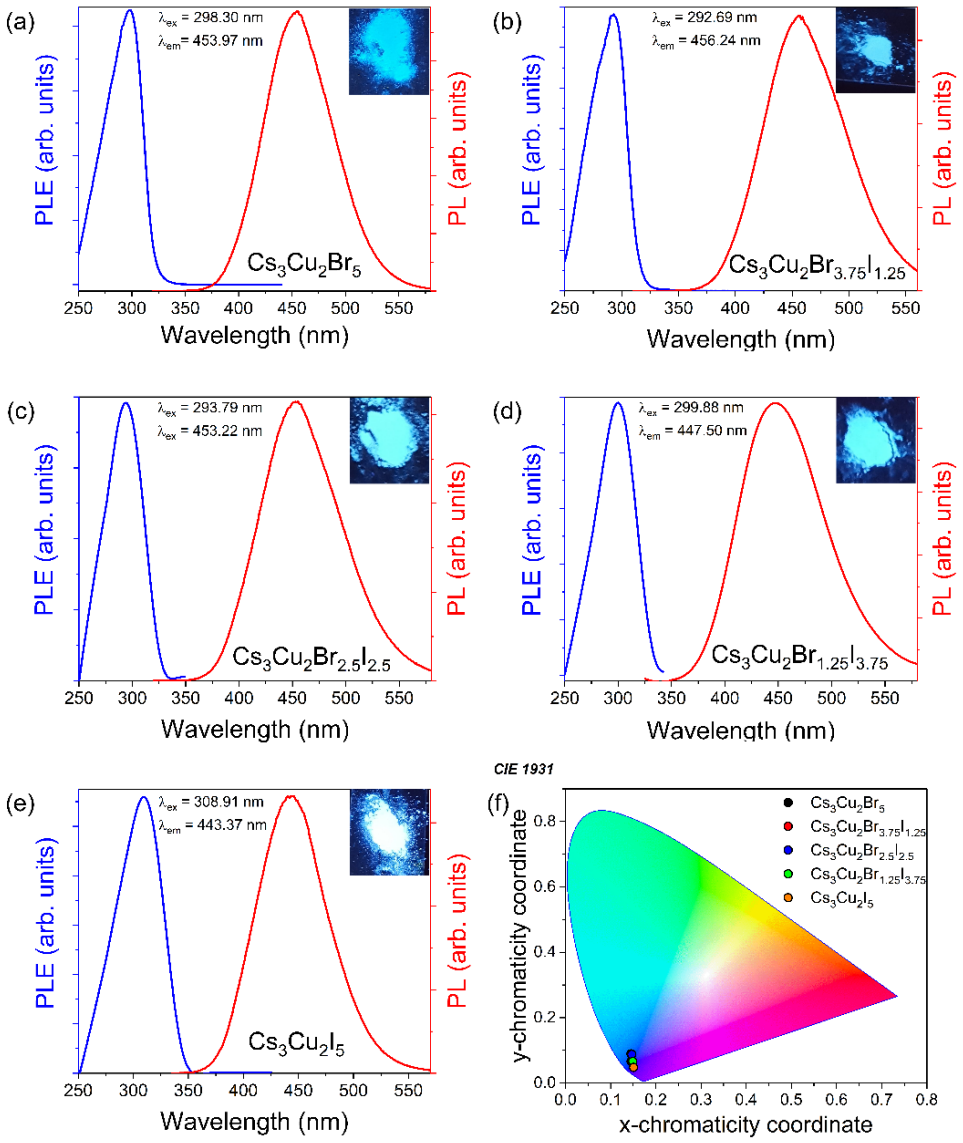


Figure 46. Photoluminescence excitation (PLE, blue lines) and emission (PL, red lines) of (a) $Cs_3Cu_2Br_5$, (b) $Cs_3Cu_2Br_{3.75}I_{1.25}$, (c) $Cs_3Cu_2Br_{2.5}I_{2.5}$, (d) $Cs_3Cu_2Br_{1.25}I_{3.75}$, (e) $Cs_3Cu_2I_5$ compounds, and (f) CIE 1931 chromaticity plot of the resulting emission of all compounds.

Table 8. Photoluminescence and colorimetry data for all compounds.

Compound	PLQY (%)	FWHM (nm)	PLE peak (nm)	PL peak (nm)	CIE coordinates (x,y)		CCT values (K)	Stokes shift (nm)
$Cs_3Cu_2Br_5$	50.1	75	298	455	0.14	0.067	1926	157
$Cs_3Cu_2Br_{3.75}I_{1.25}$	53.8	85	293	456	0.14	0.089	2555	164
$Cs_3Cu_2Br_{2.5}I_{2.5}$	55.2	89	294	453	0.15	0.087	2449	159
$Cs_3Cu_2Br_{1.25}I_{3.75}$	60.4	93	300	448	0.15	0.066	1885	148
$Cs_3Cu_2I_5$	98.7	99	309	443	0.15	0.048	1727	135

In addition to the remarkable increase in charge localization and emission efficiency, lowering of crystal structure dimensionality in hybrid organic-inorganic metal halides produces large Stokes shifts such as in the case of $(C_4N_2H_{14}Br)_4SnBr_6$.[66, 68, 409, 420, 429] In agreement with these reports, we also observed very large Stokes shifts ranging from 135 to 164 nm for $Cs_3Cu_2Br_{5-x}I_x$. Typically, PL emission spectra with such large Stokes shifts in hybrid metal halides are attributed to STEs that are formed when the free exciton couples strongly to lattice by distorting it.[409, 429] Indeed, Jun et al. also recently studied the optical properties of $Cs_3Cu_2I_5$ attributing the observed large Stoke-shifted emission in this material to an excited-state structural reorganization mechanism caused by the Jahn-Teller distorted Cu tetrahedral site (see the Supporting Information further discussion on possible Jahn-Teller effect in $Cs_3Cu_2X_5$).[183] However, defect-induced emission can be significant in copper halides as shown by the PL spectra recorded for CuI, which has been reported to exhibit an emission maximum at 410 nm that can red shift to 428 nm depending on the concentration of defects.[430]

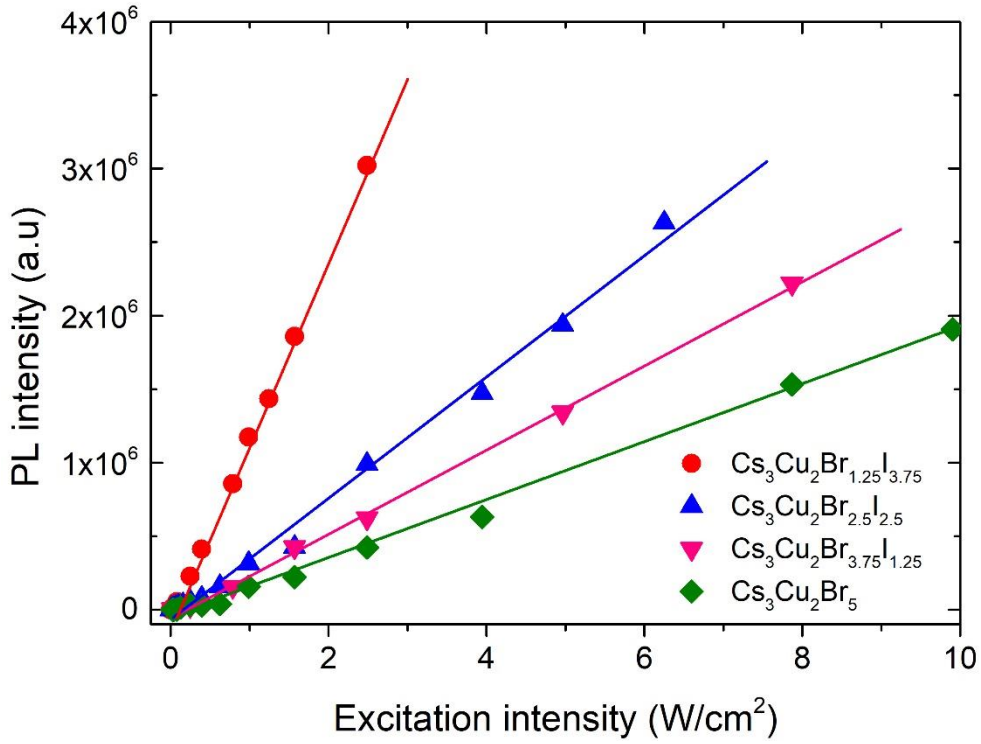


Figure 47 PL intensity versus excitation power density for $Cs_3Cu_2X_5$ (X = I, Br).

To confirm the nature of the PL emission peaks in $Cs_3Cu_2Br_{5-x}I_x$, we additionally performed measurements of PL as a function of excitation intensity as shown in Figure 47. It is worth noting that the concentration and recombination lifetime of permanent defects are finite, therefore, their PL could be saturated at high excitation power.[431] However, the observed PL intensity for $Cs_3Cu_2Br_{5-x}I_x$ present a linear dependence with excitation power, and the absence of saturation suggests that the emission is likely to originate from STEs rather than defects in this system.[63, 106, 108, 274, 432]

4.2.6 Density Functional Theory Calculations for $Cs_3Cu_2X_5$ (X = Br, I)

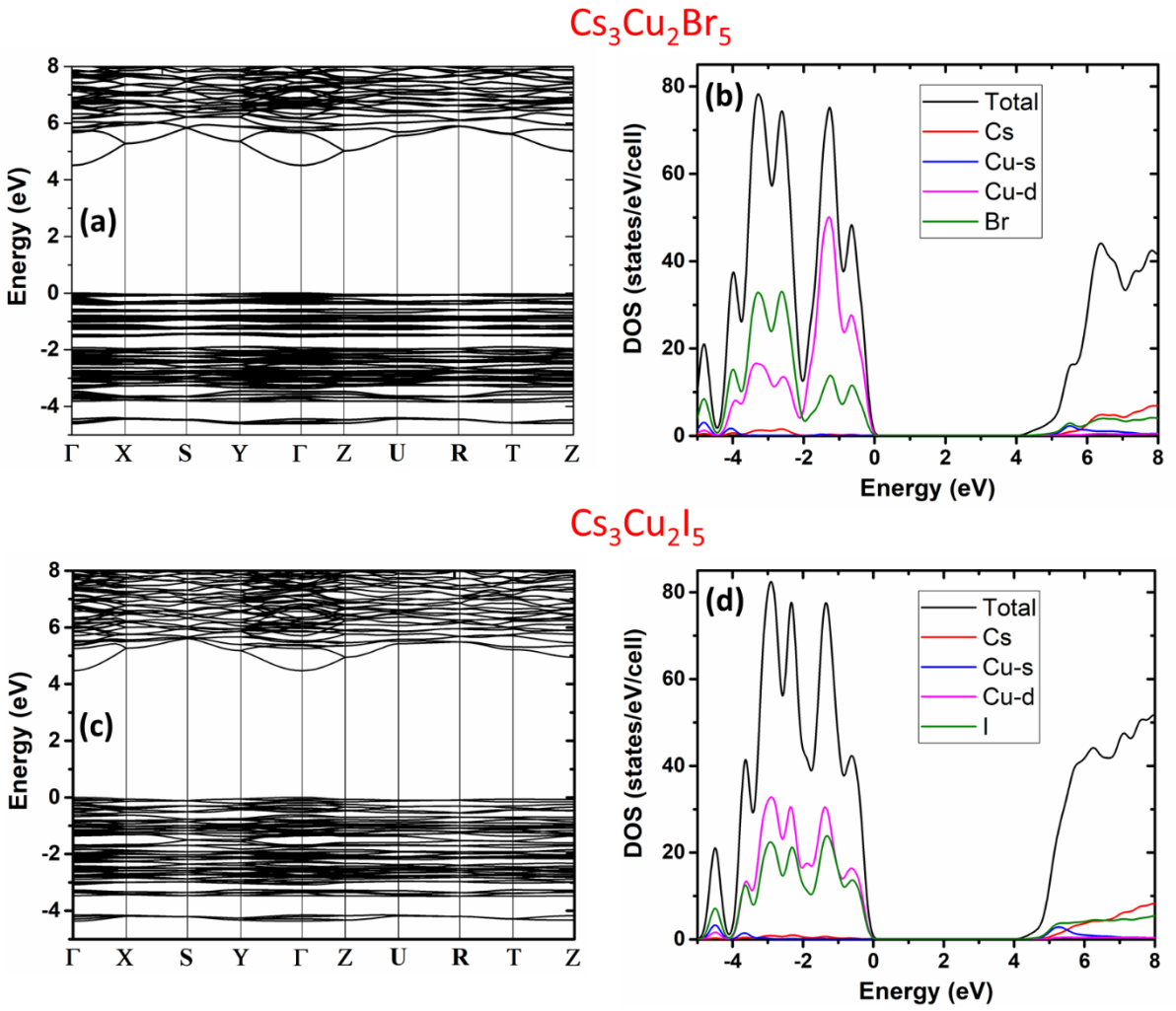


Figure 48. Electronic band structure and density of states (DOS) of $Cs_3Cu_2Br_5$ (a-b) and $Cs_3Cu_2I_5$ (c-d).

Figure 48 shows the electronic band structures and the density-of-states (DOS) of $Cs_3Cu_2Br_{5-x}I_x$ ($0 \leq x \leq 5$). The valence and the conduction bands are mainly made up of Cu-3d and Cu-4s states, respectively. Both compounds have a direct band gap at the Γ point. Since both the valence and the conduction bands are dominated by the Cu states, the band gaps of $Cs_3Cu_2Br_5$ (4.51 eV) and $Cs_3Cu_2I_5$ (4.47 eV) are very close to each other. This finding explains the measured small differences PL emission peaks (Table 8) between $Cs_3Cu_2Br_5$, $Cs_3Cu_2I_5$ and

intermediate compositions. For both compounds, the Cu-3d dominated valence band is flat while the Cu-4s-derived conduction band is much more dispersive. However, despite the dispersive conduction

Table 9. Binding energies of the unrelaxed spin-singlet ($\boldsymbol{E_B^{unrelax}}$) and the relaxed spin-triplet ($\boldsymbol{E_B^{relax}}$) excitons as well as the exciton excitation and emission energies of $Cs_3Cu_2Br_5$ and $Cs_3Cu_2I_5$. The exciton excitation and the emission energies were calculated based on the spin-singlet and the spin-triplet excitons, respectively. The experimentally measured excitation and emission peak energies are shown in parentheses. All the results are based on hybrid functional PBE0 calculations.

	$Cs_3Cu_2Br_5$	**$Cs_3Cu_2I_5$**
$\boldsymbol{E_B^{unrelax}}$**(eV)**	0.40	0.33
$\boldsymbol{E_B^{relax}}$**(eV)**	1.24	1.10
Excitation Energy (eV)	4.11 (4.14)	4.14 (4.02)
Emission Energy (eV)	2.41 (2.67)	2.61 (2.79)

band, the excitons in the two compounds are strongly localized due to the strong Coulomb binding between the electron and the hole and the strong local structural distortion of the $Cu_2X_5^{3+}$ cluster upon excitation as discussed below. The calculated binding energies of the unrelaxed excitons in $Cs_3Cu_2Br_5$ and $Cs_3Cu_2I_5$ are 0.40 eV and 0.33 eV, respectively, which are already significant due to the strong Coulomb binding; further exciton structural relaxation increases the binding energies to 1.24 eV and 1.10 eV, respectively as shown in Table 9. The strong exciton localization and binding should lead to exciton emission. The structural distortion due to the exciton localization is significant in both compounds, as shown in Figure 49a-b for the case of $Cs_3Cu_2Br_5$.

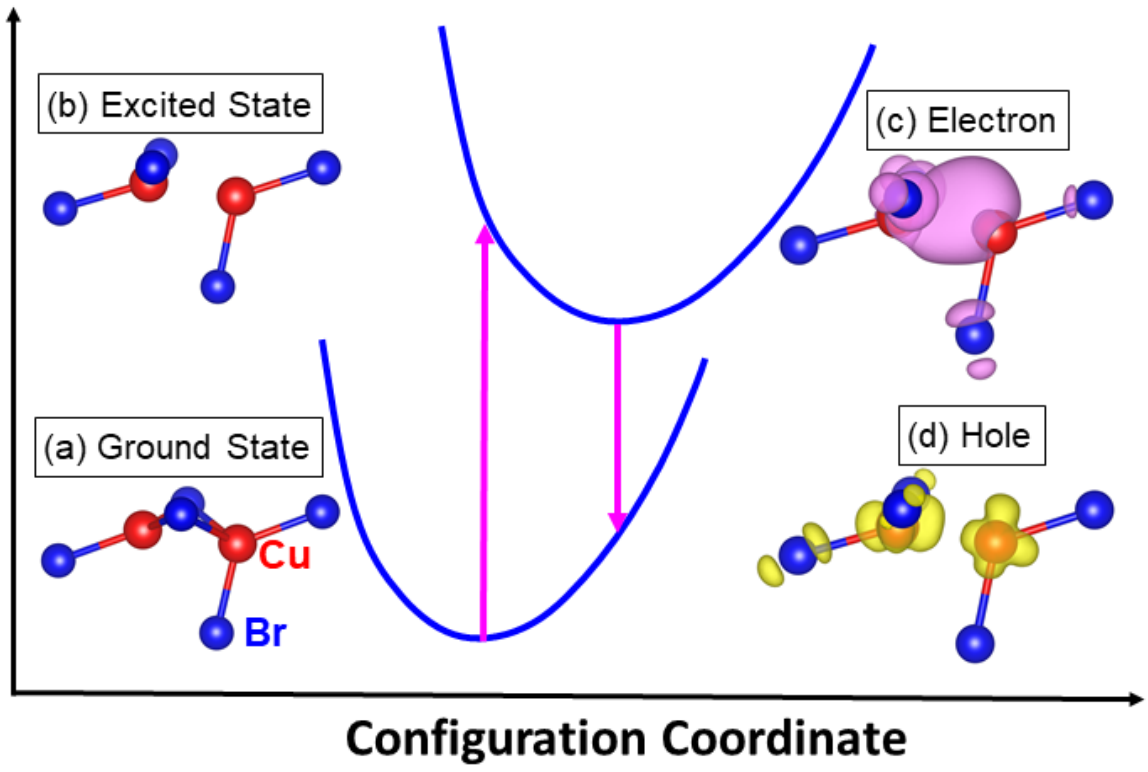


Figure 49. The configuration coordinate diagram for the excitation, relaxation, and emission in $Cs_3Cu_2Br_5$. (a) and (b) show the ground-state and the relaxed excited-state of the Cu_2Br_5 cluster. The curves and the straight arrows represent potential energy surfaces and optical transitions, respectively. The ground-state and the relaxed excited-state structures are shown in (a) and (b), respectively. The partial densities of the electron and the hole in the relaxed exciton are shown in (c) and (d), respectively. The Cu and the Br atoms are represented by the red and blue spheres, respectively.

The structural relaxation breaks two Cu-halogen bonds and move the two Cu atoms closer to each other; the Cu-Cu distance decreases from 2.51 Å to 2.32 Å in $Cs_3Cu_2Br_5$ and from 2.49 Å to 2.35 Å in $Cs_3Cu_2I_5$. The partial density contours of the electron and the hole of the exciton in $Cs_3Cu_2Br_5$ are shown in Figure 49c-d. The hole has Cu-3d character and is localized on the two Cu atoms in the Cu_2Br_5 cluster, while the electron is localized mostly in the bond-center position between the two Cu atoms. The spatial distribution of the electron and hole of the exciton in $Cs_3Cu_2I_5$ is similar to that in $Cs_3Cu_2Br_5$. The calculated exciton excitation

and emission energies in both compounds are shown in Table 9; they are in good agreement with the experimental results, which suggest that the calculated electron excitation and excited-state structural relaxation are reliable. The large excited-state structural relaxation in $Cs_3Cu_2X_5$ (X = Br, I) as revealed in the calculation explains the observed large Stokes shifts and the absence of the significant spectral overlap between the excitation and emission (Figure 46); these are important for hindering the exciton migration (by resonant transfer of the excitation energy) and the subsequent nonradiative recombination at defects.[77]

In summary, we report a solid solution behavior in $Cs_3Cu_2Br_{5-x}I_x$ ($0 \leq x \leq 5$), which are nontoxic, highly efficient blue emitters with improved stability compared to the well-known Pb- and Sn-based halides. The compounds can be conveniently prepared through classic solid-state synthesis techniques. The observed near-unity PLQY values are attributed to the specifics of the crystal structure of this family, 0D structure based on dimeric Cu_2X_5 units that promotes significant charge localization and enables the presence of room-temperature stable excitons. Indeed, our computational results show that $Cs_3Cu_2Br_5$ and $Cs_3Cu_2I_5$ feature high exciton binding energies of 0.40 eV and 0.33 eV, respectively. The exciton localization in these compounds results a significant structural reorganization of Cu_2X_5 molecules in excited state, which further enhances the binding energies to 1.24 eV and 1.10 eV for $Cs_3Cu_2Br_5$ and $Cs_3Cu_2I_5$, respectively. Importantly, this work paves the way for consideration of Cu-based multinary halides for nontoxic, earth-abundant, low-cost and high-efficiency light emission applications.

4.3 The $CsCu_2X_3$ (X = Cl, Br, I) System

Here, we report the optical properties of the nontoxic, stable, and highly emissive one-dimensional (1D) all-inorganic halides $CsCu_2X_3$ (X = Cl, Br, I). Photoluminescence (PL) measurements show a tunable bright room temperature visible emission in the 527 to 587 nm range with photoluminescence quantum yields (PLQY) ranging from 0.38% ($CsCu_2Br_{1.5}I_{1.5}$) to 48.0% ($CsCu_2Cl_3$). Power-dependent PL measurements suggest that the emission results from self-trapped excitons induced by strong charge localization and structural distortions within the lD ribbon structure of $CsCu_2X_3$.

4.3.1 Synthesis and Methods for $CsCu_2X_3$ (X = Cl, Br, I)

4.3.1.1 Reagents Used in the Synthesis of $CsCu_2X_3$ (X = Cl, Br, I)

Chemicals utilized in this study were used as purchased: (i) copper (I) chloride, 99.99%, Acros Orcganics; (ii) copper(I) bromide, 99.999%, Aldrich; (iii) copper iodide, 99.9%, Aldrich; (iv) cesium chloride, 99.99%, Acros Organics; (v) cesium bromide, 99.9%, Acros Organics; (vi) cesium iodide, 99.999%, Acros Organics.

4.3.1.2 Synthesis of $CsCu_2X_3$ (X = Cl, Br, I)

Crystalline ingots were prepared using a 1:2 stoichiometric ratio of CsX to CuX (X = I, Br, Cl) ground in an agate mortar, pelletized and sealed under dynamic vacuum in quartz ampules. Pelletized samples were annealed at 410 °C for 48 hours and slowly cooled over 20 hours to room temperature resulting in polycrystalline ingots. Attempts to grow crystals using multiple solution growth methods including slow evaporation of saturated solutions and antisolvent crystallization were unsuccessful.[183]

4.3.1.3 Powder X-ray Diffraction

Powder X-ray diffraction (PXRD) measurements were performed on a Rigaku MiniFlex600 system equipped with a Dtex detector using a Ni-filtered Cu-Kα radiation source. All scans were performed at room temperature from the 5-90˚ (2θ) range, with a step size of 0.2˚. All data were corrected for the amorphous background of the glass slides used during collection and fitted using the Pawley fitting method using Rigaku's PDXL2 software package. To check the air stability, samples were left in ambient air for more than two months with periodic PXRD measurements using the same condition mentioned above.

4.3.1.4 Thermal Analysis

Simultaneous thermogravimetric analysis (TGA) and differential scanning calorimetry (DSC) measurements were carried out on a TA Instruments SDT650 unit. Measurements were performed using 90 µL alumina crucibles on 8-10 mg samples under a 100 mL/min flow of dry nitrogen in the 100 – 575 °C range with 5 °C/min heating rate.

4.3.1.5 Optical Measurements

Room temperature Diffuse reflectance spectra of polycrystalline powder of $CsCu_2X_3$ of were measured using a high-resolution PerkinElmer LAMBDA 750 UV−vis−NIR spectrometer equipped with a 100 mm InGaAs integrating sphere attachment. The diffuse reflectance data were converted to absorption spectra according to the the Kubelka-Munk equation:[433] ($F(R) = \alpha/S = (1-R)^2/(2R)$, where R is the reflectance, α is the absorption coefficient, S is the scattering coefficient.

Photoluminescence excitation (PLE), and photoluminescence quantum yield (PLQY) measurements were performed at ambient temperature, on polycrystalline powder samples, using a HORIBA Jobin Yvon Fluorolog-3 spectrofluorometer equipped with a Xenon lamp and

Quanta-φ integrating sphere. PLQY data were analyzed using the two-curve method in a varied range from 280 – 800 nm using the imbedded QY software in the Horiba-Jobin Yvon software.

Time resolved photoluminescence (TRPL) measurements were done on polycrystalline powder samples using a HORIBA Jobin Yvon Fluorolog-3 spectrofluorometer equipped with a time-correlated single photon counting module. HORIBA Jobin Yvon NanoLEDs (pulsed light-emitting diodes) were used as the excitation source. The duration of the light pulse was shorter than 2 ns. Temperature and power dependence PL spectra were measured using a Princeton Instruments PIXIS-eXcelon silicon CCD. The excitation wavelength was the 325 nm (3.815 eV) line of a He-Cd laser (Kimmon Electric HeCd dual-wavelength laser; model: IK552R-F). The samples were placed in a helium bath cryostat, and the measurements were performed between 4 and 295 K.

4.3.2 $CsCu_2X_3$ (X = Cl, Br, I) Structure

As previously reported in literature and illustrated in Figure 50, $CsCu_2X_3$ (X = Cl, Br, I) crystallize in the orthorhombic space group *Cmcm*,[434-435] featuring edge-sharing $[Cu_2X_3]^-$ anionic 1D ribbons separated by rows of Cs^+ atoms. Isolation of the copper halide tetrahedra as ribbons can be seen most prominently down the *b* and *c* axis (as shown in Figure 50b-c) where the Cs cations create channels within the structure and thus effectively creates nanowires which may be the origin of the efficient room temperature photoluminescence reported in this work. Interestingly, there are several reported isostructural Rb-based analogues such as $RbCu_2Cl_3$[412] reported in literature. Measurement quality samples of $CsCu_2X_3$ could only be formed through solid-state synthesis, although single crystal growth via slow evaporation was also attempted with mixed results. Purity of all phases were assessed through room temperature PXRD measurements. The PXRD results were refined using the Pawley (decomposition) method, as

shown in Figure 51, confirming that the lattice parameters for $CsCu_2X_3$ increase linearly with the size of the halide anion following Vegard's law (Figure 52). This is a common observation also reported for other CsX-CuX compounds,[111] $FA_{1-x}Cs_xPbBr_3$,[436] $(Me_3S)_2Pb_5I_{18}$,[437] $Cu_2ZnSn(S_x,Se_{1-x})_4$,[438] and $CH_3NH_3PbI_xCl_{3-x}$.[439]

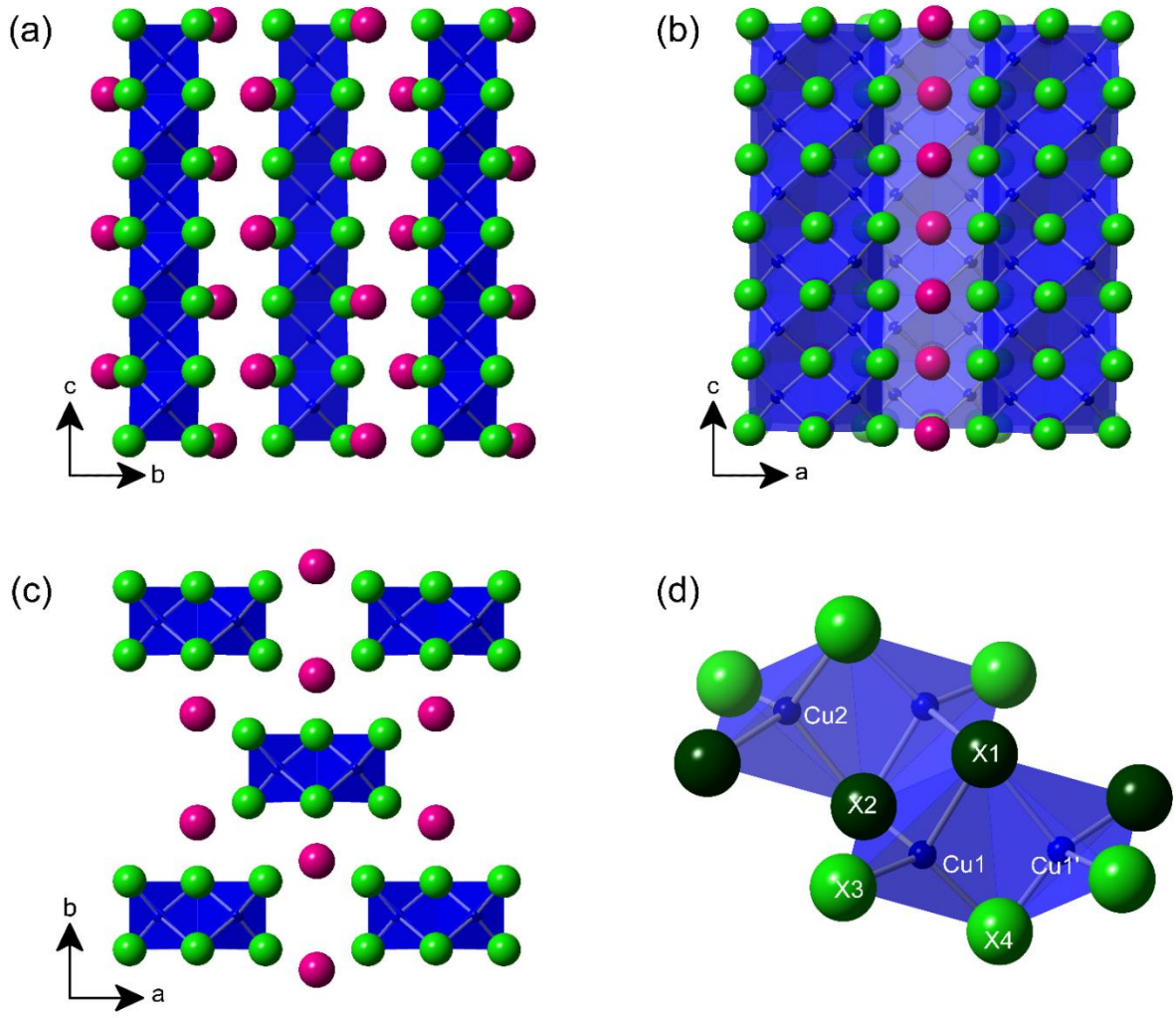


Figure 50. Crystal structures of $CsCu_2X_3$ (X = Cl, Br, I) projected along (a) a-, (b) b- and (c) c-axes. Pink and green spheres represent Cs and the halides, respectively and the blue tetrahedron represent Cu. Di-tetrahedral cluster connectivity is represented in (d) which are labeled according to the convention in Table A1.13 in **Appendix 1** and shown with all dark green and lime green halides occupying specific corresponding crystallographic positions according to the reported CIF files.[434 435]

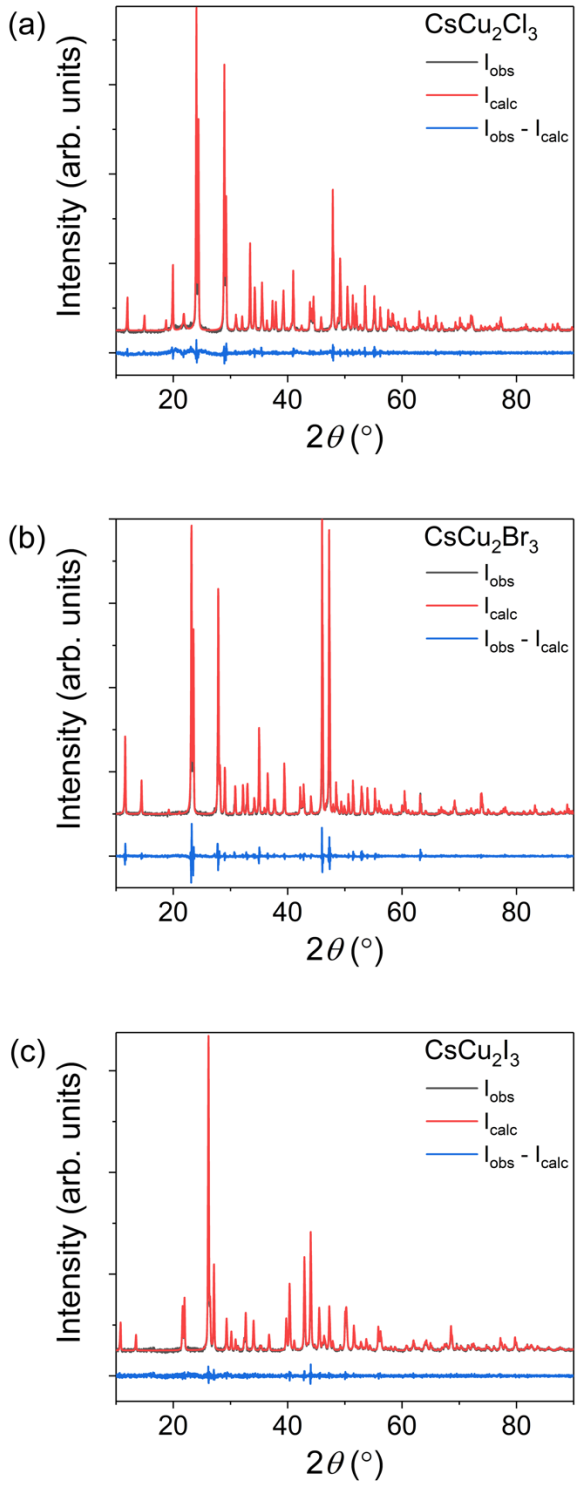


Figure 51. Room temperature powder X-ray diffraction (PXRD) patterns (black lines) for (a) $CsCu_2Cl_3$, (b) $CsCu_2Br_3$, (c) $CsCu_2I_3$. Pawley fits of the data are shown in red and difference plots shown in blue.

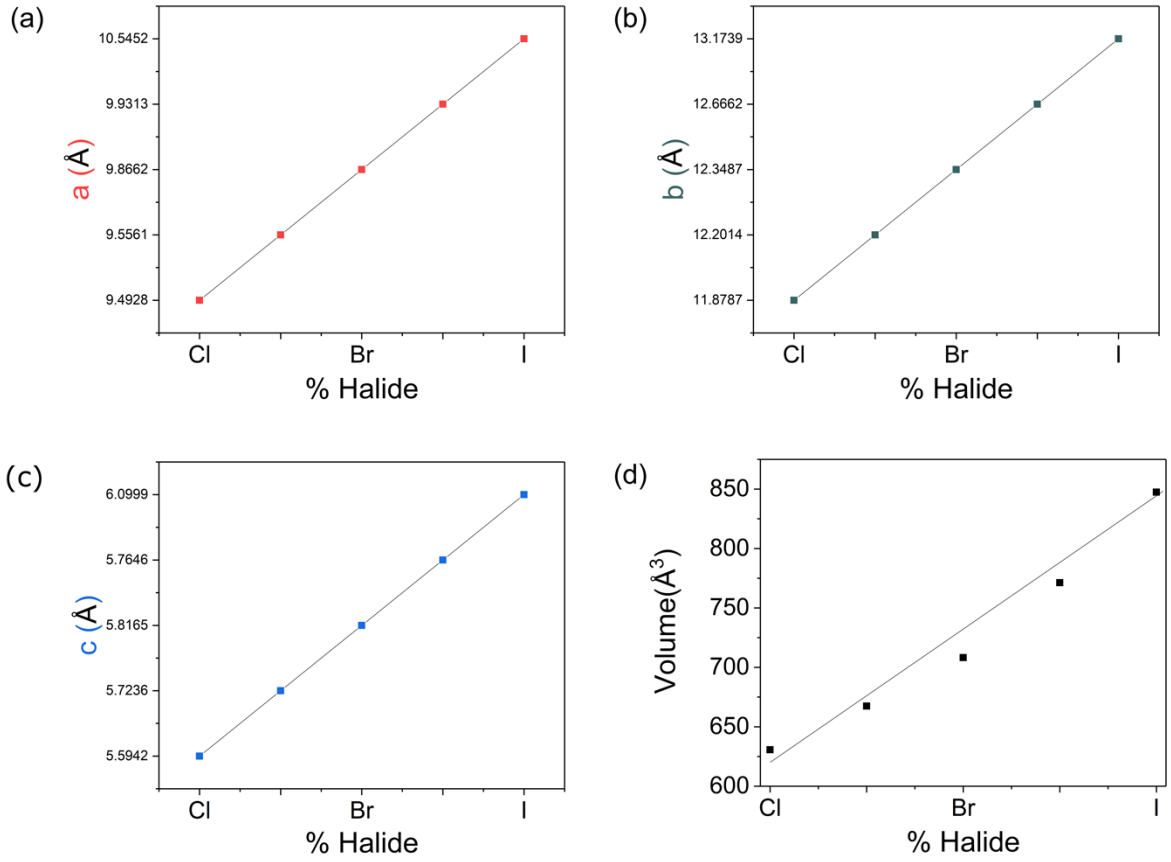


Figure 52. PXRD (a) refined lattice parameters and (b) unit cell volume shown as a function of halide content as alloying progresses from Cl to Br to I.

In octahedra-based metal halides, connectivity of octahedral building blocks and magnitude of distortion are known to affect the band structure, emission properties, and defect formation within a perovskite lattice. Typically, these are evaluated using the metal-halide bond lengths and angles, and the volume of the individual octahedra.[90] Deviation from the ideal octahedral geometry results in an increase in distortion within metal halide perovskites, which has been shown to negatively affect the overlap between the orbitals of the metal and halides. This results in wider band gaps, blue shifts the onset of absorption,[59] and causes a decrease in the PL efficiency and lifetime due to an increase in the reduced mass of excitons within the system.[129] Among the quantitative methods used to determine the magnitude of distortion

within a perovskite system are the variation in octahedral distance (Δd),[43] angle (σ^2_{oct}),[440] and the overall octahedral elongation ($<\lambda_{oct}>$).[440] In particular, these parameters have been used to directly relate an increase in calculated values to an increase in octahedral distortion which is then attributed to an increase in Stokes-shifts, full width at half maximum (FWHM) values, and consequently, broadband white-light emission.[274, 301, 303, 441] Such broadband luminescence is commonly seen in alkali halides,[441-442] hybrid-organic inorganic materials,[85, 108, 113, 303, 345, 347, 443-445] and recently in all inorganic metal halides such as $A_3M_2I_9$ (A = Cs, Rb; M = Bi, Sb),[446] $CsZnCl_2I$,[447] $(C_8NH_{12})_4Bi_{0.57}Sb_{0.43}Br_7$,[448] and $Cs_2AgInCl_6$.[449] In the interest of correlating the optical properties observed in the $CsCu_2X_3$ family to that of other metal halides based on octahedral building blocks, attempts were made to relate the calculated tetrahedral distortion to the optical properties reported below. However, note that the effect of the tetrahedral distortion on optoelectronic properties in solid-state structures has been poorly studied with no reports comparing the magnitude of distortion to the observed luminescence properties.

Robinson et al. were the first to propose quantitative tetrahedral distortion parameters that directly correlated to their octahedral analogs σ^2_{oct} and λ_{oct}, which would allow for a direct comparison of the amount of distortion present in completely different polyhedra-based systems.[440] The tetrahedral angle variance ($\sigma^2_{\theta\,(tet)}$) and the average tetrahedral elongation $<\lambda_{tet}>$ are given by the following equations:[440]

$$\sigma^2_{\theta\,(tet)} = \frac{1}{5}\sum_{i=1}^{5}(\theta_t - 109.47°)^2 \tag{11}$$

$$\langle\lambda_{tet}\rangle = \frac{1}{4}\sum_{i=1}^{4}\left(\frac{l_i}{l_0}\right)^2 \tag{12}$$

where σ^2_{tet} is deviation in bond angle of the system, θ_{tet} is the individual tetrahedral angles between the center metal and each adjacent ligand, $\langle\lambda_{tet}\rangle$ is the overall octahedral elongation, l_i is the measured distance between the metal center and each ligand, and l_0 is the ideal bond distance determined from the ionic radii. Only octahedral Δd and $\Delta\theta_{XMX}$ relationships have been previously reported, however, they can be adapted for tetrahedral systems via the following equations:

$$\Delta d = \frac{1}{4}\sum_{n=1,4}\left(\frac{d_n - d}{d}\right)^2 \tag{13}$$

$$\Delta\theta_{XMX} = \frac{1}{6}\sum_{n=1,6}\left(\frac{\theta_{XMX(n)} - \langle\theta\rangle}{\langle\theta\rangle}\right)^2 \tag{14}$$

where Δd is one fourth of the summation of each difference of each individual bond distance (d_n) the average bond distance (d) of the tetrahedra in question squared, and $\Delta\theta_{XMX}$ is one sixth of the summation of the absolute value of the difference of each individual angle ($\theta_{XMX(n)}$) and the average angle of the tetrahedra in question $\langle\theta\rangle$ squared. The results of the polyhedral distortion analysis are summarized in Table 10.

Table 10. Results of the tetrahedral distortion estimation indicate a linear decrease in distortion with increase in the halide ion size.

	$CsCu_2Cl_3$	**$CsCu_2Br_3$**	**$CsCu_2I_3$**
$\sigma^2_{(tet)}$	49.49	14.22	10.33
$\langle\lambda_{tet}\rangle$	0.9785	0.9537	0.8984
Δd	21.67 x 10^{-4}	13.59 x 10^{-4}	3.05 x 10^{-4}
$\Delta\theta$	68.84 x 10^{-4}	19.44 x 10^{-4}	14.37 x 10^{-4}

A noticeable trend can be observed for $\sigma^2_{\theta\,(tet)}$, $<\lambda_{tet}>$, Δd, and $\Delta\theta_{XMX}$ as all values decrease from $CsCu_2Cl_3$ to $CsCu_2Br_3$ to $CsCu_2I_3$ and if we relate the magnitude of these values directly to the distortion within the tetrahedral system, then tetrahedral distortion decreases from $CsCu_2Cl_3$ to $CsCu_2Br_3$ to $CsCu_2I_3$. Therefore, if tetrahedral distortion is directly related to the experimentally observed luminescence phenomena of FWHM and the Stoke's shift, one would expect $CsCu_2Cl_3$ to have the largest FWHM, whereas $CsCu_2I_3$ is expected to have the smallest. However, the experimentally measured trend in FWHM values suggest the opposite trend (Table 7), with $CsCu_2I_3$ exhibiting the broadest PL peak with FWHM of 126 nm and $CsCu_2Cl_3$ showing a FWHM of 102 nm. Therefore, a direct relationship between tetrahedral distortion and the observed PL peak broadness in CsCu2X3 family cannot be directly established.

4.3.3 Ambient and Thermal Stability of $CsCu_2X_3$ (X = Cl, Br, I)

The stability of a material in ambient air/moisture and over a large range of temperatures is highly important for optoelectronic device applications. All-inorganic materials are expected to exhibit higher stability than hybrid materials due to the lack of volatile organic molecules[418-419] and numerous phase transitions typically seen in hybrids.[20] For instance, hybrid perovskites such as $CH_3NH_3PbI_3$[20] and $CH_5N_2SnI_3$[177] suffer from degradation due to moisture under ambient conditions. Furthermore, they are reported to have thermal decomposition temperatures of 176 °C and 100 °C, respectively. It has been reported that the use of Cs^+ instead of organic cations promote much more stable compounds, as seen in $CsPbI_2Br$, which is thermally stable up to 463 °C, although this material also suffers from moisture degradation within hours of being left in air under ambient conditions.[450] For the $CsCu_2X_3$ family, the use of both Cs^+ and Cu^+ affords a significant improvement of the air and thermal stability. All

members of this family exhibit no noticeable sign of impurity formation or loss of crystallinity according to our periodic PXRD measurement over two months (Figure 53), suggesting their excellent stability under ambient air and moisture conditions. Interestingly, high stability has also been reported for $Cs_3Cu_2I_5$,[183, 451] suggesting that the phases in CsX-CuX system are favorable in this regard compared to the analogous heavily-studied CsX-PbX_2 system. $CsCu_2X_3$ shows no signs of thermal decomposition up to 495 °C (Figure 53) after two heating-cooling cycles of DSC/TGA. These results are in a stark contrast to that reported for the state-of-the-art photovoltaic material $CH_3NH_3PbI_3$.[423]

Phase transitions within operation temperature range of materials such as $MAPbI_3$ have been shown to detrimentally reduce device lifetime and overall efficiency,[452] making the structural and phase transitions of new materials prior to incorporating them into devices that much more important. DSC measurements were performed to confirm the results previously reported in the CsX-CuX phase diagrams.[413-414, 453] From these measurements, as shown in Figure 54, the $CsCu_2X_3$ family members exhibit congruent melting behavior, with melting occurring at 270 °C, 351 °C and 374 °C for $CsCu_2Cl_3$, $CsCu_2Br_3$ and $CsCu_2I_3$, respectively, which are in excellent agreement with the melting points reported in literature.[413-414] In addition, the presence of a small peak feature in each sample close to their melting transitions suggests the presence of a minor CsX impurity. Indeed, based on the literature reported phase diagrams,[413-414, 453] CsX impurities are known to form a lower melting eutectic together with $CsCu_2X_3$.[413-414]

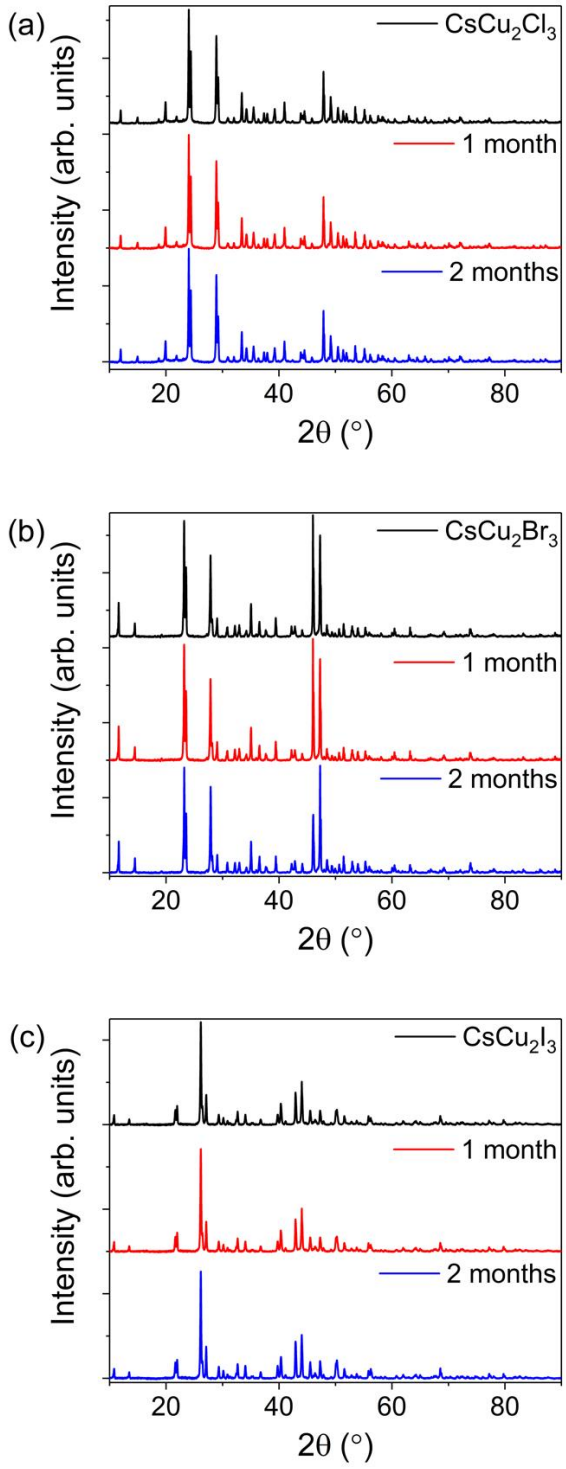


Figure 53. PXRD patterns of (a) $CsCu_2Cl_3$, (b) $CsCu_2Br_3$, and (c) $CsCu_2I_3$ left out in ambient conditions and measured over a period of 2 months.

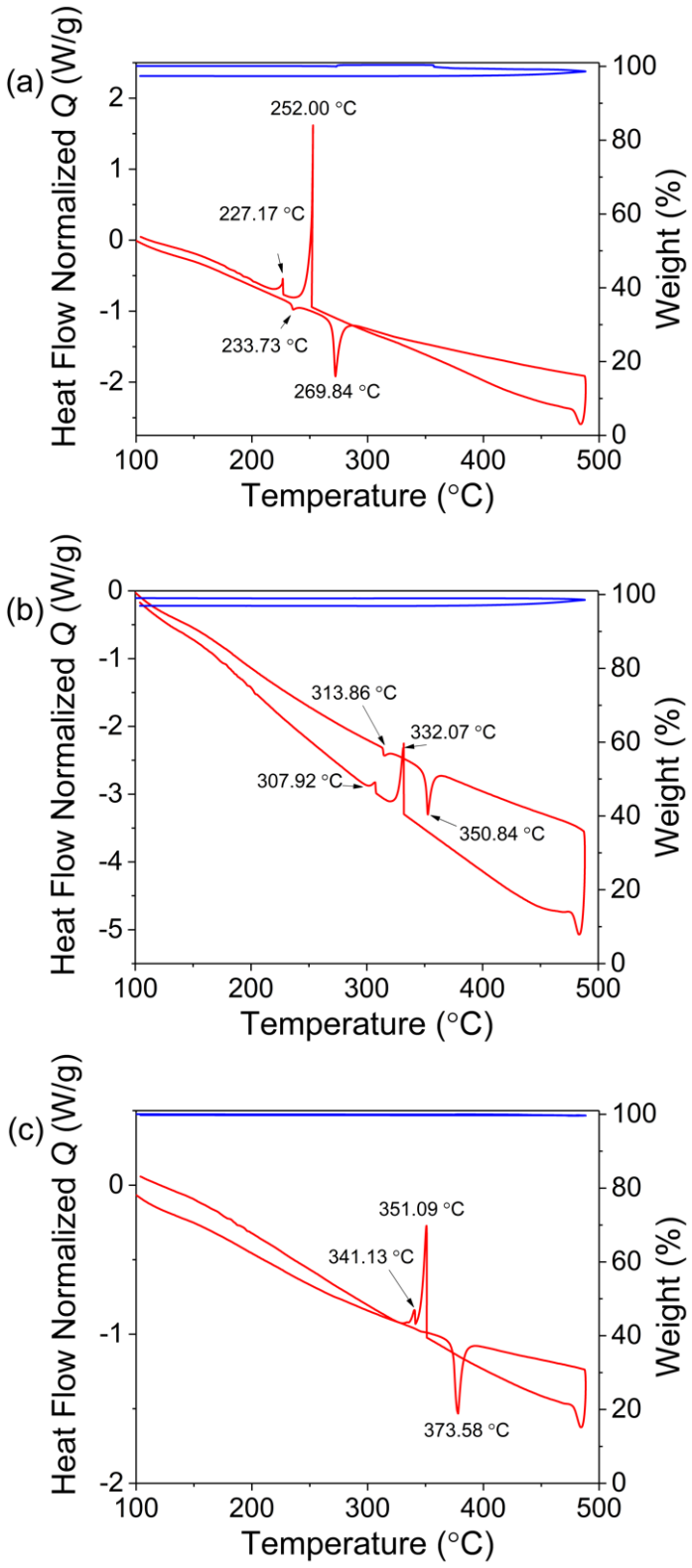


Figure 54. Tandem differential scanning calorimetry (red) and thermal gravimetric analysis (blue) of (a) $CsCu_2Cl_3$, (b) $CsCu_2Br_3$, and (c) $CsCu_2I_3$.

4.3.4 Diffuse Reflectance and Photoluminescence

Optical band gaps of $CsCu_2X_3$ were estimated through the measurements of diffuse reflectance spectra of the powdered samples using the Kubelka–Munk model. The measured values range from 3.4 to 3.8 eV depending on the direct and indirect Tauc fits of the reflectance data (Figure 55). As expected from the trend in electronegativity of halogens, $CsCu_2Cl_3$ exhibits the largest band gap in the family, however, the variation of the band gaps is nonlinear, which is especially noticeable for the mixed halide compositions. This in contrast to the linear changes observed in the lattice parameters in this family (Figure 52), which follows Vegard's law. The observed nonlinearity in the estimated band gaps could be attributed to the presence of local inhomogeneities in the mixed halide samples (i.e., the presence of end member impurities). This conjecture is also supported by the results of PL measurements (i.e., broader PL peaks are measured for the mixed halide compositions), which are discussed next (Table 11).

Table 11. Photoluminescence information table for all members.

Compound	**PLQY (%)**	**FWHM (nm)**	**PLE peak (nm)**	**PL peak (nm)**	**CIE coordinates (x,y)**	**CCT values (K)**	**Stokes shift (nm)**	**Lifetime (ns)**
$CsCu_2I_3$	3.23	126	334	576	(0.43, 0.47)	3561	242	62
$CsCu_2Br_{1.5}I_{1.5}$	0.38	128	335	584	(0.48, 0.51)	3094	249	26.6
$CsCu_2Br_3$	18.3	106	319	533	(0.27, 0.53)	6872	214	18
$CsCu_2Cl_{1.5}Br_{1.5}$	17.1	200	347	587	(0.09, 0.52)	12577	240	15.1
$CsCu_2Cl_3$	48.0	102	319	527	(0.29, 0.52)	6437	208	13.8

Under 325 nm UV excitation, $CsCu_2X_3$ show tunable, highly Stokes-shifted, room-temperature bright visible light emission ranging from 527 to 587 nm with PLQYs values ranging from 0.38% ($CsCu_2Br_{1.5}I_{1.5}$) to 48.0% ($CsCu_2Cl_3$) with CIE 1931 x,y-coordinates of

(0.31, 0.55), (0.32, 0.53), and (0.46, 0.50) for $CsCu_2Cl_3$, $CsCu_2Br_3$ and $CsCu_2Cl_3$, respectively (Table 11 and Figure 56). The excitation spectra (PLE) recorded with an appropriate detection wavelength at the maximum emission of $CsCu_2X_3$ show a maximum excitation ranging from 319 for $CsCu_2Cl_3$ to 347 nm for $CsCu_2Cl_{1.5}Br_{1.5}$ (Table 11 and Figure 56). High PLQY values have been previously observed in analogous low-dimensional metal halides, where the observed bright room temperature emission has been attributed to strong quantum confinement and highly localized charges promoting a high exciton binding energy (few hundreds of meV)[454] and thus affording room temperature stable excitonic emission.[289, 306, 318, 321-322, 448, 451, 455-457] However, the presence of permanent defect states in semiconductors has also been shown to create broadband emission.[276] To probe this possibility, excitation power dependence PL measurements (Figure 57) were performed, which show linear behavior for all studied compounds and the absence of saturation excludes the possibility of permanent defect emission, since the concentration and lifetime of permanent defects are finite.[108, 274, 345] Therefore, we attribute the largely Stokes-shifted broadband emission of $CsCu_2X_3$ to STEs.

Figure 58 shows the room temperature time-resolved photoluminescence (TRPL) measurements of $CsCu_2X_3$. All decay profiles can be fitted using the two-exponential function,

$$I(t) = A_1 \times \exp\left(\frac{-t}{\tau_1}\right) + A_2 \times \exp\left(\frac{-t}{\tau_2}\right) + I_0 \qquad (15)$$

where the first term accounts for the radiative decay and the second term accounts for the non-radiative decay. The full refinement results are provided in Table 12. The first lifetime component of 1-2 ns for all peaks of **1** and **2** is due to the instrumental response because of the duration of the light pulse (2 ns). Exciton lifetime varies between 13.8 and 62.0 ns. Importantly, exciton lifetime increases going from Cl, Br, to I, which is inversely proportional to the

measured PLQYs (48% for the Cl, 18.3% for the Br, and 3.23% for the I-based compounds). This trend supports our attribution for the emission of $CsCu_2X_3$ to STEs. STE lifetime was discussed by Mott and Stoneham based on the consideration of an energy barrier that is required to be surmounted for STE formation.[458] The potential barrier between STEs and free-excitons should be higher for $CsCu_2I_3$ compared to $CsCu_2Cl_3$, which explain the longer relaxation time for excitons in $CsCu_2I_3$ compared to $CsCu_2Br_3$ and $CsCu_2Cl_3$.

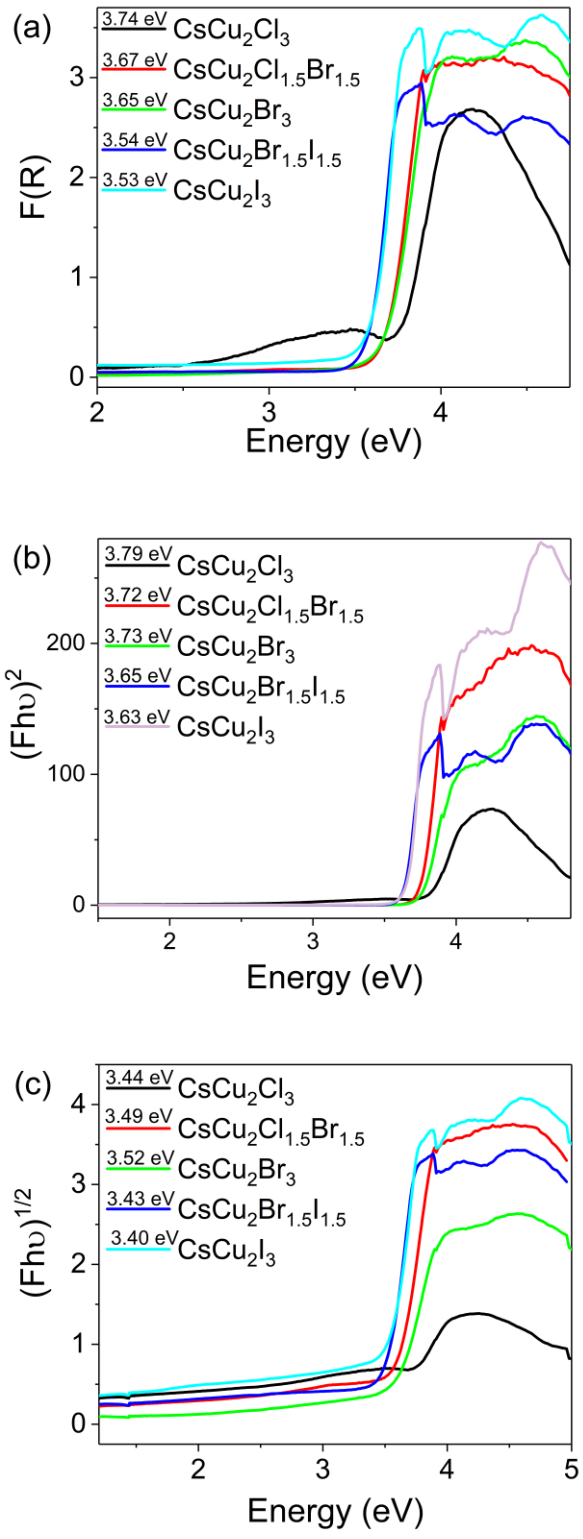


Figure 55. Diffuse reflectance spectra of polycrystalline powders of $CsCu_2X_3$ performed at room temperature.

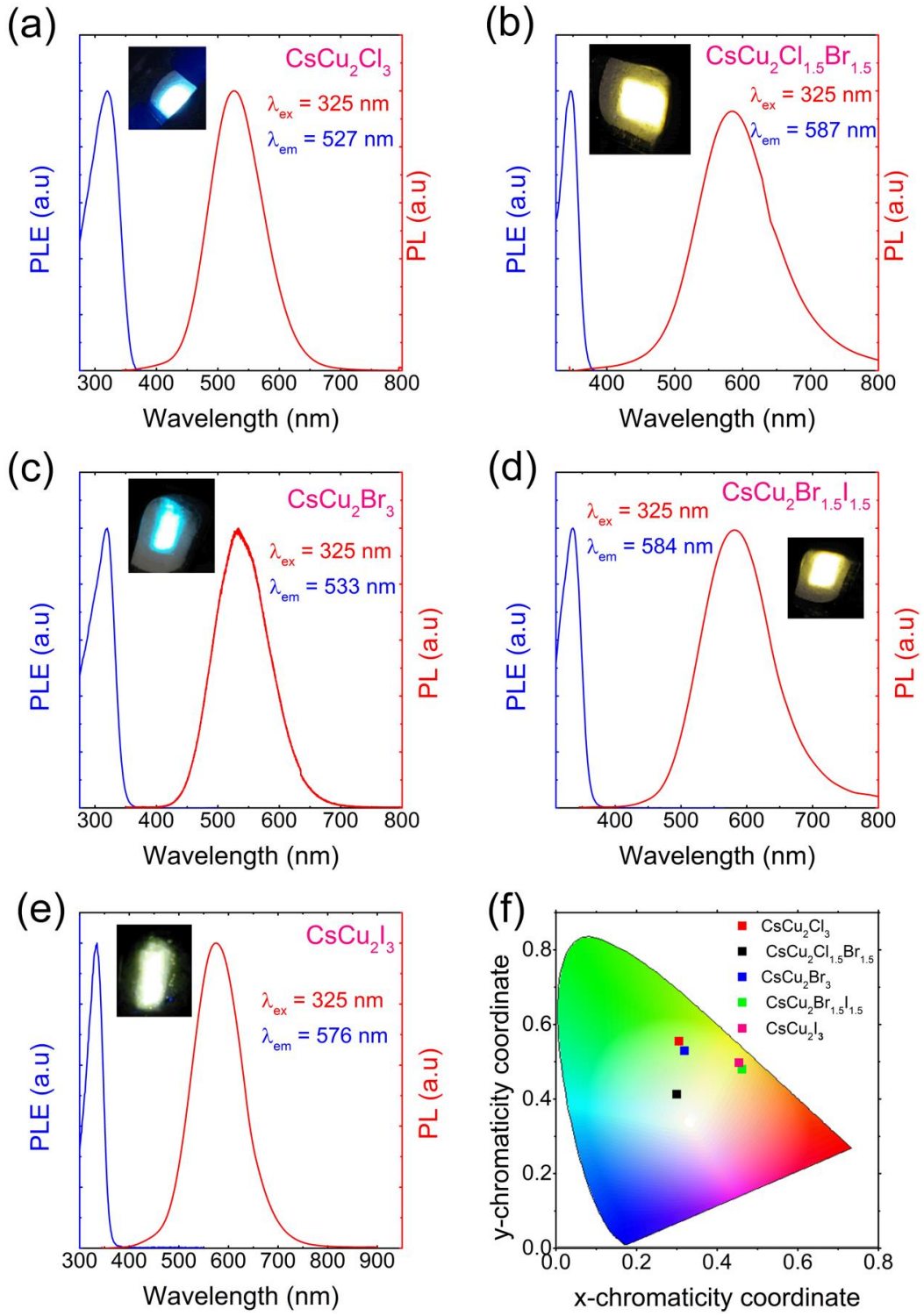


Figure 56. Photoluminescence excitation (blue) and emission (red) for (a) $CsCu_2Cl_3$, (b) $CsCu_2Cl_{1.5}Br_{1.5}$, (c) $CsCu_2Br_3$, (d) $CsCu_2Br_{1.5}I_{1.5}$, and (e) $CsCu_2I_3$. (d) CIE 1931 plot with the emission colors of all constituents.

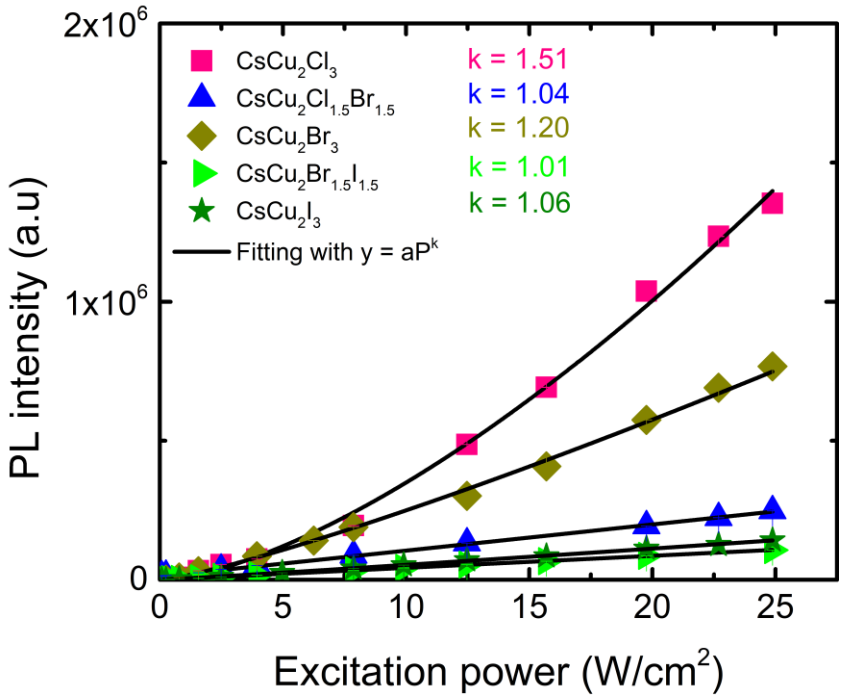


Figure 57. Power dependence PL spectra of $CsCu_2X_3$ measured at 4 K, under 325 nm excitation. Black curves shows the fitting using $y = P^k$, with y, P, and k are the PL intensity, the excitation power, and the refinement coefficient, respectively.[110]

Table 12. Summary of the refinement results of time resolved PL measurements of $CsCu_2X_3$.

Sample	**$CsCu_2Cl_3$**	**$CsCu_2Cl_{1.5}Br_{1.5}$**	**$CsCu_2Br_3$**	**$CsCu_2Br_{1.5}I_{1.5}$**	**$CsCu_2I_3$**
Excitation (nm)	314	333	314	333	333
Emission (nm)	527	587	533	584	576
I_0	152.5 ± 0.6	85 ± 0.5	49.9 ± 0.27	15.2 ± 0.5	35.2 ± 0.7
A_1	$8.8\ 10^{22}$ ± $6.4\ 10^{22}$	$1.5\ 10^{30}$ ± $7.2\ 10^{29}$	$7.7\ 10^{24}$ ± $3\ 10^{24}$	$2.9\ 10^{3}$ ± 241	$5.7\ 10^{3}$ ± $1.3\ 10^{2}$
τ_1 (ns)	2.1 ± 0.04	1.6 ± 0.02	1.9 ± 0.01	72.2 ± 1.7	62± 2
A_2	$6.4\ 10^{4}$ ± $5.7\ 10^{4}$	$3.9\ 10^{4}$ ± $2\ 10^{4}$	$2.3\ 10^{4}$ ± $3.2\ 10^{2}$	$4.2\ 10^{4}$ ± $2.6\ 10^{3}$	356 ± 197
τ_2 (ns)	13.8 ± 0.6	15.1 ± 1.1	18 ± 0.01	26.6 ± 0.7	126.5 ± 20

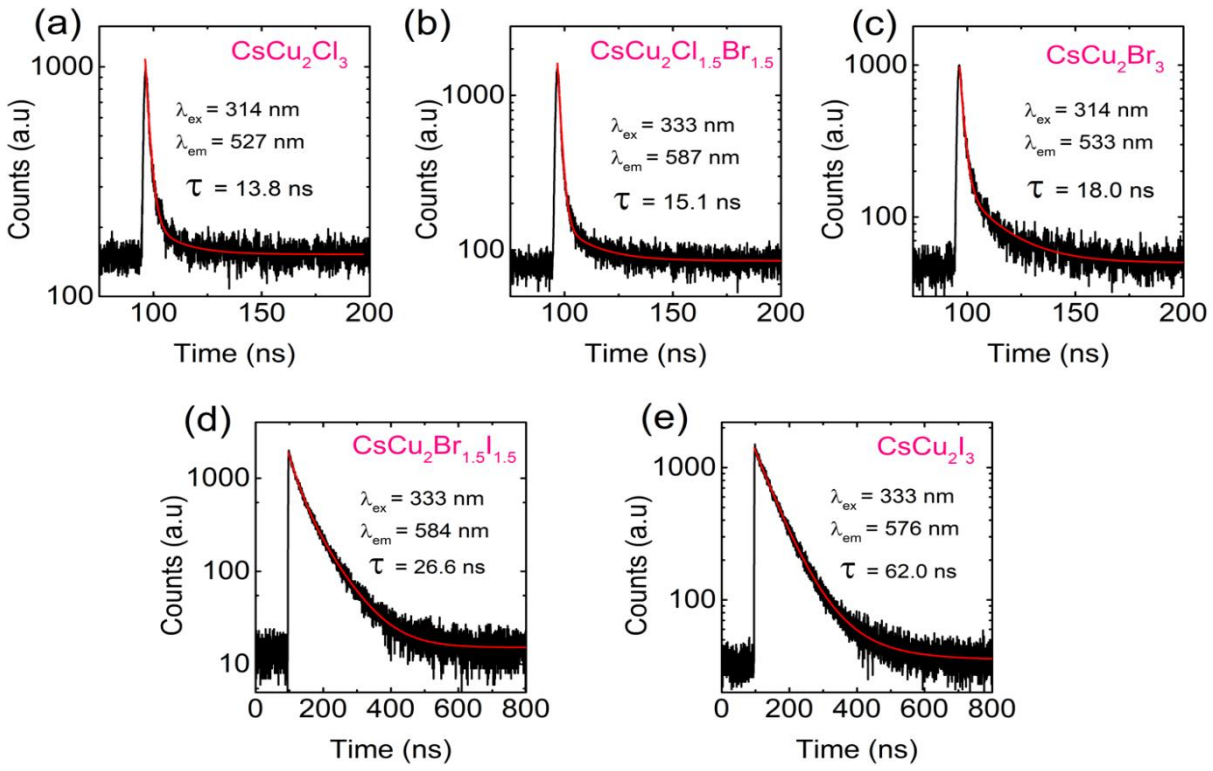


Figure 58. Room temperature time-resolved PL of (a) $CsCu_2Cl_3$, (b) $CsCu_2Cl_{1.5}Br_{1.5}$, (c) $CsCu_2Br_3$, (d) $CsCu_2Br_{1.5}I_{1.5}$, (e) $CsCu_2I_3$.

To obtain further information on the STEs dynamics and the exciton-phonon interaction, we measured the temperature dependence PL of $CsCu_2X_3$, under 325 nm excitation (Figure 59a, and Figure 60). The PL intensity of the highly efficient $CsCu_2Cl_3$, shown in Figure 59a, slightly quenches (~ 3 times) upon heating. However, the thermal quenching is much more significant for $CsCu_2I_3$ (~ 4.5 times) and the alloyed compound $CsCu_2Br_{1.5}I_{1.5}$ (~ 60 times). This is consistent with the trend of the measured PLQYs values (Table 11) which confirms that excitons are much more thermally stable in $CsCu_2Cl_3$.

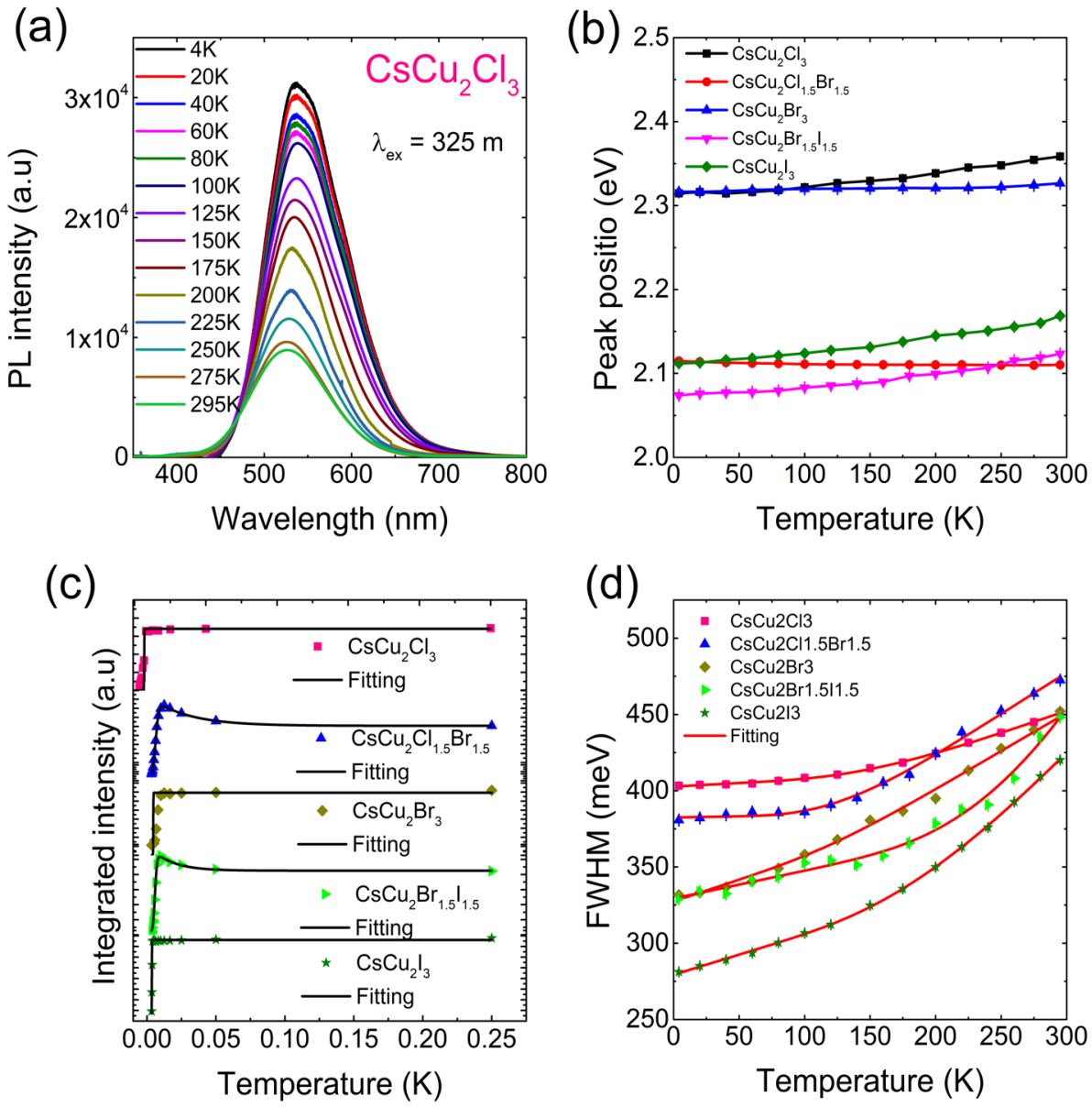


Figure 59. (a) Temperature dependence PL spectra of $CsCu_2Cl_3$, under 325 nm excitation. Thermal evolution of (b) position, (c) integrated intensity, and (d) FHWM of PL peaks of $CsCu_2X_3$. The integrated PL intensity were refined (black curves) based on Eqs (12-14). FWHM were refined based on Eq (12) (red curves).

Based on the temperature dependence PL data, we studied the thermal evolution of the integrated intensity, the position, and FWHM of PL peaks of $CsCu_2X_3$ (Figure 59b-d). In semiconductors, free exciton PL peak red-shifts upon heating is often described by Varshni's

model.[459] Here, the position of PL peaks of $CsCu_2X_3$ are slightly blue-shifted with temperature, particularly for $CsCu_2I_3$ (Figure 59b). Such a blue-shift was also observed in some metal halides[85, 460] and PbS quantum dot,[461] and was attributed to the strong electron-phonon coupling. Moreover, for the non-alloy compounds $CsCu_2Cl_3$, $CsCu_2Br_3$ and $CsCu_2I_3$, the integrated PL intensity quenches upon cooling and then saturates at 100 K (Figure 59c). This quenching can be described by the Arrhenius-type model,[462]

$$I_{PL} = \frac{I_0}{(1 + a \times exp(\frac{-E_b}{k_B T}))} \quad (16)$$

where I_0 is the low-temperature PL intensity, k_B is the Boltzmann constant, a is the ratio between the radiative and the nonradiative decay rates, and E_b is the exciton binding energy. The best fit gives E_b of 201 ± 6 meV, 155 ± 4 meV, and 128 ± 1 meV, for $CsCu_2Cl_3$, $CsCu_2Br_3$ and $CsCu_2I_3$, respectively. These high E_b values are much larger than that of the 3D perovskite $CsPbX_3$ (~18 meV),[463] and are characteristic of low-dimensional materials as discussed earlier. Importantly, the trend of the exciton binding energy furthermore supports the increase of the PLQYs values from 3.23 for $CsCu_2I_3$ to 48% for $CsCu_2Cl_3$ discussed above.[464-466] On the other hand, the integrated PL intensity of the alloys $CsCu_2Cl_{1.5}Br_{1.5}$ and $CsCu_2Br_{1.5}I_{1.5}$, first increases with temperature increasing from 4 to 80 K, then decreases at higher temperature (Figure 59c). The initial increase of PL intensity with temperature is termed "negative thermal quenching"[467] and has been observed in semiconductors,[468-469] and attributed to phonon-assisted nonradiative recombination. These data can be refined using the Shibata model,[467] which involves two competing processes: the quenching of the PL intensity with increasing temperature due to thermal dissociation of the electron-hole pair and the subsequent decrease of the exciton population, and negative thermal quenching due to the thermal excitation of low-energy

nonradiative STEs states towards the higher energy radiative STEs states responsible for the quenching of the PL of the two alloys, $CsCu_2Br_{1.5}I_{1.5}$ and $CsCu_2Br_{1.5}I_{1.5}$.

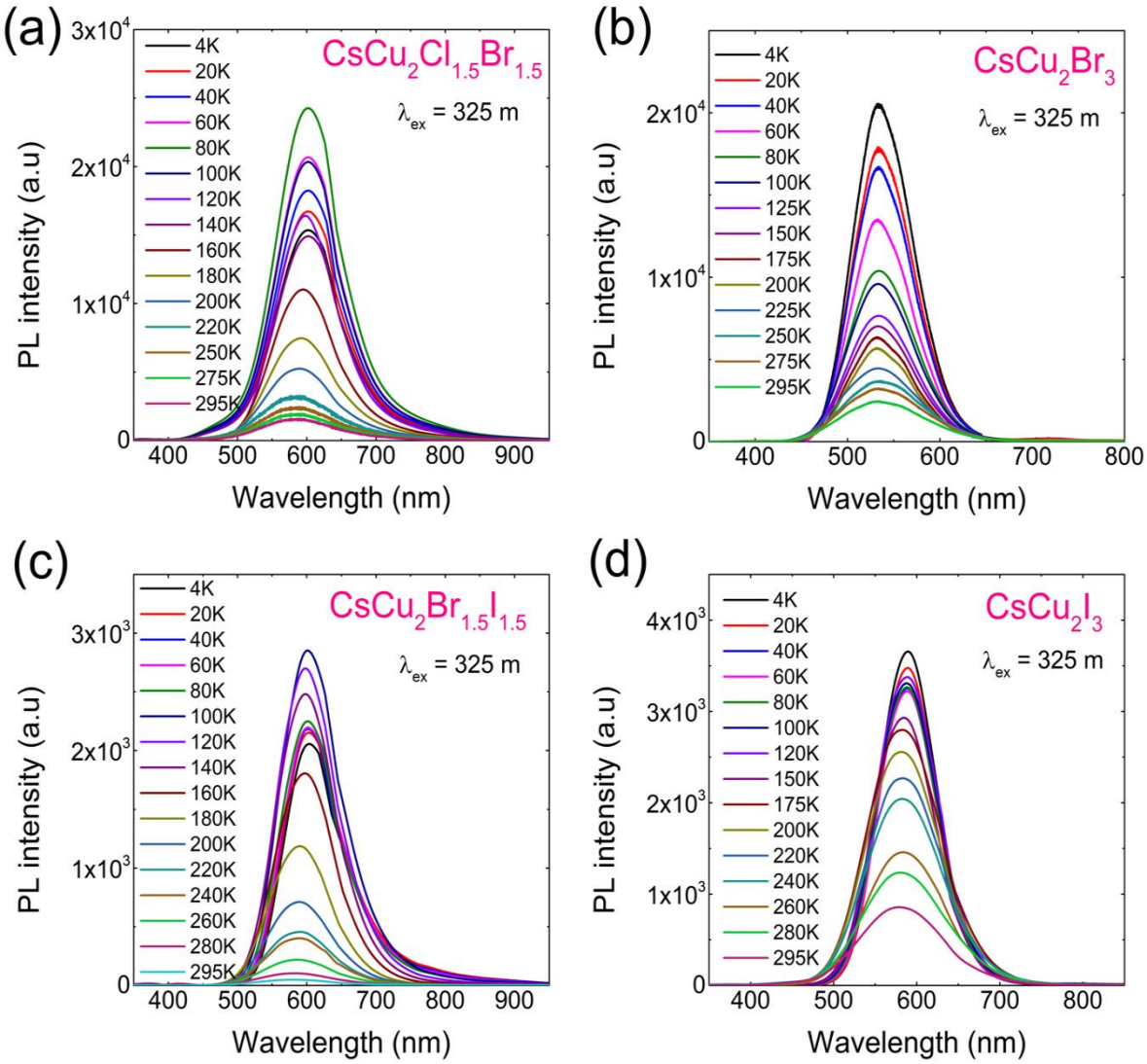


Figure 60. Temperature dependence PL of (a) $CsCu_2Cl_{1.5}Br_{1.5}$, (b) $CsCu_2Br_3$, (c) $CsCu_2Br_{1.5}I_{1.5}$, and (d) $CsCu_2I_3$, under 325 nm irradiation. $CsCu_2Cl_3$ is shown in Figure 59.

In addition, detrapping of the excitons, from STEs to free excitons states, may also lead to thermal quenching of the PL emission.[301] To account for this, we consider two activation

energies for the thermal quenching process. Therefore, the temperature dependence PL intensity is given by,

$$I(T) = I_0 \frac{1 + c \times exp\,(-E_c/k_B T)}{1 + a \times exp\,(-E_a/k_B T) + b \times exp\,(-E_b/k_B T)} \quad (17)$$

where I_0 is the low temperature PL intensity. The activation energies E_b is associated to exciton binding energy, E_a is the self-trapped depth ($E_a = E_{FE} - E_{STE}$), E_c describe the thermal quenching of the PL intensity, and *a*, *b* and *c* are fitting parameters. The best refinement yields E_a = 25 ± 0.8 meV, E_b = 138 ± 5 meV, and E_c = 5.9 ± 0.4 meV for $CsCu_2Cl_{1.5}Br_{1.5}$ and E_a = 29 ± 5 (3) meV, E_b = 98 ± 8 meV, and E_c = 12.2 ± 0.7 meV for $CsCu_2Br_{1.5}I_{1.5}$. Note that E_a is close to the room temperature thermal energy (~ 26 meV), so it would be reasonable to expect free excitonic emission at room temperature. However, the absence of the free exciton peaks is probably due to the sharper STEs emission band compared to free-exciton emission. This furthermore confirms the intrinsic nature of the trapping mechanism.[108, 345, 446] Moreover, the thermal broadening in linewidth of PL of $CsCu_2X_3$ (Figure 59c) originates from exciton-phonon coupling, and described by,

$$\Gamma(T) = \Gamma_0 + \Gamma_{AC} \times T + \Gamma_{LO} \times (1 + exp(\frac{E_{LO}}{k_B T}))^{-1} \quad (18)$$

where the first term is the natural line width at 0 K, the second term represents the broadening induced by acoustic phonons, and the third term corresponds to the contribution of optical phonons to the peak broadening. There, Γ_{LO} is the exciton-phonon coupling constant and E_{LO} is the optical phonon energy. The best refinement parameters, summarized in Table 13, gives Γ_{LO} and E_{LO} values ranging from 471 to 910 meV K^{-1} and from 4.1 to 12.2 meV, respectively. These high exciton- phonon coupling constant values are one order of magnitude larger than

those of lead-based 3D hybrid perovskites (Γ_{LO} of 40-61 meV)[470] and more than two times higher than the reported value of $Cs_3Bi_2I_6Cl_3$,[471] supporting the strength of the electron-phonon coupling in $CsCu_2X_3$. The slight broadening of the emission at lower temperatures can also be attributed to the emission of small CsX impurities only at low temperatures as its identified in our DSC/TGA measurements.[472-474]

Table 13. Refinement results of the temperature dependence FWHM of $CsCu_2X_3$**.**

Sample	**$CsCu_2Cl_3$**	**$CsCu_2Cl_{1.5}Br_{1.5}$**	**$CsCu_2Br_3$**	**$CsCu_2Br_{1.5}I_{1.5}$**	**$CsCu_2I_3$**
Γ_{AC} (meV.K^{-1})	0.05 ± 0.01	0.02 ± 0.008	0.3 ± 0.04	0.18 ± 0.04	027 ± 0.01
Γ_{LO} (meV.K^{-1})	471 ± 13	712 ± 32	512 ± 62	910 ± 42	617 ± 22
E_{LO} (meV)	6.4 ± 0.3	6.2 ± 0.6	5.1 ± 0.2	11.5 ± 0.2	4.3± 0.3

The calculated E_{LO} values of 6.2 and 11.5 for $CsCu_2Cl_{1.5}Br_{1.5}$ and $CsCu_2Cl_{1.5}Br_{1.5}$, respectively, are in excellent agreement with the E_c values of 5.9 ± 0.4 meV and 12.2 ± 0.7 deduced from the fitting of the PL intensity using Shibata's model. Together, these findings support the assignment of the broad PL emission of $CsCu_2X_3$ to phonon-assisted recombination of STEs.

Finally, we want to mention our preliminary attempts to make efficient LED devices based on $CsCu_2X_3$ (see Figure 61). In order to fabricate LEDs, a $CsCu_2I_3$ was used as a yellow emitter in an 1,3-Bis(N-carbazolyl)benzene (mCP) host layer. An ITO is used as a transparent bottom anode. A MoO_3 and a 4,4′-Cyclohexylidenebis[N,N-bis(4-methylphenyl)benzenamine] (TAPC) are used as a hole injection layer and a hole transport layer, respectively. A $CsCu_2I_3$ (10 vol. %) doped in mCP host is used as a yellow emission layer. A 1,3,5-tri (m-pyrid-3-yl-phenyl) - benzene (TmTyPB) and a LiF are used as an electron transport layer and the electron

injection layer, respectively. An Al is used as a top reflective cathode. The $CsCu_2I_3$-based LED shows a yellow emission light with the peak wavelength of 554nm. The quantum efficiency (QE) of ~ 0.1 % was achieved at the luminance of 1 cd/m^2. However, this preliminary device needs more optimization to quantify the efficiency and the stability, which we are currently working on.

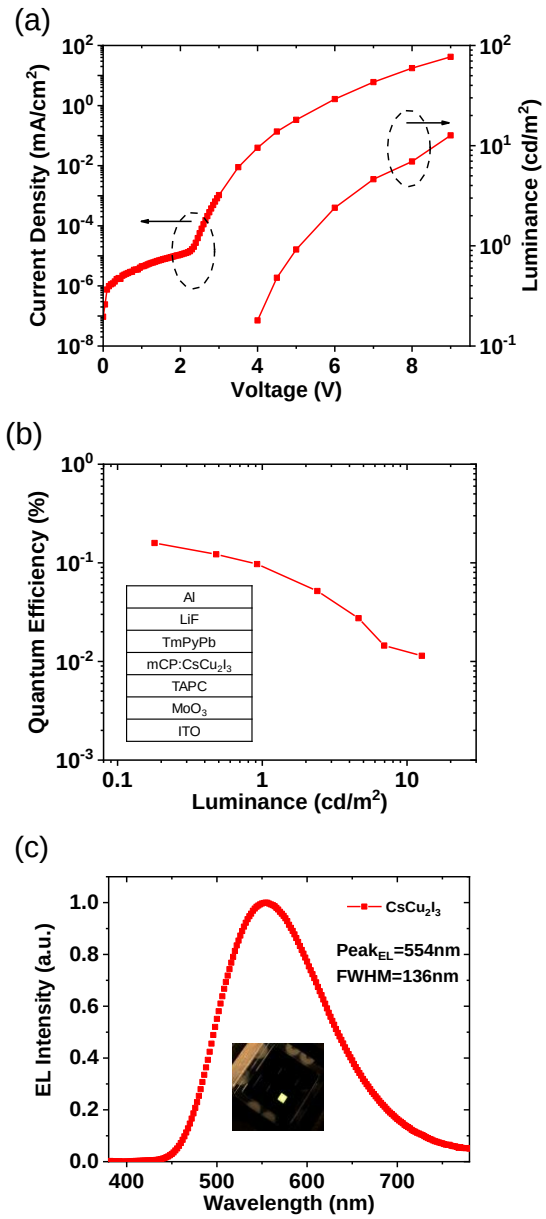


Figure 61. Light-emitting diode (LED) fabricated using $CsCu_2I_3$ as a dopant in a mCP host. (a) Luminance-current-voltage (LIV) characteristics, (b) Quantum efficiency (inset: the device structure), and (c) Electroluminescence (EL) spectrum (inset: a photo image of the LED operating at 8 V) of the LED.

4.3.5 Summary

In conclusion, we report the optical properties of nontoxic, remarkably stable, and highly emissive 1D metal halides $CsCu_2X_3$ (X = Cl, Br, I). Bright, room temperature visible-emission attributed to STEs was observed with PLQY values reaching 48% for $CsCu_2Cl_3$. The photophysical properties of $CsCu_2X_3$ were investigated through temperature and power dependence PL measurements. High exciton binding energies ranging from 98 to 201 meV and high exciton-phonon coupling energies were estimated from the thermal evolution of PL intensity and FWHM. These findings support the assignment of the broad PL emission of $CsCu_2X_3$ to phonon-assisted recombination of STEs.

Through the development of nontoxic and earth-abundant halide light emitting materials, such as $CsCu_2X_3$, a major advancement toward the realization of practically viable environmentally friendly materials technologies for solid-state lighting can be made.

Chapter 5: Future Work And Conclusions

5.1 Summary

The inspiration for this work was drawn from the reports on halide perovskites: their structural diversity and remarkable range of optoelectronic properties they exhibit. The high degree of chemical and structural tunability afforded by the perovskite family has resulted in many new materials that range in structural and electronic dimensionality, giving rise to luminescence properties that are both tunable through chemical composition and structural dimensionality. Most research in the field has focused on $CH_3NH_3PbI_3$ and other Pb- and Sn-based families due to their notable optoelectronic properties which led to their successful incorporation in solar cells[1] and LEDs,[475] but despite this success, the Pb- and Sn-based perovskites suffer from Pb toxicity and poor thermal, air and moisture stability, respectively.[149] While Sb- and Bi-based compositions have been suggested as alternatives to the more toxic Pb-based analogs, the resulting materials, while interesting, lack desirable optoelectronic properties which include suitable direct band gaps for solar and efficient luminescence for LED applications.[133, 152-154] Therefore, major challenges still exist in the field of halide perovskites including (1) the exploration of compositions beyond the dominant Pb- and Sn-based systems, (2) the systematic study of other crystal structure types formed by metal halides, and (3) the effects of connectivity (e.g. edge-sharing, face-sharing, corner-sharing) and thus dimensionality on the properties resulting from these differences.[27] To address these critical challenges, Pb-free metal halide systems were chosen due to their earth-abundance, low cost and lower toxicity in comparison to Pb (e.g., Cu, Zn). Interestingly, despite these advantageous characteristics, many of these metal halide systems have remained relatively unexplored.[199, 242-243, 428] Of the metal candidates, a few metals such as cadmium[223-224, 245] and mercury[185, 476] halides have been

previously synthesized and structurally characterized, but little has been done in the realm of hybrid organic-inorganic structures or optoelectronic property investigations. Therefore, to address this gap in knowledge, the crystal structures and optical properties of multiple R-M-X compounds containing inorganic or organic cations (R = Cs^+, $CH_3NH_3^+$, $C_5H_7N_2^+$, $C_{15}H_{26}N^+$), metals (M = Cu, Zn, Cd, Hg), and halides (X = Cl, Br, I) were studied for this purpose.

In Chapters 2 and 3, we investigated the structural and optical properties of three different low-dimensional hybrid organic-inorganic families, MA_2CdX_4 (MA = CH_3NH_3; X = Cl, Br, I), $4AMP_2MBr_4$ (4AMP = $C_5H_7N_2$, M = Zn, Hg), and R-M-X (R = $C_{15}H_{26}N$, M = Zn, Cd, X = Br, I), as a means to fundamentally probe structure-property relationships in hybrid halides of group 12 metals. The MA_2CdX_4 family demonstrated a change in structure and optical properties as a result of the change in halogen anion down the group, showing a stark difference between the crystal and electronic structure, and optical properties of MA_2CdX_4 members. Thus, it was discovered that MA_2CdCl_4 adopts a 2D layered perovskite structure, whereas MA_2CdBr_4 and MA_2CdI_4 adopt 0D cluster structures. This observation cannot simply be explained through the size effects as calculated tolerance and octahedral factors for all members of the family are within the acceptable ranges for the formation of the perovskite structure. Therefore, we attribute this observation to the electronic effects (i.e., isolated tetrahedral anion clusters are preferable energetically for the heavier bromides and iodides). Indeed, a brief inspection of literature reveals that among the transition metal-based systems, there are a number of known layered perovskite chlorides, whereas examples of bromides and especially iodides adopting the perovskite structure are very limited.[27]

In the $4AMP_2MBr_4$ family, the effect of the change in metal going down the group was examined and was found to result in no significant change in the crystal structure, as both

$4AMP_2ZnBr_4$ and $4AMP_2HgBr_4 \cdot H_2O$ form 0D pseudo-layered non-perovskite structures based on isolated tetrahedra. However, a marked difference in the electronic structures of the Zn and Hg compounds were found based on DFT calculations. Thus, the energy gap of the inorganic cluster is lower than that of the organic molecule for the Hg compound, whereas the opposite is true for the Zn compound, which is consistent with our initial hypothesis that the inorganic cluster's conduction band energy could be customized through metal substitution.

We further examined the effect of the organic cation on the electronic structure of group 12 metal halide systems by studying the crystal and electronic structures, and optical properties of the R-M-X (R = $C_{15}H_{26}N$, M = Zn, Cd, X = Br, I) family. As in the 4AMP family, the presence of the bulky organic (R^+) cation causes the compounds to form 0D crystal structures featuring alternating layers of isolated inorganic anions based on metal tetrahedra and organic cations. The separation of the crystal structure into distinct inorganic and organic molecular units leads to flat bands near the band gap indicative of highly localized electronic states, as was found in the 4AMP family. Furthermore, the 0D molecular structures allow for the localization of the excitons on either anionic or cationic molecular units depending on their chemistries, leading to a change from type I to type II band alignments as Zn is substituted for Cd. It was also determined that the exciton was localized on the organic cation in $(R)ZnBr_3(DMSO)$, adding to the few examples of broadband emission from the organic component of hybrid organic-inorganic materials.[17, 108, 212, 395]

By comparing the three hybrid organic-inorganic group 12 metal halide families, we can clearly see the impact of the organic cation and B-metal variation. The increase in organic cation size from MA^+ to $4AMP^+$ to $C_{15}H_{26}N^+$, leads to the flattening of electronic bands and greater exciton localization. The greater charge localization in both the $4AMP_2MBr_4$ and R-M-

X families is sufficient to stabilize STEs and enable efficient room temperature STE emission, whereas the MA_2CdX_4 family cannot stabilize STEs as well since it features much smaller organic cations and as a result the family does not luminesce at room temperature. Another effect of the organic cation can be seen in the MA_2CdX_4 system, where the small organic cation MA^+ does not contribute to the states at the valence band maxima (VBM) or conduction band minima (CBM) because its orbitals are too far removed from the band edges (i.e., VBM and CBM). Thus in this family, MA^+ merely act as spacer ions filling the voids between the CdX_4^{2-} anions. However, in both the $4AMP_2MBr_4$ and the R-M-X families, the aromatic organic cation actively contributes to the VBM of $4AMP_2HgBr_4$, the CBM of $RCdI_3$(DMSO) and R_2CdBr_4·DMSO, and both the VBM and CBM of the $4AMP_2ZnBr_4$ and $RZnBr_3$(DMSO). This is a rare example in literature that clearly demonstrates that depending upon the HOMO and LUMO energy levels of the organic cation, it can actively contribute to the observed optoelectronic properties of hybrid metal halides. Thus, we show through these systems that band alignment engineering can be achieved in hybrid organic-inorganic halides to controllably create type I and type II band alignments and improve luminescence through careful selection of the organic and inorganic components. The broadband emission offered by these compounds suggests potential applications as phosphor or scintillation materials, and are currently being considered for these applications in collaboration with Dr. DoYoung Kim at OSU Tusla.

Despite the relatively good stability and luminescence of the group 12 metal halide families presented in this dissertation, improvement for both were sought and found in the all-inorganic CsX-CuX system presented in Chapter 4. By replacing the organic cations with Cs^+, air and moisture stability of over two months was achieved, along with thermal stability up to 500 °C. By further replacing the group 12 metals halides with copper halides, far greater

luminescence was achieved by the $Cs_3Cu_2X_5$ (X = Br, I) and $CsCu_2X_3$ (X = Cl, Br, I) families. Both families exhibit tunable, visibly bright room temperature emission with measured PLQY up to unity, where the highest for the hybrid organic-inorganic group 12 metal halide families was 19%. In both $Cs_3Cu_2X_5$ and $CsCu_2X_3$, emission was attributed to STEs. Unlike the hybrid halides of group 12 metals, the emission in all-inorganic copper halides is noticeably narrower. This can be explained by the fact that all-inorganic copper halides do not have emissive organic cations that contribute to the observed luminescence properties. DFT calculations for the $Cs_3Cu_2X_5$ family suggested strong exciton localization as a result of significant structural reorganization of Cu_2X_5 moieties in the excited state, which further enhances the binding energies and thus their emission. In-depth electronic band structure and excitonic calculations are currently underway for the $CsCu_2X_3$ family to determine the physical mechanism of emission, but structural reorganization caused by strong exciton localization is likely to be the cause of the emission in this system as well. The remarkably efficient luminescence of Cu-based halides prepared in this project allows for the consideration of $Cs_3Cu_2X_5$ and $CsCu_2X_3$ for practical applications (e.g., in LEDs). In fact, some preliminary device studies have already been performed and further optimization of LED devices are planned through a collaboration with Dr. DoYoung Kim's group at OSU Tulsa.

5.2 Future Work

The Cu, Zn, Cd and Hg halide systems presented here demonstrate how room temperature luminescence can be systematically enhanced through the alteration of chemical composition and crystal structure. The mechanism of luminescence in these materials, in particular hybrid organic-inorganic materials, is quite complicated and may involve

contributions from defects, surface states, and excitons localized on organic molecular cations and inorganic anions. To continue on the route to discovering new and better luminescent materials, different organic cations and metals can be systematically introduced to gain a better understanding of how size, composition, electronegativity and bonding/coordination affect the color of emission, color purity and rendition, and the luminescence efficiency of the resulting crystal families.

To begin, current work involving the systematic study of the effects of changing both the metal and halide on the luminescence of the R_2MX_4 (R = $C_6H_5C_2H_4NH_3$, M = Zn, Cd, Hg; X = Cl, Br, I) system is underway. Preliminary results show that most compounds in this family adopt a 0D structure composed of isolated inorganic tetrahedral anions unlike the Pb and Sn-based analogs, which adopt 2D layered structures. Our group 12 metal based R_2MX_4 compounds exhibit emission ranging from orange to purple depending upon the metal and halogen composition with PLQYs ranging from 4.2% to 0.1%. As the halide composition is varied down the group for M = Zn and Hg, the emission color blue shifts, whereas emission from the M = Cd compounds red shift from blue to green. A similar study is also being carried out to determine the effects of substituting the halide anion with a pseudo-halide (e.g., SCN^-) in the $4AMP_2MCl_{1-x}SCN_x$ (M = Zn, Cd, Hg). Interestingly, the thiocyanate ion can bind to the metal through either S or N end depending on the metal. Our preliminary results suggest yellow and blue emission for $4AMP_2ZnCl(NCS)_3$ and $4AMP_2CdCl_2(NCS)_2$, respectively, with the highest PLQY of 6.8% for $4AMP_2CdCl_2(NCS)_2$. Luminescence of other PEA and 4AMP containing hybrid halide structures such as PEA_2PbCl_4 and our $4AMP_2ZnBr_4$ show white-light emission which has been attributed to self-trapped excitons localized on the organic molecules.[112, 477] Therefore, it is possible that the emission originates from the organic molecule

in these new systems as well. However, further investigations including DFT calculations, power-dependent, temperature-dependent and time-resolved PL measurements are needed to confirm the mechanism of luminescence and the extent to which the organic molecule contributes to the emission spectrum.

The ability to change the band alignment type by selecting organic cations with HOMO-LUMO gaps that are similar in energy to that created by the metal halide systems, suggests the possibility of more selective crystal engineering for tuning of physical properties for various applications. To delve into the possibility of structurally engineering type-I and type-II quantum-well materials, the first step is to determine the effect of the alteration of the structure of the organic cation on the resulting system. Work in this direction was started through an ongoing collaboration with Dr. Matthew Houck from Dr. Daniel T. Glatzhofer's group, who systematically removed the methyl groups around the aromatic ring of the $C_{15}H_{26}N^+$ molecule used in the reported R-M-X compounds,[113] resulting in the bromide salts of the $C_{14}H_{23}N^+$, $C_{13}H_{20}N^+$, $C_{12}H_{17}N^+$, and $C_{11}H_{14}N^+$ cations (denoted as A below).[478] Using these cations, a series of 0D isolated tetrahedra based $AFeBr_4$ compounds were synthesized that exhibit room temperature blue emission with the highest PLQY value of 2% for the $C_{15}H_{26}NFeBr_4$ compound. This is an unexpected finding given the fact that transition metals such as Fe based halides are known to exhibit numerous defects that are detrimental to luminescence properties. However, in our case, preliminary results suggest that emission may be originating from the organic molecules based on the comparisons between PL spectra of $AFeBr_4$ and the corresponding organic salts emission spectra. However, further investigations including DFT calculations and more in-depth optical characterization are needed to confirm the origin of the luminescence and the extent to which the organic molecule contributes to the emission

spectrum. Future directions will also include the modification of other ammonium containing cations such as 4-dimethylaminopyridine, or functionalized naphthalene or anthracene molecules which would provide a change in size and width of the molecule. Importantly, heavily conjugated π-systems can also alter the contribution of the organic molecule to the luminescence properties and the band structure of the materials they are successfully incorporated in, which may lead to better phosphors and emitters for LED applications. Finally, supporting our interest in potential radiation detection materials based on hybrid halides, naphthalene- and anthracene-based organic molecules may also find applications in this area.[479]

It will also be beneficial to examine other transition metal halide systems to determine if the perovskite structure is accessible within these systems and to explore hitherto unknown, brand new exotic structure types that may be discovered during the process. Structures featuring other first row transition metals would be of great interest as the majority are earth abundant, inexpensive, relatively nontoxic, and may offer interesting new physical properties (e.g., magnetic, ferroelectric etc.) through the influence of their partially filled *d*-orbitals.[13] Currently, other systems containing first row transition metals such as Mn, Fe, Co, and Cu are being considered for such studies. Preliminary results show the formation of new 0D isolated tetrahedra-based structures of PEA_2MnI_4, $MAFeCl_4$, $MAFeBr_4$, and $4AMP_2CoX_4$ and $4AMP_2CuX_4$ (MA = CH_3NH_3, X = Cl, Br, I) families. The earth abundance and interesting properties afforded by the use of other transition metals opens the door for other potential applications of these materials.

Due to the earth abundant, cost effective, and nontoxic nature of copper metal, continued exploration of Cu halide-based systems like those reported here should offer rich and promising discoveries. To start, the simplest modification is the substitution of the Cs^+ or X^- positions. In

confirmation of this concept, recently, two compounds substituting the Cs^+ position $KCuCl_3$[480] and $CH_3NH_3Cu_2I_3$[481] were used to demonstrate desirable optoelectronic properties with $KCuCl_3$ being reported as a viable photodetector material. Our own preliminary results on the optical properties of Rb_2CuCl_3 also show promise, as the family shows remarkable blue emission under excitation and is a current topic under investigation by our group. Pseudo-halogens such as SCN^-, $SeCN^-$ or OCN^- could also offer alternative routes to crystal structure modification and consequently optical properties manipulations.[482]

In summary, our work originally inspired by the groundbreaking discoveries in the field of hybrid organic-inorganic halide perovskites has evolved into the discoveries of brand-new compounds with exotic crystal structures and outstanding light emission properties. The fundamental study of low-dimensional metal halides of both perovskite and non-perovskite structure types is of great importance as the field works towards a greater understanding of the structure-property relationships that arise within these fascinating materials. Our work confirms the essentially limitless chemical diversity of low-dimensional metal halides for the creation of custom-design materials that controllably exhibit luminescence from each of the components including organic cations, inorganic anions and/or defects and impurities.

References

1. Bi, D.; Tress, W.; Dar, M. I.; Gao, P.; Luo, J.; Renevier, C.; Schenk, K.; Abate, A.; Giordano, F.; Correa Baena, J.-P.; Decoppet, J.-D.; Zakeeruddin, S. M.; Nazeeruddin, M. K.; Grätzel, M.; Hagfeldt, A., Efficient luminescent solar cells based on tailored mixed-cation perovskites. *Sci. Adv.* **2016,** *2* (1), e1501170.
2. Mitzi, D. B., Templating and structural engineering in organic–inorganic perovskites. *J. Chem. Soc., Dalton Trans.* **2001,** (1), 1-12.
3. Kojima, A.; Teshima, K.; Shirai, Y.; Miyasaka, T., Organometal Halide Perovskites as Visible-Light Sensitizers for Photovoltaic Cells. *J. Am. Chem. Soc.* **2009,** *131* (17), 6050-6051.
4. Aydin, E.; De Bastiani, M.; Yang, X.; Sajjad, M.; Aljamaan, F.; Smirnov, Y.; Hedhili, M. N.; Liu, W.; Allen, T. G.; Xu, L., Zr-Doped Indium Oxide (IZRO) Transparent Electrodes for Perovskite-Based Tandem Solar Cells. *Adv. Funct. Mater.* **2019**, 1901741.
5. Laboratory, N. R. E., Best Research-Cell Efficiencies. 53 ed.; Golden, CO, 2019.
6. Era, M.; Morimoto, S.; Tsutsui, T.; Saito, S., Organic-inorganic heterostructure electroluminescent device using a layered perovskite semiconductor $(C_6H_5C_2H_4NH_3)_2PbI_4$. *Appl. Phys. Lett.* **1994,** *65* (6), 676-678.
7. Tan, Z.-K.; Moghaddam, R. S.; Lai, M. L.; Docampo, P.; Higler, R.; Deschler, F.; Price, M.; Sadhanala, A.; Pazos, L. M.; Credgington, D.; Hanusch, F.; Bein, T.; Snaith, H. J.; Friend, R. H., Bright light-emitting diodes based on organometal halide perovskite. *Nat. Nano.* **2014,** *9*, 687.
8. Wang, N.; Cheng, L.; Ge, R.; Zhang, S.; Miao, Y.; Zou, W.; Yi, C.; Sun, Y.; Cao, Y.; Yang, R., Perovskite light-emitting diodes based on solution-processed self-organized multiple quantum wells. *Nat. Photon.* **2016,** *10* (11), 699.
9. Jaramillo-Quintero, O. A.; Sanchez, R. S.; Rincon, M.; Mora-Sero, I., Bright Visible-Infrared Light Emitting Diodes Based on Hybrid Halide Perovskite with Spiro-OMeTAD as a Hole-Injecting Layer. *J. Phys. Chem. Lett.* **2015,** *6* (10), 1883-1890.
10. Zhong, J.; Chen, D.; Zhou, Y.; Wan, Z.; Ding, M.; Bai, W.; Ji, Z., New Eu^{3+}-activated perovskite $La_{0.5}Na_{0.5}TiO_3$ phosphors in glass for warm white light emitting diodes. *Dalton Trans.* **2016,** *45* (11), 4762-4770.
11. Xu, W.; Hu, Q.; Bai, S.; Bao, C.; Miao, Y.; Yuan, Z.; Borzda, T.; Barker, A. J.; Tyukalova, E.; Hu, Z., Rational molecular passivation for high-performance perovskite light-emitting diodes. *Nat. Photon.* **2019**, 418.
12. Lin, T. A.; Chatterjee, T.; Tsai, W. L.; Lee, W. K.; Wu, M. J.; Jiao, M.; Pan, K. C.; Yi, C. L.; Chung, C. L.; Wong, K. T., Sky-blue organic light emitting diode with 37% external quantum efficiency using thermally activated delayed fluorescence from spiroacridine-triazine hybrid. *Adv. Mater.* **2016,** *28* (32), 6976-6983.
13. Smith, M. D.; Connor, B. A.; Karunadasa, H. I., Tuning the Luminescence of Layered Halide Perovskites. *Chem. Rev.* **2019,** *119* (5), 3104-3139.
14. Yin, W. J.; Shi, T.; Yan, Y., Unique properties of halide perovskites as possible origins of the superior solar cell performance. *Adv. Mater.* **2014,** *26* (27), 4653-4658.
15. Frost, J. M.; Butler, K. T.; Brivio, F.; Hendon, C. H.; Van Schilfgaarde, M.; Walsh, A., Atomistic origins of high-performance in hybrid halide perovskite solar cells. *Nano Lett.* **2014,** *14* (5), 2584-2590.

16. Zhang, Y.; Saidaminov, M. I.; Dursun, I.; Yang, H.; Murali, B.; Alarousu, E.; Yengel, E.; Alshankiti, B. A.; Bakr, O. M.; Mohammed, O. F., Zero-dimensional Cs_4PbBr_6 perovskite nanocrystals. *J. Phys. Chem. Lett.* **2017,** *8* (5), 961-965.
17. Smith, M. D.; Karunadasa, H. I., White-Light Emission from Layered Halide Perovskites. *Acc.Chem. Res.* **2018,** *51* (3), 619-627.
18. Lyu, M.; Yun, J. H.; Chen, P.; Hao, M.; Wang, L., Addressing Toxicity of Lead: Progress and Applications of Low-Toxic Metal Halide Perovskites and Their Derivatives. *Adv. En. Mater.* **2017,** *7* (15), 1602512.
19. Zhao, X.; Park, N.-G. In *Stability issues on perovskite solar cells*, Photonics, Multidisciplinary Digital Publishing Institute: 2015; pp 1139-1151.
20. Leijtens, T.; Eperon, G. E.; Noel, N. K.; Habisreutinger, S. N.; Petrozza, A.; Snaith, H. J., Stability of metal halide perovskite solar cells. *Adv. En. Mater.* **2015,** *5* (20), 1500963.
21. Etgar, L., The merit of perovskite's dimensionality; can this replace the 3D halide perovskite? *Energy & Environ. Sci.* **2018,** *11* (2), 234-242.
22. Liao, J.-F.; Rao, H.-S.; Chen, B.-X.; Kuang, D.-B.; Su, C.-Y., Dimension engineering on cesium lead iodide for efficient and stable perovskite solar cells. *J. Mater. Chem. A* **2017,** *5* (5), 2066-2072.
23. Smith, I. C.; Hoke, E. T.; Solis-Ibarra, D.; McGehee, M. D.; Karunadasa, H. I., A Layered Hybrid Perovskite Solar-Cell Absorber with Enhanced Moisture Stability. *Angew. Chem. Int. Ed.* **2014,** *53* (42), 11232-11235.
24. Tombe, S.; Adam, G.; Heilbrunner, H.; Apaydin, D. H.; Ulbricht, C.; Sariciftci, N. S.; Arendse, C. J.; Iwuoha, E.; Scharber, M. C., Optical and electronic properties of mixed halide (X= I, Cl, Br) methylammonium lead perovskite solar cells. *J. Mater. Chem.* **2017,** *5* (7), 1714-1723.
25. Weber, D., $CH_3NH_3PbX_3$, ein Pb (II)-system mit kubischer perowskitstruktur/ $CH_3NH_3PbX_3$, a Pb (II)-system with cubic perovskite structure. *Z. Natur. B* **1978,** *33* (12), 1443-1445.
26. Mitzi, D. B.; Feild, C.; Harrison, W.; Guloy, A., Conducting tin halides with a layered organic-based perovskite structure. *Nature* **1994,** *369* (6480), 467.
27. Saparov, B.; Mitzi, D. B., Organic–Inorganic Perovskites: Structural Versatility for Functional Materials Design. *Chem. Rev.* **2016,** *116* (7), 4558-4596.
28. Cava, R.; Batlogg, B.; Krajewski, J.; Farrow, R.; Rupp, L., A. E. White, K. Short, W. F. Peck and T. Kometani. *Nature* **1988,** *332*, 814.
29. McClure, E. T.; Ball, M. R.; Windl, W.; Woodward, P. M., Cs_2AgBiX_6 (X= Br, Cl): new visible light absorbing, lead-free halide perovskite semiconductors. *Chem. Mater.* **2016,** *28* (5), 1348-1354.
30. Goldschmidt, V. M., Die gesetze der krystallochemie. *Naturwissenschaften* **1926,** *14* (21), 477-485.
31. Kieslich, G.; Sun, S.; Cheetham, A. K., An extended tolerance factor approach for organic–inorganic perovskites. *Chem. Sci.* **2015,** *6* (6), 3430-3433.
32. Travis, W.; Glover, E.; Bronstein, H.; Scanlon, D.; Palgrave, R., On the application of the tolerance factor to inorganic and hybrid halide perovskites: a revised system. *Chem. Sci.* **2016,** *7* (7), 4548-4556.
33. Liang, L.; Wencong, L.; Nianyi, C., On the criteria of formation and lattice distortion of perovskite-type complex halides. *J. Phys. Chem. Solids* **2004,** *65* (5), 855-860.

34. Li, C.; Soh, K. C. K.; Wu, P., Formability of ABO_3 perovskites. *J. Alloys Compd.* **2004,** *372* (1-2), 40-48.
35. Li, C.; Lu, X.; Ding, W.; Feng, L.; Gao, Y.; Guo, Z., Formability of ABX_3 (X= F, Cl, Br, I) Halide Perovskites. *Acta Crystallogr. Sect. B.* **2008,** *64* (6), 702-707.
36. Swainson, I.; Chi, L.; Her, J.-H.; Cranswick, L.; Stephens, P.; Winkler, B.; Wilson, D. J.; Milman, V., Orientational ordering, tilting and lone-pair activity in the perovskite methylammonium tin bromide, $CH_3NH_3SnBr_3$. *Acta Crystallogr. Sect. B.* **2010,** *66* (4), 422-429.
37. Zarychta, B.; Bujak, M.; Zaleski, J., Distortions of $[Sb_2Cl_{10}]_4$ Bioctahedra and Phase Transitions in the Chloroantimonate (III)$(C_3H_5NH_3)_2$ $[SbCl_5]\cdot(C_3H_5NH_3)Cl$. *Z. Natur. B* **2007,** *62* (1), 44-50.
38. Worhatch, R. J.; Kim, H.; Swainson, I. P.; Yonkeu, A. L.; Billinge, S. J., Study of Local Structure in Selected Organic–Inorganic Perovskites in the $Pm\bar{3}m$ Phase. *Chem. Mater.* **2008,** *20* (4), 1272-1277.
39. Donaldson, J. D.; Silver, J.; Hadjiminolis, S.; Ross, S. D., Effects of the presence of valence-shell non-bonding electron pairs on the properties and structures of caesium tin (II) bromides and of related antimony and tellurium compounds. *Dalton Trans.* **1975,** (15), 1500-1506.
40. Christensen, A. N.; Rasmussen, S., A ferroelectric chloride of perovskite type. *Acta Chem. Scand* **1965,** *19*, 421-428.
41. Winkler, B.; Milman, V.; Lee, M.-H., Pressure-induced change of the stereochemical activity of a lone electron pair. *J. Chem. Phys.* **1998,** *108* (13), 5506-5509.
42. Yamada, K.; Isobe, K.; Tsuyama, E.; Okuda, T.; Furukawa, Y., Chloride ion conductor $CH_3NH_3GeCl_3$ studied by Rietveld analysis of X-ray diffraction and ^{35}Cl NMR. *Solid State Ionics* **1995,** *79*, 152-157.
43. Lufaso, M. W.; Woodward, P. M., Jahn–Teller distortions, cation ordering and octahedral tilting in perovskites. *Acta Crystallogr. Sect. B.* **2004,** *60* (1), 10-20.
44. Mizokawa, T. In *Jahn-Teller effects in transition-metal compounds with small charge-transfer energy*, J. Phys. Conf. Ser., IOP Publishing: 2013; p 012020.
45. Willett, R. D.; Liles Jr, O.; Michelson, C., Electronic absorption spectra of monomeric copper (II) chloride species and the electron spin resonance spectrum of the square-planar $CuCl_4^{2-}$ion. *Inorg. Chem.* **1967,** *6* (10), 1885-1889.
46. Bellitto, C.; Day, P., Bis (monoalkylammonium) tetrachlorochromates (II): a new series of two-dimensional ionic ferromagnets. *J. Chem. Soc., Chem. Commun.* **1976,** (21), 870-871.
47. de la Garanderie, P., H. Complexes Luminescents du Chlorure de Manganèse avuc les Amines. *CR Hebd. Seances Acad. Sci* **1962,** *254*, 2739.
48. De Jongh, L.; Botterman, A.; De Boer, F.; Miedema, A., Transition Temperature of the Two-Dimensional Heisenberg Ferromagnet with S= ½. *J. Appl. Phys.* **1969,** *40* (3), 1363-1365.
49. de Jongh, L. J.; Miedema, A. R., Experiments on simple magnetic model systems. *Adv. Phys.* **1974,** *23* (1), 1-260.
50. Mitzi, D. B., A layered solution crystal growth technique and the crystal structure of $(C_6H_5C_2H_4NH_3)_2PbCl_4$. *J. Solid State Chem.* **1999,** *145* (2), 694-704.

51. Stoumpos, C. C.; Cao, D. H.; Clark, D. J.; Young, J.; Rondinelli, J. M.; Jang, J. I.; Hupp, J. T.; Kanatzidis, M. G., Ruddlesden–Popper hybrid lead iodide perovskite 2D homologous semiconductors. *Chem. Mater.* **2016,** *28* (8), 2852-2867.
52. Mitzi, D. B.; Liang, K.; Wang, S., Synthesis and characterization of $[NH_2C(I)NH_2]_2ASnI_5$ with A= iodoformamidinium or formamidinium: the chemistry of cyanamide and tin (II) iodide in concentrated aqueous hydriodic acid solutions. *Inorg. Chem.* **1998,** *37* (2), 321-327.
53. Li, Y.; Lin, C.; Zheng, G.; Cheng, Z.; You, H.; Wang, W.; Lin, J., Novel<110>-Oriented Organic− Inorganic Perovskite Compound Stabilized by N-(3-Aminopropyl) imidazole with Improved Optical Properties. *Chem. Mater.* **2006,** *18* (15), 3463-3469.
54. Zaleski, J.; Pietraszko, A., Structure at 200 and 298 K and X-ray investigations of the phase transition at 242 K of $[NH_2(CH_3)_2]_3Sb_2Cl_9$(DMACA). *Acta Crystallogr. Sect. B.* **1996,** *52* (2), 287-295.
55. Kallel, A.; Bats, J., Tris(trimethylammonium) nonachlorodiantimonate (III), $[NH(CH_3)_3]_3[Sb_2Cl_9]$. *Acta Crystallogr. Sect. C.* **1985,** *41* (7), 1022-1024.
56. Mitzi, D. B., Synthesis, structure, and properties of organic-inorganic perovskites and related materials. *Prog. Inorg. Chem.* **1999**, 1-121.
57. Mitzi, D. B.; Dimitrakopoulos, C. D.; Kosbar, L. L., Structurally tailored organic− inorganic perovskites: optical properties and solution-processed channel materials for thin-film transistors. *Chem. Mater.* **2001,** *13* (10), 3728-3740.
58. Xu, Z.; Mitzi, D. B.; Dimitrakopoulos, C. D.; Maxcy, K. R., Semiconducting perovskites $(2\text{-}XC_6H_4C_2H_4NH_3)_2SnI_4$ (X= F, Cl, Br): steric interaction between the organic and inorganic layers. *Inorg. Chem.* **2003,** *42* (6), 2031-2039.
59. Knutson, J. L.; Martin, J. D.; Mitzi, D. B., Tuning the Band Gap in Hybrid Tin Iodide Perovskite Semiconductors Using Structural Templating. *Inorg. Chem.* **2005,** *44* (13), 4699-4705.
60. Du, K.-z.; Tu, Q.; Zhang, X.; Han, Q.; Liu, J.; Zauscher, S.; Mitzi, D. B., Two-dimensional Lead (II) halide-based hybrid perovskites templated by acene alkylamines: crystal structures, optical properties, and piezoelectricity. *Inorg. Chem.* **2017,** *56* (15), 9291-9302.
61. Billing, D. G.; Lemmerer, A., Inorganic–organic hybrid materials incorporating primary cyclic ammonium cations: The lead iodide series. *CrystEngComm* **2007,** *9* (3), 236-244.
62. Li, Y.; Zheng, G.; Lin, C.; Lin, J., Synthesis, structure and optical properties of different dimensional organic–inorganic perovskites. *Solid State Sciences* **2007,** *9* (9), 855-861.
63. Yuan, Z.; Zhou, C.; Messier, J.; Tian, Y.; Shu, Y.; Wang, J.; Xin, Y.; Ma, B., A Microscale Perovskite as Single Component Broadband Phosphor for Downconversion White-Light-Emitting Devices. *Adv. Opt. Mater.* **2016,** *4* (12), 2009-2015.
64. Weber, O. J.; Marshall, K. L.; Dyson, L. M.; Weller, M. T., Structural diversity in hybrid organic–inorganic lead iodide materials. *Acta Crystallog. B* **2015,** *71* (6), 668-678.
65. Wang, S.; Mitzi, D. B.; Feild, C. A.; Guloy, A., Synthesis and characterization of $[NH_2C(I)=NH_2]_3MI_5$ (M= Sn, Pb): stereochemical activity in divalent tin and lead

halides containing Single <110> Perovskite sheets. *J. Am. Chem. Soc.* **1995,** *117* (19), 5297-5302.
66. Zhou, C.; Tian, Y.; Wang, M.; Rose, A.; Besara, T.; Doyle, N. K.; Yuan, Z.; Wang, J. C.; Clark, R.; Hu, Y., Low-Dimensional Organic Tin Bromide Perovskites and Their Photoinduced Structural Transformation. *Angew. Chem.* **2017,** *129* (31), 9146-9150.
67. Benin, B. M.; Dirin, D. N.; Morad, V.; Wörle, M.; Yakunin, S.; Rainò, G.; Nazarenko, O.; Fischer, M.; Infante, I.; Kovalenko, M. V., Highly Emissive Self-Trapped Excitons in Fully Inorganic Zero-Dimensional Tin Halides. *Angew. Chem. Int. Ed.* **2018,** *57* (35), 11329-11333.
68. Zhou, C.; Tian, Y.; Yuan, Z.; Lin, H.; Chen, B.; Clark, R.; Dilbeck, T.; Zhou, Y.; Hurley, J.; Neu, J.; Besara, T.; Siegrist, T.; Djurovich, P.; Ma, B., Highly Efficient Broadband Yellow Phosphor Based on Zero-Dimensional Tin Mixed-Halide Perovskite. *ACS Appl. Mater. Inter.* **2017,** *9* (51), 44579-44583.
69. Han, K.; Zhang, R.; Mao, X.; Yang, Y.; Yang, S.; Zhao, W.; Wumaier, T.; Deng, W., Air-Stable, Lead-Free Zero-Dimensional Mixed Bismuth-Antimony Perovskite Single Crystals with Ultrabroad Band Emission. *Angew. Chem.* **2019,** *131* (9), 2751-2755.
70. Dobrzycki, L.; Woźniak, K., 1D vs 2D crystal architecture of hybrid inorganic–organic structures with benzidine dication. *J. Mol. Struc.* **2009,** *921* (1-3), 18-33.
71. Zhou, C.; Lin, H.; Tian, Y.; Yuan, Z.; Clark, R.; Chen, B.; van de Burgt, L. J.; Wang, J. C.; Zhou, Y.; Hanson, K., Luminescent zero-dimensional organic metal halide hybrids with near-unity quantum efficiency. *Chem. Sci.* **2018,** *9* (3), 586-593.
72. Pilania, G.; Balachandran, P. V.; Kim, C.; Lookman, T., Finding new perovskite halides via machine learning. *Front. Mater.* **2016,** *3*, 19.
73. Yuan, Z.; Zhou, C.; Tian, Y.; Shu, Y.; Messier, J.; Wang, J. C.; Van De Burgt, L. J.; Kountouriotis, K.; Xin, Y.; Holt, E., One-dimensional organic lead halide perovskites with efficient bluish white-light emission. *Nat. Commun.* **2017,** *8*, 14051.
74. Lin, H.; Zhou, C.; Tian, Y.; Siegrist, T.; Ma, B., Low-Dimensional Organometal Halide Perovskites. *ACS Energy Letters* **2018,** *3* (1), 54-62.
75. Hoffman, R. *Solids and Surfaces: A Chemist's View of Bonding in Extended Structures*; Cornell University: 1988.
76. Fox, A. M., Optical Properties of Solids. 2 ed.; Oxford University Press: 2010.
77. Han, D.; Shi, H.; Ming, W.; Zhou, C.; Ma, B.; Saparov, B.; Ma, Y.-Z.; Chen, S.; Du, M.-H., Unraveling luminescence mechanisms in zero-dimensional halide perovskites. *J. Mater. Chem.* **2018,** *6* (24), 6398-405.
78. Huang, J.; Yuan, Y.; Shao, Y.; Yan, Y., Understanding the physical properties of hybrid perovskites for photovoltaic applications. *Nat. Rev. Mat.* **2017,** *2* (7), 17042.
79. Straus, D. B.; Kagan, C. R., Electrons, excitons, and phonons in two-dimensional hybrid perovskites: connecting structural, optical, and electronic properties. *J. Phys. Chem. Lett.* **2018,** *9* (6), 1434-1447.
80. Bohun, A.; Dolejší, J.; Barta, Č., The absorption and luminescence of $(PbCl_6)_4$ and $(PbBr_6)_4$ complexes. *Czech. J. Phys. B* **1970,** *20* (7), 803-807.
81. Pelant, I.; Valenta, J., *Luminescence spectroscopy of semiconductors*. Oxford University Press: 2012.
82. Mitzi, D. B.; Chondroudis, K.; Kagan, C. R., Organic-inorganic electronics. *IBM J. Res. Dev.* **2001,** *45* (1), 29-45.

83. Dragoman, D.; Dragoman, M., *Optical characterization of solids*. Springer Science & Business Media: 2013.
84. Böer, K. W.; Pohl, U. W.; Böer, K. W.; Pohl, U. W., Excitons. *Semiconductor Physics* **2019**, 1-41.
85. Yangui, A.; Pillet, S.; Bendeif, E.-E.; Lusson, A.; Triki, S.; Abid, Y.; Boukheddaden, K., Broadband Emission in a New Two-Dimensional Cd-Based Hybrid Perovskite. *ACS Photon.* **2018,** *5* (4), 1599-1611.
86. Lin, Q.; Armin, A.; Nagiri, R. C. R.; Burn, P. L.; Meredith, P., Electro-optics of perovskite solar cells. *Nat. Photon.* **2015,** *9* (2), 106.
87. Ishihara, T., Optical Properties of Pb-based inorganic-organic perovskites. In *Optical Properties of Low–Dimensional Materials*, World Scientific: 1995; pp 288-339.
88. Hong, X.; Ishihara, T.; Nurmikko, A. V., Dielectric confinement effect on excitons in PbI_4-based layered semiconductors. *Phys. Rev. B* **1992,** *45* (12), 6961-6964.
89. Miyata, A.; Mitioglu, A.; Plochocka, P.; Portugall, O.; Wang, J. T.-W.; Stranks, S. D.; Snaith, H. J.; Nicholas, R. J., Direct measurement of the exciton binding energy and effective masses for charge carriers in organic–inorganic tri-halide perovskites. *Nat. Phys.* **2015,** *11* (7), 582.
90. Cortecchia, D.; Yin, J.; Petrozza, A.; Soci, C., White light emission in low-dimensional perovskites. *J. Mater. Chem.* **2019,** *7* (17), 4956-4969.
91. Muljarov, E.; Tikhodeev, S.; Gippius, N.; Ishihara, T., Excitons in self-organized semiconductor/insulator superlattices: PbI-based perovskite compounds. *Phys. Rev. B* **1995,** *51* (20), 14370.
92. Keldysh, L., Coulomb interaction in thin semiconductor and semimetal films. *Sov. J. Exper. Theor. Phy. Lett.* **1979,** *29*, 658.
93. Shi, H.; Du, M.-H., Discrete electronic bands in semiconductors and insulators: Potential high-light-yield scintillators. *Phys. Rev. App.* **2015,** *3* (5), 054005.
94. Tanaka, K.; Sano, F.; Takahashi, T.; Kondo, T.; Ito, R.; Ema, K., Two-dimensional Wannier excitons in a layered-perovskite-type crystal $(C_6H_{13}NH_3)_2PbI_4$. *Solid State Commun.* **2002,** *122* (5), 249-252.
95. Tanaka, K.; Takahashi, T.; Kondo, T.; Umeda, K.; Ema, K.; Umebayashi, T.; Asai, K.; Uchida, K.; Miura, N., Electronic and Excitonic Structures of Inorganic–Organic Perovskite-Type Quantum-Well Crystal $(C_4H_9NH_3)_2PbBr_4$. *Jpn. J. Appl. Phys.* **2005,** *44* (8), 5923-5932.
96. Takagi, H.; Kunugita, H.; Ema, K., Influence of the image charge effect on excitonic energy structure in organic-inorganic multiple quantum well crystals. *Phys. Rev. B* **2013,** *87* (12), 125421.
97. Ema, K.; Umeda, K.; Toda, M.; Yajima, C.; Arai, Y.; Kunugita, H.; Wolverson, D.; Davies, J., Huge exchange energy and fine structure of excitons in an organic-inorganic quantum well material. *Phys. Rev. B* **2006,** *73* (24), 241310.
98. Kitazawa, N., Excitons in two-dimensional layered perovskite compounds:$(C_6H_5C_2H_4NH_3)_2Pb(Br, I)_4$ and $(C_6H_5C_2H_4NH_3)_2Pb(Cl, Br)_4$. *Mater. Sci. Eng. B* **1997,** *49* (3), 233-238.
99. Gauthron, K.; Lauret, J.; Doyennette, L.; Lanty, G.; Al Choueiry, A.; Zhang, S.; Brehier, A.; Largeau, L.; Mauguin, O.; Bloch, J., Optical spectroscopy of two-dimensional layered $(C_6H_5C_2H_4NH_3)_2PbI_4$ perovskite. *Opt. Express* **2010,** *18* (6), 5912-5919.

100. Ishihara, T.; Takahashi, J.; Goto, T., Optical properties due to electronic transitions in two-dimensional semiconductors (C_nH_{2n+1} $NH_3)_2PbI_4$. *Phys. Rev. B* **1990,** *42* (17), 11099.
101. Emin, D., *Polarons*. Cambridge University Press: 2013.
102. Song, K.; Williams, R. T., *Self-trapped excitons*. Springer Science & Business Media: 2013; Vol. 105.
103. Zhu, X.-Y.; Podzorov, V., Charge carriers in hybrid organic–inorganic lead halide perovskites might be protected as large polarons. *J. Phys. Chem. Lett.* **2015,** *6* (23), 4758-4761.
104. Zhou, C.; Lin, H.; He, Q.; Xu, L.; Worku, M.; Chaaban, M.; Lee, S.; Shi, X.; Du, M.-H.; Ma, B., Low dimensional metal halide perovskites and hybrids. *Mater. Sci. Eng. R* **2019,** *137*, 38-65.
105. Hayashi, T.; Kobayashi, T.; Iwanaga, M.; Watanabe, M., Exciton dynamics related with phase transitions in $CsPbCl_3$ single crystals. *J. Lumin.* **2001,** *94*, 255-259.
106. Dohner, E. R.; Hoke, E. T.; Karunadasa, H. I., Self-Assembly of Broadband White-Light Emitters. *J. Am. Chem. Soc.* **2014,** *136* (5), 1718-1721.
107. Dohner, E. R.; Jaffe, A.; Bradshaw, L. R.; Karunadasa, H. I., Intrinsic White-Light Emission from Layered Hybrid Perovskites. *J. Am. Chem. Soc.* **2014,** *136* (38), 13154-13157.
108. Yangui, A.; Garrot, D.; Lauret, J.-S.; Lusson, A.; Bouchez, G.; Deleporte, E.; Pillet, S.; Bendeif, E.-E.; Castro, M.; Triki, S., Optical investigation of broadband white-light emission in self-assembled organic–inorganic perovskite $(C_6H_{11}NH_3)_2PbBr_4$. *J. Phys. Chem. C* **2015,** *119* (41), 23638-23647.
109. Yangui, A.; Pillet, S.; Lusson, A.; Bendeif, E.-E.; Triki, S.; Abid, Y.; Boukheddaden, K., Control of the white-light emission in the mixed two-dimensional hybrid perovskites $(C_6H_{11}NH_3)_2$ $[PbBr_{4-x}I_x]$. *J. Alloys Compd.* **2017,** *699*, 1122-1133.
110. Shibata, H.; Sakai, M.; Yamada, A.; Matsubara, K.; Sakurai, K.; Tampo, H.; Ishizuka, S.; Kim, K.-K.; Niki, S., Excitation-power dependence of free exciton photoluminescence of semiconductors. *Jpn. J. Appl. Phys.* **2005,** *44* (8R), 6113.
111. Roccanova, R.; Yangui, A.; Nhalil, H.; Shi, H.; Du, M.-H.; Saparov, B., Near-Unity Photoluminescence Quantum Yield in Blue-Emitting $Cs_3Cu_2Br_{5-x}I_x$ ($0 \leq x \leq 5$). *ACS App. Electr.Mater.* **2019,** *1* (3), 269-274.
112. Yangui, A.; Roccanova, R.; McWhorter, T. M.; Wu, Y.; Du, M.-H.; Saparov, B., Hybrid Organic–Inorganic Halides $(C_5H_7N_2)_2MBr_4$ (M = Hg, Zn) with High Color Rendering Index and High-Efficiency White-Light Emission. *Chem. Mater.* **2019,** *31* (8), 2983-2991.
113. Roccanova, R.; Houck, M.; Yangui, A.; Han, D.; Shi, H.; Wu, Y.; Glatzhofer, D. T.; Powell, D. R.; Chen, S.; Fourati, H.; Lusson, A.; Boukheddaden, K.; Du, M.-H.; Saparov, B., Broadband Emission in Hybrid Organic–Inorganic Halides of Group 12 Metals. *ACS Omega* **2018,** *3* (12), 18791-18802.
114. Matsui, A.; Mizuno, K.-i.; Tamai, N.; Yamazaki, I., Transient free-exciton luminescence and exciton—lattice interaction in pyrene crystals. *Chem. Phys.* **1987,** *113* (1), 111-117.
115. Fujisawa, J.-i.; Ishihara, T., Excitons and biexcitons bound to a positive ion in a bismuth-doped inorganic-organic layered lead iodide semiconductor. *Phys. Rev. B* **2004,** *70* (20), 205330.

116. Varshni, Y. P., Temperature dependence of the energy gap in semiconductors. *Physica* **1967,** *34* (1), 149-154.
117. Crosby, G. A.; Demas, J. N., Measurement of photoluminescence quantum yields. Review. *J. Phys. Chem.* **1971,** *75* (8), 991-1024.
118. Bai, X.; Caputo, G.; Hao, Z.; Freitas, V. T.; Zhang, J.; Longo, R. L.; Malta, O. L.; Ferreira, R. A.; Pinna, N., Efficient and tuneable photoluminescent boehmite hybrid nanoplates lacking metal activator centres for single-phase white LEDs. *Nat. Commun.* **2014,** *5*, 5702.
119. Phillips, J. M.; Coltrin, M. E.; Crawford, M. H.; Fischer, A. J.; Krames, M. R.; Mueller-Mach, R.; Mueller, G. O.; Ohno, Y.; Rohwer, L. E.; Simmons, J. A., Research challenges to ultra-efficient inorganic solid-state lighting. *Laser & Photonics Rev.* **2007,** *1* (4), 307-333.
120. Schubert, E. F., Light-emitting diodes Cambridge University Press. *New York* **2006**, 35-40.
121. Krames, M. R.; Shchekin, O. B.; Mueller-Mach, R.; Mueller, G. O.; Zhou, L.; Harbers, G.; Craford, M. G., Status and future of high-power light-emitting diodes for solid-state lighting. *J. Disp. Tech.* **2007,** *3* (2), 160-175.
122. George, N. C.; Denault, K. A.; Seshadri, R., Phosphors for solid-state white lighting. *Ann. Rev. Mat. Rea.* **2013,** *43*, 481-501.
123. Kim, Y.-H.; Cho, H.; Lee, T.-W., Metal halide perovskite light emitters. *Proceed. Nat. Acad. Sci.* **2016,** *113* (42), 11694-11702.
124. Schubert, E. F.; Kim, J. K., Solid-state light sources getting smart. *Science* **2005,** *308* (5726), 1274-1278.
125. Lin, C. C.; Liu, R.-S., Advances in Phosphors for Light-emitting Diodes. *J. Phys. Chem. Let.* **2011,** *2* (11), 1268-1277.
126. Silver, J. W., R, Color Conversion Phosphors for LEDs. In *Luminescent Materials and Applications*, Kitai, A., Ed. John Wiley & Sons: Chichester, U.K., 2008; pp 75-109.
127. Ye, S.; Xiao, F.; Pan, Y.; Ma, Y.; Zhang, Q., Phosphors in phosphor-converted white light-emitting diodes: Recent advances in materials, techniques and properties. *Mater. Sci. Eng. R* **2010,** *71* (1), 1-34.
128. Papavassiliou, G. C.; Koutselas, I.; Lagouvardos, D.; Kapoutsis, J.; Terzis, A.; Papaioannou, G., Optical and related properties of some natural three and lower dimensional semiconductor systems. *Mole. Cryst. Liq. Cryst. Sci. Tech. A* **1994,** *253* (1), 103-112.
129. Kawano, N.; Koshimizu, M.; Sun, Y.; Yahaba, N.; Fujimoto, Y.; Yanagida, T.; Asai, K., Effects of organic moieties on luminescence properties of organic–inorganic layered perovskite-type compounds. *J. Phys. Chem. C* **2014,** *118* (17), 9101-9106.
130. Gong, X.; Voznyy, O.; Jain, A.; Liu, W.; Sabatini, R.; Piontkowski, Z.; Walters, G.; Bappi, G.; Nokhrin, S.; Bushuyev, O., Electron–phonon interaction in efficient perovskite blue emitters. *Nat. Mat.* **2018,** *17*, 550-556.
131. Tan, S. T.; Sun, X.; Demir, H. V.; DenBaars, S., Advances in the LED materials and architectures for energy-saving solid-state lighting toward "lighting revolution". *IEEE J. Photon.* **2012,** *4* (2), 613-619.
132. Fang, H. H.; Yang, J.; Tao, S.; Adjokatse, S.; Kamminga, M. E.; Ye, J.; Blake, G. R.; Even, J.; Loi, M. A., Unravelling Light-Induced Degradation of Layered Perovskite

Crystals and Design of Efficient Encapsulation for Improved Photostability. *Adv. Funct. Mater.* **2018,** *28* (21), 1800305.
133. Slavney, A. H.; Smaha, R. W.; Smith, I. C.; Jaffe, A.; Umeyama, D.; Karunadasa, H. I., Chemical Approaches to Addressing the Instability and Toxicity of Lead-Halide Perovskite Absorbers. *Inorg. Chem.* **2017,** *56* (1), 46-55.
134. Xie, R.-J.; Hirosaki, N., Silicon-based oxynitride and nitride phosphors for white LEDs—A review. *Sci. Tech. Adv. Mater.* **2007,** *8* (7-8), 588.
135. Nakamura, S.; Pearton, S.; Fasol, G., *The blue laser diode: the complete story*. Springer Science & Business Media: 2013.
136. Pimputkar, S.; Speck, J. S.; DenBaars, S. P.; Nakamura, S., Prospects for LED lighting. *Nat. Photon.* **2009,** *3* (4), 180.
137. Jacoby, M., Tuning phosphors for better white light. *C&E News* **2018,** *96* (46), 28-32.
138. Hong, X.; Ishihara, T.; Nurmikko, A., Photoconductivity and electroluminescence in lead iodide based natural quantum well structures. *Solid State Commun.* **1992,** *84* (6), 657-661.
139. Hattori, T.; Taira, T.; Era, M.; Tsutsui, T.; Saito, S., Highly efficient electroluminescence from a heterostructure device combined with emissive layered-perovskite and an electron-transporting organic compound. *Chem. Phys. Lett.* **1996,** *254* (1-2), 103-108.
140. Liang, D.; Peng, Y.; Fu, Y.; Shearer, M. J.; Zhang, J.; Zhai, J.; Zhang, Y.; Hamers, R. J.; Andrew, T. L.; Jin, S., Color-pure violet-light-emitting diodes based on layered lead halide perovskite nanoplates. *ACS Nano* **2016,** *10* (7), 6897-6904.
141. Lova, P.; Cortecchia, D.; S. Krishnamoorthy, H. N.; Giusto, P.; Bastianini, C.; Bruno, A.; Comoretto, D.; Soci, C., Engineering the emission of broadband 2D perovskites by polymer distributed bragg reflectors. *ACS Photonics* **2018,** *5* (3), 867-874.
142. Ronda, C.; Wieczorek, H.; Khanin, V.; Rodnyi, P., Scintillators for Medical Imaging: A Tutorial Overview. *ECS J. Solid State Sci. Tech.* **2016,** *5* (1), R3121-R3125.
143. Birks, J. B., *The Theory and Practice of Scintillation Counting: International Series of Monographs in Electronics and Instrumentation*. Pergamon Press: Oxford, 1967.
144. Shibuya, K.; Koshimizu, M.; Murakami, H.; Muroya, Y.; Katsumura, Y.; Asai, K., Development of ultra-fast semiconducting scintillators using quantum confinement effect. *Jpn. J. Appl. Phys.* **2004,** *43* (10B), L1333.
145. Shibuya, K.; Koshimizu, M.; Takeoka, Y.; Asai, K., Scintillation properties of $(C_6H_{13}NH_3)_2PbI_4$: exciton luminescence of an organic/inorganic multiple quantum well structure compound induced by 2.0 MeV protons. *Nuc. Inst. Meth. Phys. Res. B* **2002,** *194* (2), 207-212.
146. Birowosuto, M. D.; Cortecchia, D.; Drozdowski, W.; Brylew, K.; Lachmanski, W.; Bruno, A.; Soci, C., X-ray scintillation in lead halide perovskite crystals. *Scientific Reports* **2016,** *6*, 37254.
147. Nikl, M.; Mihokova, E.; Pejchal, J.; Vedda, A.; Fasoli, M.; Fontana, I.; Laguta, V.; Babin, V.; Nejezchleb, K.; Yoshikawa, A., Scintillator materials—achievements, opportunities, and puzzles. *IEEE Trans. Nucl. Sci.* **2008,** *55* (3), 1035-1041.
148. Kawano, N.; Koshimizu, M.; Okada, G.; Fujimoto, Y.; Kawaguchi, N.; Yanagida, T.; Asai, K., Scintillating organic–inorganic layered perovskite-type compounds and the gamma-ray detection capabilities. *Sci. Rep.* **2017,** *7* (1), 14754.

149. Stranks, S. D.; Snaith, H. J., Metal-halide perovskites for photovoltaic and light-emitting devices. *Nat. Nano.* **2015,** *10* (5), 391-402.
150. Lee, S. J.; Shin, S. S.; Kim, Y. C.; Kim, D.; Ahn, T. K.; Noh, J. H.; Seo, J.; Seok, S. I., Fabrication of efficient formamidinium tin iodide perovskite solar cells through SnF_2–pyrazine complex. *J. Am. Chem. Soc.* **2016,** *138* (12), 3974-3977.
151. Krishnamoorthy, T.; Ding, H.; Yan, C.; Leong, W. L.; Baikie, T.; Zhang, Z.; Sherburne, M.; Li, S.; Asta, M.; Mathews, N., Lead-free germanium iodide perovskite materials for photovoltaic applications. *J. Matrt. Chem. A* **2015,** *3* (47), 23829-23832.
152. Tran, T. T.; Panella, J. R.; Chamorro, J. R.; Morey, J. R.; McQueen, T. M., Designing indirect–direct bandgap transitions in double perovskites. *Mater. Horiz.* **2017,** *4* (4), 688-693.
153. McCall, K. M.; Stoumpos, C. C.; Kostina, S. S.; Kanatzidis, M. G.; Wessels, B. W., Strong Electron–Phonon Coupling and Self-Trapped Excitons in the Defect Halide Perovskites $A_3M_2I_9$ (A = Cs, Rb; M = Bi, Sb). *Chem. Mater.* **2017,** *29* (9), 4129-4145.
154. Saparov, B.; Hong, F.; Sun, J.-P.; Duan, H.-S.; Meng, W.; Cameron, S.; Hill, I. G.; Yan, Y.; Mitzi, D. B., Thin-Film Preparation and Characterization of $Cs_3Sb_2I_9$: A Lead-Free Layered Perovskite Semiconductor. *Chem. Mater.* **2015,** *27* (16), 5622-5632.
155. Mousdis, G. A.; Ganotopoulos, N. M.; Barkaoui, H.; Abid, Y.; Psycharis, V.; Savvidou, A.; Raptopoulou, C. P., One-Dimensional Organic–Inorganic Hybrid Materials Based on Antimony. *Eur. J. Inorg. Chem.* **2017,** *2017* (28), 3401-3408.
156. Zhou, C.; Worku, M.; Neu, J.; Lin, H.; Tian, Y.; Lee, S.; Zhou, Y.; Han, D.; Chen, S.; Hao, A., Facile Preparation of Light Emitting Organic Metal Halide Crystals with Near-Unity Quantum Efficiency. *Chem. Mater.* **2018,** *30* (7), 2374-2378.
157. Dammak, H.; Triki, S.; Mlayah, A.; Abid, Y.; Feki, H., Structural, vibrational and optical properties of a new self assembled organic–inorganic nanowire crystal $(C_6H_{14}N)_2[BiBr_5]$. A Density Functional Theory approach. *J. Lumin.* **2015,** *166*, 180-186.
158. Kawai, T.; Ishii, A.; Kitamura, T.; Shimanuki, S.; Iwata, M.; Ishibashi, Y., Optical Absorption in Band-Edge Region of $(CH_3NH_3)_3Bi_2I_9$ Single Crystals. *J. Phys. Soc. Jpn.* **1996,** *65* (5), 1464-1468.
159. Tan, Z.; Li, J.; Zhang, C.; Li, Z.; Hu, Q.; Xiao, Z.; Kamiya, T.; Hosono, H.; Niu, G.; Lifshitz, E., Highly Efficient Blue-Emitting Bi-Doped Cs_2SnCl_6 Perovskite Variant: Photoluminescence Induced by Impurity Doping. *Adv. Funct. Mater.* **2018,** *28* (29), 1801131.
160. Bartel, C. J.; Sutton, C.; Goldsmith, B. R.; Ouyang, R.; Musgrave, C. B.; Ghiringhelli, L. M.; Scheffler, M., New tolerance factor to predict the stability of perovskite oxides and halides. *Sci. Adv.* **2019,** *5* (2), eaav0693.
161. Rademeyer, M.; Billing, D. G.; Lemmerer, A., catena-Poly [(2-phenylethyl) ammonium [dichloromercurate (II)-μ3-chloro]]. *Acta Crystallogr. Sect. Sect. E: Struct. Rep. Online* **2006,** *62* (7), m1716-m1718.
162. Helgesson, G.; Josefsson, M.; Jagner, S., Tetramethylammonium catena-di-μ-chloro-argentate (I). *Acta Crystallogr. Sect. C.* **1988,** *44* (10), 1729-1731.
163. Geshi, K., Phase transitions in monoclinic rubidium tetraiodozincate Rb_2ZnI_4. *J. Phys. Soc. Jpn.* **1984,** *53* (11), 3850-3854.

164. Wiegand, D. A., Low-Temperature Luminescence and Photoconductivity of AgCl. *Phys. Rev.* **1959,** *113* (1), 52.
165. Goto, T.; Takahashi, T.; Ueta, M., Exciton luminescence of CuCl, CuBr and CuI single crystals. *J. Phys. Soc. Jpn.* **1968,** *24* (2), 314-327.
166. Smith, G. C., Luminescence and Photoconductivity in Silver Halides. *Phys. Rev.* **1965,** *140* (1A), A221.
167. Nakayama, M.; Ichida, H.; Nishimura, H., Bound-biexciton photoluminescence in CuCl thin films grown by vacuum deposition. *J. Phys.: Condens. Matter* **1999,** *11* (39), 7653.
168. Ichida, H.; Kanematsu, Y.; Shimomura, T.; Mizoguchi, K.; Kim, D.; Nakayama, M., Photoluminescence dynamics of exciton-exciton scattering processes in CuI thin films. *Phys. Rev. B* **2005,** *72* (4), 045210.
169. O'Reilly, L.; Lucas, O.; McNally, P. J.; Reader, A.; Natarajan, G.; Daniels, S.; Cameron, D. C.; Mitra, A.; Martinez-Rosas, M.; Bradley, A. L., Room-temperature ultraviolet luminescence from γ-Cu Cl grown on near lattice-matched silicon. *J. Appl. Phys.* **2005,** *98* (11), 113512.
170. Mochizuki, S.; Ohta, Y., Excitons in AgI. *J. Lumin.* **2000,** *87*, 299-301.
171. Babin, P.; Voropaev, S.; Silukova, T.; Troilin, V., Spectral and luminescent properties of gold bromides. *J. Appl. Spectrosc.* **1977,** *26* (5), 615-618.
172. Silukova, T. N. B., P. A.; Voropaev, S. F.; Plekhanov, V. G., Exciton Luminescence in Gold Monochloride. *Opt. Spektrosk.* **1979,** *46* (2), 395-396.
173. Silukova, T. N. B., P. A.; Voropaev, S. F.; Plekhanov, V. G., Conjucation of free and self-localized excitons in gold halides. *Elektronnye i Ionnye Protsessy v Ionnykh Kristallakh* **1980,** *8*, 168-182.
174. Koshevoy, I. O.; Karttunen, A. J.; Kritchenkou, I. S.; Krupenya, D. V.; Selivanov, S. I.; Melnikov, A. S.; Tunik, S. P.; Haukka, M.; Pakkanen, T. A., Sky-Blue Luminescent AuI–AgI Alkynyl-Phosphine Clusters. *Inorg. Chem.* **2013,** *52* (7), 3663-3673.
175. Belyaev, A. A.; Krupenya, D. V.; Grachova, E. V.; Gurzhiy, V. V.; Melnikov, A. S.; Serdobintsev, P. Y.; Sinitsyna, E. S.; Vlakh, E. G.; Tennikova, T. B.; Tunik, S. P., Supramolecular AuI–CuI Complexes as New Luminescent Labels for Covalent Bioconjugation. *Bioconjugate Chem.* **2015,** *27* (1), 143-150.
176. Shakirova, J. R.; Grachova, E. V.; Melnikov, A. S.; Gurzhiy, V. V.; Tunik, S. P.; Haukka, M.; Pakkanen, T. A.; Koshevoy, I. O., Toward Luminescence Vapochromism of Tetranuclear AuI–CuI Clusters. *Organometallics* **2013,** *32* (15), 4061-4069.
177. Wei, F.; Deng, Z.; Sun, S.; Zhang, F.; Evans, D. M.; Kieslich, G.; Tominaka, S.; Carpenter, M. A.; Zhang, J.; Bristowe, P. D., Synthesis and properties of a lead-free hybrid double perovskite: $(CH_3NH_3)_2AgBiBr_6$. *Chem. Mater.* **2017,** *29* (3), 1089-1094.
178. Volonakis, G.; Haghighirad, A. A.; Milot, R. L.; Sio, W. H.; Filip, M. R.; Wenger, B.; Johnston, M. B.; Herz, L. M.; Snaith, H. J.; Giustino, F., $Cs_2InAgCl_6$: a new lead-free halide double perovskite with direct band gap. *J. Phys. Chem. Lett.* **2017,** *8* (4), 772-778.
179. Liu, X.; Moritomo, Y.; Nakamura, A.; Matsuba, S.; Kojima, N., Pressure-induced phase transition in quasi-1D mixed-valence gold complexes. *J. Phys. Soc. Jpn.* **2000,** *69* (10), 3158-3161.

180. Liu, X.; Moritomo, Y.; Nakamura, A.; Kojima, N., Pressure-induced phase transition in mixed-valence gold complexes Cs 2 Au 2 X 6 (X= Cl and Br). *The Journal of chemical physics* **1999,** *110* (18), 9174-9178.
181. Worley, C.; Yangui, A.; Roccanova, R.; Du, M.-H.; Saparov, B., $(CH_3NH_3)AuX_4 \cdot H_2O$ (X= Cl, Br) and $(CH_3NH_3)AuCl_4$: Low-band gap lead-free layered gold halide perovskite materials. *Chem. Eur. J.* **2019,** *25*, 9875.
182. Cortecchia, D.; Dewi, H. A.; Yin, J.; Bruno, A.; Chen, S.; Baikie, T.; Boix, P. P.; Grätzel, M.; Mhaisalkar, S.; Soci, C., Lead-free $MA_2CuCl_xBr_{4-x}$ hybrid perovskites. *Inorg. Chem.* **2016,** *55* (3), 1044-1052.
183. Jun, T.; Sim, K.; Iimura, S.; Sasase, M.; Kamioka, H.; Kim, J.; Hosono, H., Lead-Free Highly Efficient Blue-Emitting $Cs_3Cu_2I_5$ with 0D Electronic Structure. *Adv. Mater.* **2018**, 1804547.
184. Yunakova, O.; Miloslavsky, V.; Kovalenko, E., Excitons in the layered insulators ZnI_2 and CdI_2:Zn. *Low Temp. Phys.* **2002,** *28* (4), 284-289.
185. Merz, J.; Wu, Z.; Van den Berg, L.; Schnepple, W., Low temperature photoluminescence of detector-grade HgI_2. *Nuc. Inst. Meth. Phys. Res.* **1983,** *213* (1), 51-64.
186. Lefi, R.; Ben Naser, F.; Guermazi, H., Structural, optical properties and characterization of $(C_2H_5NH_3)_2CdCl_4$, $(C_2H_5NH_3)_2CuCl_4$ and $(C_2H_5NH_3)_2Cd_{0.5}Cu_{0.5}Cl_4$ compounds. *J. Alloys Compd.* **2017,** *696*, 1244-1254.
187. Chu, K.; Zhou, Y.-H.; Song, J.-L.; Zhang, C., An ABX_3 organic–inorganic perovskite-type material with the formula $(C_5N_2H_9)CdCl_3$: Application for detection of volatile organic solvent molecules. *Polyhedron* **2017,** *131*, 22-26.
188. Lassoued, M. S.; Abdelbaky, M. S.; Lassoued, A.; Gadri, A.; Ammar, S.; Salah, A. B.; García-Granda, S., Structural characterization and physicochemical features of new hybrid compound containing chlorate anions of cadmate (II). *J. Mol. Struct.* **2017,** *1141*, 390-399.
189. Beebeejaun-Boodoo, B. M. P.; Erasmus, R.; Rademeyer, M., Tetrahalometallate salts of N-(4-picolinium)-1,8-naphthalimide: structures and solid-state fluorescence. *CrystEngComm* **2018,** *20* (33), 4875-4887.
190. Nhalil, H.; Whiteside, V. R.; Sellers, I. R.; Ming, W.; Du, M.-H.; Saparov, B., Synthesis, crystal and electronic structures and optical properties of $(HIm)_2Hg_3Cl_8$ and (HIm) HgI_3 (HIm= imidazolium). *J. Solid State Chem.* **2018,** *258*, 551-558.
191. Pidzyrailo, M.; Vistovsky, V.; Antonyak, O., Impurity luminescence of K_2ZnI_4:Sn crystals. *Opt. Commun.* **2001,** *199* (1-4), 149-153.
192. Berdychevsky, O.; Gnyp, R.; Maximovych, K.; Pidzyrailo, M., Optical and spectral properties of the Tl_2ZnI_4 and Tl_2ZnI_4:Mn crystals. *Opt. Commun.* **2001,** *195* (5-6), 443-448.
193. Kutsyk, M.; Pidzyrailo, M.; Pashuk, I., Luminescence peculiarities of Tl_2ZnI_4 crystals. *Rad. Meas.* **1998,** *29* (3-4), 243-246.
194. Xie, Y.; Wu, J., Synthesis, structure and properties of (4, 4'-H_2bipy)[$ZnBr_4$]. *Indian J. Chem.* **2007,** *46A*, 1401-1405.
195. Saidaminov, M. I.; Mohammed, O. F.; Bakr, O. M., Low-dimensional-networked metal halide perovskites: the next big thing. *ACS Energy Lett.* **2017,** *2* (4), 889-896.
196. Sánchez-Guadarrama, O.; López-Sandoval, H.; Sánchez-Bartéz, F.; Gracia-Mora, I.; Höpfl, H.; Barba-Behrens, N., Cytotoxic activity, X-ray crystal structures and

spectroscopic characterization of cobalt(II), copper(II) and zinc(II) coordination compounds with 2-substituted benzimidazoles. *J. Inorg. Biochem.* **2009,** *103* (9), 1204-1213.
197. Malhotra, K.; Chaudhry, S., The nature of the complexes of zinc (II), cadmium (II) and mercury (II) halides with benzoin. *Aust. J. Chem.* **1974,** *27* (1), 79-85.
198. Quiroz-Castro, E.; Bernès, S.; Barba-Behrens, N.; Tapia-Benavides, R.; Contreras, R.; Nöth, H., Structural and spectroscopic characterisation of tris(2-benzimidazolylmethyl)amine coordination compounds of Zn(II), Cd(II) and Hg(II). *Polyhedron* **2000,** *19* (12), 1479-1484.
199. Lee, C. K.; Ling, M. J.; Lin, I. J., Organic–inorganic hybrids of imidazole complexes of palladium (II), copper (II) and zinc (II). Crystals and liquid crystals. *Dalton Trans.* **2003,** (24), 4731-4737.
200. Altermatt, D.; Arend, H.; Gramlich, V.; Niggli, A.; Petter, W., Low-temperature phases in Cs_2CdBr_4 and Cs_2HgBr_4. *Acta Crystallogr. Sect. B: Struct. Sci.* **1984,** *40* (4), 347-350.
201. De Oliveira, O. A.; Chagas, A. P.; Airoldi, C., Synthesis, characterization, and thermochemistry of adducts of zinc, cadmium and mercury halides with N,N-dimethylformamide. *Inorg. Chem.* **1983,** *22* (1), 136-140.
202. Chin, X. Y.; Cortecchia, D.; Yin, J.; Bruno, A.; Soci, C., Lead Iodide Perovskite Light-Emitting Field-Effect Transistor. *Nat. Commun.* **2015,** *6*, 7383.
203. Ha, S.-T.; Shen, C.; Zhang, J.; Xiong, Q., Laser cooling of organic–inorganic lead halide perovskites. *Nat. Photonics* **2015,** *10*, 115.
204. Sutherland, B. R.; Sargent, E. H., Perovskite photonic sources. *Nat. Photonics* **2016,** *10* (5), 295-302.
205. Liang, F.-X.; Liang, L.; Zhao, X.-Y.; Luo, L.-B.; Liu, Y.-H.; Tong, X.-W.; Zhang, Z.-X.; Huang, J. C. A., A Sensitive Broadband (UV–vis–NIR) Perovskite Photodetector Using Topological Insulator as Electrodes. *Adv. Opt. Mater.* **2018,** *7* (4), 1801392.
206. Kishimoto, S.; Shibuya, K.; Nishikido, F.; Koshimizu, M.; Haruki, R.; Yoda, Y., Subnanosecond time-resolved x-ray measurements using an organic-inorganic perovskite scintillator. *Appl. Phys. Lett.* **2008,** *93* (26), 261901.
207. Zhao, B.; Bai, S.; Kim, V.; Lamboll, R.; Shivanna, R.; Auras, F.; Richter, J. M.; Yang, L.; Dai, L.; Alsari, M.; She, X.-J.; Liang, L.; Zhang, J.; Lilliu, S.; Gao, P.; Snaith, H. J.; Wang, J.; Greenham, N. C.; Friend, R. H.; Di, D., High-efficiency perovskite–polymer bulk heterostructure light-emitting diodes. *Nat. Photonics* **2018,** *12*, 783–789.
208. Zhao, X.; Liu, S.; Zhang, H.; Chang, S.-Y.; Huang, W.; Zhu, B.; Shen, Y.; Shen, C.; Wang, D.; Yang, Y.; Wang, M., 20% Efficient Perovskite Solar Cells with 2D Electron Transporting Layer. *Adv. Funct. Mater. 29* (4), 1805168.
209. Roccanova, R.; Ming, W.; Whiteside, V. R.; McGuire, M. A.; Sellers, I. R.; Du, M.-H.; Saparov, B., Synthesis, crystal and electronic structures, and optical properties of $(CH_3NH_3)_2CdX_4$ (X= Cl, Br, I). *Inorg. Chem.* **2017,** *56* (22), 13878-13888.
210. Veldhuis, S. A.; Boix, P. P.; Yantara, N.; Li, M.; Sum, T. C.; Mathews, N.; Mhaisalkar, S. G., Perovskite Materials for Light-Emitting Diodes and Lasers. *Adv. Mater.* **2016,** *28* (32), 6804-6834.
211. Dou, L.; Yang, Y.; You, J.; Hong, Z.; Chang, W.-H.; Li, G.; Yang, Y., Solution-processed hybrid perovskite photodetectors with high detectivity. *Nat. Commun.* **2014,** *5*, 5404.

212. Manser, J. S.; Christians, J. A.; Kamat, P. V., Intriguing Optoelectronic Properties of Metal Halide Perovskites. *Chem. Rev.* **2016,** *116* (21), 12956-13008.
213. Heo, J. H.; Im, S. H.; Noh, J. H.; Mandal, T. N.; Lim, C.-S.; Chang, J. A.; Lee, Y. H.; Kim, H.-j.; Sarkar, A.; Nazeeruddin, M. K.; Grätzel, M.; Seok, S. I., Efficient inorganic–organic hybrid heterojunction solar cells containing perovskite compound and polymeric hole conductors. *Nat. Photon.* **2013,** *7* (6), 486-491.
214. Yakunin, S.; Sytnyk, M.; Kriegner, D.; Shrestha, S.; Richter, M.; Matt, G. J.; Azimi, H.; Brabec, C. J.; Stangl, J.; Kovalenko, M. V.; Heiss, W., Detection of X-ray photons by solution-processed lead halide perovskites. *Nat. Photon.* **2015,** *9* (7), 444-449.
215. Stoumpos, C. C.; Malliakas, C. D.; Peters, J. A.; Liu, Z.; Sebastian, M.; Im, J.; Chasapis, T. C.; Wibowo, A. C.; Chung, D. Y.; Freeman, A. J.; Wessels, B. W.; Kanatzidis, M. G., Crystal Growth of the Perovskite Semiconductor $CsPbBr_3$: A New Material for High-Energy Radiation Detection. *Cryst. Growth Des.* **2013,** *13* (7), 2722-2727.
216. Boatner, L. A.; Wisniewski, D.; Neal, J. S.; Ramey, J. O.; Kolopus, J. A.; Chakoumakos, B. C.; Wisniewska, M.; Custelcean, R., Single-crystal $CeCl_3(CH_3OH)_4$: A new metal-organic cerium chloride methanol adduct for scintillator applications. *Appl. Phys. Lett.* **2008,** *93* (24), 244104.
217. Vaughn, S. A.; Chakoumakos, B. C.; Custelcean, R.; Ramey, J. O.; Smith, M. D.; Boatner, L. A.; zur Loye, H.-C., New Family of Cerium Halide Based Materials: CeX_3·ROH Compounds Containing Planes, Chains, and Tetradecanuclear Rings. *Inorg. Chem.* **2012,** *51* (20), 10503-10511.
218. Kamat, P. V., Photochemistry on nonreactive and reactive (semiconductor) surfaces. *Chem. Rev.* **1993,** *93* (1), 267-300.
219. Shkel, Y. M.; Klingenberg, D. J., Material parameters for electrostriction. *J. Appl. Phys.* **1996,** *80* (8), 4566-4572.
220. Allred, A. L., Electronegativity values from thermochemical data. *J. Inorg. Nucl. Chem.* **1961,** *17* (3), 215-221.
221. Zaanen, J.; Sawatzky, G. A.; Allen, J. W., Band gaps and electronic structure of transition-metal compounds. *Phys. Rev. Lett.* **1985,** *55* (4), 418-421.
222. Chapuis, G.; Arend, H.; Kind, R., X-Ray study of the structural first-order phase transition (*Cmca-P*4_2/*ncm*) in $(CH_3NH_3)_2CdCl_4$. *Phys. Status Solidi A* **1975,** *31* (2), 449-454.
223. Chapuis, G. K., R.; Arend, H., X-Ray Study of Structural Phase Transitions in the Perovskite-Type Layer Compound $(CH_3NH_3)_2CdCl_4$. *Phys. Status Solidi A* **1976,** *36*, 285-295.
224. Alternatt, D. A., H.; Niggli, A.; Petter, W., New Tetrahedrally Coordinated A_2CdBr_4 Compounds (A = Cs, CH_3NH_3). *Mat. Res. Bull.* **1979,** *14*, 1391-1396.
225. Jeon, N. J.; Noh, J. H.; Kim, Y. C.; Yang, W. S.; Ryu, S.; Seok, S. I., Solvent engineering for high-performance inorganic–organic hybrid perovskite solar cells. *Nat. Mater.* **2014,** *13* (9), 897-903.
226. Linden, A., Chemistry and structure in Acta Crystallographica Section C. *Acta Crystallogr. Sect. C* **2015,** *71* (1), 1-2.
227. Sheldrick, G., SHELXT - Integrated space-group and crystal-structure determination. *Acta Crystallogr. Sect. A* **2015,** *71* (1), 3-8.

228. Perdew, J. P.; Burke, K.; Ernzerhof, M., Generalized Gradient Approximation Made Simple. *Phys. Rev. Lett.* **1996,** *77* (18), 3865-3868.
229. Kresse, G.; Furthmüller, J., Efficiency of ab-initio total energy calculations for metals and semiconductors using a plane-wave basis set. *Comput. Mater. Sci.* **1996,** *6* (1), 15-50.
230. Kresse, G.; Joubert, D., From ultrasoft pseudopotentials to the projector augmented-wave method. *Phys. Rev. B* **1999,** *59* (3), 1758-1775.
231. Villars, P. C., K., Pearson's Crystal Data: Crystal Structure Database for Inorganic Compounds (on DVD). ASM International: Materials Park, Ohio, USA, Release 2016/17.
232. Mac Gillavry, C. H.; Nijveld, H.; Dierdorp, S.; Karsten, J., Die Krystallstruktur von NH_4CdCl_3 und $RbCdCl_3$. *Recl. Trav. Chim. Pays-Bas* **1939,** *58* (3), 193-200.
233. Brandenberger, E., Die Kristallstruktur von K($CdCl_3$). *Experientia* **1947,** *3* (4), 149-149.
234. Plesko, S.; Kind, R.; Roos, J., Structural Phase Transitions in $CsPbCl_3$ and $RbCdCl_3$. *J. Phys. Soc. Jpn.* **1978,** *45* (2), 553-557.
235. Dronskowski, R., Synthesis, Crystal Structure, and Electronic Structure of $InCdBr_3$. *J. Solid State Chem.* **1995,** *116* (1), 45-52.
236. Kieslich, G.; Sun, S.; Cheetham, A. K., Solid-State Principles Applied to Organic-Inorganic Perovskites: New Tricks for an Old Dog. *Chem. Sci.* **2014,** *5* (12), 4712-4715.
237. Li, C.; Lu, X.; Ding, W.; Feng, L.; Gao, Y.; Guo, Z., Formability of ABX_3 (X = F, Cl, Br, I) halide perovskites. *Acta Crystallogr. Sect. B: Struct. Sci.* **2008,** *64* (6), 702-707.
238. Kruglik, A. I.; Vasilyev, A. D.; Aleksandrov, K. S., The crystal structure of Rb_2CdCl_4 in para- and ferroelastic phases. *Phase Transitions* **1989,** *15* (1), 69-76.
239. Siegel, S.; Gebert, E., The structures of hexagonal $CsCdCl_3$ and tetragonal Cs_2CdCl_4. *Acta Crystallogr.* **1964,** *17* (6), 790.
240. Ben, A., Le tetrabromomercurate(II) de monomethylammonium. *J. Appl. Crystallogr.* **1983,** *16* (1), 142-143.
241. Körfer, M.; Fuess, H.; Bats, J., Struktur und Eigenschaften von Doppelhalogeniden von substituiertem Ammonium und Quecksilber (II). VI [1]. Die Kristallstruktur von $(CH_3NH_3)_2HgBr_4$ und $(CH_3NH_3)_2HgI_4$. *Z. Anorg. Allg. Chem.* **1986,** *543* (12), 104-110.
242. Pabst, I.; Korfer, M.; Fuess, H.; Bats, J., Crystal structures of Methylammonium Mercury (II) Bromides and Iodides. *Z. Kristallog.* **1986,** *174* (1-4), 167-168.
243. Knorr, K.; Jahn, I. R.; Heger, G., Birefringence, X-ray and neutron diffraction measurements on the structural phase transitions of $(CH_3NH_3)_2MnCl_4$ and $(CH_3NH_3)_2FeCl_4$. *Solid State Commun.* **1974,** *15* (2), 231-238.
244. Rao, C. N. R.; Ganguly, S.; Swamy, H. R.; Oxton, I. A., Infrared studies of the phase transitions of alkylammonium halides, RNH_3X, and bis-(alkylammonium) tetrahalogenometallates(II), $(RNH_3)_2MX_4$, (R = alkyl, M = metal, X = Cl or Br). *J. Chem. Soc. Faraday Trans.* **1981,** *77* (10), 1825-1836.
245. Nakayama, H.; Eguchi, T.; Nakamura, N., Molecular reorientation in solid $(CH_3NH_3)_2CdBr_4$ as studied by ^{79}Br and ^{81}Br nuclear quadrupole resonance and ^{1}H nuclear magnetic resonance. *J. Chem. Soc., Faraday Trans.* **1992,** *88* (20), 3067-3070.

246. Ishida, H. T., Kentaro; Terashima, Mifune; Nakamura, Daiyu, A Highly Disordered New Solid Phase Containing Isotropically Reorienting Cations in $(CH_3NH_3)_2CdBr_4$ Studied by ^1H NMR and Thermal Measurements. *Z. Naturforsch., A: Phys. Sci.* **1990,** *45* (9-10).
247. Henke, S.; Schneemann, A.; Fischer, R. A., Massive Anisotropic Thermal Expansion and Thermo-Responsive Breathing in Metal–Organic Frameworks Modulated by Linker Functionalization. *Adv. Funct. Mater.* **2013,** *23* (48), 5990-5996.
248. Gao, H.; Wei, W.; Li, Y.; Wu, R.; Feng, G.; Li, W., Uniaxial Negative Thermal Expansion and Mechanical Properties of a Zinc-Formate Framework. *Materials* **2017,** *10* (2).
249. Howse, J. R.; Jones, R. A. L.; Ryan, A. J.; Gough, T.; Vafabakhsh, R.; Golestanian, R., Self-Motile Colloidal Particles: From Directed Propulsion to Random Walk. *Phys. Rev. Lett.* **2007,** *99* (4), 048102.
250. Hassen, R. B.; Salah, A. B.; Kallel, A.; Daoud, A.; Jaud, J., Crystal structure of monomethylammonium tribromocadmate(II). *J. Chem. Crystallogr.* **2002,** *32* (11), 427-430.
251. Dastidar, S.; Egger, D. A.; Tan, L. Z.; Cromer, S. B.; Dillon, A. D.; Liu, S.; Kronik, L.; Rappe, A. M.; Fafarman, A. T., High Chloride Doping Levels Stabilize the Perovskite Phase of Cesium Lead Iodide. *Nano Lett.* **2016,** *16* (6), 3563-3570.
252. Pollini, I.; Thomas, J.; Coehoorn, R.; Haas, C., Optical reflectivity and electronic structure of layered cadmium halides. *Phys. Rev. B* **1986,** *33* (8), 5747-5755.
253. Elleuch, S.; Dammak, T.; Abid, Y.; Mlayah, A.; Boughzala, H., Synthesis, structural and optical properties of a novel bilayered organic–inorganic perovskite $C_5Pb_2I_5$. *J. Lumin.* **2010,** *130* (4), 531-535.
254. Dammak, T.; Koubaa, M.; Boukheddaden, K.; Bougzhala, H.; Mlayah, A.; Abid, Y., Two-Dimensional Excitons and Photoluminescence Properties of the Organic/Inorganic $(4\text{-}FC_6H_4C_2H_4NH_3)_2[PbI_4]$ Nanomaterial. *J. Phys. Chem. C* **2009,** *113* (44), 19305-19309.
255. Lefi, R.; Ben Nasr, F.; Hrichi, H.; Guermazi, H., Optical, electrical properties and characterization of $(C_2H_5NH_3)_2CdCl_4$ compound. *Optik* **2016,** *127* (13), 5534-5541.
256. Ohnishi, A.; Tanaka, K.-i.; Kitaura, M.; Otomo, T.; Yoshinari, T., Optical Spectra of Inorganic-Organic Compounds $(C_2H_5NH_3)_2CdCl_4$ in 3-30 eV Range. *J. Phys. Soc. Jpn.* **2001,** *70* (11), 3424-3427.
257. Kazutoshi, S.; Seiichi, M.; Masataka, H., Luminescence Study of Thermally-Oxidized Porous Si under Subgap or Overgap Excitation. *Jpn. J. Appl. Phys.* **1998,** *37* (4R), 1684.
258. Kalem, S.; Curtis, A.; Hartmann, Q.; Moser, B.; Stillman, G., Sub-Gap Excited Photoluminescence in III–V Compound Semiconductor Heterostructures. *Phys. Status Solidi B* **2000,** *221* (1), 517-522.
259. Mao, L.; Wu, Y.; Stoumpos, C. C.; Wasielewski, M. R.; Kanatzidis, M. G., White-Light Emission and Structural Distortion in New Corrugated Two-Dimensional Lead Bromide Perovskites. *J. Am. Chem. Soc.* **2017,** *139* (14), 5210-5215.
260. Nakagawa, H.; Hayashi, K.; Matsumoto, H., Luminescence of $CdCl_2$-$CdBr_2$ Solid Solutions. *J. Phys. Soc. Jpn.* **1977,** *43* (5), 1655-1663.
261. Matsumoto, H.; Nakagawa, H., Relaxed excitonic states in CdI_2 crystals. *J. Lumin.* **1979,** *18*, 19-22.

262. Hayashi, T.; Ohata, T.; Koshino, S., Indirect exciton luminescense and Raman scattering in CdI_2. *Solid State Commun.* **1981,** *38* (9), 845-847.
263. Ohnishi, A.; Kitaura, M.; Nakagawa, H., Determination of Optical Gain of Self-Trapped Exciton Luminescence in CdI_2. *J. Phys. Soc. Jpn.* **1994,** *63* (12), 4648-4654.
264. Nakagawa, H.; Kitaura, M. In *Nonradiative branching processes of self-trapped excitons in cadmium halide crystals*, International Conference on Excitonic Processes in Condensed Matter, 1995; pp 294-303.
265. Kitaura, M.; Nakagawa, H.; Fukui, K.; Fujita, M.; Miyanaga, T.; Watanabe, M., Decay Time Studies on UV-Luminescence in $CdBr_2CdCl_2$ Mixed Crystals. *J. Electron. Spectrosc. Relat. Phenom.* **1996,** *79*, 175-178.
266. Kawabata, S.; Kitaura, M.; Nakagawa, H., Life-time resolved emission spectra in $CdCl_2$ crystals. *Phys. Stat. Solidi (c)* **2005,** *2* (1), 53-56.
267. Ohnishi, A.; Yamada, T.; Yoshinari, T.; Akimoto, I.; Kan'no, K.; Kamikawa, T., Emission spectra and decay characteristics in photo-stimulated $(C_nH_{2n+1}NH_3)_2CdCl_4$: n=1, 2, 3. *J. Electron. Spectrosc. Relat. Phenom.* **1996,** *79*, 163-166.
268. Biswas, K.; Du, M.-H., Energy transport and scintillation of cerium-doped elpasolite Cs_2LiYCl_6: Hybrid density functional calculations. *Phys. Rev. B* **2012,** *86* (1).
269. Du, M.-H.; Biswas, K., Electronic structure engineering of elpasolites: Case of Cs_2AgYCl_6. *J. Lumin.* **2013,** *143*, 710-714.
270. Shi, C.; Yu, C. H.; Zhang, W., Predicting and Screening Dielectric Transitions in a Series of Hybrid Organic-Inorganic Double Perovskites via an Extended Tolerance Factor Approach. *Angew. Chem. Int. Ed. Engl.* **2016,** *55* (19), 5798-802.
271. Wei, H.; Du, M.-H.; Stand, L.; Zhao, Z.; Shi, H.; Zhuravleva, M.; Melcher, C. L., Scintillation Properties and Electronic Structures of the Intrinsic and Extrinsic Mixed Elpasolites $Cs_2NaRBr_3I_3$ (R=La, Y). *Phys. Rev. Appl.* **2016,** *5* (2), 024008.
272. Cortecchia, D.; Yin, J.; Bruno, A.; Lo, S.-Z. A.; Gurzadyan, G. G.; Mhaisalkar, S.; Bredas, J.-L.; Soci, C., Polaron self-localization in white-light emitting hybrid perovskites. *J. Mater. Chem.* **2017,** *5* (11), 2771-2780.
273. Yin, J.; Li, H.; Cortecchia, D.; Soci, C.; Brédas, J.-L., Excitonic and Polaronic Properties of 2D Hybrid Organic–Inorganic Perovskites. *ACS Energy Lett.* **2017,** *2* (2), 417-423.
274. Hu, T.; Smith, M. D.; Dohner, E. R.; Sher, M.-J.; Wu, X.; Trinh, M. T.; Fisher, A.; Corbett, J.; Zhu, X. Y.; Karunadasa, H. I.; Lindenberg, A. M., Mechanism for Broadband White-Light Emission from Two-Dimensional (110) Hybrid Perovskites. *J. Phys. Chem. Lett.* **2016,** *7* (12), 2258-2263.
275. Shang, M.; Li, C.; Lin, J., How to produce white light in a single-phase host? *Chem. Soc. Rev.* **2014,** *43* (5), 1372-1386.
276. Bowers, M. J.; McBride, J. R.; Rosenthal, S. J., White-Light Emission from Magic-Sized Cadmium Selenide Nanocrystals. *J. Am. Chem. Soc.* **2005,** *127*, 15378.
277. Reineke, S.; Lindner, F.; Schwartz, G.; Seidler, N.; Walzer, K.; Lüssem, B.; Leo, K., White organic light-emitting diodes with fluorescent tube efficiency. *Nature* **2009,** *459*, 234.
278. Yum, J.-h.; Seo, S.-Y.; Lee, S.; Sung, Y.-E., $Y_3Al_5O_{12}$:$Ce_{0.05}$ Phosphor Coatings on Gallium Nitride for White Light Emitting Diodes. *J. Electrochem. Soc.* **2003,** *150* (2), H47-H52.

279. Lee, K. H.; Lee, S. W. R. In *Process development for yellow phosphor coating on blue light emitting diodes (LEDs) for white light illumination*, 2006 8th Electronics Packaging Technology Conference, 6-8 Dec. 2006; 2006; pp 379-384.
280. Ohno, Y. In *Color rendering and luminous efficacy of white LED spectra*, 4th International Conference on Solid State Lighting, International Society for Optics and Photonics: **2004**; pp 88-99.
281. Speier, I.; Salsbury, M. In *Color temperature tunable white light LED system*, 6th International Conference on Solid State Lighting, International Society for Optics and Photonics: **2006**; p 63371F.
282. Im, W. B.; George, N.; Kurzman, J.; Brinkley, S.; Mikhailovsky, A.; Hu, J.; Chmelka, B. F.; DenBaars, S. P.; Seshadri, R., *Adv. Mater.* **2011,** *23*, 2300.
283. Pan, M.; Du, B.-B.; Zhu, Y.-X.; Yue, M.-Q.; Wei, Z.-W.; Su, C.-Y., Highly Efficient Visible-to-NIR Luminescence of Lanthanide(III) Complexes with Zwitterionic Ligands Bearing Charge-Transfer Character: Beyond Triplet Sensitization. *Chem. Eur. J* **2016,** *22* (7), 2440-2451.
284. Wu, J. L.; Gundiah, G.; Cheetham, A. K., *Chem. Phys. Lett.* **2007,** *441*, 250.
285. Ye, S.; Xiao, F.; Pan, Y. X.; Ma, Y. Y.; Zhang, Q. Y., Phosphors in Phosphor-Converted White Light-Emitting Diodes: Recent Advances in Materials, Techniques and Properties. *Mater. Sci. Eng., R* **2010,** *71*, 1.
286. Stoumpos, C. C.; Kanatzidis, M. G., Halide Perovskites: Poor Man's High-Performance Semiconductors. *Adv. Mater.* **2016,** *28* (28), 5778-5793.
287. Chen, D.; Wan, Z.; Zhou, Y.; Zhou, X.; Yu, Y.; Zhong, J.; Ding, M.; Ji, Z., Dual-Phase Glass Ceramic: Structure, Dual-Modal Luminescence, and Temperature Sensing Behaviors. *ACS Appl. Mater. Interfaces* **2015,** *7* (34), 19484-19493.
288. Bai, X.; Caputo, G.; Hao, Z.; Freitas, V. T.; Zhang, J.; Longo, R. L.; Malta, O. L.; Ferreira, R. A. S.; Pinna, N., Efficient and tuneable photoluminescent boehmite hybrid nanoplates lacking metal activator centres for single-phase white LEDs. *Nat. Commun.* **2014,** *5*, 5702.
289. Saparov, B.; Mitzi, D. B., Organic–Inorganic Perovskites: Structural Versatility for Functional Materials Design. *Chem. Rev.* **2016,** *116*, 4558.
290. Mercier, N.; Louvain, N.; Bi, W., Structural diversity and retro-crystal engineering analysis of iodometalate hybrids. *CrystEngComm* **2009,** *11* (5), 720-734.
291. Billing, D. G.; Lemmerer, A., Inorganic–organic hybrid materials incorporating primary cyclic ammonium cations: The lead bromide and chloride series. *CrystEngComm* **2009,** *11* (8), 1549.
292. Yangui, A.; Sy, M.; Li, L.; Abid, Y.; Naumov, P.; Boukheddaden, K., Rapid and robust spatiotemporal dynamics of the first-order phase transition in crystals of the organic-inorganic perovskite $(C_{12}H_{25}NH_3)_2PbI_4$. *Sci. Rep.* **2015,** *5*, 16634.
293. Gebhardt, J.; Rappe, A. M., Mix and Match: Organic and Inorganic Ions in the Perovskite Lattice. *Adv. Mater.* **2018,** 1802697.
294. Dammak, H.; Yangui, A.; Triki, S.; Abid, Y.; Feki, H., Structural characterization, vibrational, optical properties and DFT investigation of a new luminescent organic–inorganic material: $(C_6H_{14}N)_3Bi_2I_9$. *J. Lumin.* **2015,** *161* (0), 214-220.
295. Mitzi, D. B.; Chondroudis, K.; C.R.Kagan, Organic-inorganic electronics. *IBM J. Res. & Dev.* **2001,** *45* (1), 29-45.

296. Yangui, A.; Pillet, S.; Garrot, D.; Triki, S.; Abid, Y.; Boukheddaden, K., Evidence and detailed study of a second-order phase transition in the $(C_6H_{11}NH3)_2[PbI_4]$ organic-inorganic hybrid material. *J. Appl. Phys.* **2015,** *117* (11), 115503: 1-9.
297. Yuan, M.; Quan, L. N.; Comin, R.; Walters, G.; Sabatini, R.; Voznyy, O.; Hoogland, S.; Zhao, Y.; Beauregard, E. M.; Kanjanaboos, P.; Lu, Z.; Kim, D. H.; Sargent, E. H., Perovskite Energy Funnels for Efficient Light-Emitting Diodes. *Nat. Nanotechnol.* **2016,** *11*, 872.
298. Pan, J.; Quan, L. N.; Zhao, Y.; Peng, W.; Murali, B.; Sarmah, S. P.; Yuan, M.; Sinatra, L.; Alyami, N. M.; Liu, J.; Yassitepe, E.; Yang, Z.; Voznyy, O.; Comin, R.; Hedhili, M. N.; Mohammed, O. F.; Lu, Z. H.; Kim, D. H.; Sargent, E. H.; Bakr, O. M., Highly Efficient Perovskite-Quantum-Dot Light-Emitting Diodes by Surface Engineering. *Adv. Mater.* **2016,** *28* (39), 8718.
299. Dohner, E. R.; Hoke, E. T.; Karunadasa, H. I., Self-Assembly of Broadband White-Light Emitters. *J. Am. Chem. Soc.* **2014,** *136* (5), 1718-1721.
300. Dohner, E. R.; Jaffe, A.; Bradshaw, L. R.; Karunadasa, H. I., Intrinsic White-Light Emission from Layered Hybrid Perovskites. *J. Am. Chem. Soc.* **2014,** *136* (38), 13154-13157.
301. Smith, M. D.; Jaffe, A.; Dohner, E. R.; Lindenberg, A. M.; Karunadasa, H. I., Structural Origins of Broadband Emission from Layered Pb–Br Hybrid Perovskites. *Chem. Sci.* **2017,** *8*, 4497.
302. Yangui, A.; Pillet, S.; Mlayah, A.; Lusson, A.; Bouchez, G.; Triki, S.; Abid, Y.; Boukheddaden, K., Structural phase transition causing anomalous photoluminescence behavior in perovskite (C6H11NH3)2[PbI4]. *J. Chem. Phys.* **2015,** *143* (22), 224201.
303. Yangui, A.; Pillet, S.; Lusson, A.; Bendeif, E. E.; Triki, S.; Abid, Y.; Boukheddaden, K., Control of the White-Light Emission in the Mixed Two-Dimensional Hybrid Perovskites (C6H11NH3)2[PbBr4–xIx]. *J. Alloys Compd.* **2017,** *699*, 1122.
304. Yuan, Z.; Zhou, C.; Messier, J.; Tian, Y.; Shu, Y.; Wang, J.; Xin, Y.; Ma, B., A Microscale Perovskite as Single Component Broadband Phosphor for Downconversion White-Light-Emitting Devices. *Adv. Opt. Mater.* **2016,** *4* (12), 2009.
305. Mao, L.; Wu, Y.; Stoumpos, C. C.; Traore, B.; Katan, C.; Even, J.; Wasielewski, M. R.; Kanatzidis, M. G., Tunable White-Light Emission in Single-Cation-Templated Three-Layered 2D Perovskites $(CH_3CH_2NH_3)_4Pb_3Br_{10-x}Cl_x$. *J. Am. Chem. Soc.* **2017,** *139*, 11956.
306. Roccanova, R.; Ming, W.; Whiteside, V. R.; McGuire, M. A.; Sellers, I. R.; Du, M. H.; Saparov, B., Synthesis, Crystal and Electronic Structures, and Optical Properties of $(CH_3NH_3)_2CdX_4$ (X = Cl, Br, I). *Inorg. Chem.* **2017,** *56* (22), 13878.
307. Zhuang, Z.; Peng, C.; Zhang, G.; Yang, H.; Yin, J.; Fei, H., Intrinsic Broadband White-Light Emission from Ultrastable, Cationic Lead Halide Layered Materials. *Angew. Chem., Int. Ed.* **2017,** *56*, 14411.
308. Peng, C.; Zhuang, Z.; Yang, H.; Zhang, G.; Fei, H., Ultrastable, cationic three-dimensional lead bromide frameworks that intrinsically emit broadband white-light. *Chem. Sci.* **2018,** *9* (6), 1627.
309. Haris, M. P. U.; Bakthavatsalam, R.; Shaikh, S.; Kore, B. P.; Moghe, D.; Gonnade, R. G.; Sarma, D. D.; Kabra, D.; Kundu, J., Synthetic Control on Structure/Dimensionality and Photophysical Properties of Low Dimensional Organic Lead Bromide Perovskite. *Inorg. Chem* **2018,** *57* (21), 13443-13452.

310. Hu, H.; Morris, S. A.; Qiao, X.; Zhao, D.; Salim, T.; Chen, B.; Chia, E. E. M.; Lam, Y. M., Molecular engineering of two-dimensional hybrid perovskites with broadband emission for white light-emitting diodes. *J. Mater. Chem. C.* **2018,** *6* (38), 10301-10307.
311. Krishnamurthy, S.; Kour, P.; Katre, A.; Gosavi, S.; Chakraborty, S.; Ogale, S., Cystamine-configured lead halide based 2D hybrid molecular crystals: Synthesis and photoluminescence systematics. *APL Mater.* **2018,** *6* (11), 114204.
312. Zhang, L.; Wu, L.; Wang, K.; Zou, B., Pressure-Induced Broadband Emission of 2D Organic–Inorganic Hybrid Perovskite $(C_6H_5C_2H_4NH_3)_2PbBr_4$. *Adv. Sci* **2018,** *6* (2), 1801628.
313. Yu, J.; Kong, J.; Hao, W.; Guo, X.; He, H.; Leow, W. R.; Liu, Z.; Cai, P.; Qian, G.; Li, S.; Chen, X.; Chen, X., Broadband Extrinsic Self-Trapped Exciton Emission in Sn-Doped 2D Lead-Halide Perovskites. *Adv. Mater.* **2018,** 31 (7), 1806385.
314. Ji, C.; Wang, S.; Li, L.; Sun, Z.; Hong, M.; Luo, J., The First 2D Hybrid Perovskite Ferroelectric Showing Broadband White-Light Emission with High Color Rendering Index. *Adv. Funct. Mater.* **2018,** 29 (6), 1805038.
315. Brochard-Garnier, S.; Paris, M.; Génois, R.; Han, Q.; Liu, Y.; Massuyeau, F.; Gautier, R., Screening Approach for the Discovery of New Hybrid Perovskites with Efficient Photoemission. *Adv. Funct. Mater.* **2019,** *29*, 1806728.
316. Yuan, Z.; Zhou, C.; Tian, Y.; Shu, Y.; Messier, J.; Wang, J. C.; van de Burgt, L. J.; Kountouriotis, K.; Xin, Y.; Holt, E.; Schanze, K.; Clark, R.; Siegrist, T.; Ma, B., One-Dimensional Organic Lead Halide Perovskites with Efficient Bluish White-Light Emission. *Nat. Commun.* **2017,** *8*, 14051.
317. Barkaoui, H.; Abid, H.; Yangui, A.; Triki, S.; Boukheddaden, K.; Abid, Y., Yellowish White-Light Emission Involving Resonant Energy Transfer in a New One-Dimensional Hybrid Material: $(C_9H_{10}N_2)PbCl_4$. *J. Phys. Chem. C* **2018,** *122* (42), 24253-24261.
318. Wang, G.-E.; Xu, G.; Wang, M.-S.; Cai, L.-Z.; Li, W.-H.; Guo, G.-C., Semiconductive 3-D haloplumbate framework hybrids with high color rendering index white-light emission. *Chem. Sci.* **2015,** *6* (12), 7222-7226.
319. Dammak, T.; Abid, Y., Quasi-white light emission involving Förster resonance energy transfer in a new organic inorganic tin chloride based material (AMPS)$[SnCl_6]H_2O$. *Opt. Mater.* **2017,** *66*, 302.
320. Krishnamurthy, S.; Naphade, R.; Mir, W. J.; Gosavi, S.; Chakraborty, S.; Vaidhyanathan, R.; Ogale, S., Molecular and Self-Trapped Excitonic Contributions to the Broadband Luminescence in Diamine-Based Low-Dimensional Hybrid Perovskite Systems. *Adv. Opt. Mater.* **2018,** *6* (20), 1800751.
321. Tsao, J. Y., Solid-state lighting: lamps, chips, and materials for tomorrow. *IEEE Circuits and Devices Magazine* **2004,** *20* (3), 28-37.
322. Rea, M. S.; Freyssinier, J. P., Color rendering: Beyond pride and prejudice. *Color Research & Appl.* **2010,** *35* (6), 401-409.
323. Kresse, G.; Joubert, D., From ultrasoft pseudopotentials to the projector augmented-wave method. *Phys. Rev. B* **1999,** *59* (3), 1758.
324. Perdew, J. P.; Burke, K.; Ernzerhof, M., Generalized gradient approximation made simple. *Phys. Rev. Lett.* **1996,** *77* (18), 3865.

325. Shannon, R. D., Revised effective ionic radii and systematic studies of interatomic distances in halides and chalcogenides. *Acta Cryst. A.* **1976,** *32* (5), 751-767.
326. Maughan, A. E.; Ganose, A. M.; Almaker, M. A.; Scanlon, D. O.; Neilson, J. R., Tolerance Factor and Cooperative Tilting Effects in Vacancy-Ordered Double Perovskite Halides. *Chem. Mater.* **2018,** *30* (11), 3909-3919.
327. Evans, H. A.; Fabini, D. H.; Andrews, J. L.; Koerner, M.; Preefer, M. B.; Wu, G.; Wudl, F.; Cheetham, A. K.; Seshadri, R., Hydrogen Bonding Controls the Structural Evolution in Perovskite-Related Hybrid Platinum(IV) Iodides. *Inorg. Chem.* **2018,** *57* (16), 10375-10382.
328. Khelifi, M.; Mkaouar, I.; Hlel, F.; Salah, A. B.; Zouari, R., Crystal structure and electrical properties study of 4-aminopyridinium chloridobismuthate (III)$(C_5N_2H_7)_4Bi_2Cl_{11}$. *Ionics* **2010,** *16* (8), 709-715.
329. Mencel, K.; Piecha-Bisiorek, A.; Jakubas, R.; Kinzhybalo, V.; Medycki, W., Hybrid organic-inorganic bismuth(III)-based material $[NH_2C_5H_4NH]_7[BiCl_6]_2Cl$. Crystal structure, dielectric properties and molecular motions of 4-aminopyridinium cations. *J. Mol. Struct.* **2019,** *1179*, 297-303.
330. Szklarz, P.; Jakubas, R.; Bator, G.; Lis, T.; Kinzhybalo, V.; Baran, J., Structural characterization, spectroscopic properties and phase transition in 4-aminopyridinium tetrachlorogallate(III): $[NH_2PyH][GaCl_4]$. *J. Phys. Chem. Solids* **2007,** *68* (12), 2303-2316.
331. Hatano, N.; Nakashima, M.; Horiuchi, K.; Terao, H.; Ishihara, H., Crystal Structure, NQR and DSC Studies of Tetrabromocadmates(II): $[H_2NC_5H_4NH]_2CdBr_4 \cdot H_2O$ and $[(CH_3)_4C_4N_2H_2]CdBr_4$. In *Z. Naturforsch. B Chem. Sci.*, 2008; Vol. 63, p 1181.
332. Kessentini, A.; Belhouchet, M.; Suñol, J. J.; Abid, Y.; Mhiri, T., Synthesis, structural, photoluminescence, vibrational and DFT investigation of the bis (4-aminopyridinium) tetrachloridocuprate(II) monohydrate. *J. Lumin.* **2014,** *149*, 341-347.
333. Jebas, S. R.; Sinthiya, A.; Ravindran Durai Nayagam, B.; Schollmeyer, D.; Raj, S. A. C., Bis(4-aminopyridinium) tetrachloridocobaltate(II). *Acta Cryst. E* **2009,** *65* (5), m521.
334. Ivanova, B. B.; Arnaudov, M. G.; Mayer-Figge, H., Molecular spectral analysis and crystal structure of the 4-aminopyridinium tetrachloropalladate(II) complex salt. *Polyhedron* **2005,** *24* (13), 1624-1630.
335. Sun, Q.; Liao, S.; Yao, J.; Wang, J.; Fang, Q., Bis(4-aminopyridinium) tetraiodidocadmate monohydrate. *Acta Cryst. E* **2012,** *68* (9), m1160-m1161.
336. Leijtens, T.; Eperon, G. E.; Noel, N. K.; Habisreutinger, S. N.; Petrozza, A.; Snaith, H. J., Stability of Metal Halide Perovskite Solar Cells. *Adv. Energ. Mater.* **2015,** *5* (20), 1500963.
337. Dastidar, S.; Egger, D. A.; Tan, L. Z.; Cromer, S. B.; Dillon, A. D.; Liu, S.; Kronik, L.; Rappe, A. M.; Fafarman, A. T., High Chloride Doping Levels Stabilize the Perovskite Phase of Cesium Lead Iodide. *Nano Lett* **2016,** *16* (6), 3563-3570.
338. Slavney, A. H.; Smaha, R. W.; Smith, I. C.; Jaffe, A.; Umeyama, D.; Karunadasa, H. I., Chemical Approaches to Addressing the Instability and Toxicity of Lead–Halide Perovskite Absorbers. *Inorg. Chem.* **2017,** *56* (1), 46-55.
339. Li, T.; Dunlap-Shohl, W. A.; Han, Q.; Mitzi, D. B., Melt Processing of Hybrid Organic–Inorganic Lead Iodide Layered Perovskites. *Chem. Mater.* **2017,** *29* (15), 6200-6204.

340. Kulicka, B.; Jakubas, R.; Ciunik, Z.; Bator, G.; Medycki, W.; Świergiel, J.; Baran, J., Structure, phase transitions and molecular dynamics in 4-methylpyridinium tetrachloroantimonate(III), $[CH_3C_5H_4NH][SbCl_4]$. *J. Phys. Chem. Solids* **2004,** *65* (5), 871-879.
341. Leijtens, T.; Prasanna, R.; Gold-Parker, A.; Toney, M. F.; McGehee, M. D., Mechanism of Tin Oxidation and Stabilization by Lead Substitution in Tin Halide Perovskites. *ACS Energy Lett.* **2017,** *2* (9), 2159-2165.
342. Tauc, J.; Grigorovici, R.; Vancu, A., Optical Properties and Electronic Structure of Amorphous Germanium. *phys. status solidi (b)* **1966,** *15* (2), 627-637.
343. Mao, L.; Wu, Y.; Stoumpos, C. C.; Wasielewski, M. R.; Kanatzidis, M. G., White-Light Emission and Structural Distortion in New Corrugated Two-Dimensional Lead Bromide Perovskites. *J. Am. Chem. Soc.* **2017,** *139*, 5210.
344. Wu, Z.; Ji, C.; sun, z.; Wang, S.; Zhao, S.; Zhang, W.; li, l.; Luo, J., Broadband white-light emission with high color rendering index in a two-dimensional organic-inorganic hybrid perovskite. *J. Mater. Chem. C* **2018,** *6* (5), 1171.
345. Smith, M. D.; Karunadasa, H. I., White-Light Emission from Layered Halide Perovskites. *Acc. Chem. Res.* **2018,** *51* (3), 619-627.
346. Yuan, Z.; Zhou, C.; Messier, J.; Tian, Y.; Shu, Y.; Wang, J.; Xin, Y.; Ma, B., A Microscale Perovskite as Single Component Broadband Phosphor for Downconversion White-Light-Emitting Devices. *Adv. Opt. Mater.* **2016,** *4* (12), 2009-2015.
347. Yu, J.; Kong, J.; Hao, W.; Guo, X.; He, H.; Leow, W. R.; Liu, Z.; Cai, P.; Qian, G.; Li, S.; Chen, X.; Chen, X., Broadband Extrinsic Self-Trapped Exciton Emission in Sn-Doped 2D Lead-Halide Perovskites. *Adv. Mater.* **2019,** *31*, 1806385.
348. Ji, C.; Wang, S.; Li, L.; Sun, Z.; Hong, M.; Luo, J., The First 2D Hybrid Perovskite Ferroelectric Showing Broadband White-Light Emission with High Color Rendering Index. *Adv. Funct. Mater.* **2019,** *29*, 1805038.
349. Tiguntseva, E. Y.; Sadrieva, Z.; Stroganov, B. V.; Kapitonov, Y. V.; Komissarenko, F.; Haroldson, R.; Balachandran, B.; Hu, W.; Gu, Q.; Zakhidov, A. A.; Bogdanov, A.; Makarov, S. V., Enhanced temperature-tunable narrow-band photoluminescence from resonant perovskite nanograting. *Appl. Surf. Sci.* **2019,** *473*, 419-424.
350. Thirumal, K.; Chong, W. K.; Xie, W.; Ganguly, R.; Muduli, S. K.; Sherburne, M.; Asta, M.; Mhaisalkar, S.; Sum, T. C.; Soo, H. S.; Mathews, N., Morphology-Independent Stable White-Light Emission from Self-Assembled Two-Dimensional Perovskites Driven by Strong Exciton–Phonon Coupling to the Organic Framework. *Chem. Mater.* **2017,** *29*, 3947.
351. Reshchikov, M. A.; Morkoç, H., Luminescence properties of defects in GaN. *J. Appl. Phys.* **2005,** *97* (6), 061301.
352. Zhou, C.; Lin, H.; Worku, M.; Neu, J.; Zhou, Y.; Tian, Y.; Lee, S.; Djurovich, P.; Siegrist, T.; Ma, B., Blue Emitting Single Crystalline Assembly of Metal Halide Clusters. *J. Am. Chem. Soc.* **2018,** *140* (41), 13181-13184.
353. Blasse, G.; Grabmaier, B. C., *Luminescent Materials*. Springer-Verlag: Berlin Heidelberg, 1994.
354. Dexter, D. L., A Theory of Sensitized Luminescence in Solids. *J. Chem. Phys.* **1953,** *21* (5), 836-850.

355. Kantor, S. W.; Hauser, C. R., Rearrangements of Benzyltrimethylammonium Ion and Related Quaternary Ammonium Ions by Sodium Amide Involving Migration into the Ring. *J. Am. Chem. Soc.* **1951,** *73* (9), 4122-4131.
356. Mitzi, D. B., Templating and structural engineering in organic-inorganic perovskites. *Dalton Trans.* **2001,** (1), 1-12.
357. Mitzi, D. B., Synthesis, structure, and properties of organic-inorganic perovskites and related materials. *Progress in Inorganic Chemistry, Volume 48* **2007**, 1-121.
358. Deschler, F.; Price, M.; Pathak, S.; Klintberg, E.; Jarausch, D. D.; Higler, R.; Hüttner, S.; Leijtens, S.; Stranks, D.; Snaith, H. J.; Atatüre, M.; Phillips, R. T.; Friend, R. H., *J. Phys. Chem. Lett.* **2014,** *5*, 1421.
359. Xing, G.; Mathews, N.; Lim, S. S.; Yantara, N.; Liu, X.; Sabba, D.; Grätzel, M.; Mhaisalkar, S.; Sum, T. C., Low-Temperature Solution-Processed Wavelength-Tunable Perovskites for Lasing. *Nat. Mater.* **2014,** *13* (5), 476.
360. Yang, W. S.; Park, B.-W.; Jung, E. H.; Jeon, N. J.; Kim, Y. C.; Lee, D. U.; Shin, S. S.; Seo, J.; Kim, E. K.; Noh, J. H.; Seok, S. I., Iodide management in formamidinium-lead-halide–based perovskite layers for efficient solar cells. *Science* **2017,** *356* (6345), 1376-1379.
361. Gong, X.; Voznyy, O.; Jain, A.; Liu, W.; Sabatini, R.; Piontkowski, Z.; Walters, G.; Bappi, G.; Nokhrin, S.; Bushuyev, O.; Yuan, M.; Comin, R.; McCamant, D.; Kelley, S. O.; Sargent, E. H., Electron–phonon interaction in efficient perovskite blue emitters. *Nat. Mater.* **2018,** *17* (6), 550-556.
362. Comin, R.; Walters, G.; Thibau, E. S.; Voznyy, O.; Lu, Z.-H.; Sargent, E. H., Structural, optical, and electronic studies of wide-bandgap lead halide perovskites. *J. Mater. Chem. C.* **2015,** *3* (34), 8839-8843.
363. Sutherland, B. R.; Sargent, E. H., Perovskite photonic sources. *Nat Photon* **2016,** *10* (5), 295-302.
364. Peng, Y.; Yao, Y.; Li, L.; Wu, Z.; Wang, S.; Luo, J., White-light emission in a chiral one-dimensional organic–inorganic hybrid perovskite. *J. Mater. Chem. C.* **2018,** *6* (22), 6033-6037.
365. Wang, G.-E.; Xu, G.; Wang, M.-S.; Cai, L.-Z.; Li, W.-H.; Guo, G.-C., Semiconductive 3-D haloplumbate framework hybrids with high color rendering index white-light emission. *Chem. Sci.* **2015,** *6* (12), 7222-7226.
366. Lou, Y.; Fang, M.; Chen, J.; Zhao, Y., Formation of highly luminescent cesium bismuth halide perovskite quantum dots tuned by anion exchange. *Chem. Comm.* **2018,** *54* (30), 3779-3782.
367. Lou, Y.; Niu, Y.; Yang, D.; Xu, Q.; Hu, Y.; Shen, Y.; Ming, J.; Chen, J.; Zhang, L.; Zhao, Y., Rod-shaped thiocyanate-induced abnormal band gap broadening in SCN− doped CsPbBr3 perovskite nanocrystals. *Nano Res.* **2018,** *11* (5), 2715-2723.
368. Zhou, C.; Worku, M.; Neu, J.; Lin, H.; Tian, Y.; Lee, S.; Zhou, Y.; Han, D.; Chen, S.; Hao, A.; Djurovich, P. I.; Siegrist, T.; Du, M.-H.; Ma, B., Facile Preparation of Light Emitting Organic Metal Halide Crystals with Near-Unity Quantum Efficiency. *Chem.Mater.* **2018,** *30* (7), 2374-2378.
369. Liu, W.; Zhu, K.; Teat, S. J.; Dey, G.; Shen, Z.; Wang, L.; O'Carroll, D. M.; Li, J., All-in-One: Achieving Robust, Strongly Luminescent and Highly Dispersible Hybrid Materials by Combining Ionic and Coordinate Bonds in Molecular Crystals. *J. Amer. Chem. Soc.* **2017,** *139* (27), 9281-9290.

370. Zhou, C.; Lin, H.; Shi, H.; Tian, Y.; Pak, C.; Shatruk, M.; Zhou, Y.; Djurovich, P.; Du, M.-H.; Ma, B., A Zero-Dimensional Organic Seesaw-Shaped Tin Bromide with Highly Efficient Strongly Stokes-Shifted Deep-Red Emission. *Angewa. Chem. Inter. Ed.* **2018,** *57* (4), 1021-1024.
371. Nhalil, H.; Whiteside, V. R.; Sellers, I. R.; Ming, W.; Du, M.-H.; Saparov, B., Synthesis, crystal and electronic structures and optical properties of $(HIm)_2Hg_3Cl_8$ and $(HIm)HgI_3$ (HIm = imidazolium). *J. Solid State Chem.* **2018,** *258*, 551-558.
372. Rademeyer, M.; Tsouris, C.; Billing, D. G.; Lemmerer, A.; Charmant, J., Robust motifs in 2-phenylethylammonium and related tetrahalometallates. *CrystEngComm* **2011,** *13* (10), 3485-3497.
373. Gillon, A. L.; Lewis, G. R.; Orpen, A. G.; Rotter, S.; Starbuck, J.; Wang, X.-M.; Rodríguez-Martín, Y.; Ruiz-Pérez, C., Organic–inorganic hybrid solids: control of perhalometallate solid state structures. *Dalton Trans.* **2000,** (21), 3897-3905.
374. Era, M.; Miyake, K.; Yoshida, Y.; Yase, K., Orientation of azobenzene chromophore incorporated into metal halide-based layered perovskite having organic–inorganic superlattice structure. *Thin Solid Films* **2001,** *393* (1-2), 24-27.
375. Tieke, B.; Chapuis, G., Solid State Polymerization of Butadienes in Layer Structures. *Molec. Cryst.Liq. Cryst.* **1986,** *137* (1), 101-116.
376. Sheldrick, G. M., SHELXT – Integrated space-group and crystal-structure determination. *Acta Cryst. Sect. A.* **2015,** *71* (Pt 1), 3-8.
377. Perdew, J. P.; Ernzerhof, M.; Burke, K., Rationale for mixing exact exchange with density functional approximations. *J. Chem. Phys.* **1996,** *105* (22), 9982-9985.
378. Shannon, R., Revised effective ionic radii and systematic studies of interatomic distances in halides and chalcogenides. *Acta Cryst. Sec. A* **1976,** *32* (5), 751-767.
379. Aristidou, N.; Sanchez-Molina, I.; Chotchuangchutchaval, T.; Brown, M.; Martinez, L.; Rath, T.; Haque, S. A., The Role of Oxygen in the Degradation of Methylammonium Lead Trihalide Perovskite Photoactive Layers. *Angew. Chemie Inter. Ed.* **2015,** *54* (28), 8208-8212.
380. Dammak, T.; Abid, Y., Quasi-white light emission involving Förster resonance energy transfer in a new organic inorganic tin chloride based material $(AMPS)[SnCl_6]H_2O$. *Optical Mater.* **2017,** *66*, 302-307.
381. Barkaoui, H.; Abid, H.; Yangui, A.; Triki, S.; Boukheddaden, K.; Abid, Y., Yellowish White-Light Emission Involving Resonant Energy Transfer in a New One-Dimensional Hybrid Material: $(C_9H_{10}N_2)PbCl_4$. *J. Phys. Chem. C.* **2018**.
382. Hernández-Andrés, J.; Lee, R. L.; Romero, J., Calculating correlated color temperatures across the entire gamut of daylight and skylight chromaticities. *Appl. Opt.* **1999,** *38* (27), 5703-5709.
383. Nakagawa, H.; Hayashi, K.; Matsumoto, H., Luminescence of $CdCl_2$-$CdBr_2$ Solid Solutions. *J. Phys. Soc. Jpn.* **1977,** *43* (5), 1655.
384. Saidaminov, M. I.; Almutlaq, J.; Sarmah, S.; Dursun, I.; Zhumekenov, A. A.; Begum, R.; Pan, J.; Cho, N.; Mohammed, O. F.; Bakr, O. M., Pure Cs_4PbBr_6: Highly Luminescent Zero-Dimensional Perovskite Solids. *ACS Energy Letters* **2016,** *1* (4), 840-845.
385. Zhang, Y.; Saidaminov, M. I.; Dursun, I.; Yang, H.; Murali, B.; Alarousu, E.; Yengel, E.; Alshankiti, B. A.; Bakr, O. M.; Mohammed, O. F., Zero-Dimensional Cs_4PbBr_6 Perovskite Nanocrystals. *J. Phys. Chem. Lett.* **2017,** *8* (5), 961-965.

386. Kitaura, M.; Nakagawa, H.; Fukui, K.; Fujita, M.; Miyanaga, T.; Watanabe, M., Decay Time Studies on UV-Luminescence in $CdBr_2/CdCl_2$ Mixed Crystals. *J. Electron Spectrosc. Relat. Phenom.* **1996,** *79*, 175.
387. Neogi, I.; Bruno, A.; Bahulayan, D.; Goh, T. W.; Ghosh, B.; Ganguly, R.; Cortecchia, D.; Sum, T. C.; Soci, C.; Mathews, N.; Mhaisalkar, S. G., Broadband-Emitting 2D Hybrid Organic–Inorganic Perovskite Based on Cyclohexane-bis(methylamonium) Cation. *ChemSusChem* **2017,** *10*, 3765.
388. Yangui, A.; Pillet, S.; Mlayah, A.; Lusson, A.; Bouchez, G.; Triki, S.; Abid, Y.; Boukheddaden, K., Structural phase transition causing anomalous photoluminescence behavior in perovskite $(C_6H_{11}NH_3)_2[PbI_4]$. *J. Chem. Phys.* **2015,** *143* (22), 224201.
389. Yangui, A.; Pillet, S.; Garrot, D.; Triki, S.; Abid, Y.; Boukheddaden, K., Evidence and detailed study of a second-order phase transition in the $(C_6H_{11}NH_3)_2[PbI_4]$ organic-inorganic hybrid material. *Journal of Applied Physics* **2015,** *117* (11), 115503: 1-9.
390. Yangui, A.; Sy, M.; Li, L.; Abid, Y.; Naumov, P.; Boukheddaden, K., Rapid and robust spatiotemporal dynamics of the first-order phase transition in crystals of the organic-inorganic perovskite $(C_{12}H_{25}NH_3)_2PbI_4$. *Sc. Rep.* **2015,** *5*, 16634.
391. Lee, J.; Koteles, E. S.; Vassell, M., Luminescence linewidths of excitons in GaAs quantum wells below 150 K. *Phys. Rev. B* **1986,** *33* (8), 5512.
392. Hehlen, M. P.; Kuditcher, A.; Rand, S. C.; Tischler, M. A., Electron–phonon interactions in $CsCdBr_3:Yb^{3+}$. *J. Chem. Phys.* **1997,** *107* (13), 4886.
393. Lockwood, D. J., Lattice vibrations of CdCl2, CdBr2, MnCl2, and CoCl2: infrared and Raman spectra*. *J. Opt. Soc. Am.* **1973,** *63* (3), 374.
394. Birks, J. B., Chapter 7 - Organic Crystal Scintillators. In *The Theory and Practice of Scintillation Counting*, Birks, J. B., Ed. Pergamon: 1964; pp 235-268.
395. Cortecchia, D.; Yin, J.; Bruno, A.; Lo, S. Z. A.; Gurzadyan, G. G.; Mhaisalkar, S. G.; Brédas, J. L.; Soci, C., Polaron Self-Localization in White-light Emitting Hybrid Perovskites. *J. Mater. Chem. C* **2017,** *5*, 2771.
396. Feldmann, C.; Jüstel, T.; Ronda, C. R.; Schmidt, P. J., Inorganic Luminescent Materials: 100 Years of Research and Application. *Adv. Funct. Mater.* **2003,** *13* (7), 511-516.
397. Deschler, F.; Price, M.; Pathak, S.; Klintberg, L. E.; Jarausch, D.-D.; Higler, R.; Hüttner, S.; Leijtens, T.; Stranks, S. D.; Snaith, H. J.; Atatüre, M.; Phillips, R. T.; Friend, R. H., High Photoluminescence Efficiency and Optically Pumped Lasing in Solution-Processed Mixed Halide Perovskite Semiconductors. *J. Phys. Chem. Lett.* **2014,** *5* (8), 1421-1426.
398. Lin, K.; Xing, J.; Quan, L. N.; de Arquer, F. P. G.; Gong, X.; Lu, J.; Xie, L.; Zhao, W.; Zhang, D.; Yan, C., Perovskite light-emitting diodes with external quantum efficiency exceeding 20 percent. *Nature* **2018,** *562* (7726), 245.
399. Di, D.; Romanov, A. S.; Yang, L.; Richter, J. M.; Rivett, J. P.; Jones, S.; Thomas, T. H.; Jalebi, M. A.; Friend, R. H.; Linnolahti, M., High-performance light-emitting diodes based on carbene-metal-amides. *Science* **2017,** *356* (6334), 159-163.
400. Dai, X.; Zhang, Z.; Jin, Y.; Niu, Y.; Cao, H.; Liang, X.; Chen, L.; Wang, J.; Peng, X., Solution-processed, high-performance light-emitting diodes based on quantum dots. *Nature* **2014,** *515* (7525), 96.

401. Zhou, C.; Lin, H.; Worku, M.; Neu, J.; Zhou, Y.; Tian, Y.; Lee, S.; Djurovich, P.; Siegrist, T.; Ma, B., Blue Emitting Single Crystalline Assembly of Metal Halide Clusters. *J. Am. Chem. Soc.* **2018**.
402. Yang, H.; Zhang, Y.; Pan, J.; Yin, J.; Bakr, O. M.; Mohammed, O. F., Room-temperature engineering of all-inorganic perovskite nanocrsytals with different dimensionalities. *Chem. Mater.* **2017,** *29* (21), 8978-8982.
403. Correa-Baena, J.-P.; Nienhaus, L.; Kurchin, R. C.; Shin, S. S.; Wieghold, S.; Putri Hartono, N. T.; Layurova, M.; Klein, N. D.; Poindexter, J. R.; Polizzotti, A.; Sun, S.; Bawendi, M. G.; Buonassisi, T., A-Site Cation in Inorganic $A_3Sb_2I_9$ Perovskite Influences Structural Dimensionality, Exciton Binding Energy, and Solar Cell Performance. *Chem. Mater.* **2018,** *30* (11), 3734-3742.
404. Zhang, J.; Yang, Y.; Deng, H.; Farooq, U.; Yang, X.; Khan, J.; Tang, J.; Song, H., High Quantum Yield Blue Emission from Lead-Free Inorganic Antimony Halide Perovskite Colloidal Quantum Dots. *ACS Nano* **2017,** *11* (9), 9294-9302.
405. Li, X.; Wu, Y.; Zhang, S.; Cai, B.; Gu, Y.; Song, J.; Zeng, H., $CsPbX_3$ Quantum Dots for Lighting and Displays: Room-Temperature Synthesis, Photoluminescence Superiorities, Underlying Origins and White Light-Emitting Diodes. *Adv. Funct. Mater.* **2016,** *26* (15), 2435-2445.
406. Keimer, B.; Kivelson, S. A.; Norman, M. R.; Uchida, S.; Zaanen, J., From quantum matter to high-temperature superconductivity in copper oxides. *Nature* **2015,** *518*, 179.
407. Song, W.-S.; Yang, H., Fabrication of white light-emitting diodes based on solvothermally synthesized copper indium sulfide quantum dots as color converters. *Appl. Phys. Lett.* **2012,** *100* (18), 183104.
408. P. Villars, K. C., Pearson's Crystal Data: Crystal Structure Database for Inorganic Compounds (on DVD). ASM International®: Materials Park, Ohio, USA, Release 2017/18.
409. Zhou, C.; Lin, H.; Shi, H.; Tian, Y.; Pak, C.; Shatruk, M.; Zhou, Y.; Djurovich, P.; Du, M. H.; Ma, B., A Zero-Dimensional Organic Seesaw-Shaped Tin Bromide with Highly Efficient Strongly Stokes-Shifted Deep-Red Emission. *Angew. Chem.* **2018,** *130* (4), 1033-1036.
410. Wu, G.; Zhou, C.; Ming, W.; Han, D.; Chen, S.; Yang, D.; Besara, T.; Neu, J.; Siegrist, T.; Du, M.-H., A One-Dimensional Organic Lead Chloride Hybrid with Excitation-Dependent Broadband Emissions. *ACS Energy Lett.* **2018**.
411. Hull, S.; Berastegui, P., Crystal structures and ionic conductivities of ternary derivatives of the silver and copper monohalides—II: ordered phases within the $(AgX)_x(MX)_{1-x}$ and $(CuX)_x(MX)_{1-x}$ (M= K, Rb and Cs; X= Cl, Br and I) systems. *J. Solid State Chem.* **2004,** *177* (9), 3156-3173.
412. Bigalke, K.; Hans, A.; Hartl, H., Synthese und Strukturuntersuchungen von Iodocupraten(I)IX. Synthese und Kristallstrukturen von $Cs_3Cu_2I_5$ und $RbCu_2I_3$. *Z. Anorg. Allg. Chem.* **1988,** *563* (1), 96-104.
413. Wojakowska, A.; Gorniak, A.; Kuznetsov, A. Y.; Wojakowski, A.; Josiak, J., Phase diagram of the system copper (I) iodide+ cesium iodide. *J. Chem. Eng. Data* **2003,** *48* (3), 468-471.
414. Wojakowska, A.; Krzyżak, E.; Wojakowski, A., Phase diagram for the CuBr–CsBr system. *Thermochim. Acta* **2000,** *344* (1-2), 55-59.

415. Asplund, M.; Jagner, S., Crystal Structure of bis- (tetraethylammonium)di-mu-bromo-dibromodicuprate(I), $[N(C_2H_5)_4]_2[Cu_2Br_4]$. *Acta Chem. Scand. A* **1984,** *38* (2).
416. Haddad, S.; Willett, R. D., Dimeric Cu(I) Bromide Species Consisting of Two Edge-Shared Tetrahedra: Crystal Structure of $(C_8H_{14}N_2)_2Cu_2Br_6$. *Inorg. Chem.* **2001,** *40* (4), 809-811.
417. Shannon, R. D., Revised effective ionic radii and systematic studies of interatomic distances in halides and chalcogenides. *Acta Crystallogr. Sect. A* **1976,** *32* (5), 751-767.
418. Bag, M.; Renna, L. A.; Adhikari, R. Y.; Karak, S.; Liu, F.; Lahti, P. M.; Russell, T. P.; Tuominen, M. T.; Venkataraman, D., Kinetics of Ion Transport in Perovskite Active Layers and Its Implications for Active Layer Stability. *J. Am. Chem. Soc.* **2015,** *137* (40), 13130-13137.
419. Eames, C.; Frost, J. M.; Barnes, P. R. F.; O'Regan, B. C.; Walsh, A.; Islam, M. S., Ionic transport in hybrid lead iodide perovskite solar cells. *Nat. Commun.* **2015,** *6*, 7497.
420. Roccanova, R.; Ming, W.; Whiteside, V. R.; McGuire, M. A.; Sellers, I. R.; Du, M.-H.; Saparov, B., Synthesis, Crystal and Electronic Structures, and Optical Properties of $(CH_3NH_3)_2CdX_4$ (X = Cl, Br, I). *Inorg. Chem.* **2017,** *56* (22), 13878-13888.
421. Saparov, B.; Sun, J.-P.; Meng, W.; Xiao, Z.; Duan, H.-S.; Gunawan, O.; Shin, D.; Hill, I. G.; Yan, Y.; Mitzi, D. B., Thin-film deposition and characterization of a Sn-deficient perovskite derivative Cs_2SnI_6. *Chem. Mater.* **2016,** *28* (7), 2315-2322.
422. Li, T.; Dunlap-Shohl, W. A.; Han, Q.; Mitzi, D. B., Melt Processing of Hybrid Organic–Inorganic Lead Iodide Layered Perovskites. *Chem. Mater.* **2017,** *29* (15), 6200-6204.
423. Leijtens, T.; Prasanna, R.; Gold-Parker, A.; Toney, M. F.; McGehee, M. D., Mechanism of Tin Oxidation and Stabilization by Lead Substitution in Tin Halide Perovskites. *ACS En. Lett.* **2017,** *2* (9), 2159-2165.
424. Lee, J.; Chen, H.-F.; Batagoda, T.; Coburn, C.; Djurovich, P. I.; Thompson, M. E.; Forrest, S. R., Deep blue phosphorescent organic light-emitting diodes with very high brightness and efficiency. *Nat. Mater.* **2015,** *15*, 92.
425. Goto, T.; Ueta, M., Luminescence of CuBr and Its Correlation to the Exciton. *J. Phys. Soc. Jpn.* **1967,** *22* (2), 488-498.
426. Chen, D.; Wang, Y.; Lin, Z.; Huang, J.; Chen, X.; Pan, D.; Huang, F., Growth Strategy and Physical Properties of the High Mobility P-Type CuI Crystal. *Cryst. Growth Des.* **2010,** *10* (5), 2057-2060.
427. Valenta, J.; Dian, J.; Gilliot, P.; Hönerlage, B., Photoluminescence and Optical Gain in CuBr Semiconductor Nanocrystals. *Phys. Status Solidi B* **2001,** *224* (1), 313-317.
428. Woggon, U.; Wind, O.; Langbein, W.; Gogolin, O.; Klingshirn, C., Confined biexcitons in CuBr quantum dots. *J. Lumin.* **1994,** *59* (3), 135-145.
429. Smith, M. D.; Watson, B. L.; Dauskardt, R. H.; Karunadasa, H. I., Broadband Emission with a Massive Stokes Shift from Sulfonium Pb–Br Hybrids. *Chem. Mater.* **2017,** *29* (17), 7083-7087.
430. Gao, P.; Gu, M.; Liu, X.; Zheng, Y. Q.; Shi, E. W., Photoluminescence study of annealing effects on CuI crystals grown by evaporation method. *Cryst. Res. Technol.* **2012,** *47* (7), 707-712.

431. Reshchikov, M. A.; Morkoç, H., Luminescence properties of defects in GaN. *J. Appl. Phys.* **2005,** *97* (6), 5-19.
432. Feldmann, J.; Peter, G.; Göbel, E.; Dawson, P.; Moore, K.; Foxon, C.; Elliott, R., Linewidth dependence of radiative exciton lifetimes in quantum wells. *Phys. Rev. Lett.* **1987,** *59* (20), 2337.
433. Kortüm, G.; Braun, W.; Herzog, G., Principles and Techniques of Diffuse-Reflectance Spectroscopy. *Angew. Chem. Int. Ed.* **1963,** *2* (7), 333-341.
434. Meyer, G., Synproportionierung am metallischen Substrat: $CsCu_2Cl_3$ und $CsCu_2Br_3$. *Z. Anorg. Allg. Chem.* **1984,** *515* (8), 127-132.
435. Jouini, N.; Guen, L.; Tournoux, M., Structure cristalline de $CsCu_2I_3$. *Rev. Chim. Mineral* **1980,** *17*, 486-491.
436. Zhang, X.; Liu, H.; Wang, W.; Zhang, J.; Xu, B.; Karen, K. L.; Zheng, Y.; Liu, S.; Chen, S.; Wang, K., Hybrid Perovskite Light-Emitting Diodes Based on Perovskite Nanocrystals with Organic–Inorganic Mixed Cations. *Adv. Mater.* **2017,** *29* (18), 1606405.
437. Starkholm, A.; Kloo, L.; Svensson, P. H., Polyiodide Hybrid Perovskites: A Strategy To Convert Intrinsic 2D Systems into 3D Photovoltaic Materials. *ACS Appl. Energy Mater.* **2019,** *2* (1), 477-485.
438. Li, J.; Wang, H.; Luo, M.; Tang, J.; Chen, C.; Liu, W.; Liu, F.; Sun, Y.; Han, J.; Zhang, Y., 10% Efficiency $Cu_2ZnSn(S,Se)_4$ thin film solar cells fabricated by magnetron sputtering with enlarged depletion region width. *Sol. Energy Mater. Sol. Cells* **2016,** *149*, 242-249.
439. Chen, X.; Li, N.; Li, Y.; Che, P., Characterization on crystal structure of $CH_3NH_3PbI_xCl_{3-x}$ perovskite by variable temperature powder X-ray diffraction. *Mater. Lett.* **2019,** *235*, 239-241.
440. Robinson, K.; Gibbs, G.; Ribbe, P., Quadratic elongation: a quantitative measure of distortion in coordination polyhedra. *Science* **1971,** *172* (3983), 567-570.
441. Mott, N. F.; Stoneham, A. M., The lifetime of electrons, holes and excitons before self-trapping. *J. Phys. C.* **1977,** *10* (17), 3391-3398.
442. Purdy, A. E.; Murray, R. B.; Song, K. S.; Stoneham, A. M., Studies of self-trapped exciton luminescence in KCl. *Phys. Rev. B* **1977,** *15* (4), 2170-2176.
443. Gautier, R.; Massuyeau, F.; Galnon, G.; Paris, M., Lead Halide Post-Perovskite-Type Chains for High-Efficiency White-Light Emission. *Adv. Mater. 0* (0), 1807383.
444. Lin, H.; Zhou, C.; Neu, J.; Zhou, Y.; Han, D.; Chen, S.; Worku, M.; Chaaban, M.; Lee, S.; Berkwits, E.; Siegrist, T.; Du, M.-H.; Ma, B., Bulk Assembly of Corrugated 1D Metal Halides with Broadband Yellow Emission. *Adv. Opt. Mater. 0* (0), 1801474.
445. Yangui, A.; Roccanova, R.; McWhorter, T. M.; Wu, Y.; Du, M.-H.; Saparov, B., Hybrid Organic–Inorganic Halides $(C_5H_7N_2)_2MBr_4$ (M = Hg, Zn) with High Color Rendering Index and High-Efficiency White-Light Emission. *Chem. Mater.* **2019**, *31* (8), 2983-2991.
446. McCall, K. M.; Stoumpos, C. C.; Kostina, S. S.; Kanatzidis, M. G.; Wessels, B. W., Strong Electron–Phonon Coupling and Self-Trapped Excitons in the Defect Halide Perovskites A3M2I9 (A = Cs, Rb; M = Bi, Sb). *Chem. Mater.* **2017,** *29* (9), 4129-4145.

447. Aamir, M.; Khan, M. D.; Sher, M.; Revaprasadu, N.; Malik, M. A.; Akhtar, J., Broadband emission in a new lead free all-inorganic 3D CsZnCl2I perovskite. *New J. Chem.* **2018,** *42* (21), 17181-17184.
448. Zhang, R.; Mao, X.; Yang, Y.; Yang, S.; Zhao, W.; Wumaier, T.; Wei, D.; Deng, W.; Han, K., Air-Stable, Lead-Free Zero-Dimensional Mixed Bismuth-Antimony Perovskite Single Crystals with Ultra-broadband Emission. *Angew. Chem.* **2019,** *131* (9), 2751-2755.
449. Luo, J.; Wang, X.; Li, S.; Liu, J.; Guo, Y.; Niu, G.; Yao, L.; Fu, Y.; Gao, L.; Dong, Q.; Zhao, C.; Leng, M.; Ma, F.; Liang, W.; Wang, L.; Jin, S.; Han, J.; Zhang, L.; Etheridge, J.; Wang, J.; Yan, Y.; Sargent, E. H.; Tang, J., Efficient and stable emission of warm-white light from lead-free halide double perovskites. *Nature* **2018,** *563* (7732), 541-545.
450. Mariotti, S.; Hutter, O. S.; Phillips, L. J.; Yates, P. J.; Kundu, B.; Durose, K., Stability and Performance of $CsPbI_2Br$ Thin Films and Solar Cell Devices. *ACS App. Mater. Inter.* **2018,** *10* (4), 3750-3760.
451. Roccanova, R.; Yangui, A.; Nhalil, H.; Shi, H.; Du, M.-H.; Saparov, B., Near-Unity Photoluminescence Quantum Yield in Blue-Emitting Cs3Cu2Br5–xIx ($0 \leq x \leq 5$). *ACS Appl. Electron. Mater.* **2019**, *1* (3), 269-274.
452. Qin, C.; Matsushima, T.; Klotz, D.; Fujihara, T.; Adachi, C., The Relation of Phase-Transition Effects and Thermal Stability of Planar Perovskite Solar Cells. *Adv. Sci.* **2019,** *6* (1), 1801079.
453. Wojakowska, A.; Krzyżak, E., Factors affecting the general shape of the phase diagram and compound formation in the binary copper (I) halide–alkali-metal halide systems. *J. Therm. Anal. Calor.* **2006,** *83* (3), 597-601.
454. Kawai, T.; Ishii, A.; Kitamura, T.; Shimanuki, S.; Iwata, M.; Ishibashi, Y., Optical Absorption in Band-Edge Region of ($CH_3NH_3)_3Bi_2I_9$ Single Crystals. *J. Phys. Soc. Jpn.* **1996,** *65* (5), 1464-1468.
455. Zhou, J.; Li, M.; Ning, L.; Zhang, R.; Molokeev, M. S.; Zhao, J.; Yang, S.; Han, K.; Xia, Z., Broad-Band Emission in a Zero-Dimensional Hybrid Organic [PbBr6] Trimer with Intrinsic Vacancies. *J. Phys. Chem. Lett.* **2019**, 1337-1341.
456. Lin, H.; Zhou, C.; Tian, Y.; Siegrist, T.; Ma, B., Low-Dimensional Organometal Halide Perovskites. *ACS Energy Lett.* **2018,** *3* (1), 54-62.
457. Zhou, C.; Lin, H.; Tian, Y.; Yuan, Z.; Clark, R.; Chen, B.; van de Burgt, L. J.; Wang, J. C.; Zhou, Y.; Hanson, K.; Meisner, Q. J.; Neu, J.; Besara, T.; Siegrist, T.; Lambers, E.; Djurovich, P.; Ma, B., Luminescent zero-dimensional organic metal halide hybrids with near-unity quantum efficiency. *Chem. Sci.* **2018,** *9* (3), 586-593.
458. Mott, N. F.; Stoneham, A. M., The lifetime of electrons, holes and excitons before self-trapping. *J. Phys. C: Solid St. Phys.* **1977,** *10* (17), 3391-3398.
459. Varshni, Y., Temperature dependence of the energy gap in semiconductors. *Physica* **1967,** *34* (1), 149-154.
460. Li, J.; Yuan, X.; Jing, P.; Li, J.; Wei, M.; Hua, J.; Zhao, J.; Tian, L., Temperature-dependent photoluminescence of inorganic perovskite nanocrystal films. *RSC Adv.* **2016,** *6* (82), 78311-78316.
461. Gaponenko, M. S.; Lutich, A. A.; Tolstik, N. A.; Onushchenko, A. A.; Malyarevich, A. M.; Petrov, E. P.; Yumashev, K. V., Temperature-dependent photoluminescence of

PbS quantum dots in glass: Evidence of exciton state splitting and carrier trapping. *Phys Rev B* **2010,** *82* (12), 125320.
462. Hong, X.; Ishihara, T.; Nurmikko, A., Dielectric confinement effect on excitons in PbI4-based layered semiconductors. *Phys Rev B* **1992,** *45* (12), 6961-6964.
463. Yang, H.; Zhang, Y.; Pan, J.; Yin, J.; Bakr, O. M.; Mohammed, O. F., Room-Temperature Engineering of All-Inorganic Perovskite Nanocrsytals with Different Dimensionalities. *Chem. Mater.* **2017,** *29* (21), 8978-8982.
464. Li, F.; Yang, L.; Cai, Z.; Wei, K.; Lin, F.; You, J.; Jiang, T.; Wang, Y.; Chen, X., Enhancing exciton binding energy and photoluminescence of formamidinium lead bromide by reducing its dimensions to 2D nanoplates for producing efficient light emitting diodes. *Nanoscale* **2018,** *10* (44), 20611-20617.
465. Longo, G.; La-Placa, M.-G.; Sessolo, M.; Bolink, H. J., High Photoluminescence Quantum Yields in Organic Semiconductor–Perovskite Composite Thin Films. *ChemSusChem* **2017,** *10* (19), 3788-3793.
466. Droseros, N.; Longo, G.; Brauer, J. C.; Sessolo, M.; Bolink, H. J.; Banerji, N., Origin of the Enhanced Photoluminescence Quantum Yield in MAPbBr3 Perovskite with Reduced Crystal Size. *ACS Energy Letters* **2018,** *3* (6), 1458-1466.
467. Shibata, H., Negative Thermal Quenching Curves in Photoluminescence of Solids. *Jpn. J. Appl. Phys.* **1998,** *37* (Part 1, No. 2), 550-553.
468. Chen, X.; Wu, X.; Yue, L.; Zhu, L.; Pan, W.; Qi, Z.; Wang, S.; Shao, J., Negative thermal quenching of below-bandgap photoluminescence in InPBi. *Appl. Phys. Lett.* **2017,** *110* (5), 051903.
469. Wu, Y.; Li, J.; Ding, H.; Gao, Z.; Wu, Y.; Pan, N.; Wang, X., Negative thermal quenching of photoluminescence in annealed ZnO–Al2O3 core–shell nanorods. *Phys. Chem. Chem. Phys* **2015,** *17* (7), 5360-5365.
470. Wright, A. D.; Verdi, C.; Milot, R. L.; Eperon, G. E.; Pérez-Osorio, M. A.; Snaith, H. J.; Giustino, F.; Johnston, M. B.; Herz, L. M., Electron–phonon coupling in hybrid lead halide perovskites. *Nat. Commun.* **2016,** *7*, 11755.
471. McCall, K. M.; Stoumpos, C. C.; Kontsevoi, O. Y.; Alexander, G. C. B.; Wessels, B. W.; Kanatzidis, M. G., From 0D $Cs_3Bi_2I_9$ to 2D $Cs_3Bi_2I_6Cl_3$: Dimensional Expansion Induces Direct Bandgap but Enhances Electron-Phonon Coupling. *Chem. Mater.* **2019**.
472. Vasil'chenko, E.; Lushchik, N.; Lushchik, C., Migrations of excitons and holes in luminescent crystals of CsBr. *J. Lumin.* **1972,** *5* (2), 117-131.
473. Lushchik, A.; Feldbach, E.; Frorip, A.; Ibragimov, K.; Savikhin, F.; Lushchik, C., Radiative decay of intrinsic electronic excitations in a wide-gap CsCl crystal. *J. Lumin.* **1995,** *63* (5), 273-278.
474. Amsler, C.; Grögler, D.; Joffrain, W.; Lindelöf, D.; Marchesotti, M.; Niederberger, P.; Pruys, H.; Regenfus, C.; Riedler, P.; Rotondi, A., Temperature dependence of pure CsI: scintillation light yield and decay time. *Nuc. Instru. Meth. Phys. Res. Sec. A:* ***2002****, 480* (2-3), 494-500.
475. Friend, R. H.; Di, D.; Lilliu, S.; Zhao, B., Perovskite LEDs. *Sci. Video Protoc* **2019,** *1* (1).
476. Bao, X.; Schlesinger, T.; James, R.; Ortale, C.; Van den Berg, L., High resolution 4.2 K near band-gap photoluminescence spectrum of mercuric iodide. *J. Appl. Phys.* **1990,** *68* (6), 2951-2954.

477. Thirumal, K.; Chong, W. K.; Xie, W.; Ganguly, R.; Muduli, S. K.; Sherburne, M.; Asta, M.; Mhaisalkar, S.; Sum, T. C.; Soo, H. S., Morphology-independent stable white-light emission from self-assembled two-dimensional perovskites driven by strong exciton–phonon coupling to the organic framework. *Chem. Mater.* **2017,** *29* (9), 3947-3953.
478. Houck, M. B., *Synthesis, Isolation, and Reactivity of Kinetically Stabilized Aromatic Nitrosamides and New Low Dimensional Organic Inorganic Hybrid Materials*. University of Oklahoma: University of Oklahoma, **2019**.
479. Morad, V.; Shynkarenko, Y.; Yakunin, S.; Brumberg, A.; Schaller, R. D.; Kovalenko, M. V., Disphenoidal Zero-Dimensional Lead, Tin, and Germanium Halides: Highly Emissive Singlet and Triplet Self-Trapped Excitons and X-ray Scintillation. *J. Am. Chem. Soc.* **2019**.
480. Zhou, H.; Liu, X.; He, G.; Fan, L.; Shi, S.; Wei, J.; Xu, W.; Yuan, C.; Chai, N.; Chen, B.; Zhang, Y.; Zhang, X.; Zhao, J.; Wei, X.; Yin, J.; Tian, D., Synthesis, Crystal Structure, UV–Vis Adsorption Properties, Photoelectric Behavior, and DFT Computational Study of All-Inorganic and Lead-Free Copper Halide Salt $K_2Cu_2Cl_6$. *ACS Omega* **2018,** *3* (10), 14021-14026.
481. Petrov, A. A.; Khrustalev, V. N.; Zubavichus, Y. V.; Dorovatovskii, P. V.; Goodilin, E. A.; Tarasov, A. B., Synthesis and crystal structure of a new hybrid methylammonium iodocuprate. *Mendeleev Commun.* **2018,** *28* (3), 245-247.
482. Madhavan, V. E.; Zimmermann, I.; Roldán-Carmona, C.; Grancini, G.; Buffiere, M.; Belaidi, A.; Nazeeruddin, M. K., Copper Thiocyanate Inorganic Hole-Transporting Material for High-Efficiency Perovskite Solar Cells. *ACS Energy Lett.* **2016,** *1* (6), 1112-1117.
483. Brink, C.; Binnendijk, N.; Van de Linde, J., The crystal structures of $CsCu_2Cl_3$ and $CsAg_2I_3$. *Acta Crystallogr.* **1954,** *7* (2), 176-180.

Appendix 1: Supplementary Figures

A1.1 Chapter 2 Figures and Tables

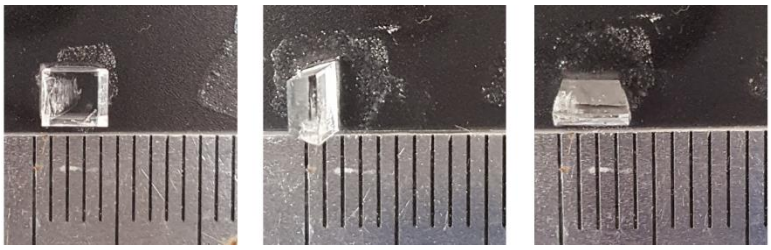


Figure A1.1. Pictures of a 4 × 3 × 2 mm^3 single crystal of MA_2CdCl_4 grown by slowly evaporating a 1 M DMF solution of MA_2CdCl_4 at room temperature.

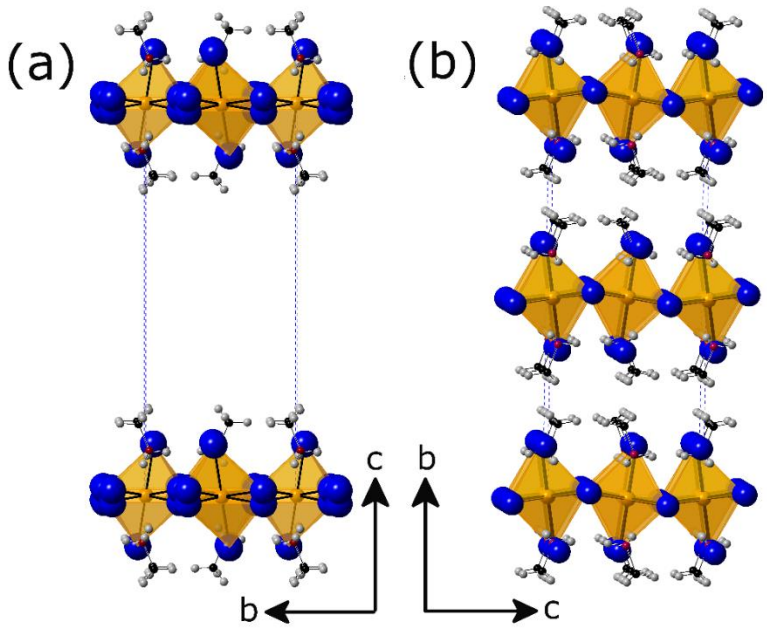


Figure A1.2. The difference between (a) the low temperature monoclinic $P2_1/a$ structure reported by Chapuis et al.[223] and (b) the $P2_1/c$ structure reported in this work. The literature reported structure has an unphysically large interlayer void.

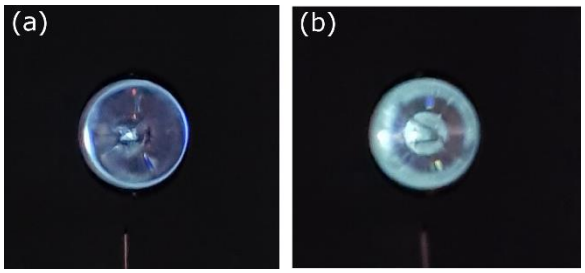


Figure A1.3. Blue and white-green emission from (a) MA_2CdBr_4 and (b) MA_2CdI_4, respectively, at 4 K upon excitation using a He-Cd laser (325 nm). Both (a) and (b) exhibit thermal quenching as the temperature is increased to room temperature.

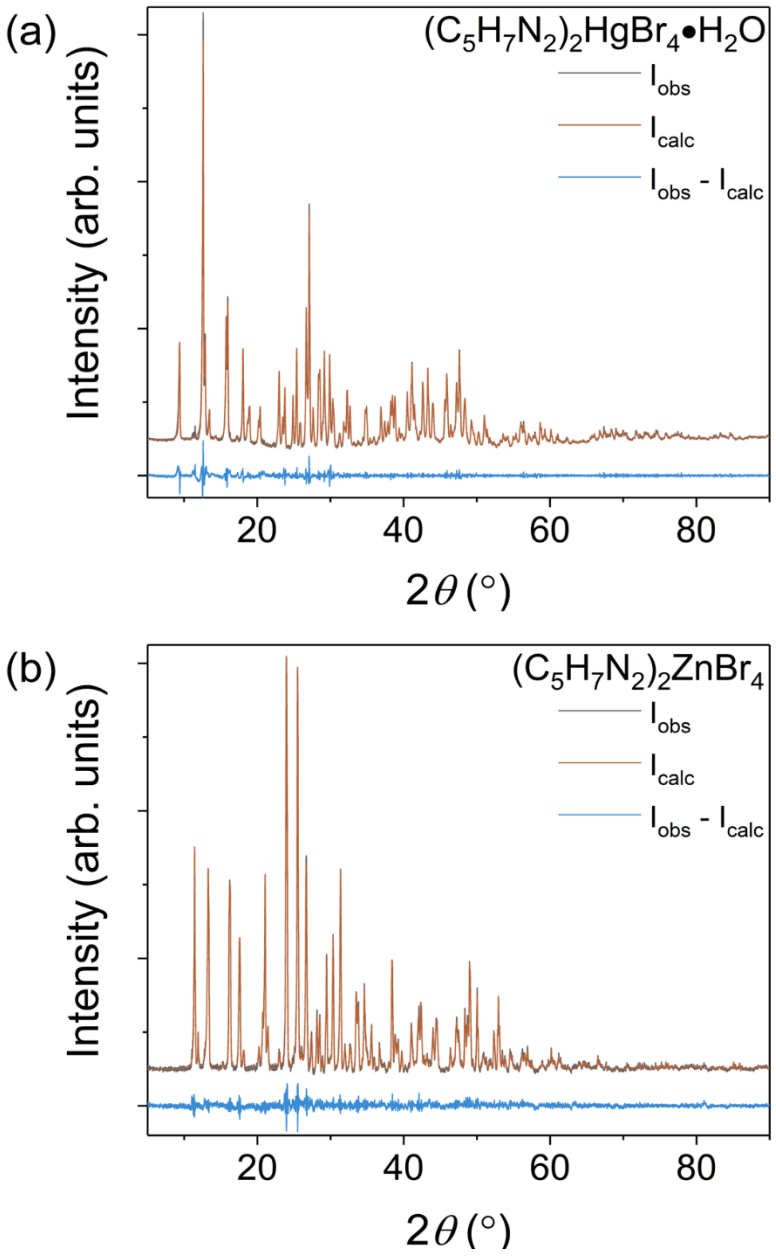


Figure A1.4. Room temperature PXRD pattern (black) with Pawley fits (red) for (a) $(C_5H_7N_2)_2HgBr_4 \cdot H_2O$ and (b) $(C_5H_7N_2)_2ZnBr_4$. Difference map is shown in blue.

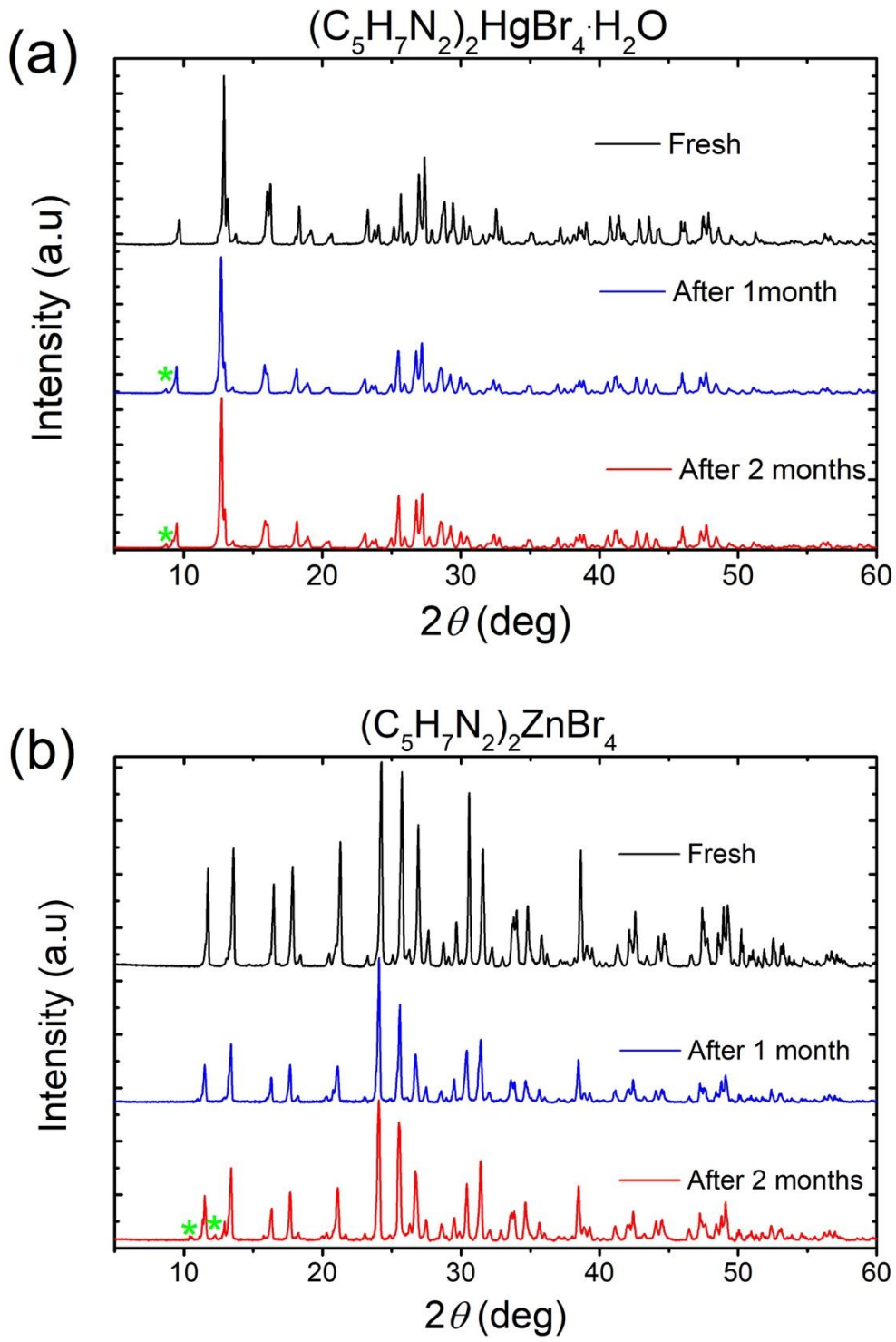


Figure A1.5. Comparison of simulated and measured Powder XRD pattern of (a) $(C_5H_7N_2)_2HgBr_4 \cdot H_2O$ and (b) $(C_5H_7N_2)_2ZnBr_4$, left in ambient air for over a period of two months. Formation of small impurities are indicated with green asterisks.

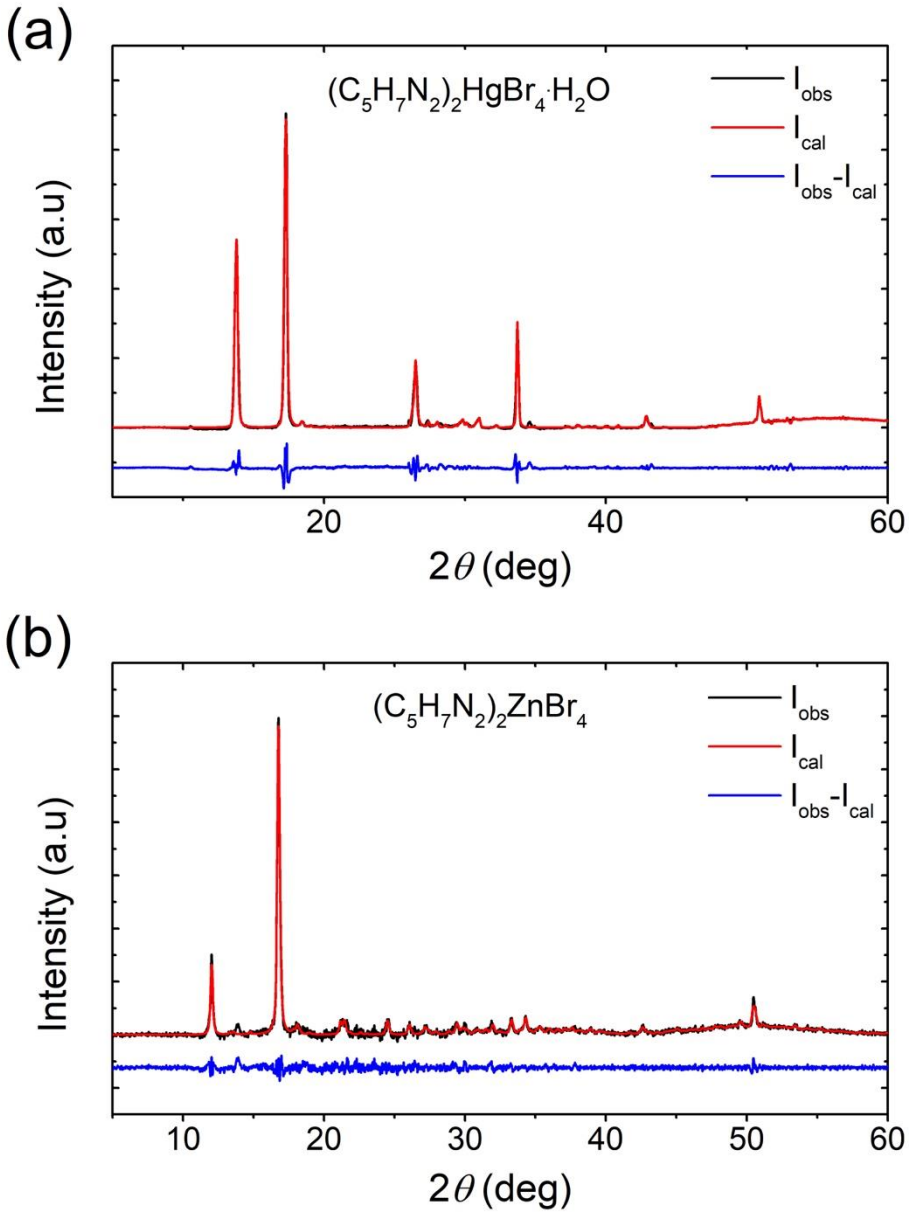


Figure A1.6. Refinement of the Powder X-ray diffraction data of thin films of (a) **1** and (b) **2** using Pawley fittings.

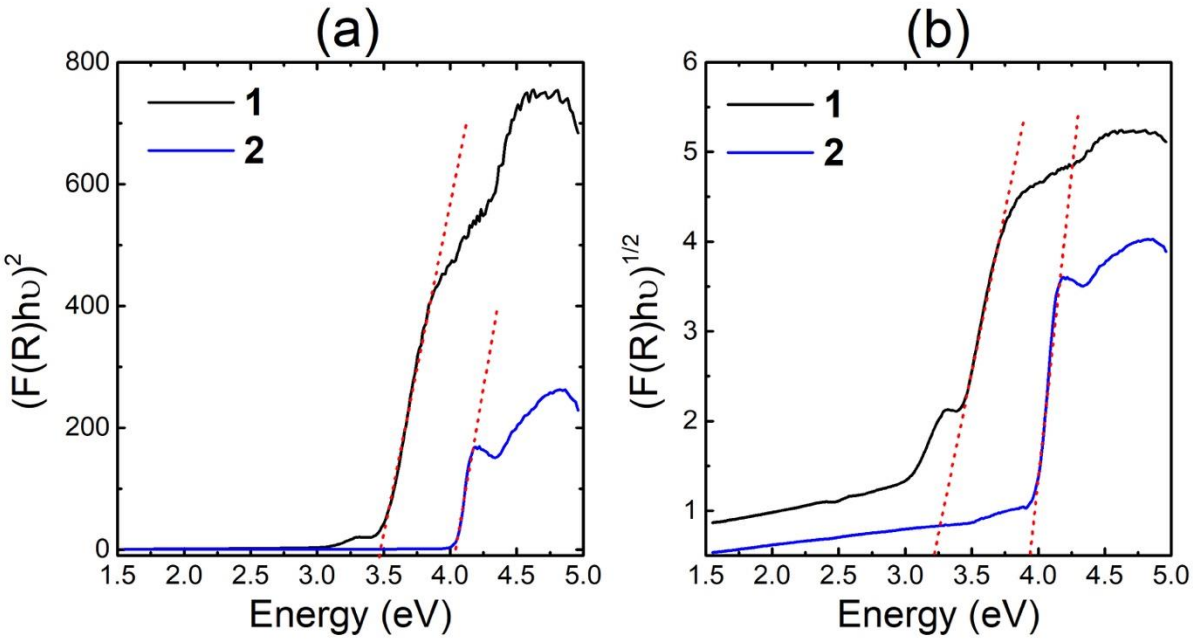


Figure A1.7. Tauc plots of **1** and **2** for the case of (a) direct and (b) indirect band gaps. The linear region is extrapolated to the x-axis to extract the estimated optical band gap (red lines).

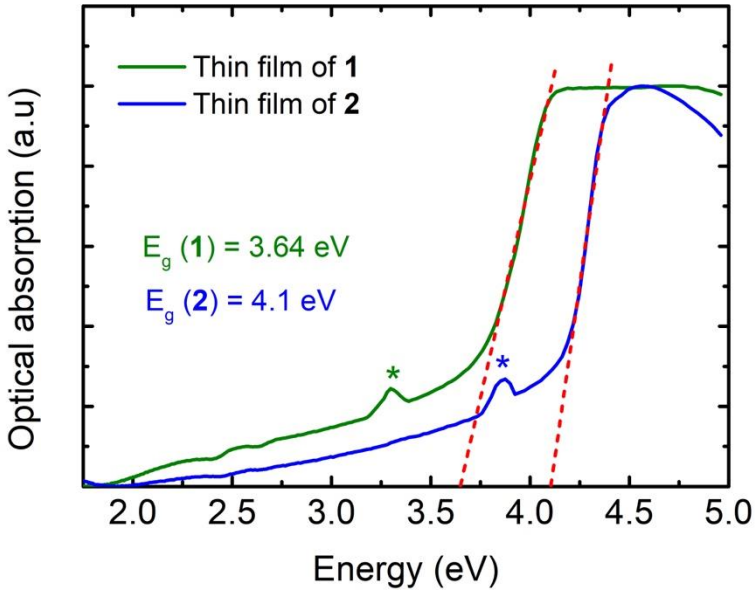


Figure A1.8. Room temperature optical absorption spectra measured on thin films of **1** (green) and **2** (blue). Excitonic feature are indicated by asterisks. Band gaps energy of 3.64 and 4.10 eV (dashed red lines) were estimated for **1** and **2**, respectively.

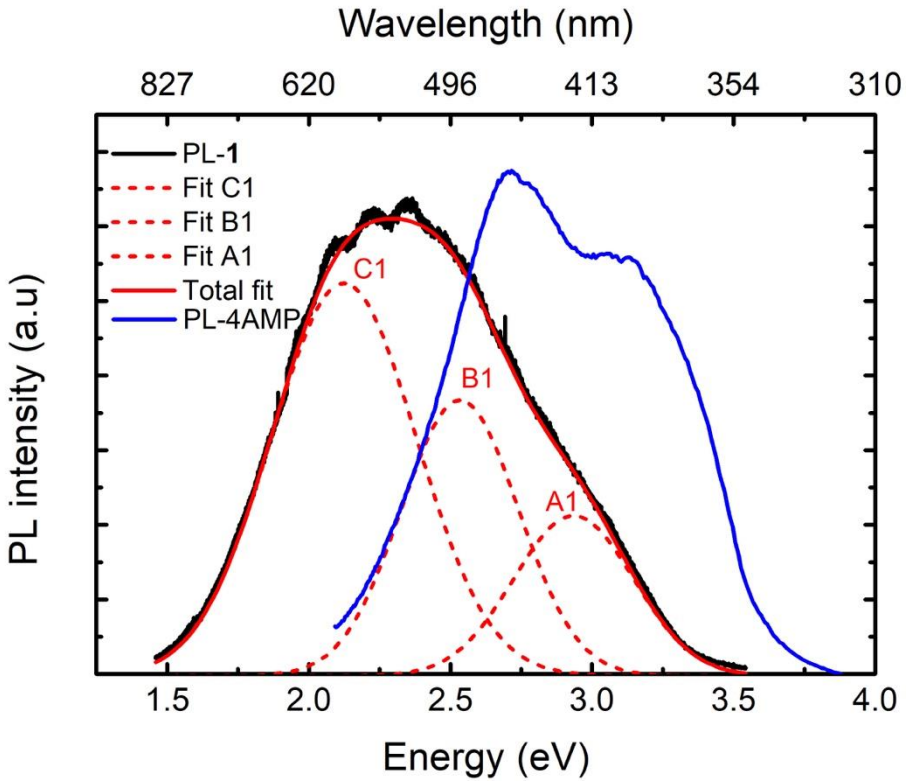


Figure A1.9. Room temperature PL spectra of **1** (black line) and 4AMP (blue line). The deconvolution of the PL of 1 using three Gaussian function are shown in red.

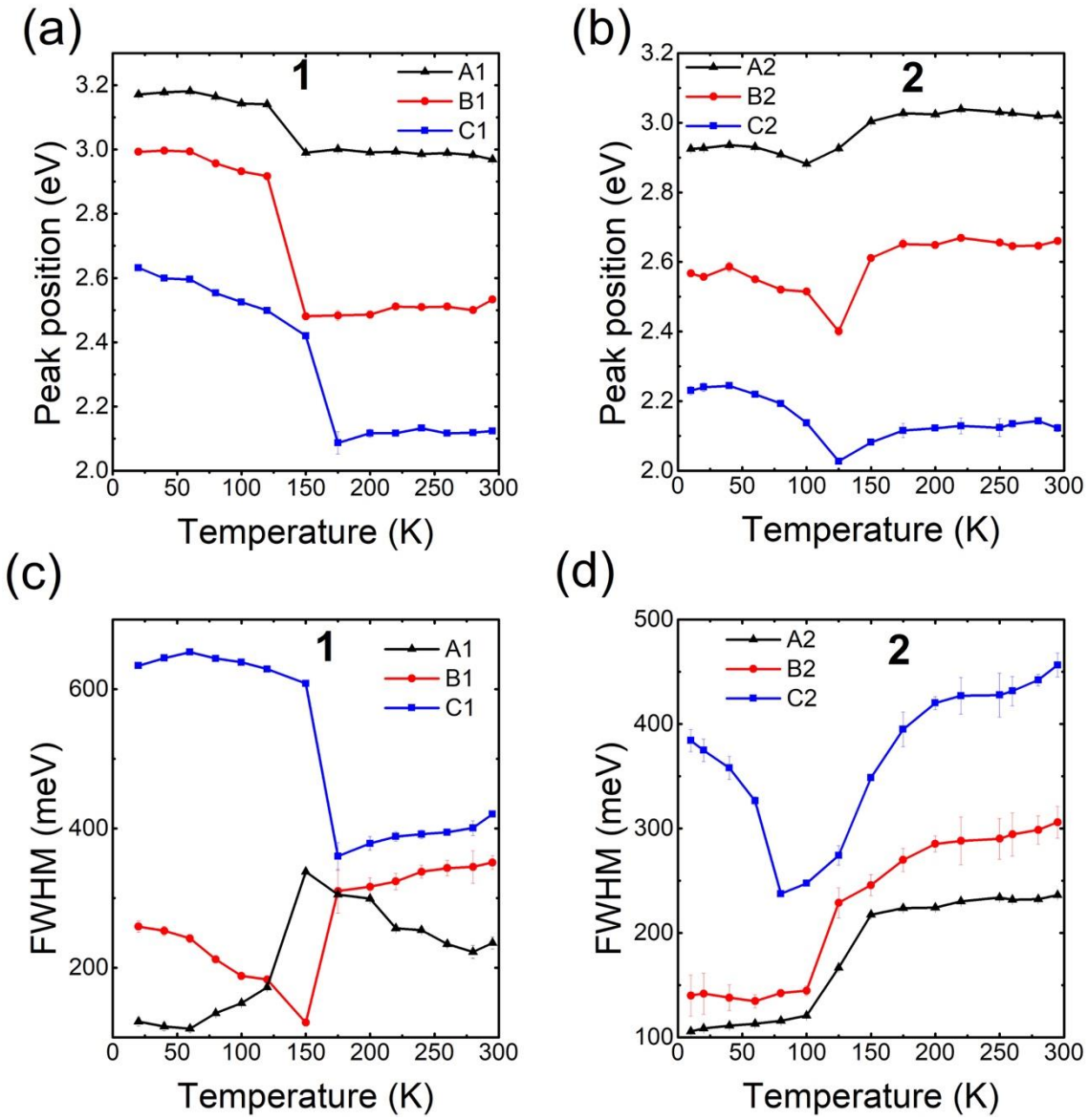


Figure A1.10. Thermal evolution of the position (a-b) and the FWHM (c-d) of **1** and **2** compounds, derived from the fitting of the temperature dependence PL data shown in Chapter 3 Figure 13.

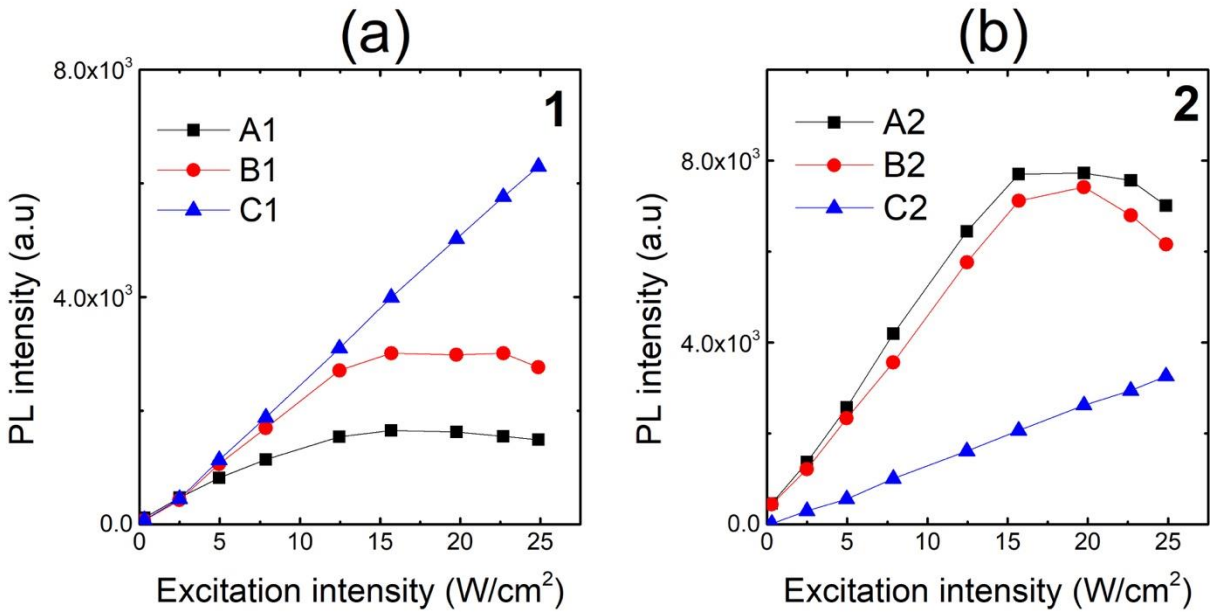


Figure A1.11. Room temperature PL intensity vs excitation power of (a) **1** and (b) **2** compounds.

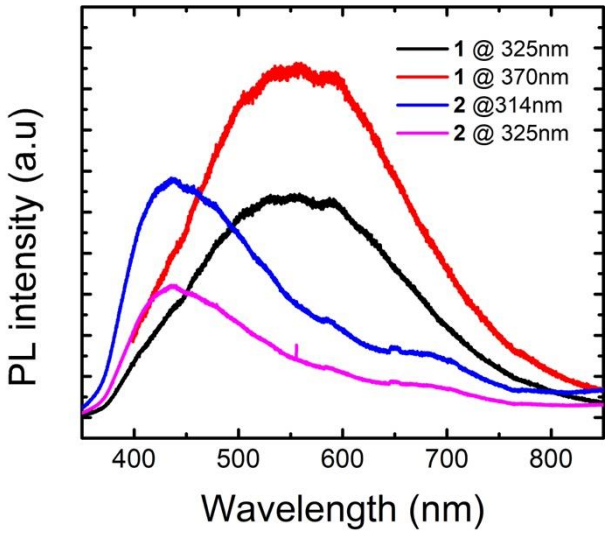


Figure A1.12. Room temperature PL spectra of **1** and **2** under different excitation wavelengths.

Table A1.1. Atomic coordinates and equivalent isotropic (U_{eq}[a]) displacement parameters for $(CH_3NH_3)_2CdBr_4$ at 298(2) K.

Atom	Wyckoff site	*x*	*y*	*z*	U_{eq}, Å^2
Cd	4*e*	0.73304(4)	0.43604(3)	0.26774(3)	0.04050(13)
Br1	4*e*	1.00204(6)	0.37166(5)	0.38391(5)	0.05313(17)
Br2	4*e*	0.69921(8)	0.36141(5)	0.05784(5)	0.05713(18)
Br3	4*e*	0.48232(7)	0.38662(5)	0.37495(6)	0.06176(19)
Br4	4*e*	0.76365(10)	0.62762(4)	0.26543(5)	0.0665(2)
N1	4*e*	0.2921(6)	0.2941(4)	0.0186(4)	0.0550(11)
H1	4*e*	0.3967	0.3144	0.032	0.083
H2	4*e*	0.2647	0.2873	-0.0585	0.083
H3	4*e*	0.2809	0.2358	0.0541	0.083
N2	4*e*	0.7782(7)	0.4006(5)	0.6230(5)	0.0665(14)
H4	4*e*	0.8485	0.4511	0.6201	0.1
H5	4*e*	0.6812	0.4167	0.5838	0.1
H6	4*e*	0.8187	0.347	0.5903	0.1
C1	4*e*	0.7557(10)	0.3793(6)	0.7451(6)	0.0727(19)
H7	4*e*	0.7953	0.4345	0.7936	0.109
H8	4*e*	0.8168	0.3205	0.7701	0.109
H9	4*e*	0.6403	0.3689	0.7521	0.109
C2	4*e*	0.1850(11)	0.3667(5)	0.0647(7)	0.077(2)
H10	4*e*	0.209	0.3704	0.1487	0.115
H11	4*e*	0.0716	0.3474	0.0451	0.115
H12	4*e*	0.2031	0.4307	0.0308	0.115

[a] U_{eq} is defined as one third of the trace of the orthogonalized U_{ij} tensor

Table A1.2. Selected interatomic distances (Å) and angles (º) in $(CH_3NH_3)_2CdBr_4$ at 298(2) K.

Label		Distance	Label	Angle
Cd–	Br1	2.5807(6)	Br3-Cd-Br1	109.82(2)
	Br2	2.5850(7)	Br3-Cd-Br2	109.29(2)
	Br3	2.5743(7)	Br1-Cd-Br2	110.25(2)
	Br4	2.5856(7)	Br3-Cd-Br4	110.09(3)
			Br2-Cd-Br4	105.17(3)
N1–	C1	1.454(8)	Br2-Cd-Br4	112.16(2)
	C2	1.443(8)		

Table A1.3. Atomic coordinates and equivalent isotropic (U_{eq}[a]) displacement parameters for $(CH_3NH_3)_2CdCl_4$ at 100(2) K.

Atom	Wyckoff site	*x*	*y*	*z*	U_{eq}, Å^2
Cd	2*a*	0.5000	0.5000	0.5000	0.0103(3)
Cl1	4*e*	0.2384(3)	0.4487(4)	0.3583(5)	0.0218(7)
Cl2	4*e*	0.4650(3)	0.7745(4)	0.2589(4)	0.0205(6)
N1	4*e*	0.2662(11)	0.0214(17)	0.4193(16)	0.027(3)
H1	4*e*	0.272(10)	0.135(12)	0.400(15)	0.041
H2	4*e*	0.331(10)	-0.031(14)	0.393(15)	0.041
H3	4*e*	0.286(10)	0.007(15)	0.542(13)	0.041
C1	4*e*	0.1300(13)	-0.051(2)	0.306(2)	0.031(3)
H4	4*e*	0.0597	0.0145	0.3401	0.046
H5	4*e*	0.1265	-0.1792	0.3367	0.046
H6	4*e*	0.1124	-0.0371	0.1669	0.046

[a] U_{eq} is defined as one third of the trace of the orthogonalized U_{ij} tensor.

Table A1.4. Atomic coordinates and equivalent isotropic (U_{eq}[a]) displacement parameters for $(CH_3NH_3)_2CdI_4$ at 298(2) K.

Atom	Wyckoff site	*x*	*y*	*z*	U_{eq}, Å^2
Cd	8*c*	0.44756(8)	0.89250(7)	0.36443(4)	0.0517(3)
I1	8*c*	0.54162(10)	1.08727(8)	0.40737(5)	0.0773(3)
I2	8*c*	0.21634(9)	0.86882(9)	0.40984(5)	0.0799(4)
I3	8*c*	0.44097(11)	0.89657(9)	0.23248(5)	0.0862(4)
I4	8*c*	0.57221(11)	0.70822(9)	0.39903(5)	0.0858(4)
N1	8*c*	0.6815(14)	0.6850(12)	0.2336(7)	0.114(5)
H1	8*c*	0.6943	0.7292	0.267	0.171
H2	8*c*	0.6163	0.6434	0.2411	0.171
H3	8*c*	0.6691	0.7253	0.1986	0.171
N2	8*c*	0.2435(14)	0.1161(11)	0.5010(6)	0.096(4)
H4	8*c*	0.2479	0.1874	0.4916	0.144
H5	8*c*	0.2255	0.0782	0.4658	0.144
H6	8*c*	0.3149	0.0935	0.5164	0.144
C1	8*c*	0.7877(15)	0.6148(12)	0.2242(10)	0.099(5)
H7	8*c*	0.8558	0.659	0.2109	0.149
H8	8*c*	0.7702	0.5611	0.1917	0.149
H9	8*c*	0.8072	0.5782	0.2636	0.149
C2	8*c*	0.1491(16)	0.0985(13)	0.5490(9)	0.095(5)
H10	8*c*	0.1857	0.0948	0.5908	0.142
H11	8*c*	0.1075	0.0307	0.5402	0.142
H12	8*c*	0.092	0.1583	0.5477	0.142

[a] U_{eq} is defined as one third of the trace of the orthogonalized U_{ij} tensor.

Table A1.5. Selected interatomic distances (Å) and angles (º) in $(CH_3NH_3)_2CdI_4$ at 298(2) K.

Label		Distance	Label	Angle
Cd–	I1	2.7340(13)	I4-Cd-I2	106.78(5)
	I2	2.7226(14)	I4-Cd-I1	115.88(5)
	I3	2.7540(15)	I2-Cd-I1	109.22(4)
	I4	2.7222(13)	I4-Cd-I3	107.04(4)
			I2-Cd-I3	108.98(5)
N1–	C1	1.458(9)	I1-Cd-I3	108.77(4)
	C2	1.46(2)		

Table A1.6. Atomic coordinates and equivalent isotropic (U_{eq}[a]) displacement parameters for $(CH_3NH_3)_2CdBr_4$ at 100(2) K.

Atom	Wyckoff site	*x*	*y*	*z*	U_{eq}, Å^2
Cd	4*e*	0.73656(3)	0.56423(2)	0.26825(2)	0.01076(6)
Br1	4*e*	0.70159(4)	0.64234(2)	0.05758(3)	0.01345(8)
Br2	4*e*	1.00534(4)	0.62913(2)	0.38749(3)	0.01366(8)
Br3	4*e*	0.47990(4)	0.60926(3)	0.37431(3)	0.01632(8)
Br4	4*e*	0.77805(5)	0.36995(2)	0.26196(3)	0.01718(8)
N1	4*e*	0.7783(4)	0.6017(2)	0.6242(2)	0.0164(6)
H1	4*e*	0.7708	0.6607	0.5826	0.025
H2	4*e*	0.6991	0.5579	0.5922	0.025
H3	4*e*	0.881	0.5741	0.621	0.025
N2	4*e*	0.7043(3)	0.2094(2)	0.4797(2)	0.0151(6)
H4	4*e*	0.7277	0.2142	0.5596	0.023
H5	4*e*	0.5959	0.1909	0.462	0.023
H6	4*e*	0.7218	0.2703	0.446	0.023
C1	4*e*	0.7520(5)	0.6222(3)	0.7495(3)	0.0234(8)
H7	4*e*	0.836	0.6705	0.7835	0.035
H8	4*e*	0.7622	0.5589	0.7947	0.035
H9	4*e*	0.6406	0.6507	0.753	0.035
C2	4*e*	0.8145(5)	0.1320(3)	0.4332(3)	0.0225(8)
H10	4*e*	0.9311	0.1523	0.4516	0.034
H11	4*e*	0.7884	0.1263	0.3473	0.034
H12	4*e*	0.7966	0.0665	0.4702	0.034

[a]U_{eq} is defined as one third of the trace of the orthogonalized U_{ij} tensor.

Table A1.7. Selected interatomic distances (Å) and angles (º) in $(CH_3NH_3)_2CdCl_4$ at 100(2) K.

Label		Distance	Label	Angle
Cd–	Cl1	2.567(3)	Cl1-Cd-Cl1	180.0
	Cl2	2.640(3)	Cl1-Cd-Cl2	88.24(9)
	Cl2	2.654(3)	Cl1-Cd-Cl2	91.76(9)
			Cl2-Cd-Cl2	91.54(4)
N1–	C1	1.463(17)	Cl1-Cd-Cl2	90.57(10)
			Cl1-Cd-Cl2	89.43(10)
			Cl2-Cd-Cl2	88.46(4)
			Cd1-Cl2-Cd1	161.27(13)

Table A1.8. Selected interatomic distances (Å) and angles (º) in $(CH_3NH_3)_2CdBr_4$ at 100(2) K.

Label		Distance	Label	Angle
Cd–	Br1	2.5953(4)	Br3-Cd-Br2	110.546(15)
	Br2	2.5804(4)	Br3-Cd-Br4	110.777(14)
	Br3	2.5749(4)	Br2-Cd-Br4	103.888(14)
	Br4	2.5924(5)	Br3-Cd-Br1	109.001(14)
			Br2-Cd-Br1	110.820(14)
N1–	C1	1.487(4)	Br4-Cd-Br1	111.750(13)
	C2	1.489(4)		

Table A1.9. Selected interatomic distances (Å) and angles (º) in $(C_5H_7N_2)_2HgBr_4 \cdot H_2O$ (**1**) and $(C_5H_7N_2)_2ZnBr_4$ (**2**) at 100(2) K.

Label		Distance	Label	Angle (°)
$(C_5H_7N_2)_2HgBr_4 \cdot H_2O$				
Hg–	Br1	2.5998(5)	Br1-Hg-Br2	113.613(15)
	Br2	2.6094(5)	Br2-Hg-Br3	110.210(10)
	Br3	2.6377(4)	Br1-Hg-Br3	105.545(10)
	Br4	2.6377(4)	Br2-Hg-Br3	110.210(10)
			Br1-Hg-Br4	105.544(10)
			Br3-Hg-Br4	111.558(16)
$(C_5H_7N_2)_2ZnBr_4$				
Zn–	Br1	2.4277(5)	Br1-Zn-Br2	105.786(18)
	Br2	2.4319(5)	Br2-Zn-Br3	109.58(2)
	Br3	2.3931(5)	Br2-Zn-Br4	107.60(2)
	Br4	2.3817(5)	Br1-Zn1-Br3	107.11(2)
			Br1-Zn-Br4	110.86(2)
			Br3-Zn-Br4	115.49(2)

A1.2 Chapter 3 Figures and Tables

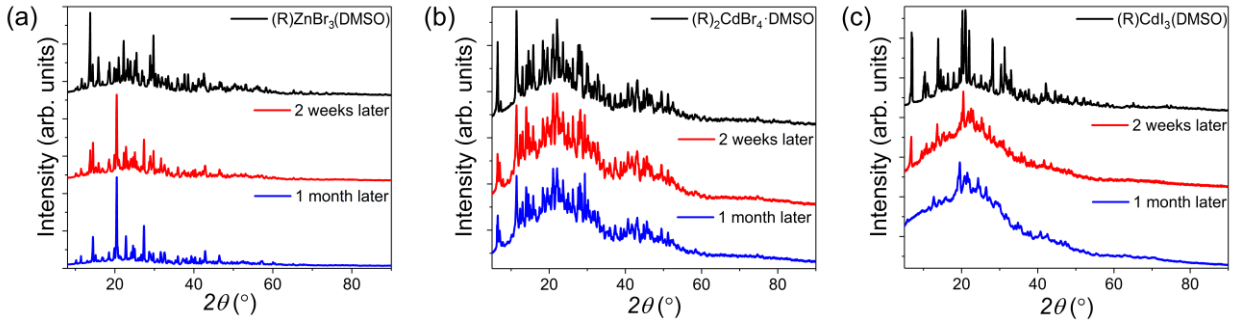


Figure A1.13. PXRD patterns of (a) (R)$ZnBr_3$(DMSO), (b) (R)$_2CdBr_4$·DMSO and (c) (R)CdI_3(DMSO) samples left in ambient air for over a period of one month.

Table A1.10. Selected single crystal data collection and refinement parameters for (R)$ZnBr_3$(DMSO), $(R)_2CdBr_4$·DMSO and (R)CdI_3(DMSO) at 100(2) K.

Formula	**(R)$ZnBr_3$(DMSO)**	**(R)$CdBr_4$·DMSO**	**(R)CdI_3(DMSO)**
Formula weight (g/mol)	603.59	950.90	791.59
Temperature (K)	100 (2)		
Radiation, wavelength (Å)	Mo Kα, 0.71073		
Crystal system	Orthorhombic	Triclinic	Orthorhombic
Space group, *Z*	$P2_12_12$, 4	*P*-1, 2	$P2_12_12$, 4
a (Å)	8.9513(16)	8.829(7)	9.2030(10)
b (Å)	28.500(6)	14.244(10)	29.304(3)
c (Å)	8.8203(16)	15.714(11)	9.3602(11)
α, º	90	72.734(10)	90
β, º	90	89.356(10)	90
γ, º	90	89.710(10)	90
Volume ($Å^3$)	2250.2(7)	1887(2)	2524.3(5)
Density (ρ_{calc}) (g/cm^3)	1.782	1.674	2.083
Absorption coefficient (μ) (mm^{-1})	6.517	4.895	4.622
$\theta_{min} - \theta_{max}$ (º)	2.31 – 26.34	1.36 – 29.23	1.39 – 31.46
Reflections collected	34552	32253	66066
Independent reflections	4193	10050	8052
R^a indices ($I > 2\sigma(I)$)	R_1 = 0.0286 wR_2 = 0.0561	R_1 = 0.0598 wR_2 = 0.1622	R_1 = 0.0419 wR_2 = 0.0915
Goodness-of-fit on F^2	1.007	1.031	1.007
Largest diff. peak and hole ($e^-/Å^3$)	0.344 and -0.335	1.351 and -3.429	1.320 and -0.926

[a] $R_1 = \sum\big||F_o| - |F_c|\big| / \sum|F_o|$; $wR_2 = \{|\sum|w(F_o^2 - F_c^2)^2| / \sum|w(F_o^2)^2||\}^{1/2}$, where $w = \{1/|\sigma^2 F_o^2 + (AP)^2 + BP|\}$, with $P = (F_o^2 + 2F_c^2)/3$ and weight coefficients *A* and *B*.

Table A1.11. Selected interatomic distances and angles in (R)$ZnBr_3$(DMSO), $(R)_2CdBr_4$·DMSO and (R)CdI_3(DMSO) at 298(2) K.

Label		Distance (Å)	Label (º)	Angle
			(R)$ZnBr_3$(DMSO)	
Zn–	O1	2.024(5)	O1-Zn-Br1	104.61(17)
	Br1	2.3796(13)	O1-Zn-Br2	100.90(14)
	Br2	2.3820(12)	O1-Zn1-Br3	104.39(17)
	Br3	2.3951(13)	Br1-Zn1-Br3	116.19(5)
			Br2-Zn-Br3	114.07(5)
			Br1-Zn-Br2	114.30(5)
			$(R)_2CdBr_4$·DMSO	
Cd–	Br1	2.6065(5)	Br1-Cd-Br4	105.105(16)
	Br2	2.6035(5)	Br1-Cd-Br3	110.057(17)
	Br3	2.5770(5)	Br4-Cd-Br3	113.073(18)
	Br4	2.5959(5)	Br1-Cd-Br2	114.355(17)
			Br4-Cd-Br2	105.954(18)
			Br3-Cd-Br2	108.321(17)
			(R)CdI_3(DMSO)	
Cd1-	O1	2.247(7)	O1-Cd1-I3	102.5(2)
	I1	2.7283(8)	O1-Cd1-I2	102.3(2)
	I2	2.7201(8)	O1-Cd1-I1	98.97(19)
	I3	2.7305(8)	I3-Cd1-I2	118.37(3)
			I3-Cd1-I1	115.43(3)
			I2-Cd1-I1	114.98(3)

Table A1.12. Selected interatomic distances (Å) and angles (º) in (R)$ZnBr_3$(DMSO), $(R)_2CdBr_4$·DMSO and (R)CdI_3(DMSO) at 100(2) K.

Label		Distance	Label	Angle
			(R)$ZnBr_3$(DMSO)	
Zn–	O1	2.026(3)	O1-Zn-Br3	104.17(9)
	Br1	2.38898)	O1-Zn-Br1	100.82(9)
	Br2	2.3967(7)	Br3-Zn-Br1	114.20(3)
	Br3	2.3812(7)	O1-Zn1-Br2	103.86(9)
			Br3-Zn-Br2	116.59(3)
			Br1-Zn-Br2	114.54(3)
			$(R)_2CdBr_4$·DMSO	
Cd–	Br1	2.571(2)	Br1-Cd-Br4	108.55(4)
	Br2	2.602(2)	Br1-Cd-Br3	112.49(5)
	Br3	2.5954(17)	Br4-Cd-Br3	105.47(5)
	Br4	2.5943(17)	Br1-Cd-Br2	110.80(3)
			Br4-Cd-Br2	114.92(6)
			Br3-Cd-Br2	104.53(4)
			(R)CdI_3(DMSO)	
Cd1-	O1	2.262(6)	O1-Cd1-I3	100.83(16)
	I1	2.7422(8)	O1-Cd1-I2	102.28(17)
	I2	2.7421(8)	O1-Cd1-I1	99.09(15)
	I3	2.7273(8)	I3-Cd1-I2	118.29(3)
			I3-Cd1-I1	115.13(3)
			I2-Cd1-I1	116.37(3)

A1.3 Chapter 4 Figures and Tables

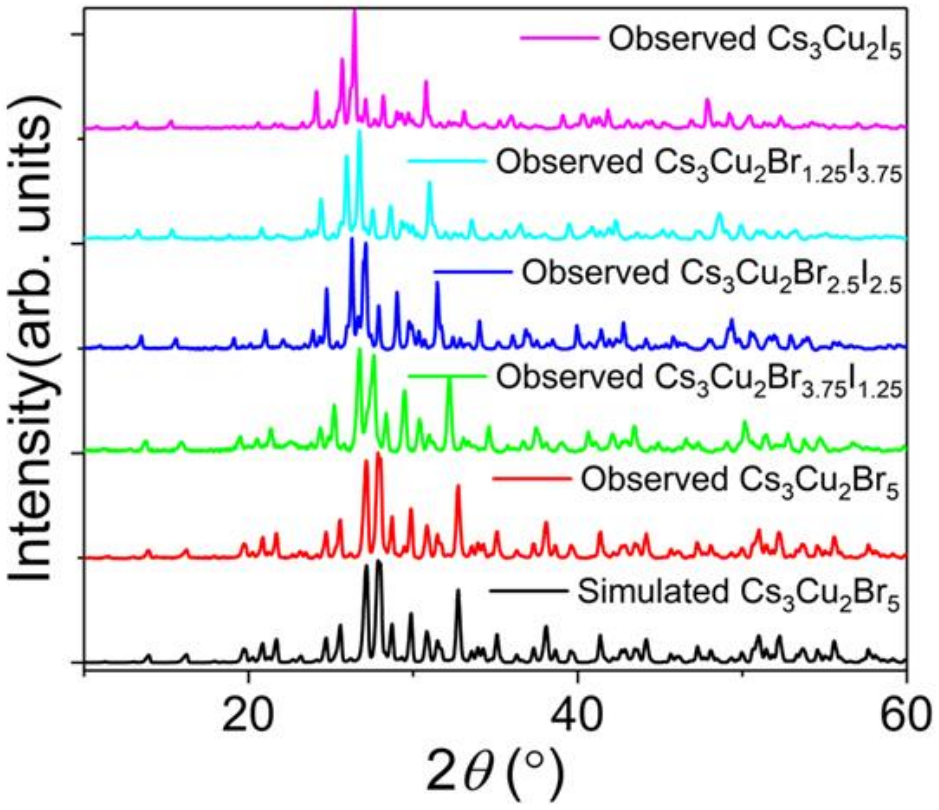


Figure A1.14. Simulated and observed powder X-ray diffraction patterns showing how the patterns change as a function of increasing I content.

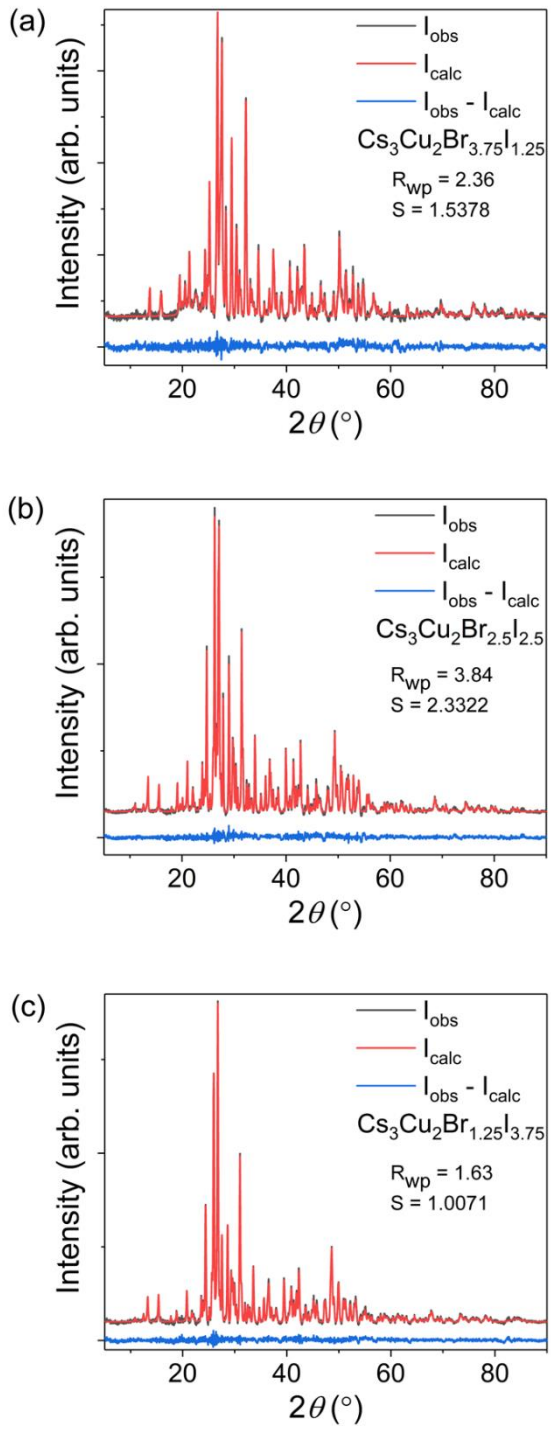


Figure A1.15. Powder X-ray diffraction data with Pawley fittings and refinement (R_{wp}) and scaling (S) factors for the $Cs_3Cu_2X_5$ Br-I alloys (a) $Cs_3Cu_2Br_{3.75}I_{1.25}$, (b) $Cs_3Cu_2Br_{2.5}I_{2.5}$, and (c) $Cs_3Cu_2Br_{1.25}I_{3.75}$.

Table A1.13. Selected interatomic distances (Å) and angles (º) in $CsCu_2X_3$ determined using Crystal Maker software from crystallographic data reported in literature,[434-435, 483] labeled in the convention as shown in Figure 1(d).

Label		**Distance**	**Label**	**Angle**
Cl				
Cu1 -	Cu1’	2.796(5)	Cl1-Cu1-Cl2	119.30(9)
	Cu2	3.119(2)	Cl1-Cu1-Cl3	107.33(5)
	Cl1	2.490(1)	Cl1-Cu1-Cl4	109.49(2)
	Cl2	2.272(8)	Cl2-Cu1-Cl3	109.49(2)
	Cl3	2.273(0)	Cl3-Cu1-Cl4	102.44(9)
	Cl4	2.490(4)	Cl2-Cu1-Cl4	119.30(9)
Br				
Cu1 -	Cu1’	2.907(2)	Br1-Cu1-Br2	106.41(4)
	Cu2	3.079(8)	Br1-Cu1-Br3	108.15(5)
	Br1	2.570(8)	Br1-Cu1-Br4	108.61(0)
	Br2	2.427(0)	Br2-Cu1-Br3	108.61(0)
	Br3	2.427(0)	Br3-Cu1-Br4	116.48(2)
	Br4	2.571(4)	Br2-Cu1-Br4	106.41(4)
I				
Cu1 -	Cu1’	3.048(8)	I1-Cu1-I2	109.80(1)
	Cu2	3.143(2)	I1-Cu1-I3	107.10(2)
	I1	2.703(4)	I1-Cu1-I4	108.91(0)
	I2	2.604(2)	I2-Cu1-I3	114.24(4)
	I3	2.604(2)	I3-Cu1-I4	114.24(4)
	I4	2.703(0)	I2-Cu1-I4	109.80(1)